UNIVERSITÄT BONN

Gravity Tests with Pulsars Using New-Generation Radio Telescopes

Dissertation

zur

Erlangung des Doktorgrades (Dr. rer. nat.)

der

Mathematisch-Naturwissenschaftlichen Fakultät

der

Rheinischen Friedrich-Wilhelms-Universität Bonn

von

Huanchen Hu

aus

Tianjin, China

Bonn, 18.10.2022

Angefertigt mit Genehmigung der Mathematisch-Naturwissenschaftlichen Fakultät der Rheinischen Friedrich-Wilhelms-Universität Bonn

Dieser Dissertation ist auf dem publication server bonndoc der ULB Bonn elektronisch publiziert (URN: https://nbn-resolving.org/urn:nbn:de:hbz:5-70590).

Promotionskommission:

Erstgutachter:	Prof. Dr. Michael Kramer
Zweitgutachter:	Prof. Dr. Norbert Langer
Fachnahes Mitglied:	Prof. Dr. Simon Stellmer
Fachfremdes Mitglied:	Prof. Dr. Valentin Blomer

Tag der Promotion:	18.04.2023
Erscheinungsjahr:	2023

Summary

Pulsar timing is a powerful tool for studying a wide range of questions in fundamental physics, including the equation of state (EOS) of super-dense matter, tests of general relativity (GR) and alternative theories of gravity, and searching for a gravitational wave (GW) background at nanohertz regime. This dissertation investigates these problems using new-generation radio telescopes: the MeerKAT telescope, the Five-hundred-meter Aperture Spherical radio Telescope (FAST), and the future Square Kilometre Array (SKA).

The first two studies focus on the still unique Double Pulsar system, PSR J0737−3039A/B. Being one of the most compact binary pulsar systems, a wealth of relativistic phenomena has been tested with unparalleled precision in the strong-field regime. With the superior sensitivity of new-generation radio telescopes, various higher-order contributions predicted by GR can be precisely tested, thereby allowing a measurement of pulsar A's moment of inertia (MOI). Such a measurement can be made via relativistic spin-orbit coupling, with the spin-down mass loss taken into account for the first time in the analysis. Based on the first MeerKAT observations of A, I simulate realistic data expected for MeerKAT and the SKA in the near future. The results suggest that an MOI measurement with 11% accuracy (68% confidence) is possible by 2030, which can provide complementary constraints on the EOS of nuclear matter. If by then the EOS is well constrained, it will allow a 7% test of Lense-Thirring precession or a 3σ-measurement of the next-to-leading-order (NLO) GW damping.

With 3-yr MeerKAT observations of PSR J0737−3039A, I then study gravitational signal propagation effects in the Double Pulsar system, in particular the NLO effects predicted by GR. These include the retardation effect caused by the movement of pulsar B while the radio signal of A propagates across the system and the deflection of the signal of A by the gravitational field of B. The result provides an independent confirmation of the NLO signal propagation effects and is 1.65 times better than the previous measurement from 16-yr data. Novel effects like lensing and profile variations caused by latitudinal deflection are also investigated but proved to be not measurable with the current data.

Recently, a new timing model has been developed for testing scalar-tensor gravity with binary pulsars. As a demonstration of this model, I explore the prospects of testing Damour–Esposito-Farèse (DEF) gravity by simulating realistic future data of the pulsar-white dwarf system PSR J2222−0137 and hypothetical pulsar-black hole systems for a number of large telescopes, including FAST. The results indicate that future observations can significantly improve the constraints on DEF gravity, and pulsar-black hole systems have the potential to place the tightest limit for a large part of the DEF gravity parameter space.

Finally, to facilitate the detection of nanohertz GWs with pulsar timing arrays, I extend and correct the time offset measurements between the maser clock at the Effelsberg telescope and UTC. This rescues more than two years of timing data with Effelsberg and improves the accuracy of the time tagging of observations, which are critical for pulsar timing. In addition, phased-array observations have been carried out with Effelsberg and FAST, which can dramatically increase the sensitivity of telescopes and advance GW detection. By coherently adding data from the largest radio telescopes in Europe and China, the world's largest and most powerful pulsar telescope will finally materialise.

The Chinese word for *universe* "宇宙 (Yǔ Zhòu)" originates from the Chinese classic *Shizi* written by Shi Jiao during the Warring States period:

四方上下曰宇，往古来今曰宙。

尸佼，约前390-前330

Yǔ means the four directions (north, east, south, and west) and up and down,
and **Zhòu** includes the past and the present.

Shi Jiao, c. 390-330 BCE

Prelude

反者道之动；弱者道之用。天下万物生于有，有生于无。

——老子《道德经》第四十章

道生一，一生二，二生三，三生万物。万物负阴而抱阳，冲气以为和。

——老子《道德经》第四十二章

约公元前五世纪

Reversion is the action of Tao. Gentleness is the function of Tao. The things of this world come from Being, and Being (comes) from Non-being.

Out of Tao, One is born; Out of One, Two; Out of Two, Three; Out of Three, the created universe. The created universe carries the yin at its back and the yang in front; Through the union of the pervading principles it reaches harmony.

Laozi, Tao Te Ching, ch. 40 & ch. 42, c. 5th century BCE
(Translated by Lin Yutang)

. . . . . .

When I began to perceive the world, I asked my father what he had studied at university. He said, "Astrophysics," with a gleam in his eyes. Even though I did not fully understand what it meant at the time, a seed was planted in my heart.

For various reasons, my father could not continue to pursue this journey, but some hopes were pinned on my name. I later learned that the name my father intended to give me at first was 寰(Huán)宸(Chén), meaning the Universe and Polaris, respectively. Unfortunately, the pronunciation of this name is rather awkward, so it was eventually changed to 奂(Huàn)晨(Chén), meaning brilliant morning. The latter character is composed of the Sun and stars. Interestingly, my family name 胡 also contains a celestial body, the Moon. Regardless of these, I was curious about Nature and in particular the outer space since my early childhood. My father was always able to answer my one-hundred-thousand whys with his encyclopedic knowledge. Among these, the most impressive parts (that I still remember) were the discussions about science fiction and extraterrestrial life.

When I was nine years old, knowing a moderate number of common Chinese characters, my mother introduced a literary classic to me, the *Tao Te Ching*. Two of my favourite chapters are presented above. Without fully understanding the meaning of these ancient words at the time (and even now), I was absorbed in Laozi's wise words and amazed by his profound insights into the principle of the universe, *Tao*. Undoubtedly, studying this classic had a lasting impact on me later in my life.

On my path forward, the first two physics teachers also play important roles. The principal of my middle school, Mr. Huaide Niu (牛怀德), gave me my first systematic physics lessons in a clear and interesting way. His rigorous attitude to physics greatly inspired me. He also encouraged students to do hands-on experiments to deepen our understanding of physics. My high school teacher, Mr. Wei Chen (陈巍), also did an excellent job. His lessons had always been vivid and full of passion. His enthusiasm for physics deeply impressed me and shaped me to think independently. It was clear at the early stage of my high school time that I wanted to explore more about physics, and one of the things that fascinated me most was the motion of celestial bodies and the power that governs them — *gravity*.

Naturally, I decided to study astrophysics at the university. I'm grateful that my parents have always been respectful and supportive of my decisions. And so the journey to explore the Universe began! At university, I voyaged through various fields of astronomy and the one that I was most enthusiastic about was still gravity — the principle of the Universe at the macroscopic scale. I also became interested in the ripples in spacetime, especially with the successful direct detection of gravitational waves in 2015.

What really led me here, however, was a crush at the beautiful Lake Como in Northern Italy. In the summer of 2017, I attended a course on Gravitational Waves and Cosmology in the International School of Physics "Enrico Fermi".[1] The course covered a variety of topics in these fields given by renowned researchers, from theories to simulations, and from experiments to observations. I particularly gravitated to a talk on pulsars given by Prof. Michael Kramer. Not having much knowledge previously, I was impressed by the wide range of strong-field gravitational experiments offered by pulsars and their capability to detect gravitational waves in the form of a pulsar timing array. Thankfully, that lecturer became my Ph.D. supervisor and gave me the opportunity to work on these thrilling projects, so that I could start this fantastic journey.

[1] I heartily appreciate the kind assistance offered by Prof. Nicola Vittorio and the full support of the Italian Physical Society, which made this trip possible.

Contents

Nomenclature

Physical constants

The values used in this dissertation are based on CODATA recommended values 2018 (Tiesinga et al., 2021).[2]

Speed of light in vacuum	c	$= 299\,792\,458\ \mathrm{m\,s^{-1}}$
Electron charge	e	$= 1.602\,176\,634 \times 10^{-19}$ C (coulombs)
Electron mass	m_e	$= 9.109\,383\,7015(28) \times 10^{-31}$ kg
Gravitational constant	G	$= 6.674\,30(15) \times 10^{-11}\ \mathrm{m^3\,kg^{-1}\,s^{-2}}$
Boltzmann constant	k_B	$= 1.380\,649 \times 10^{-23}\mathrm{J\,K^{-1}}$

Astronomical constants and units

Astronomical unit	1 AU	$= 1.495\,978\,707 \times 10^{11}$ m
Parsec	1 pc	$= 648\,000/\pi$ AU
Milliarcsecond	1 mas	$= \pi/648\,000\,000$ rad
Nominal solar mass parameter	$(\mathcal{GM})^\mathrm{N}_\odot$	$= 1.327\,1244 \times 10^{20}\ \mathrm{m^3 s^{-2}}$
(IAU 2015 Resolution B3, Prša et al., 2016)	$T_\odot$	$= (\mathcal{GM})^\mathrm{N}_\odot/c^3 \approx 4.925\,490\,947\,641\ \mu$s
Solar mass (derived)	$\mathrm{M}_\odot$	$= (\mathcal{GM})^\mathrm{N}_\odot/G \approx 1.998\,410(45) \times 10^{30}$ kg

List of symbols

$\odot$	The Sun
$\varnothing_\mathrm{eff}$	Effective diameter of radio telescope
α	Right ascension (RA) of source position in equatorial coordinate
δ	Declination (DEC) of source position in equatorial coordinate
α_0, β_0	Coupling strength parameters in STG
β_O	Dimensionless orbital velocity, $(GMn_\mathrm{b})^{1/3}/c$
$\Gamma^\mathrm{B}_\mathrm{A}, \Gamma^\mathrm{A}_\mathrm{B}$	Strong-field coupling function
γ_E	Amplitude of the Einstein delay
Λ_u	Argument of the Shapiro delay
μ_α, μ_δ	Proper motion in RA, DEC
Δ_R	Rømer delay
Δ_E	Einstein delay
Δ_S	Shapiro delay or signal propagation delay (in the case of the Double Pulsar)
Δ_A	Aberration delay
δ_r, δ_θ	Relativistic deformation of orbit

[2] *Committee on Data of the International Science Council*, see http://physics.nist.gov/constants.

Θ_0	Galactic circular velocity at the location of the Sun
ν	Pulsar spin frequency
$\dot{\nu}$, $\ddot{\nu}$	First/second spin frequency derivative
π_x	Timing parallax
ρ_0	Nuclear density
$\rho_{\rm drip}$	Neutron drip density
$\sigma_{\rm A,B}$	Generic strong-field spin-orbit coupling constant
$\sigma_{\rm J}$	Jitter noise
$\sigma_{\rm TOA}$	TOA uncertainty
$\tau_{\rm s}$	Scattering time
Φ	Newtonian gravitational potential
ϕ	Rotational phase of pulsar
χ^2, $\chi^2_{\rm red}$	Chi-squared test, reduced
ψ	Longitude of pulsar with respect to the ascending node
Ω	Longitude of the ascending node
$\Omega_{\rm p}^{\rm SO}$	Geodetic spin precession of pulsar
ω	Longitude of periastron
$\dot{\omega}$	Relative advance of periastron
$\mathcal{A}, \mathcal{B}$	Aberration coefficients
$A_{\rm eff}$	Effective collecting area of a telescope
$a_{\rm p}$	Semi-major axis of pulsar's orbit
$a_{\rm R}$	Semi-major axis of the relative orbit
b	Galactic latitude
l	Galactic longitude
b_0	Slope parameter at the radius of the Sun (see Eq. 3.16)
$\mathcal{D}$	Dispersion constant
D	Doppler factor between SSB and pulsar system
d	distance
$\dot{E}^{\rm rot}$	Rotational kinetic energy
e^-	Electron
e	Orbital eccentricity (or electron charge for Eq. 2.3)
$e_{\rm T}$	Time eccentricity
f	Frequency
$\mathcal{G}$	Generalised gravitational constant
G	Telescope gain
H	Hydrogen
h, $h_{\rm c}$	Strain/characteristic strain of gravitational waves
$I_{\rm A}$	MOI of pulsar A
i	Orbital inclination
K_z	Vertical contribution of the Galactic acceleration
M	Total system mass
$m_{\rm A}$	Mass of pulsar A
$m_{\rm B}$	Mass of pulsar B
$m_{\rm c}$	Mass of companion
$m_{\rm p}$	Mass of pulsar
N	Nuclei
N_0	Pulse number at a reference epoch t_0

$N_{\rm free}$	Degree of freedom
n	Neutron
$n_{\rm b}$	Orbital angular frequency, $2\pi/P_{\rm b}$
$n_{\rm e}$	Electron number density
P	Spin period of pulsar
$\dot{P}$	Spin period derivative
$P_{\rm b}$	Orbital period of a binary system
$\dot{P}_{\rm b}$	Change of orbital period
p	Proton
R	Mass ratio $m_{\rm A}/m_{\rm B}$
R_0	Distance from the Sun to the Galactic centre
r	Range parameter of the Shapiro delay
s	Shape parameter of the Shapiro delay
$S_{\rm mean}$	Mean flux density
T_0	Epoch of periastron passage
$T_{\rm p}$	Proper time of a pulsar
$T_{\rm sys}$	System temperature
t	Time
t_0	Reference epoch
$t_{\rm corr}$	Time correction
$t_{\rm D}$	Dispersive time delay
$t_{\rm int}$	Integration time
$t_{\rm SSB}$	Barycentric TOA
$t_{\rm topo}$	Topocentric TOA
u	Relativistic eccentric anomaly
v	Velocity
W	Pulse width
x	Projected semi-major axis of the pulsar orbit
$\dot{x}$	Change of projected semi-major axis
$x_{\rm A,B}$	Mass fraction $m_{\rm A,B}/M$
z	Galactic height
z_s	Logarithmic Shapiro shape, $z_s \equiv -\ln(1-s)$

Frequently used acronyms

BIPM	Bureau International des Poids et Mesure
BH	Black hole
DD	Damour-Deruelle
DEF	Damour–Esposito-Farèse
DM	Dispersion measure
DNS	Double neutron star
EFF	Effelsberg 100-m Radio Telescope
EOS	Equation of state
EPTA	European Pulsar Timing Array
FAST	Five-hundred-meter Aperture Spherical Telescope
GBT	Green Bank Telescope
GPS	Global Positioning System

GR	General Relativity
GW	Gravitational wave
GWB	Gravitational wave background
IAU	International Astronomical Union
IPTA	International Pulsar Timing Array
ISM	Interstellar medium
JRT	Jingdong 120-m Pulsar Radio Telescope
LEAP	Large European Array for Pulsars
LIGO	Laser Interferometer Gravitational-Wave Observatory
LISA	Laser Interferometer Space Antenna
LOS	Line of sight
LT	Lense-Thirring (Chapter 3) or Lovell Telescope (Chapter 5 and 6)
MJD	Modified Julian Date
MOI	Moment of inertia
MS	Main sequence
MSP	Millisecond pulsar
NIST	National Institute of Standards and Technology
NLO	Next-to-leading-order
NRT	Nançay Radio Telescope
NS	Neutron star
PEAPA	Pan-EurAsia Pulsar Array
PK	Post-Keplerian
PN	Post-Newtonian
PPA	Polarisation position angle
PPK	Parameterised post-Keplerian
PSR	Pulsar
PTA	Pulsar timing array
QTT	Xinjiang Qitai 110-m Radio Telescope
RM	Rotation measure
RMS	Root mean square
SKA	Square Kilometre Array
SMBHB	Supermassive black hole binary
S/N	Signal to noise ratio
SRT	Sardinia Radio Telescope
SSB	Solar System barycentre
STG	Scalar-tensor gravity
TAI	International Atomic Time
TCB	Barycentric Coordinate Time
TCG	Geocentric Coordinate Time
TDB	Barycentric Dynamical Time
TOA	Time of arrival
TOV	Tolman-Oppenheimer-Volkoff
TT	Terrestrial Time
UTC	Coordinated Universal Time
VLBI	Very-long-baseline interferometry
WD	White dwarf
WRST	Westerbork Synthesis Radio Telescope

CHAPTER 1

Introduction

1.1 An overview of gravity experiments

Gravity, one of the four fundamental interactions in nature, has been systematically studied for over three centuries.[1] The classical gravity theory formulated by Isaac Newton (Newton, 1687) was derived from empirical observations of planetary motions by Johannes Kepler. Since it came out, Newton's law of universal gravitation had reached a great success, including the prediction of the existence of Neptune on the basis that the motion of Uranus could not be explained by the actions of other planets (for details see e.g. Grosser, 1979). However, with ~150 years of observational data on Mercury, in 1859, Urbain Le Verrier first recognised an unexplained advance in the perihelion of Mercury with Newtonian gravity (Le Verrier, 1859). The modern value of this discrepancy is about 43" per century.

A half-century search on multiple explanations for this discrepancy, including a hypothetical planet ("Vulcan") near Mercury, had yielded no results. Yet things became clearer when an unprecedented theory came out — *General Relativity* (GR). Instead of being seen as an attractive force, gravity is perceived to be the effect of the curvature of four-dimensional spacetime acting on the motion of other objects. Just one week before Albert Einstein presented his field equations of gravitation to the Prussian Academy of Science (Einstein, 1915a), he had successfully demonstrated that his gravity theory naturally explains the anomalous precession of Mercury's perihelion (Einstein, 1915b). This is regarded as the first experimental test of GR in hindsight. Four years later, the second test, the deflection of starlight by the gravity of the Sun, was measured during the total solar eclipse on 29 May 1919 (Dyson et al., 1920), which is in agreement with GR and disfavours "Newtonian prediction" (half of GR's value) or prediction from aether (no deflection).[2] Besides deflection, another effect results from curved spacetime is a time delay, where light takes longer time to travel when passing near a massive body. It was discovered by radio astronomer Irwin Shapiro in 1964 as a prediction of GR (I. I. Shapiro, 1964). The Shapiro delay, together with the other two, forms the classical tests of GR.[3]

Before the 1970s, gravity tests were limited to the Solar System, where only weak-field slow-motion aspects of gravitation can be investigated. It became evident that the Solar System would not be sufficient to be the only testbed for gravity theories, since many alternative theories of gravity agreed with GR so closely in the weak-field slow-motion regime that could pass all the Solar System tests (Will, 1981; Will,

[1] The other three fundamental interactions are electromagnetic interaction, strong interaction and weak interaction.

[2] A hypothetical matter that fills the Universe as the medium of travelling light or gravity.

[3] The three experimental tests proposed by Einstein himself also includes gravitational redshift, in addition to light deflection and perihelion precession of planetary orbits (Einstein, 1916a). But the gravitational redshift, as a consequence of the *Equivalence Principle*, is common to every metric theory of gravity, hence in some regards not a test of GR.

2018). But it does not necessarily mean that they would also agree with predictions in the strong gravity regime. In GR, one often distinguishes strong and weak gravity using the quantity $\epsilon = |\Phi|/c^2$, where Φ denotes the Newtonian gravitational potential and c the speed of light in vacuum. For Solar System, $\epsilon \sim 10^{-6}$; in contrast, at the surface of a neutron star (NS) $\epsilon \sim 0.2$, and near the event horizon of a black hole (BH) $\epsilon \sim 1$, these are the regimes of strong gravity.

The discovery of the first binary pulsar by Russell Hulse and Joseph Taylor in 1974 (Hulse & Taylor, 1975) opened new arenas for precision gravity tests in two new gravity regimes — the *quasi-stationary strong-field regime* and the *radiative regime* (Damour & Taylor, 1992; Wex, 2014). It not only allowed the classical GR tests to be performed in a regime where the spacetime curvature is 13 orders of magnitude larger than that caused by the Sun, but also confirmed the existence of gravitational waves (GWs) predicted by GR for the first time. More specifically, the rate of change of the orbital period measured in this system was consistent with GR's prediction for the rate of orbital energy loss due to GW emission (Taylor et al., 1979). This had immediately excluded certain alternative theories (Will, 1993; Yunes & Siemens, 2013).

Nowadays, thanks to the advanced technology and numerous space missions, Solar System tests have been much improved in precision. With the astrometric satellite *Hipparcos* (Froeschle et al., 1997) in the optical and very-long-baseline interferometry (VLBI) (Lebach et al., 1995; S. S. Shapiro et al., 2004; Fomalont et al., 2009) in the radio, light deflection was confirmed to agree with GR at a precision of 1.5×10^{-4}. Measurement of frequency shifts in radio signals to and from the Cassini spacecraft, with signals passing near the Sun, verified the Shapiro delay to an accuracy of 10^{-5} with GR (Bertotti et al., 2003). In addition, GR has passed many other Solar System tests, including the Lunar Laser Ranging experiment for the de Sitter precession of the Moon's orbit and the strong equivalence principle (Nordtvedt, 1999), the Gravity Probe B for the geodetic and frame-dragging effects (Everitt et al., 2011), and the Lense-Thirring effect with satellite laser ranging (Ciufolini & Pavlis, 2004; Ciufolini et al., 2019).

Meanwhile, many more binary pulsars have been discovered, either accompanied by planets, main-sequence (MS) stars, NSs or white dwarfs (WDs), and even in triple systems.[4] Some of them are excellent laboratories for testing GR and alternative gravity theories, involving the renowned "Double Pulsar", which provides so far the most precise test of quadrupolar GWs (Kramer et al., 2006b; Kramer et al., 2021a). Besides, a global effort using pulsar timing array (PTA) to search for nanohertz GWs from inspiralling supermassive black hole binaries (SMBHBs) has collected data for over two decades, and may soon give us the first detection (Antoniadis et al., 2022).

In addition, on 14 September 2015, the centenary year of the publication of Einstein's general theory of relativity, the Laser Interferometer Gravitational-Wave Observatory (LIGO), for the first time, directly detected the signal of GW — a wave in the fabric of spacetime itself — from merging black holes (B. P. Abbott et al., 2016a). This opens up a new regime for gravity tests: highly dynamical strong field regime.

To compare pulsars with other gravity tests, it is useful to introduce the four gravity regimes (Wex, 2014, see Figure 1.1 for an illustration):

SW *Quasi-stationary weak-field regime*: Masses move slowly compared to the speed of light ($v \ll c$), and the spacetime is nearly flat (close to Minkowski space). A well known example is the Solar System.

SS *Quasi-stationary strong-field regime*: Masses move slowly compared to the speed of light ($v \ll c$), but one or more bodies in the system are strongly self-gravitating. The spacetime in the vicinity of such bodies is strongly curved. Binary pulsars are the prime examples.

[4] A pulsar–black hole binary would be a powerful tool for gravity test, but such a system is still missing (Wex & Kopeikin, 1999; Liu et al., 2014a).

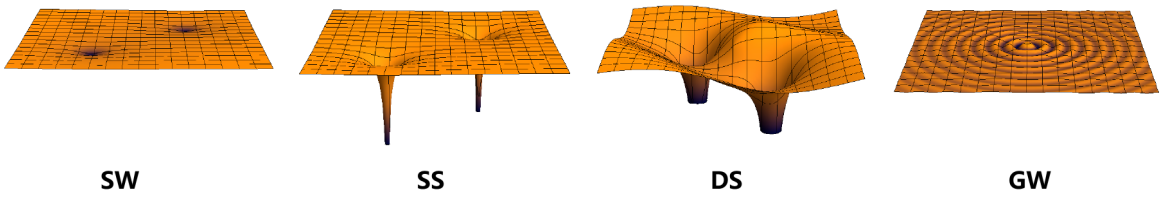

Figure 1.1: Illustration of four different gravity regimes, courtesy of Norbert Wex. SW: quasi-stationary weak-field regime; SS: quasi-stationary strong-field regime; DS: highly-dynamical strong-field regime; GW: radiation regime.

DS *Highly-dynamical strong-field regime*: Masses move at a speed closes to the speed of light ($v \sim c$). The spacetime is strongly curved and highly dynamical near the masses. This is the case for the merging BHs and NSs observed by GW detectors (BH-BH, BH-NS, and NS-NS).

GW *Radiation regime*: Properties of gravitational radiation, or GW. This regime coexists with all three regimes above. However, the GW luminosity of the Solar System is of the order of 10^4 W, about 21 orders of magnitude smaller than that of the Double Pulsar. Another relevant example here is the nanohertz GW emitted by inspiraling SMBHBs, which will soon be detectable with PTA.

To date, after more than a century of observations and examinations, GR has passed all experimental tests with flying colours, including those with binary pulsars. However, there are still enigmas that remain unsolved, such as the incompatibility between GR and quantum mechanics, the difficulty in solving the singularity problem, and the requirement of substantial dark matter and dark energy to explain the observations (Clifton et al., 2012). That's why scientists are still putting lots of effort into testing GR, and seeking for possible deviations from it. Every experimental test is a probe for new physics. In particular, the Double Pulsar system is a prime laboratory for testing gravity in the quasi-stationary strong-field regime, which is the main focus of this dissertation. In the next section, we start with the basics of pulsars, followed by showing how fascinating they are in testing many aspects of gravity.

1.2 Pulsars: precision gravity probes

NSs are named after their main ingredient, *neutrons*, which were discovered by Chadwick (1932). Already before that, Chandrasekhar (1931) had presented a calculation of the maximum mass of a stable WD star, known as *Chandrasekhar limit*,[5] above which the electron degeneracy pressure in the stellar core cannot support against its own gravitational self-attraction, resulting in further gravitational collapse. An independent calculation was done by Landau (1932), which also speculated on the existence of stars heavier than this limit, and concluded that "*the density of matter becomes so great that atomic nuclei come in close contact, forming one gigantic nucleus*". Soon after, based on the observations of supernova explosions, Baade & Zwicky (1934a) made the actual theoretical prediction of NSs that "*supernovae represent the transitions from ordinary stars to neutron stars*"(see also Baade & Zwicky, 1934b; Baade & Zwicky, 1934c). A few years later, Tolman (1939) and Oppenheimer & Volkoff (1939) independently derived the equation of hydrostatic equilibrium for a spherically symmetric star in the framework of GR, known as Tolman-Oppenheimer-Volkoff (TOV) equation. This equation is the basis for constructing (non-rotating) NS models, when supplementing with the key ingredient — the *equation of state* (EOS) of dense matter in NSs, which describes the dependence of pressure on mass density and temperature, where the temperature dependence is negligible.

[5] The accepted value today is about 1.4 solar masses (Hawking & Israel, 1989).

Despite some attempts to search for NSs in X-rays, the association of those X-ray sources with NSs were not convincing at that time (Giacconi et al., 1962; Bowyer et al., 1964). NSs remained theoretical until 1967, when Jocelyn Bell detected repeating radio signals using the Interplanetary Scintillation Array in Cambridge. Further measurements revealed that this pulsating source — *pulsar*, now known as PSR B1919+21, has a great regularity of about 1.337 s, and is located far outside the Solar System (Hewish et al., 1968). More pulsars were soon discovered, while their nature was hotly debated, with hypotheses of being oscillating WDs or NSs. This issue was solved by the discoveries of short-period pulsars: the Vela pulsar (Large et al., 1968) and the Crab pulsar (Staelin & Reifenstein, 1968), with period of only 89 ms and 33 ms. WDs can neither rotate nor oscillate at such a rapid period; oscillating NSs were also ruled out based on the slowdown observed in the period of the Crab pulsar (Richards & Comella, 1969). Finally, the model independently developed by Pacini (1967) before the discovery of PSR B1919+21, and by Gold (1968) shortly after the discovery, won out that *pulsars are rotating magnetised neutron stars*.

In Section 1.2.1, we introduce the fundamental properties of NSs and pulsars that are essential for understanding this work, and refer the interested readers to e.g. Haensel et al. (2007), Lorimer & Kramer (2004), and A. G. Lyne & Graham-Smith (2006) for details and other aspects. In Section 1.2.2, we present scientific applications of pulsars, in particular those that are mostly relevant to this dissertation.

1.2.1 Basics of neutron stars and pulsars

Formation

NSs are the finale of the evolution of MS stars with masses between 10 and 25 solar masses ($M_\odot$) (Heger et al., 2003). A MS star supports itself by balancing the inward self-gravity and outward thermal and radiation pressure from nuclear fusion. Eventually, all active stars evolve to a point that the nuclear fuel in the core is exhausted and fails to resist the gravitational force, resulting in the formation of a compact star. For stars with masses lower than $8\,M_\odot$, like our Sun, its core temperature is insufficient to fuse carbon. After expelling its outer layers and creating a planetary nebula, a core remnant called WD is left, typically composed of carbon and oxygen (CO), and supported by electron degenerate pressure.[6] For stars with masses above $8\,M_\odot$, an iron-rich core forms at the late stage. Once the mass of the core exceeds Chandrasekhar limit, electron degenerate pressure is overcome by gravity and leads to further core collapse and violent explosion, known as core-collapse supernova. A giant neutron-rich nuclei is formed via electron capture. Neutron degeneracy pressure is the last hope to stop gravitational collapse, with the help of repulsive nuclear forces. If the mass of the remnant core is smaller than the TOV limit (Oppenheimer & Volkoff, 1939), i.e., $\sim 3\,M_\odot$, a NS is formed. Otherwise, the combination of neutron degeneracy pressure and nuclear forces is insufficient to support against gravity, and the core inevitably collapses into a BH.

Alternatively, a NS can be formed via Type Ia supernova if a WD accretes enough mass from a binary companion (Nomoto et al., 1984), or merges with a second WD (Webbink, 1984), which exceeds the Chandrasekhar limit.

Structure and the equation of state

NSs are the smallest and densest object known in the Universe, except for BHs and hypothetical objects (e.g. quark stars and strange stars). They have a typical mass of $1.4\,M_\odot$, with a radius of only ~ 10 km, and a mean density about 4×10^{14} times of the Sun. The structure and composition of a NS depends on

[6] Stars with mass lower than $0.5\,M_\odot$ could form helium WDs, and with mass between $8\,M_\odot$ and $10\,M_\odot$ may form oxygen–neon–magnesium WDs. The majority known WDs are CO WDs.

the EOS at supranuclear density, which is still not precisely known, although many models have been proposed (Lattimer & Prakash, 2001; Lattimer & Prakash, 2016). Quite generally, a NS can be divided into four regions as shown in Figure 1.2(a) (Degenaar & Suleimanov, 2018). It is surrounded by a thin *atmosphere* (a few cm) of hydrogen H, and an *ocean* of ion liquid about 100-m thick. Below which is the *crust*, covering about 10% of the radius. The solid *outer crust* consists of electrons e^- and nuclei N, and extends from the bottom of the atmosphere to the neutron drip density, $\rho_{\rm drip} \sim 4 \times 10^{11}\,{\rm g\,cm^{-3}}$. The *inner crust* also contains neutrons n as it covers the region from the neutron drip density, where neutrons begin to drip out from the nuclei, to nuclear density $\rho_0 \sim 2.3 \times 10^{14}\,{\rm g\,cm^{-3}}$, where neutrons transform to superfluid. The density and pressure keep rising with depth, beyond ρ_0 one enters the *core*, which makes up the major portion of a NS. All nuclei are dissolved here, leaving abundant degenerate neutrons and a few percent of protons p and electrons in the *outer core*. The ingredients of the *inner core* is unclear, which may involve exotic matters such as hyperons, pions, and kaons. The central density can be as high as (10-15)ρ_0, depending on the EOS.

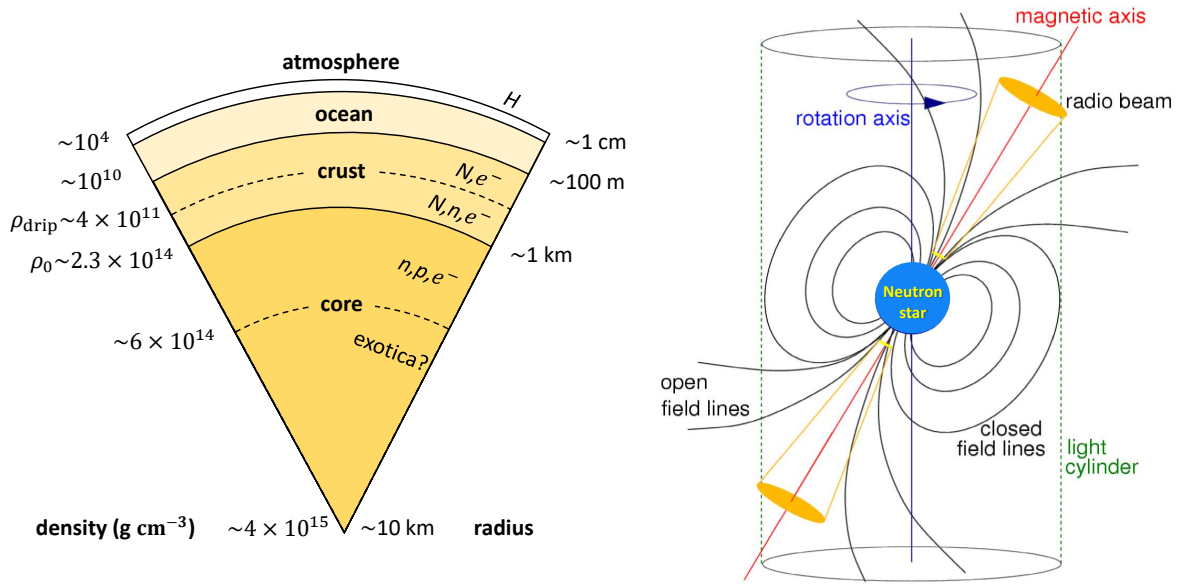

(a) NS structure

(b) pulsar model

Figure 1.2: (a) Schematic structure of a NS adapted from Degenaar & Suleimanov (2018). Rough numbers for density and size of each region are shown along the sides of the sector. Main composition are listed, where H stands for hydrogen, N for nuclei, e^- for electrons, n for neutrons, and p for protons. The dashed lines separate the inner and outer parts of the crust and core. (b) Simplified model of pulsar magnetosphere, adapted from Lorimer & Kramer (2004).

Pulsar model

Pulsars are strongly magnetised NSs, with dipolar field strength about 10^{7-14} gauss, depending on the age and the type of pulsars. These strong magnetic fields are consistent with the magnetic flux conservation from their progenitor stars (Woltjer, 1964). Magnetic dipole radiation is powered by rotational kinetic energy of the NS, and creates a plasma-filled magnetosphere surrounding the pulsar. A simplified model is shown in Figure 1.2(b). The magnetosphere co-rotates with the pulsar until it reaches the speed of light. This limit defines an imaginary surface called *light cylinder*, with radial distance $r_c = c/\Omega$, where Ω is angular velocity. The magnetic field lines are closed within the light cylinder and open beyond the light cylinder. Radio beams are emitted along the magnetic axis of the pulsar, which is not necessarily aligned

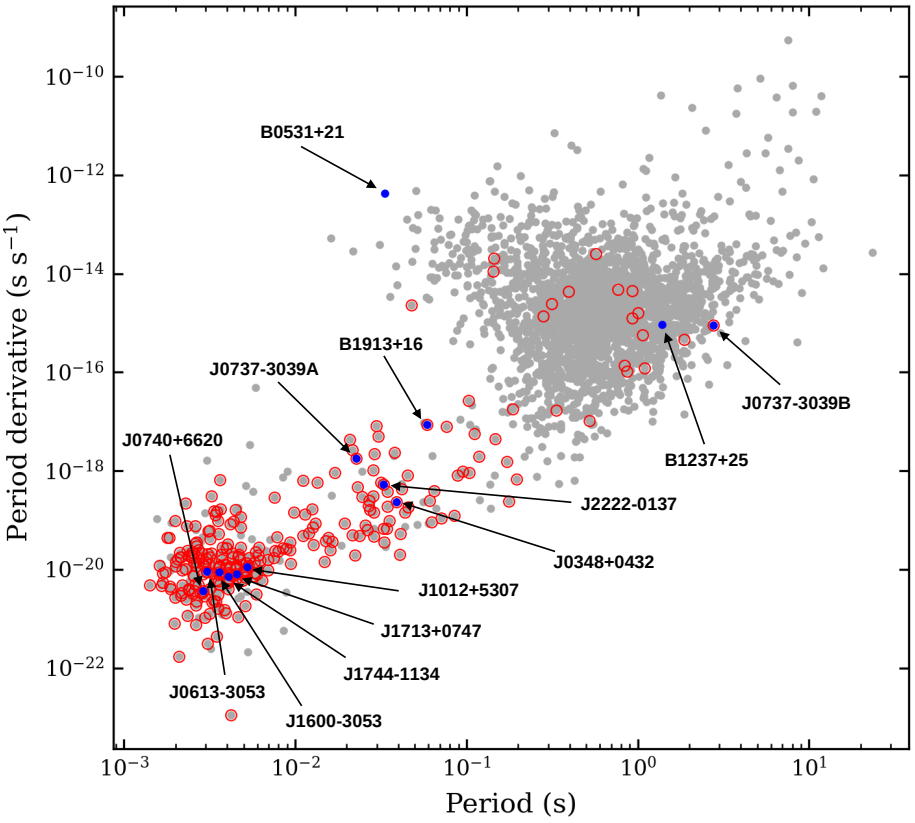

Figure 1.3: $P - \dot{P}$ diagram of known pulsars plotted in log-log scale. Pulsars in binary systems are marked with a red circle, and pulsars featured in this dissertation are highlighted in blue with their name labelled. The cluster of pulsars on the top right are normal pulsars, whereas MSPs are on the bottom left. Data were taken from the ATNF Pulsar Catalogue (version 1.68, Manchester et al., 2005).

with the rotational axis, possibly due to asymmetrical supernova explosion. This misalignment allows the beam to be seen once or twice (if the magnetic and spin axes are almost orthogonal) per rotation of the pulsar if it happens to sweep across the Earth, and leads to pulsed signals like a lighthouse. Radio beams are generally considered to be formed in the open field line region, where the charged particles are accelerated along the curved field lines due to a large electrostatic field induced by the magnetic field, and resulting in curvature radiation most readily observed at radio frequencies (A. G. Lyne & Graham-Smith, 2006).

Pulsar evolution

NSs rotate extremely fast after their formation owing to the conservation of angular momentum. Over time, pulsars gradually slow down due to the loss of rotational kinetic energy. Both spin period P and the spin-down rate $\dot{P}$ can be precisely measured through observations. These quantities provide a classical way to track the spin evolution of pulsars via the $P - \dot{P}$ diagram shown in Figure 1.3. To date, more than 3000 pulsars have been discovered (ATNF Pulsar Catalogue,[7] Manchester et al., 2005), where majority are *normal pulsars* ($P \sim 0.5$ s and $\dot{P} \sim 10^{-15}$s s^{-1}) occupying the top right of the diagram, and *millisecond pulsars* (MSPs, $P \lesssim 20$ ms and $\dot{P} \sim 10^{-20}$s s^{-1}) populating the bottom left.

A simplified model to explain the evolution of various types of pulsar systems is shown in Figure 1.4

[7] https://www.atnf.csiro.au/research/pulsar/psrcat/

(see e.g. Bhattacharya & van den Heuvel, 1991). We start from a binary star system, as more than 70% massive stars are found to have companions (Sana et al., 2012). The initially more massive star (primary) evolves first to form a NS via supernova explosion, where the majority of binaries disrupt during this catastrophic process and produce a high-velocity isolated NS and a runaway star. The young pulsar is born with a short spin period, and gradually spins down as a normal pulsar over a timescale of 10^{6-7} yr, moving from the top left of the $P - \dot{P}$ diagram towards bottom right, and eventually becomes too faint to be detected.

For those few binaries that survive, and in which the secondary star is massive enough to evolve into a red giant and overflows the Roche lobe, the pulsar accretes matter from its companion, forming an accretion disk and is visible as an X-ray binary. The mass accretion transfers orbital angular momentum to the NSs and spins them up to a shorter period, hence these pulsars are often referred to as *recycled pulsars*. For low-mass systems, the mass transfer lasts longer and spins up the NS to a few milliseconds. At the end, the secondary star sheds its outer layers and results in a MSP-WD binary. For high-mass systems, the secondary star is massive enough to undergo a supernova explosion and forms a NS. If the binary is lucky enough to survive, the result is a double NS (DNS) system. Such systems are rare because they have to survive two supernova explosions.

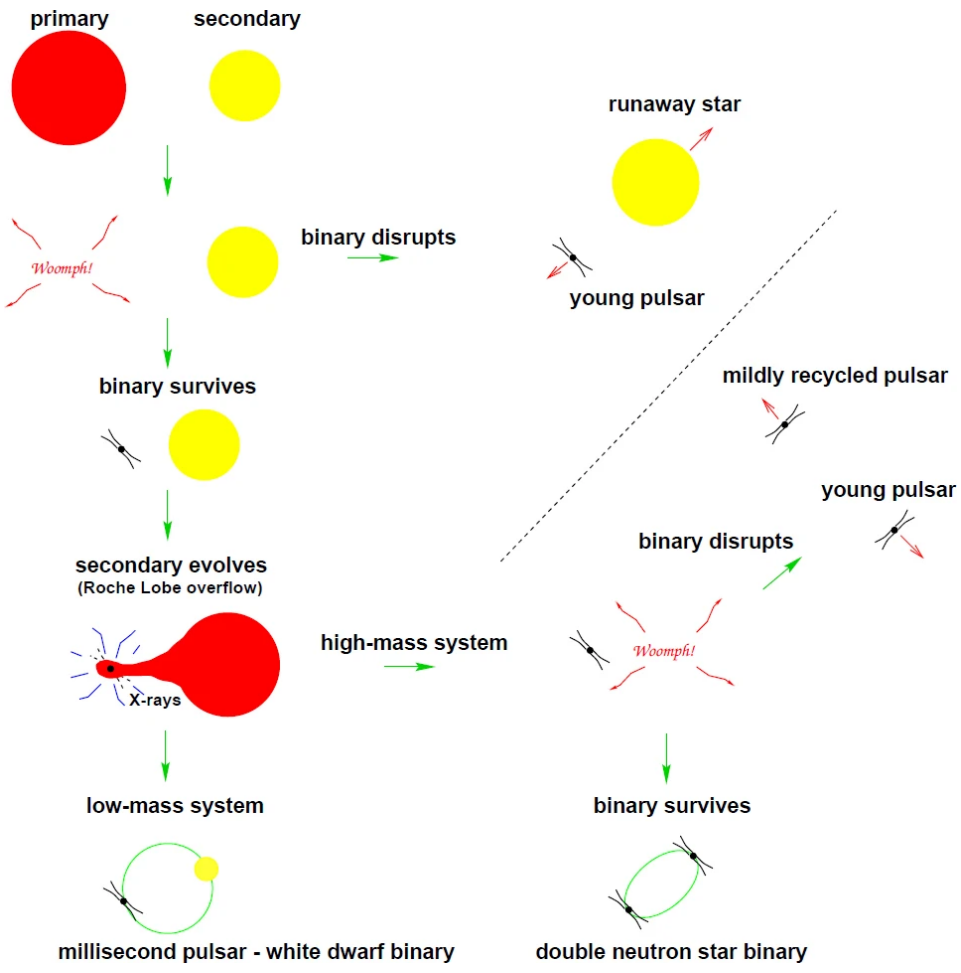

Figure 1.4: Evolution scenario cartoon involving binary pulsars. Figure reproduced from Lorimer (2001) under a Creative Commons Attribution 4.0 International License.

1.2.2 Interesting science with pulsars

MSPs are very stable in rotation, some of them can rival the best atomic clocks in terms of stability on long timescales (G. Hobbs et al., 2012; G. Hobbs et al., 2020). This characteristic makes them the ideal tool for precision measurements. Recording the arrival time of pulses at radio telescopes and keeping track of their rotational phases provide access to their orbital information. This technique is called *pulsar timing*, more details to follow in Chapter 2.

The first gravity tests with NSs were enabled by the discovery of the Hulse-Taylor pulsar, PSR B1913+16, i.e. the first binary pulsar and also the first DNS system (Hulse & Taylor, 1975). It provides the first evidence for the existence of GWs through the back reaction of GWs on its orbit (Taylor et al., 1979). Yet the current record of the most precise measurement of quadrupolar GW comes from the Double Pulsar, PSR J0737−3039A/B, validating GR at a level of 1.3×10^{-4} with 95% confidence (Kramer et al., 2021a). This system consists of a recycled 23-ms pulsar (A) and a young 2.8-s pulsar (B), orbiting each other in a highly relativistic, slightly eccentric 2.45-hr orbit (Burgay et al., 2003; A. G. Lyne et al., 2004). In addition, this unique system provides a wide range of gravity tests more than in any other pulsar systems, including orbital precession, time dilation (second order Doppler effect and gravitational redshift), Shapiro delay, spin precession, and two recently enabled tests: relativistic deformation of the orbit and higher-order signal propagation effects in a strong-field regime (Kramer et al., 2006b; Breton et al., 2008; Kramer et al., 2021a). Some of these are rarely tested or only accessible with this system. Further studies on higher-order signal propagation effects in the Double Pulsar are continued in this work, based on high precision data from the MeerKAT telescope (Chapter 4).

Binary pulsars are precision gravity probes, not only in testing GR, but also for constraining alternative theories of gravity. In particular, due to asymmetry in their compactness, PSR-WD systems, such as PSR J2222−0137, are useful tools to constrain dipolar GWs and the variation of the gravitational constant, which are predicted in many alternative theories due to a violation of the strong equivalence principle (Will, 2014; Wex, 2014; Wex & Kramer, 2020; Guo et al., 2021). Despite the similar compactness of two bodies, PSR J0737−3039A/B also provides some of the best limits on these tests for certain alternative theories (Kramer et al., 2021a). Prospects of testing certain alternative theories with binary pulsars of various compactness will be discussed in Chapter 5.

Apart from probing gravity in the strong-field regime, pulsars are also important for understanding NS structure. The rotational instability observed in pulsars, known as "glitches", enables studies on NS's solid crust, superfluid interior, and couplings between them (Andersson et al., 2012; Haskell & Melatos, 2015). Through the measurement of relativistic effects in binary pulsars, the masses of pulsar and its companion can be determined with excellent precision. The heaviest pulsars, such as PSR J0348+0432 (Antoniadis et al., 2013) and PSR J0740+6620 (Fonseca et al., 2021), yield that the maximum NS mass needs to be at least $2M_{\odot}$, which excludes a number of EOSs. As will be shown in Chapter 3, PSR J0737−3039A promises to provide a reliable measurement of the moment of inertia (MOI) via spin-orbit coupling in the near future, which will further improve our knowledge of the EOS. In fact, the unrivalled timing precision has already allowed us to start probing the MOI of PSR J0737−3039A (Kramer et al., 2021a).

Furthermore, pulsars can serve as tools for detecting GWs at nanohertz frequencies (Sazhin, 1978; Detweiler, 1979) in the form of a PTA (Foster & Backer, 1990). The primary sources of GWs in the nanohertz band are inspiralling SMBHBs, with orbital timescales of decades. The PTA project is aiming to search for a common stochastic signal of GW background (GWB) from many superposed SMBHB GW signals. Such a detection can provide unique insight into SMBHB evolution and place astrophysical constraints on the SMBHB population. This work has contributed to improving the accuracy of the PTA in two ways: the accuracy of clocks and the sensitivity of telescopes (Chapter 6).

In addition, pulsar observations provide valuable information on plasma physics in extreme environments (Kramer & Stairs, 2008), on the interstellar medium and the structure of the Galaxy (e.g. Han et al., 2018), and on the processes of stellar and binary evolution (e.g. Tauris et al., 2017), just to name a few.

1.3 Chapter summaries

This dissertation aims to address four scientific questions using pulsar timing: improving our knowledge of the EOS at supranuclear density, increasing the precision of strong-field gravity tests and exploring higher-order relativistic effects, constraining certain alternative gravity theories, and enhancing the sensitivity of nanohertz GW detection. This chapter provided basic knowledge about NSs and pulsars that helps in understanding this work and demonstrated the important role of pulsars in testing gravity in the strong-field and radiative regimes. The remainder of this dissertation is organised as follows:

Chapter 2 provides an overview of the pulsar timing technique employed throughout this study. This includes a description of pulsar observations and propagation effects caused by the interstellar medium, as well as a basic introduction to data reduction and data analysis methods.

Chapter 3 revisits the previously proposed method for measuring the MOI of binary pulsar via relativistic spin-orbit coupling and applies it in pulsar analysis for the first time. The prospect of the MOI measurement of PSR J0737−3039A is studied by simulating realistic future data based on the early MeerKAT observations, with spin-down mass loss considered in the analysis. Such an MOI measurement will provide important additional constraints on the EOS of NSs. The prospects for testing Lense-Thirring effect and measuring the next-to-leading-order (NLO) GW damping are also discussed, as are expected MOI measurements of DNS systems with shorter orbital periods than the Double Pulsar from future discoveries.

Chapter 4 reports on the timing results of PSR J0737−3039A based on three years of MeerKAT observations. It highlights the improved measurements on Shapiro delay and NLO signal propagation effects, including the retardation effect caused by the movement of pulsar B during the propagation of the signal of A and the deflection of the signal of A by the gravitational field of B. Novel effects like lensing and latitudinal deflection are also investigated using observation data and simulated future data.

Chapter 5 explores the prospects of testing Damour–Esposito-Farèse (DEF) gravity using the recently developed timing model for scalar-tensor gravity with binary pulsars. Included are a basic background of DEF gravity and a brief summary of this timing model, as well as application to the pulsar-white dwarf system PSR J2222−0137 using existing and simulated data for a number of large telescopes. The constraints on DEF gravity expected from pulsar-black hole systems are also investigated.

Chapter 6 mainly discusses two efforts that help to facilitate the detection of nanohertz GWs with PTAs. The first part documents the work of extending and correcting the clock offsets between the maser at the Effelsberg telescope and UTC, which rescued more than two years of timing data with Effelsberg and improves the accuracy of the time tagging of observations. The second part describes a collaborative project to build the most sensitive pulsar telescope through phased-array observations with the largest radio telescopes in Europe and China. Preliminary results and prospects based on the first observations are discussed.

Chapter 7 concludes this dissertation with a brief summary of the main results of this work and a discussion of ongoing and future work.

CHAPTER 2

Pulsar timing

As seen in Chapter 1, the rotational stability of pulsars enables studies of a wide variety of phenomena that affect their pulse propagation by monitoring the pulsar rotation, with a typical cadence of weeks to months over a span of years to decades. This technique, *pulsar timing*, aims at creating a coherent timing solution that accounts for every rotation of the pulsar from the first observation to the last. Dealing with data at precision from a few microseconds to sub-hundred nanoseconds, a sophisticated timing analysis process is required to ensure the precision of data and enable high accuracy gravity tests. This chapter provides an overview of pulsar timing technique, including the effects that need to be considered in the analysis. The contents are limited to those aspects most relevant to this dissertation and not intended to be exhaustive. For a more comprehensive description, see e.g., Lorimer & Kramer (2004).

2.1 Effects of propagation through ionised media

The space between the star systems in the Galaxy is filled with a dilute medium called *interstellar medium* (ISM), which contains (among others) ionised gas. While propagating through the space from the pulsar to Earth, the radio waves are influenced by their interactions with the ionised media, primarily the ISM. In addition, two other distinct media also play a role: the interplanetary medium dominated by the *Solar wind* and Earth's ionosphere. Due to the interaction with the ionised media, the observed pulsar signals are affected in several ways, including frequency-dependent *dispersion* delays, change of polarisation due to *Faraday rotation*, intensity variations caused by *scintillation*, and *pulse scattering* as a consequence of multi-path propagation. These effects need to be accounted for or carefully treated in the observation and data analysis. The basic concepts of these effects are described below.

Dispersion

When the electromagnetic radiation from pulsars (and other astronomical sources) travels through the ISM, it suffers a frequency-dependent index of refraction, causing its group velocity to be smaller than the speed of light. Consequently, the signal at frequency f along a path length d from the pulsar to the Earth suffers a time delay with respect to the signal at infinite frequency by

$$t_{\mathrm{D}} = \mathcal{D} \times \frac{\mathrm{DM}}{f^2}\,, \tag{2.1}$$

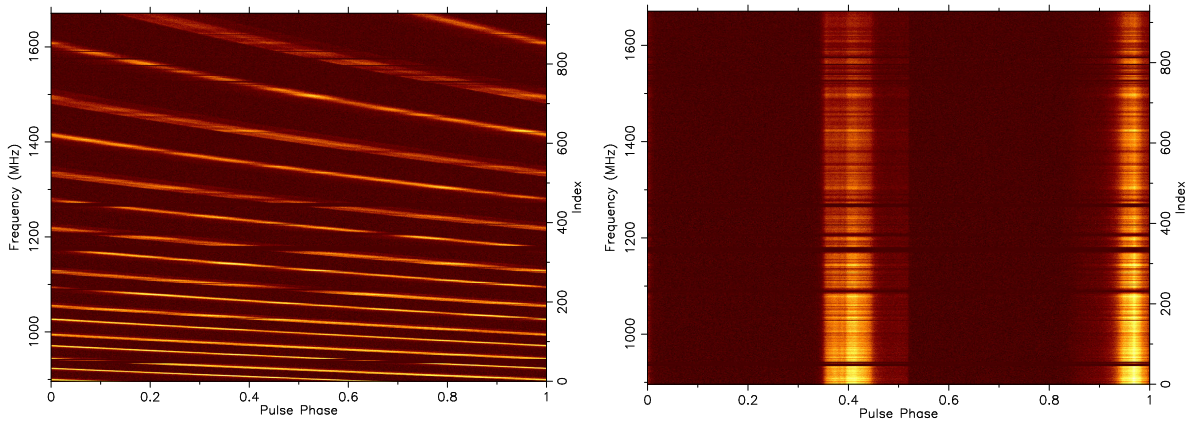

(a) (b)

Figure 2.1: Example of the ISM dispersion effect observed in the timing data of PSR J0737−3039A. Panel (a) shows a frequency-dependent delay caused by dispersion, whereas panel (b) shows an aligned profile after coherent de-dispersion with the correct DM. The data were acquired with the MeerKAT L-band receiver with a frequency range of 896-1672 MHz.

where the *dispersion measure*

$$\mathrm{DM} = \int_0^d n_\mathrm{e} \mathrm{d}l \tag{2.2}$$

is usually expressed in unit of $\mathrm{pc\,cm^{-3}}$. The quantity n_e is the electron number density and the *dispersion constant* is defined as

$$\mathcal{D} = \frac{e^2}{2\pi m_\mathrm{e} c}\,, \tag{2.3}$$

where e and m_e are the charge and mass of an electron, and c is the speed of light in vacuum. Most pulsar software adopts the definition introduced by Manchester & Taylor (1972) that $1/\mathcal{D} \equiv 2.41 \times 10^{-4}\,\mathrm{MHz^{-2}\,pc\,cm^{-3}\,s^{-1}}$, i.e. $\mathcal{D} \approx 4.15 \times 10^3\,\mathrm{MHz^2\,pc^{-1}\,cm^3\,s}$.[1] The time delay between the two frequencies f_low and f_high is therefore (Lorimer & Kramer, 2004)

$$\Delta t_\mathrm{D} \simeq 4.15 \times 10^3\,\mathrm{s} \times \left[\left(\frac{f_\mathrm{low}}{\mathrm{MHz}}\right)^{-2} - \left(\frac{f_\mathrm{high}}{\mathrm{MHz}}\right)^{-2}\right] \times \left(\frac{\mathrm{DM}}{\mathrm{pc\,cm^{-3}}}\right). \tag{2.4}$$

Figure 2.1(a) shows an example of this dipersive effect on PSR J0737−3039A. The pulse signal can be completely smeared out if not taking this effect into account in the observation and data analysis. The process that corrects for this effect is known as *de-dispersion*. For timing observations of pulsars with known DM, the dispersion can be removed completely using *coherent de-dispersion* (Hankins & Rickett, 1975). This is performed by applying the inverse of the transfer function (which caused the dispersion) to Fourier-transformed data and then transforming it back to the time domain.

Faraday rotation

In addition to the ISM itself, the presence of a magnetic field (primarily from the Galaxy) also has an impact, which forces the free electrons to move in a circular motion due to the Lorentz force. This effect can be characterised as different propagation speeds of the left- and right-hand circularly polarised waves

[1] A more precise definition is provided by Kulkarni (2020) based on the latest definitions of physical constants: $\mathcal{D} = 4.148\,806\,4239(11) \times 10^3\,\mathrm{MHz^2\,pc^{-1}\,cm^3\,s}$. The choice of this constant does not have an influence on the results as long as the analysis is done with the same definition.

in the magnetised ISM. As the combination of the left- and right-hand circular polarisations composes a linear polarisation, the differential phase rotation between these two circular polarisations leads to a change in the linear polarisation position angle (PPA), namely the *Faraday rotation*. This ISM Faraday rotation has a dependence on the wavelength of light λ:

$$\Delta\Psi_{\rm PPA} = \lambda^2 \times {\rm RM}\,, \tag{2.5}$$

and is therefore different in every frequency channel. The strength of this effect is characterised by the *rotation measure*

$${\rm RM} = \frac{e^3}{2\pi m_{\rm e}^2 c^4} \int_0^d n_{\rm e} B_\parallel {\rm d}l\,, \tag{2.6}$$

where $B_\parallel$ is the Galactic magnetic field along the line of sight (LOS). With the measurement of both DM and RM, one can estimate the average Galactic magnetic field strength along the LOS, which can be used to study the large-scale structure of the Galactic magnetic field (Han et al., 2006; Han et al., 2018).

Scattering and scintillation

So far, the discussions are based on the assumption of a homogeneous ISM. In reality, however, the ISM is turbulent and inhomogeneous, which leads to two additional effects: scattering and scintillation.

Turbulence in the ISM can bend the pulsar radiation along different LOSs, causing variable path lengths. As a result, the arrival time of the scattered rays are delayed with different offsets in pulse phase, which broadens the pulse shape when combining them together, a phenomenon known as *pulse scattering*. The scattered profile shows a one-sided exponential tail, where the $1/e$ time constant is referred to as the scattering time $\tau_{\rm s}$. In the thin-screen model developed by Scheuer (1968), the *scattering time* is related to the distance of the pulsar and the observing frequency via $\tau_{\rm s} \propto d^2 f^{-4}$. Therefore, distant pulsars observed at low frequencies are more likely to be scattered. This scatter broadening can greatly decrease the observed flux density and the timing precision of pulsars.

An effect closely related to scattering is *interstellar scintillation*. The irregularity of the ISM produces a strong modulation of the observed pulsar intensity in both the frequency and time domains. This effect is analogous to the 'twinkling' of stars caused by the Earth's atmosphere. In the thin-screen model (Scheuer, 1968), the intensity modulation for a given observing frequency f has a characteristic *scintillation bandwidth* $\Delta f_{\rm ISS} \propto 1/\tau_{\rm s} \propto f^4$. Generally, diffractive scintillation occurs over a bandwidth of kHz to hundreds of MHz on timescales of minutes to hours, and can lead to intensity fluctuations of up to 100%. Such modulations can be sufficiently extreme to make an otherwise bright pulsar almost undetectable when it is "scintillated-down". Refractive scintillation, on the other hand, occurs on timescales of weeks with amplitudes typically less than a factor of two (Sieber, 1982). Since in many pulsars the profile shape evolves in frequency, combining this profile evolution with the scintillation effect can introduce additional noise into the data (see discussions in Section 2.4).

Turbulent ISM, as well as changes in the Solar wind, also leads to variations in the DM, which becomes a red noise source (i.e. a noise source characterised by long time-scale variations) if not modelled properly in the timing analysis.

2.2 Basics of pulsar timing

Pulsars are weak radio sources whose single pulses exhibit large variations in their signal-to-noise ratio (S/N) and shape (see the pulse time series in Figure 2.2). These stochastic pulse-shape variations are known as jitter noise. For a given pulsar, despite the different shapes of the individual pulses, the

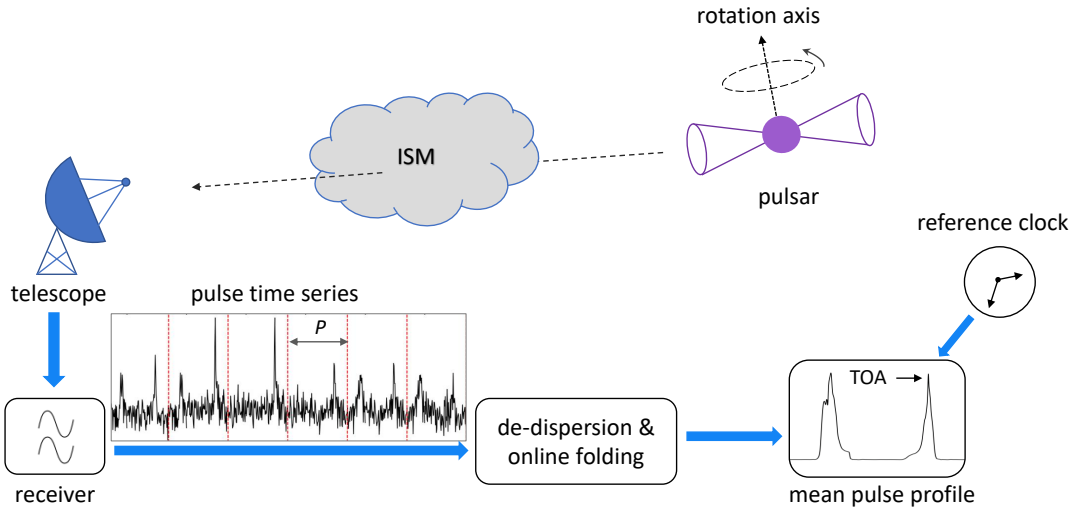

Figure 2.2: Basic concept of pulsar timing observations. The pulse time series and mean pulse profile are taken from MeerKAT observations of PSR J0737-3039A, with the red dashed lines marking the spin period of the pulsar.

integrated pulse profile (folded over many hundreds or even thousands of pulses) usually remains stable for a given frequency. To obtain a significant detection, the incoming pulses received by the radio telescope are amplified by receivers before being de-dispersed and folded at the topocentric pulsar period. A sketch of pulsar timing observations is shown in Figure 2.2.

Usually, further (coherent) addition of pulses is needed in order to obtain a high S/N and morphologically stable pulse profile, which is then cross-correlated with a noise-free template known as the *standard profile* (which is different for every pulsar) to obtain the time of arrival (TOA) of a pulse. The TOA obtained at the telescope is the key observing quantity in pulsar timing. It is usually defined as the arrival time of the nearest pulse to the midpoint of the span of the averaged pulses (Lorimer & Kramer, 2004). The timestamp of the profile, i.e. the TOA, is determined from the observatory local time, which is usually maintained by a hydrogen maser. This topocentric arrival time is then transformed to the Solar System barycentre (SSB) via a series of clock corrections and barycentric corrections. Finally, these barycentric TOAs are compared with predictions from a timing model, which describes the rotational and kinetic properties of the pulsar, resulting in a solution of timing parameters.

More information on timing procedures is outlined in the following sections, although an in-depth overview is beyond the scope of this dissertation. Section 2.2.1 and 2.2.2 describe the data acquisition system and telescopes used in this dissertation, and Section 2.2.3 and 2.2.4 introduce the data reduction methods. The timing model and the data analysis method are explained in Section 2.3 and 2.4 respectively.

2.2.1 Data acquisition

The acquisition of astronomical radio signals involves three core components: a reflecting and focusing surface, a frontend (receiver), and a backend (data recording machine). These components vary widely in design and configuration and an example is presented in Figure 2.3. For a typical single-dish parabolic telescope, the surface reflects the radio waves and directs them towards the focal point of the antenna, so that the radiations arriving at the receiver are coherently summed in amplitude and phase. Additionally, some telescopes can redirect the radio waves to a secondary focal point where additional receivers are available.

The initial portion of the receiving system are typically referred to as *frontend*. The signal path starts at the receiver, where the two orthogonal polarisations of the incoming waves are recorded. The weak

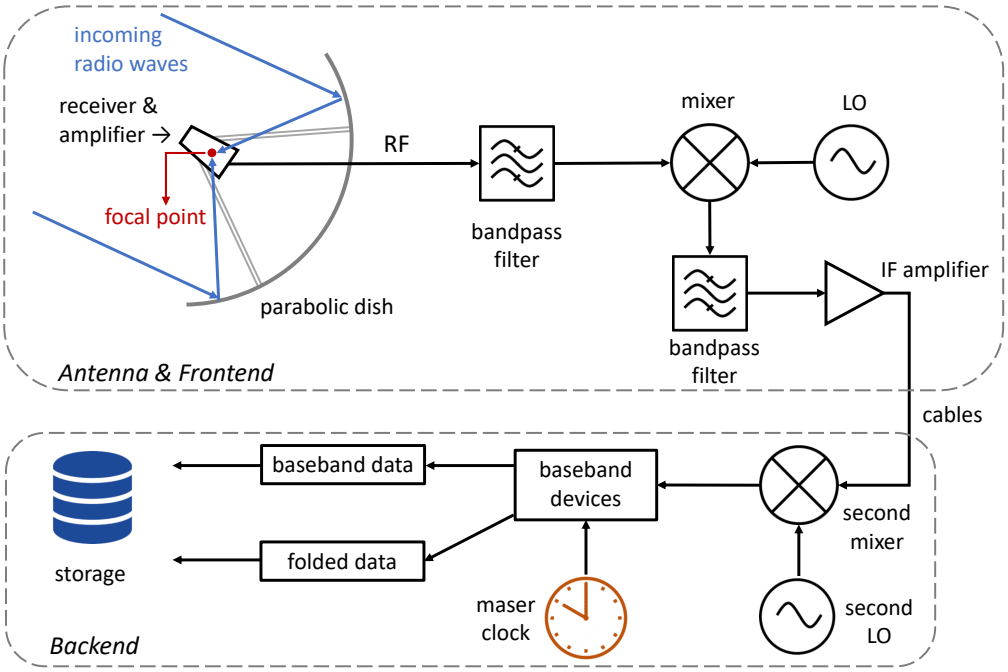

Figure 2.3: Schematic diagram of the signal path through a telescope frontend and backend for a single polarisation channel. The backend configuration displayed here is that of the baseband sampling. Modern backend systems such as the Effelsberg Direct Digitization (EDD) backend no longer require mixers and local oscillators (LO).

radio signals are then amplified by a low-noise amplifier that responses in a specific frequency range centred on the radio frequency (RF), $f_{\rm RF}$. Afterwards, the amplified signals pass through a bandpass filter, which filters out any signals outside of the band of interest. Next, the RF signals arrive at a *mixer* and are mixed with a monochromatic signal produced by a *local oscillator* (LO), to then be converted to a lower intermediate frequency (IF): $f_{\rm IF} = f_{\rm RF} - f_{\rm LO}$. This process is necessary to both reduce the signal loss due to cable transmission, which is worse at higher frequencies, and to choose a frequency that is easier to be processed by the hardware. Modern backend systems, such as the Effelsberg Direct Digitization (EDD) backend,[2] do not need mixers and LOs anymore. The signals are then processed through IF bandpass filters and amplifiers before being transmitted to the backend system via cables.

While the frontend is typically designed as a universal instrument that serves multiple astronomical purposes, the *backend* is more specialised and are responsible for digitising the data into a format that can be easily processed. For pulsar observations, the most common types of backend are *filterbank*, *baseband sampling* (Stairs et al., 2000) and *folded mode*. As filterbank is used for searching unknown pulsars which is not relevant to this dissertation, we only explain the latter ones here. A simple form of baseband sampling backend involves mixing the IF signals with a second LO, which produces a real and an imaginary signal for each polarisation. These signals are then sampled at Nyquist frequency and combined into complex voltage, followed by channelisation in frequency. Each digital sample is timestamped by a maser clock. Both the amplitude and phase of the original IF voltages are retained in these complex data, which allows coherent de-dispersion within each channel bandwidth. The resulting baseband data can be written directly to storage for later processing, converted to search mode data in filterbank format, or folded online during timing observations before written to storage. The folded profiles are averaged over a sub-integration interval (typically ~10 s), forming a data cube of pulse amplitude versus pulse phase for each frequency channel.

[2] https://mpifr-bdg.pages.mpcdf.de/edd_documentation/index.html

2.2.2 Telescopes involved in this work

This section briefly introduces the telescopes that are primarily involved in the data collection for this dissertation. Details relating to the different observations are described in more detail in the corresponding chapters.

The Effelsberg 100-m Radio Telescope

The Effelsberg 100-m Radio Telescope, operated by the *Max Planck Institute for Radio Astronomy* in Bonn, is one of the largest fully steerable radio telescopes on Earth. It is located in an Eifel valley about 40 km southwest of Bonn, and turned 50 in 2021 since its inauguration in 1971. This 100-m diameter parabolic telescope can observe sources with declinations from 90° to approximately −31°. The receivers are mounted on the primary and secondary focus and cover frequencies from 0.3 to 96 GHz. The telescope operates primarily as a standalone instrument, but is also actively involved in VLBI networks, such as the Large European Array for Pulsars (LEAP, Bassa et al., 2016) and the European VLBI Network (EVN). For more information, see https://www.mpifr-bonn.mpg.de/en/effelsberg.

Figure 2.4: The Effelsberg 100-m telescope.

The Five-hundred-meter Aperture Spherical radio Telescope (FAST)

Figure 2.5: The Five-hundred-meter Aperture Spherical radio Telescope (FAST) in China. Credit: Xinhua.

The world's largest filled-aperture radio telescope is the Five-hundred-meter Aperture Spherical radio Telescope (FAST) in China. It was first proposed in 1994 as a prototype for the *Square Kilometre Array* (SKA), an international project to build the world's largest radio telescope. However, the SKA eventually opted for small antenna arrays in the Southern Hemisphere. Nevertheless, FAST was built as a National Key Science & Technology Infrastructure Project of China under the leadership of Nan Rendong and was completed in 2016. It is operated by the *National Astronomical Observatories, Chinese Academy of Sciences*. Located in a natural karst depression in Guizhou, FAST has a 500-m diameter reflective surface which focuses radio waves onto a feed cabin suspended 140 m above it by six towers. It has an active surface design that can be deformed into a parabolic antenna aligned with the targeted source. The illuminated aperture is 300 m for sources with a zenith angle less than 26.4°. It can cover sources with a maximum zenith angle of 40°, that is, a declination of −15° to 65°. Technical information of FAST can be found, e.g., in Jiang et al. (2019).

The MeerKAT telescope

Figure 2.6: The MeerKAT telescope in South Africa. Credit: SARAO.

The MeerKAT telescope is a precursor for the SKA mid-frequency array (350 MHz to 14 GHz). It is located in the Northern Cape of South Africa and is operated by the *South African Radio Astronomy Observatory* (SARAO). MeerKAT is an array of 64 antennas, each with a diameter of 13.5 m. Of these, 48 antennas are concentrated in a core area with a diameter of ∼1 km, while the remaining antennas are placed in a more extended distribution with baselines up to 8 km long. Its observation elevation ranges from 15° to 88°, therefore allowing the observation of sources with declination δ from 40° to −90°. Its location is particularly desirable for observing the Galactic centre ($\delta = -29°$) and pulsars south of $\delta = -35°$, which are not optimal or inaccessible by the telescopes in the Northern Hemisphere. Details of pulsar observations with MeerKAT are described in Bailes et al. (2020).

2.2.3 Data reduction

Artefacts due to ISM, instrumental or terrestrial interference could contaminate the pulsar signal. Therefore, before generating TOAs, we need to ensure that these external influences are removed from the data so that we can get the maximum information from the pulsar itself. Emissions that are not from the target source are named *radio frequency interference* (RFI). Modern use of telecommunication devices, microwave ovens, and ground-based radars are common sources of RFI, which can affect both the frequency and time domains, either short-term or long-term. The RFI signals can introduce artefacts in the pulsar profile or even be strong enough to mask the signal of a weak pulsar. Therefore, RFI mitigation is necessary to restore the intrinsic pulsar signal. This process is commonly carried out with an automatic algorithm (e.g., Lazarus et al., 2016), followed by a further manual inspection (e.g., with PSRCHIVE, Hotan et al., 2004).

The two orthogonal polarisations of the incoming electromagnetic wave are recorded by the receiver using independent electronics, resulting in different gains and phases of the signal and thus a distortion the total intensity profile and systematic errors in timing. Polarisation calibration is therefore important for precise timing and polarimetry studies and can be done, for example, by observing a noise diode or a well-studied highly polarised radio source. Furthermore, as described in Section 2.1, ISM Faraday rotation can change the PPA, which can be corrected by measuring the RM and applying it to each frequency channel. Additionally, one can calibrate the flux for the studies of emission mechanism and NS population, but this is not critical for timing analysis.

Lastly, the data need to be reduced to the desired frequency and time resolution in order to be ready for the TOA creation. The choice of decimation depends on the purpose of the study and the properties of the pulsar. For the frequency domain, the profile evolution needs to be taken into account. A sufficient number of sub-bands also allows an accurate measurement of DM. For the time domain, pulsars used for the pulsar timing array (PTA) experiments are typically averaged over 30 min to 1 hr, whereas pulsars in relativistic binaries are averaged over shorter time intervals to obtain sufficient orbital coverage. In the

case of the Double Pulsar, since pulsar A is eclipsed by pulsar B on a timescale of ~30 s, to keep both a good S/N and good time resolution, an optimal integration time of ~30 s is used in order to measure higher-order light propagation effects (see Section 2.3.2) at and near the eclipse.

2.2.4 Measurement of TOAs

After the above procedures, the data are cross-correlated with a high S/N and noise-free template to generate TOAs and the associated uncertainties. This template is made by either fitting Gaussian functions (Kramer et al., 1994; Kramer, 1994) or smoothing with a wavelet transform (P. B. Demorest et al., 2013) to the best pulse profile. Since the pulse profile varies with the emission frequency of the pulsar, for observations with wideband receivers, a frequency-dependent template, or so-called "2D template", can be employed to improve the accuracy of TOAs (Liu et al., 2014b; Pennucci, 2019).

The accuracy of the TOA measurements can be estimated from the ratio of pulse width W to profile S/N. Following the radiometer equation in Dicke (1946), the TOA uncertainty derived from radiometer noise is expected to scale as follows (Lorimer & Kramer, 2004):

$$\sigma_{\rm TOA} \simeq \frac{W}{\rm S/N} \propto \frac{T_{\rm sys}}{\mathsf{G}\sqrt{t_{\rm int}\Delta f}} \times \frac{W^{3/2}}{S_{\rm mean}\sqrt{P-W}} \,. \tag{2.7}$$

Here, $T_{\rm sys}$ is the system temperature that accounts for the noise contributions from the sky, atmosphere, ground, and receivers. The telescope gain $\mathsf{G} = A_{\rm eff}/(2k_{\rm B})$ describes the raw sensitivity of the telescope and is determined by the effective collecting area of the telescope $A_{\rm eff}$, with $k_{\rm B}$ being the Boltzmann constant. The first term in Eq. (2.7) describes the dependence of TOA uncertainty on the properties of the observing system. Observations with a large gain telescope, low system temperature $T_{\rm sys}$, long integration time $t_{\rm int}$ and broad observing bandwidth Δf yield high accuracy TOAs. The second term describes the dependence of TOA uncertainty on the characteristics of the pulsar itself. Pulsars with high mean flux density $S_{\rm mean}$, short spin period P, and narrow pulse width are ideal for high precision timing.

2.3 Timing model

With TOA measurements, a timing model is required in order to extract the information of the pulsar and the propagation medium. A typical timing model includes 4 fundamental parts: (a) *astrometric parameters* describing the position, proper motion, and the parallax of the pulsar; (b) *spin parameters* including the pulsar rotation frequency (ν), its derivative ($\dot{\nu}$) and (in some cases) higher derivatives ($\ddot{\nu}$, $\dddot{\nu}$, ...); (c) *ISM parameters* accounting for the propagation delays in the ISM; (d) *binary parameters* characterising the orbital motions and the effects of signal propagation in the binary spacetime.

To study the effects on the pulse TOAs, we employ the following expression, which describes the pulsar rotation in the comoving reference frame with the pulsar. The "proper time" of a pulsar $T_{\rm p}$ is related to its rotational phase ϕ via the rotational frequency ν and its derivatives (Blandford & Teukolsky, 1976):[3]

$$\frac{\phi(T_{\rm p})}{2\pi} = N_0 + \nu(T_{\rm p} - t_0) + \frac{1}{2}\dot{\nu}(T_{\rm p} - t_0)^2 + \cdots \,, \tag{2.8}$$

where N_0 is the pulse number at the reference epoch t_0. The correct counting of the rotational phase requires the observer to be in an inertial reference frame, which is not the case with a telescope on Earth due to the movement of the Earth in the Solar System. Therefore, TOAs received by observatories on

[3] Actually, this is the proper time as measured by a hypothetical clock on the pulsar (Blandford & Teukolsky, 1976), which is proportional to the proper time τ.

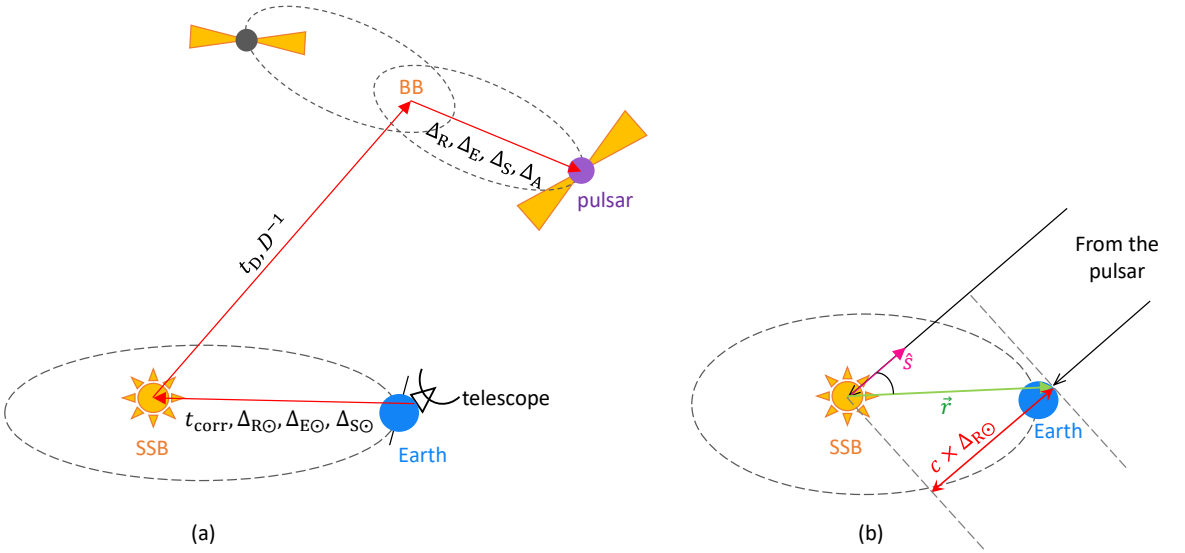

Figure 2.7: (a) Geometry of time corrections from the observed TOAs at the telescope to the "proper time" of the pulsar via the reference frame SSB and binary barycentre (BB).[4] (b) Geometry of Rømer delay between the telescope and the SSB. $\hat{s}$ is a unit vector pointing from the SSB to the pulsar, and $\vec{r}$ is the vector pointing from the SSB to the telescope. The difference of light travel distance from pulsar to the telescope and to the SSB (marked in red) is $c \times \Delta_{R\odot} = -\vec{r} \cdot \hat{s}$. It is easy to imagine that Rømer delay causes an annual sinusoidal variation in pulse arrival time due to Earth's orbital motion around the Sun. In both figures, the size of the objects and distances are not to scale.

Earth need to be transferred to the Solar System barycentre (SSB), which is, to a good approximation, an inertial reference frame. The transformation from a topocentric TOA, t_{topo}, to a barycentric TOA (at infinite frequency), t_{SSB}, follows

$$t_{SSB} = t_{topo} + t_{corr} + \Delta_{R\odot} + \Delta_{E\odot} + \Delta_{S\odot} - t_D \,, \tag{2.9}$$

where t_{corr} denotes clock corrections, which are discussed in detail in Section 2.3.1. The term $\Delta_{R\odot}$ accounts for the Rømer delay, i.e. the difference in light travel time from pulsar to the observer and to the SSB. It is calculated as $\Delta_{R\odot} = -\vec{r} \cdot \hat{s}/c$, where $\hat{s}$ is a unit vector pointing from the SSB to the pulsar, and $\vec{r}$ is the vector pointing from the SSB to the phase centre of the telescope. Therefore, precise knowledge of the location of the telescope and, of course, the location of the SSB is required. An illustration of the geometry of the Rømer delay is shown in Figure 2.7(b). The term $\Delta_{E\odot}$ stands for the Einstein delay, which consists of the time dilation due to the Earth's motion and the gravitational redshift caused by the other bodies in the Solar System; and $\Delta_{S\odot}$ describes the Shapiro delay due to the spacetime curvature caused by the presence of masses in the Solar System, chiefly by the Sun. The computation of barycentric corrections requires precise knowledge of the positions and masses of all major bodies in the Solar System, for which a *Solar System ephemeris* such as the DE ephemerides produced by the Jet Propulsion Laboratory is used.[5] The concepts of these three delays are discussed in more detail in Section 2.3.2 with regard to binary pulsars. From the Rømer and Shapiro delay corrections, the astrometric parameters of the pulsar can be measured. With the aforementioned corrections, topocentric TOAs are transformed into barycentric TOAs at barycentric frequency f_{SSB}, which need to be converted to infinite frequency by removing the dispersive delay caused by the ISM, i.e. $t_D = \mathcal{D} \times \mathrm{DM}/f_{SSB}^2$ (see Section 2.1).

[4] Between BB and the SSB, there should also exist a constant vacuum propagation delay (in addition to the Doppler shift), which is often neglected as it is not relevant to the results.

[5] https://ssd.jpl.nasa.gov/orbits.html#planets

2.3.1 Clock and barycentric corrections

The term $t_{\rm corr}$ in Eq. (2.9) summarises various clock corrections, which are explained below. The TOAs received at the telescope are recorded based on the local time of the observatory, which is usually maintained by a hydrogen maser. Maser clocks are good frequency standards at short timescales, but they are known to drift with time and so are inadequate for long-term precision pulsar timing. Therefore, we constantly compare the observatory time to Coordinated Universal Time (UTC) via the Global Positioning System (GPS), which provides measurements by the *National Institute of Standards and Technology* (NIST) and is often referred to as UTC(NIST). The offsets between these two time standards are recorded in a clock file. UTC is based on International Atomic Time (TAI) with leap seconds added to compensate for the time difference due to irregularities and slowdown of the Earth's rotation: TAI = UTC + ΔT, with ΔT being a certain integral number of all leap seconds.[6] Through this expression, TOAs are transformed into TAI, a smooth and high-precision time standard as realised on the proper time of the rotating geoid (mean sea level) of the Earth. Maintained by *Bureau International des Poids et Mesures* (BIPM), TAI is a weighted average of time measured by over 400 atomic clocks (mainly caesium clocks) in more than 50 national laboratories worldwide to overcome the stochastic errors of individual atomic clocks. Finally, TOAs are transformed from TAI to Terrestrial Time (TT), a theoretical ideal that is tied to TAI by a constant for historical reasons: TT(TAI) = TAI + 32.184 s. Both TAI and TT are in units of SI second. Since TAI is never revised once published, the correction of errors are calculated annually by BIPM. With this correction, TOAs are converted to the timescale of TT(BIPM).

So far, TOAs in the TT standard still refer to the Earth's frame, which needs to be transformed to the SSB by taking into account other corrections in Eq. (2.9). All these corrections are performed via the pulsar software TEMPO (D. Nice et al., 2015)[7] or TEMPO2 (G. B. Hobbs et al., 2006)[8]. With TEMPO, the result is an arrival time in Barycentric Dynamical Time (TDB); whereas with TEMPO2, TT is transformed to Geocentric Coordinate Time (TCG)[9] and eventually to Barycentric Coordinate Time (TCB) (Edwards et al., 2006) as recommended by the International Astronomical Union (IAU) 2006 Resolution B3.[10] While TDB was never defined in a self-consistent way, TCB was proposed by the IAU in 1991 as a successor (see Soffel et al., 2003) and is equivalent to the proper time experienced by a clock at rest in a coordinate frame comoving with the SSB. It therefore ticks faster than TDB and clocks on Earth as it is outside the gravity well of the Solar System. In IAU 2006 Resolution B3, TDB is defined as a linear transformation of TCB:

$$\mathrm{TDB} = \mathrm{TCB} - L_{\rm B} \times (\mathrm{JD}_{\rm TCB} - T_0) \times 86400\,\mathrm{s} + \mathrm{TDB}_0\,, \tag{2.10}$$

with T_0 = JD 2443144.5003725, $L_{\rm B} = 1.550519768 \times 10^{-8}$, $\mathrm{TDB}_0 = -6.55 \times 10^{-5}$s. To transfer from TDB to TCB, parameters with units of time need to be divided by the constant factor $(1 - L_{\rm B})$. Further information on the definitions of time standards can be found, e.g., in Soffel & Langhans (2013).

2.3.2 Relativistic effects in binary pulsars

For pulsars in binary systems, additional time transformations are needed to account for the binary motion and propagation effects inside the binary system. The barycentric TOA (at infinite frequency) is

[6] As of 28 Feb. 2022, ΔT = 37s.

[7] http://tempo.sourceforge.net/

[8] https://bitbucket.org/psrsoft/tempo2/src/master/

[9] TT is defined to differ from TCG by a constant rate (IAU 2000 resolutions, Soffel et al., 2003).

[10] https://www.iau.org/static/resolutions/IAU2006_Resol3.pdf

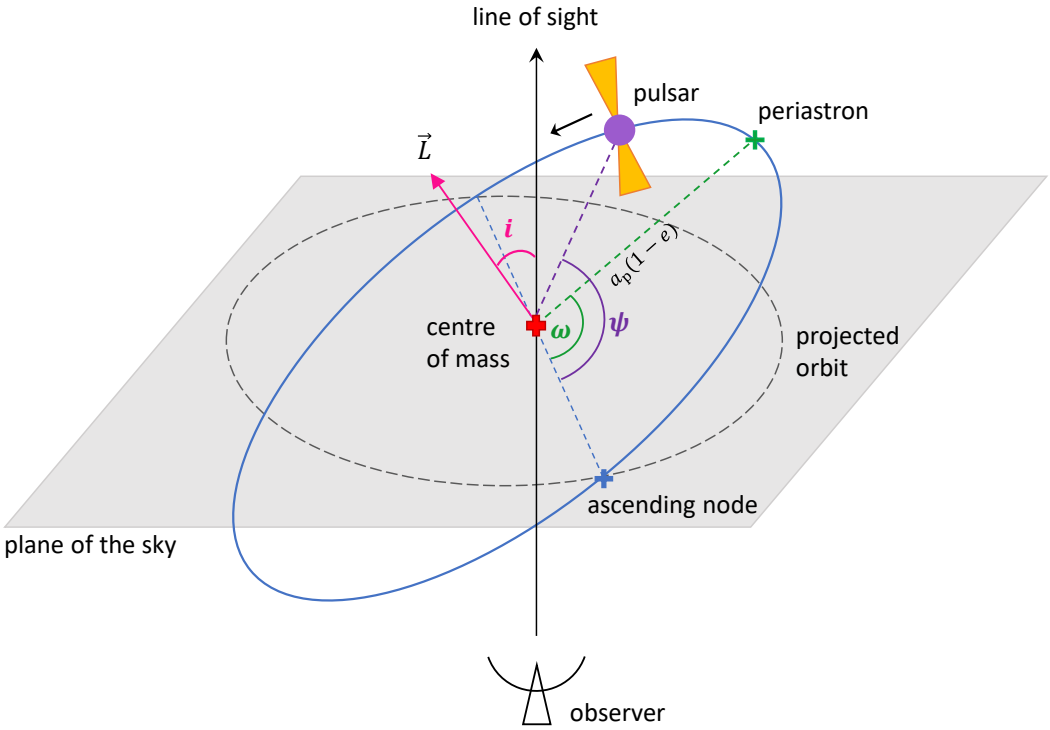

Figure 2.8: Schematic diagram of an elliptical Keplerian orbit. The blue ellipse is the orbit of a pulsar projected onto the plane of the sky (in grey) perpendicular to the LOS of the observer. The ascending node (blue cross) is the point where the pulsar crosses the plane of the sky travelling away from the observer. The orbital inclination i is the angle between the LOS and the orbital angular momentum $\vec{L}$, and also the angle between the orbital plane and the plane of the sky. The periastron (green cross) marks the closest point in the pulsar's orbit to the centre of mass (red cross), the distance between which is $a_p(1-e)$, where a_p and e are the semi-major axis and eccentricity of the pulsar orbit. Both the longitude of periastron ω and longitude of the pulsar ("orbital phase") ψ are measured relative to the ascending node.

therefore linked to the proper time of the pulsar T_p via the expression:

$$t_{SSB} - t_0 = D^{-1} \times \left[T_p + \Delta_R(T_p) + \Delta_E(T_p) + \Delta_S(T_p) + \Delta_A(T_p)\right] , \tag{2.11}$$

where t_0 is the reference epoch and D is the Doppler factor due to the (unknown) radial velocity of the pulsar system with respect to the SSB. As only temporal changes of D are of interest, $D \equiv 1$ can be chosen at a given epoch (see Damour & Deruelle, 1986). The quantity Δ_R accounts for the Rømer delay due to the orbital motion of the pulsar; Δ_E describes the Einstein delay, which to leading order consists of the gravitational redshift caused by the companion and the second-order Doppler effect; Δ_S comprises delays related to the curved spacetime of the companion object, which to leading order is the well-known Shapiro delay; and finally, Δ_A corresponds to the aberration effects, owing to the fact that the pulsar acts as a moving "light-house" with beam pointing at a specific direction. The geometry of the transformation from a topocentric TOA to the proper time of the pulsar is illustrated in Figure 2.7(a).

Unlike Newtonian theory, which has an exact solution for the equation of motion of two gravitationally interacting masses, general relativity (GR) has no such analytical solution. In GR, the two-body problem can only be solved numerically or based on approximation methods. To test the quasi-stationary strong-field regime and the radiation regime with binary pulsars, a phenomenological approach, commonly known as *parameterised post-Keplerian* (PPK) formalism, was introduced by Damour & Deruelle (1986) and developed by Damour & Taylor (1992). The PPK formalism parameterises all observable effects

that can be independently obtained from observational data of binary pulsars, and accordingly allows the extraction of theory-independent information from binary pulsar observations by fitting for a set of *Keplerian* and *post-Keplerian* (PK) parameters.

The six Keplerian parameters that describe the Newtonian motion of a binary pulsar are listed below:

- orbital period of the binary system, $P_{\rm b}$;
- projected semi-major axis of the pulsar orbit, $x \equiv a_{\rm p} \sin i/c$;
- orbital eccentricity, e;
- longitude of periastron, ω;
- epoch of periastron passage, T_0;
- longitude of the ascending node, Ω;

where $a_{\rm p}$ is the semi-major axis of pulsar's orbit, and i is the orbital inclination defined as the angle between the orbital angular momentum and the LOS toward the pulsar system. A schematic diagram of an elliptical pulsar orbit is shown in Figure 2.8. The first five Keplerian parameters can be easily measured from pulsar timing, whereas Ω can only be measured in specific cases (e.g. with wide orbits) and is only important for evolutionary studies or certain tests of alternative theories (Zhu et al., 2015; Zhu et al., 2019).

In many gravity theories, PK parameters can be expressed as a function of Keplerian parameters and *a prior* unknown masses of pulsar and companion, $m_{\rm p}$ and $m_{\rm c}$.[11] Two PK parameters allow the determination of two masses within the framework of the assumed theory. Measuring more than three PK parameters is thus the key to test gravity theories.

The contributions $\Delta_i (i = {\rm R, E, S, A})$ in Eq. (2.11) depend on these Keplerian and PK parameters, which are briefly explained below. A detailed discussion can be found in Kramer et al. (2021a).

Rømer delay

The orbital motion of binary pulsars can be described with Damour-Deruelle solution to the first post-Newtonian (PN) equation of motion (simple quasi-Keplerian form) (Damour & Deruelle, 1985; Damour & Deruelle, 1986). The *Rømer delay* caused by the orbital motion of the pulsar is given by

$$\Delta_{\rm R} = x \sin\omega \left[\cos u - e_{\rm T}(1+\delta_r)\right] + x\cos\omega \left[1 - e_{\rm T}^2 (1+\delta_\theta)^2\right]^{1/2} \sin u \,, \tag{2.12}$$

where the "relativistic" eccentric anomaly u is related to the proper time of the pulsar via Kepler's equation

$$u - e_{\rm T} \sin u = 2\pi \left[\left(\frac{T_{\rm p} - T_0}{P_{\rm b}}\right) - \frac{\dot{P}_{\rm b}}{2}\left(\frac{T_{\rm p} - T_0}{P_{\rm b}}\right)^2\right] . \tag{2.13}$$

This equation describes the motion of a pulsar in an elliptical orbit as shown in Figure 2.8. The time eccentricity $e_{\rm T}$ corresponds to the observed eccentricity fitted in the timing model. The PK parameter $\dot{P}_{\rm b}$ accounts for all secular changes (either intrinsic or external) in the orbital period $P_{\rm b}$, and therefore includes the orbital period decay caused by gravitational wave (GW) damping. The PK parameters δ_r and δ_θ describe the relativistic deformation of the orbit, which shows a periodic change to a Keplerian motion. While δ_r can be absorbed by spin parameters (see discussions in Damour & Deruelle, 1986; Kramer et al., 2021a), δ_θ has been measured in both the Hulse-Taylor pulsar (Weisberg & Huang, 2016) and the Double Pulsar (Kramer et al., 2021a) with low precision.

[11] Some higher-order contributions also depend on the moment of inertia and spin parameters.

Einstein delay

For an eccentric orbit, the time dilation of the "pulsar clock" changes periodically due to a change of the gravitational redshift caused by the gravitational field of the companion and a variation in the orbital velocity of the pulsar (i.e. second-order Doppler effect). This so-called *Einstein delay* to leading order follows (Blandford & Teukolsky, 1976; Damour & Deruelle, 1986)

$$\Delta_{\rm E} = \gamma_{\rm E} \sin u \,, \tag{2.14}$$

where the amplitude $\gamma_{\rm E}$ is a PK parameter.

Shapiro delay and higher-order corrections

For binary pulsars with a sufficiently edge-on orbit ($i \sim 90°$), the pulsar signal suffers a significant propagation delay due to the curved spacetime of the companion star. To leading order (LO) we have the well-known *Shapiro delay*, which follows (Blandford & Teukolsky, 1976; Damour & Deruelle, 1986)

$$\Delta_{\rm S}^{\rm (LO)} = -2r \ln \Lambda_u \,, \tag{2.15}$$

$$\Lambda_u = 1 - e_{\rm T} \cos u - s \left[\sin\omega \left(\cos u - e_{\rm T} \right) + \left(1 - e_{\rm T}^2 \right)^{1/2} \cos\omega \sin u \right] , \tag{2.16}$$

where r and s are two PK parameters representing the *range* and *shape* of the Shapiro delay. This expression was obtained by integrating along a straight line in harmonic coordinates and assuming a static mass distribution as the pulsar signal propagates through the system (Blandford & Teukolsky, 1976). In reality, the pulsar signal propagates along a curved path due to the gravitational field of the companion, resulting in a *lensing correction* to the Shapiro delay. This effect has not yet been observed in any pulsar system, but for completeness one can extend Eq. (2.16) by an adapted version of the approximation in Eq. (73) of Klioner & Zschocke (2010): $\Lambda_u \to \Lambda_u + \delta\Lambda_u^{\rm len}$ with $\delta\Lambda_u^{\rm len} = 2rc/a_{\rm R}$, where $a_{\rm R}$ is the semi-major axis of the relative orbit. For relativistic binary pulsars such as the Double Pulsar, one needs to account for the fact that the companion star moves while the pulsar signal propagates across the system. This is known as *retardation effect* or 1.5PN correction of the Shapiro delay (Kopeikin & Schäfer, 1999; Rafikov & Lai, 2006a). The signal propagation delay can be extended as

$$\Delta_{\rm S} = -2r \ln \left(\Lambda_u + \delta\Lambda_u^{\rm len} + \delta\Lambda_u^{\rm ret} \right) , \tag{2.17}$$

where the retardation correction $\delta\Lambda_u^{\rm ret}$ can be taken directly from Eq. (130) in Kopeikin & Schäfer (1999).

Aberration

In pulsar timing, the aberration results from the "lighthouse" property of the pulsar that the direction of the pulse emission changes to compensate for the relative transverse motion of the pulsar and the Earth (Smarr & Blandford, 1976; Damour & Deruelle, 1986). To leading order, the aberration effect reads

$$\Delta_{\rm A}^{\rm (LO)} = \mathcal{A} \left[\sin\psi + e_{\rm T} \sin\omega \right] + \mathcal{B} \left[\cos\psi + e_{\rm T} \cos\omega \right] , \tag{2.18}$$

where ψ is the longitude of the pulsar with respect to the ascending node, and $\mathcal{A}$ and $\mathcal{B}$ are aberration coefficients. This expression assumes a flat spacetime for the propagation of the pulsar signal, which is no longer sufficient to describe the observations of highly inclined ($i \sim 90°$) relativistic binary pulsars, such as the Double Pulsar, particularly at the superior conjunction. One needs to additionally account for the gravitational deflection of pulsar's signal caused by its companion (Doroshenko & Kopeikin,

1995; Rafikov & Lai, 2006b), which adds a lensing correction to the classical longitudinal aberration of Eq. (2.18). Besides, the lensing correction to the latitudinal aberration around the superior conjunction may lead to a temporal change in the observed pulse profile, as the LOS cuts a different region of the pulsar beam (Rafikov & Lai, 2006a; Rafikov & Lai, 2006b). Further details are provided in Chapter 4.

2.3.3 Post-Keplerian parameters in GR

In GR, to leading order, the most well-known PK parameters are listed below (Damour & Deruelle, 1986) and expressed in terms of the PN approximation. The first five parameters correspond to the effects at 1PN order (i.e. order v^2/c^2, where v is the typical velocity of the relative motion), parameterising the quasi-stationary strong-field effects. The last parameter, the orbital period decay due to GW damping, is related to the radiation regime. In GR, the leading order contribution enters the equations of motion at 2.5PN level (order v^5/c^5, quadrupolar GWs), whereas in many alternative gravity theories, the leading order already occurs at 1.5PN level (v^3/c^3) due to the emission of dipolar GWs.

Relativistic advance of periastron
$$\dot{\omega}^{\rm 1PN} = 3\, n_{\rm b}^{5/3}\, T_\odot^{2/3} \frac{1}{1-e_{\rm T}^2} M^{2/3}\,, \tag{2.19}$$

Amplitude of the Einstein delay
$$\gamma_{\rm E} = n_{\rm b}^{-1/3}\, T_\odot^{2/3} e_{\rm T} \frac{m_{\rm c}(m_{\rm p}+2m_{\rm c})}{M^{4/3}}\,, \tag{2.20}$$

Range of the Shapiro delay
$$r = T_\odot m_{\rm c}\,, \tag{2.21}$$

Shape of the Shapiro delay
$$s = \sin i = n_{\rm b}^{2/3}\, T_\odot^{-1/3} x \frac{M^{2/3}}{m_{\rm c}}\,, \tag{2.22}$$

Geodetic spin precession rate
$$\Omega_{\rm p}^{\rm SO} = n_{\rm b}^{5/3}\, T_\odot^{2/3} \frac{1}{1-e_{\rm T}^2} \frac{m_{\rm c}(4m_{\rm p}+3m_{\rm c})}{2M^{4/3}}\,, \tag{2.23}$$

Orbital period decay due to GW damping
$$\dot{P}_{\rm b}^{\rm 2.5PN} = -\frac{192\pi}{5} \frac{n_{\rm b}^{5/3}\, T_\odot^{5/3}}{(1-e_{\rm T}^2)^{7/2}} \frac{m_{\rm p} m_{\rm c}}{M^{1/3}} \left(1 + \frac{73}{24} e_{\rm T}^2 + \frac{37}{96} e_{\rm T}^4\right)\,, \tag{2.24}$$

where $n_{\rm b} = 2\pi/P_{\rm b}$ is the orbital frequency, and $M = m_{\rm p} + m_{\rm c}$ is the total mass of the system. The constant $T_\odot = (\mathcal{GM})_\odot^{\rm N}/c^3$, where $(\mathcal{GM})_\odot^{\rm N} = 1.327\,124\,4 \times 10^{20}\,{\rm m^3 s^{-2}}$ is the nominal solar mass parameter defined by the IAU 2015 Resolution B3 (Prša et al., 2016). For simplicity, all masses expressed in the unit of solar mass $\rm M_\odot$ are referred to the nominal solar mass by taking the ratio $Gm_{\rm object}/(\mathcal{GM})_\odot^{\rm N}$.

For most known binary pulsars, only the leading-order term of the PK parameters is measurable. But for highly relativistic systems, such as the Double Pulsar, higher-order contributions for some PK parameters are now relevant. Further details will be provided in Chapters 3 and 4. The two additional PK parameters that start to become relevant for some relativistic binary pulsars are the orbital deformation parameters, δ_r and δ_θ. In GR, they take the form (Damour & Deruelle, 1986):

$$\delta_r = n_{\rm b}^{2/3}\, T_\odot^{2/3} \frac{3m_{\rm p}^2 + 6m_{\rm p}m_{\rm c} + 2m_{\rm c}^2}{M^{4/3}}\,, \tag{2.25}$$

$$\delta_\theta = n_{\rm b}^{2/3}\, T_\odot^{2/3} \frac{\frac{7}{2}m_{\rm p}^2 + 6m_{\rm p}m_{\rm c} + 2m_{\rm c}^2}{M^{4/3}}\,. \tag{2.26}$$

2.4 Residuals and noise sources

The goal of pulsar timing is to find a phase-coherent solution that accounts for every single rotation of the pulsar to within a small fraction of the pulsar's spin period. With Eqs. (2.9) and (2.11), the observed topocentric TOAs are converted to the proper time of pulsar emission $T_{\rm p}$. Starting from a minimal set of parameters, one can compare the difference in rotational phase between the pulse emission time $\phi(T_{\rm p})$ and the arrival time predicted by this model $\phi(T_{\rm model})$, to form *timing residuals*. The timing model can be refined by minimising the least squares of these residuals in a χ^2 test (Taylor & Weisberg, 1989) with TEMPO or TEMPO2, and the reduced χ^2 is given as

$$\chi^2_{\rm red} = \frac{1}{N_{\rm free}} \sum_i \left[\frac{\phi_i(T_{\rm p}) - \phi_i(T_{\rm model})}{\sigma_i} \right]^2 , \tag{2.27}$$

where the degree of freedom $N_{\rm free}$ is the difference between the number of TOAs and the number of fitted parameters, and σ_i is the uncertainty associated with the i-th TOA. Lack of parameters in the model can result in different signatures in the post-fit residuals. A correct and complete timing model should yield $\chi^2_{\rm red} \approx 1$, and the residuals follow a Gaussian distribution around zero with a root mean square (RMS) comparable to the TOA uncertainties. It should be noted that the least-squares approximation assumes no correlation between timing parameters or TOAs. To obtain more reliable uncertainties for strongly correlated parameters, one could run through a grid of values for these parameters and create a χ^2 map, or use Bayesian approach (e.g., TEMPONEST, Lentati et al., 2014).

Since the timing model is always incomplete to some extent, the residuals often show scatter in excess of that predicted by the TOA uncertainty, i.e. RMS $> \sigma_{\rm TOA}$. This excess can originate from noises that typically consist of two classes: white noise (uncorrelated between observing epochs) and time-correlated red noise. If these noise sources are not taken into account in the timing analysis, this can result in an underestimation of the TOA uncertainties and therefore to a bias in the values and uncertainties of the timing parameters.

The noise can be intrinsic to the pulsar or extrinsic, and its power spectrum can be white (flat at all frequencies) or red (increasing power at low frequencies). In addition to the radiometer noise (Eq. (2.7)), another important source of white noise is *jitter noise*, which is caused by stochastic pulse-shape variation intrinsic to the pulse emission (Shannon et al., 2014). These variations can occur both in amplitude and phase and are usually uncorrelated from pulse to pulse. In almost all pulsars observed with high sensitivity, the single pulses show variations beyond those expected from radiometer noise, leading to $\chi^2_{\rm red} > 1$ (e.g., Shannon et al., 2014; Lam et al., 2019; Parthasarathy et al., 2021). For the majority of pulsars, radiometer noise still dominates jitter noise. However, as the radiometer noise decreases significantly with the large telescopes such as MeerKAT, FAST, and the SKA, the jitter noise will become an important noise contributor and limit the timing accuracy for more pulsars in the future. Since jitter noise scales inversely with the number of averaged pulses ($N_{\rm p}$) as $\sigma_{\rm J} \propto 1/\sqrt{N_{\rm p}}$, increasing the integration time is the only way to overcome it. White noise sources can be modelled by employing the parameters 'EFAC' and 'EQUAD' in the timing model to re-scale the initially measured TOA uncertainty σ to $\hat{\sigma}^2 = (\sigma \times {\rm EFAC})^2 + {\rm EQUAD}^2$. EFAC accounts for possible errors in the estimation of formal TOA uncertainty calculated in the cross-correlation of pulse profiles with a standard template, whereas EQUAD accounts for additional TOA scatter, such as jitter noise, and is added in quadrature.

The most well-known intrinsic red noise source is *spin noise* caused by the rotational irregularity of pulsars, especially the young ones. The nature of spin noise is still poorly understood, while various mechanisms have been proposed to explain it, including magnetospheric torque variations (A. Lyne et al., 2010), superfluid turbulence (Melatos & Link, 2014), and coupling between solid crust and superfluid

(Jones, 1990).

The dominant extrinsic red noise source is DM variation, which is primarily caused by turbulence in the ISM, but is also influenced by the Solar wind (Tiburzi et al., 2021) and local weather in the vicinity of the pulsar (e.g. from its companion, P. C. Freire et al., 2003). The variations in DM typically range from 10^{-4} to 10^{-3} cm^{-3} pc every year, with a power spectrum $\propto f^{-8/3}$ (Keith et al., 2013). Normally, DM variations are undetectable during an observing session, but can be observed between epochs. The best way to mitigate DM noise is to have sufficient frequency coverage for each observation and to remove the dispersive delay according to the DM measurement of the corresponding observation.

Other ISM-related sources of red noise include scattering variations, which can be measured by studying scintillation arcs (Main et al., 2020), and the combined effect of profile evolution and scintillation (Lentati et al., 2017). If the data are averaged over frequency and the template does not take into account profile evolution, the change of intensity in frequency caused by scintillation would result in temporal profile variations and degrade the accuracy of the TOAs generated from the cross-correlation process.

In addition, inaccuracies in the terrestrial time standard (G. Hobbs et al., 2012), errors in the Solar System ephemeris (Caballero et al., 2018; Guo et al., 2018), and the stochastic GW background (GWB, Antoniadis et al., 2022) can also induce red noise in the data. Since the primary goal of the PTA experiment is to detect stochastic GWB, it is very important to understand and minimise red noise from other sources (Chen et al., 2021). This can be achieved by a simultaneous fitting of timing parameters and power-law noise models (for both red noise and DM noise) using a Bayesian approach (e.g. with TEMPONEST) that accounts for possible covariance between the timing and noise parameters. From Bayesian noise analysis, one can obtain the covariance matrix of noise models and perform a generalised least-squares fit to obtain more accurate timing parameters.

CHAPTER 3

Constraining the dense matter equation-of-state with radio pulsars

- **H. Hu**, M. Kramer, N. Wex, D. J. Champion, and M. S. Kehl, Constraining the dense matter equation-of-state with radio pulsars, *Monthly Notices of the Royal Astronomical Society*, Volume 497, Issue 3, September 2020, Pages 3118–3130, DOI: 10.1093/mnras/staa2107

Summary

Radio observations of binary pulsars provide some of the most important constraints for our understanding of matter at supranuclear densities. So far, these constraints are mostly given by precision mass measurements of neutron stars (NS). By combining single measurements of the two most massive pulsars known, PSR J0348+0432 and PSR J0740+6620, the resulting lower limit of the maximum NS mass, $1.98\,M_\odot$ (99% confidence), has excluded a large number of equations of state (EOSs).

Further EOS constraints, complementary to other methods, are likely to come from the measurement of the moment of inertia (MOI) of binary pulsars via relativistic spin-orbit coupling (Damour & Schäfer, 1988). This spin-orbit coupling leads to a precession of the orbit known as Lense-Thirring precession. The Double Pulsar, PSR J0737−3039A/B, is the most promising system for the first robust measurement of the MOI via pulsar timing. Reviewing this method, based in particular on the first MeerKAT observations of the Double Pulsar, we provided well-founded projections into the future by simulating timing observations with MeerKAT, MeerKAT+, and SKA 1-mid. We developed a consistent method to measure the MOI of pulsar A along with the masses of two pulsars using three post-Keplerian (PK) parameters: the advance of periastron $\dot{\omega}$, the Shapiro shape parameter s, and the rate of change of the orbital period $\dot{P}_\mathrm{b}$. For the first time, we accounted for the change of orbital period caused by spin-down mass loss (of pulsar A) in pulsar analysis, because of its considerable impact on the measurement of the MOI.

We found that an MOI measurement with 11% accuracy (68% confidence and hereafter) is possible by the end of this decade, given that sufficient knowledge of the Galactic gravitational potential is likely to be available in the near future, e.g. from *Gaia* mission (Gaia Collaboration, 2016). Such a measurement promises an important constraint on the EOS complementary to those obtained from LIGO/Virgo and NICER. In the future, with more double NS (DNS) mergers detected by LIGO/Virgo and other gravitational wave (GW) detectors, more X-ray observations by NICER and future missions,

and advances in the nuclear theory, our knowledge of the EOS will most likely be sufficient to enable novel gravity tests with the Double Pulsar.

The first test that can be performed, with a sufficiently well-known EOS, is to in turn test Lense-Thirring precession in a theory-independent manner. This is done by measuring the relative deviation of the spin-orbit coupling parameter $\sigma_A/\mathcal{G}$ from the prediction by general relativity (GR). Assuming a 5% error in the MOI of pulsar A and improved knowledge in the Galactic gravitational potential, we found that the Double Pulsar will allow for a 7% test of Lense-Thirring precession by 2030. This complements to Breton et al. (2008) where they found a 13% constraint on $\sigma_B/\mathcal{G}$ from the geodetic precession of pulsar B.

The second one that we studied is the measurability of the next-to-leading-order (NLO) GW damping predicted by GR, i.e. at 3.5PN order. With simulations, we predicted that the uncertainty of the 3.5PN order correction $X_{3.5\mathrm{PN}}$ will fall below its theoretical value starting from SKA-1 mid and a 3σ-measurement is possible by 2030. Therefore, in a few years we will start to be sensitive to the 3.5PN contribution and have to account for it in our analysis.

Finally, we discussed the prospects of measuring the MOI with DNS systems that have much shorter orbital periods than the Double Pulsar and are likely to be discovered by pulsar surveys from MeerKAT, FAST and the SKA in the near future. we demonstrated that such systems promise significant improvements in the MOI measurements. For example, for a DNS system that mimics the evolved Double Pulsar system with an orbital period of 50 min, the precision of MOI measurement is expected to be 1.5% after 10-yr timing, which is about one order of magnitude better than that expected from the Double Pulsar. Such discoveries, if achievable, could place quite competitive limits on the EOS and improve our understanding of NS matter.

As the lead author of this publication, I developed the simulation code, simulated and analysed the data, produced the figures (except for Figures 3.1 and 3.6) as well as interpreted the results and wrote the manuscript.

3.1 Introduction

Neutron stars (NSs) are among the most compact and exotic objects in nature, comprised of extraordinarily dense matter that is not accessible in laboratory experiments. Determining the properties and structure of the cold dense matter inside NSs is therefore a tremendous challenge in nuclear physics. Thus far, a variety of equations of state (EOSs) have been proposed to describe the pressure – density relation inside NSs (see e.g., Lattimer & Prakash, 2001; Lattimer & Prakash, 2016). Constraining the EOS is crucial for understanding aspects of fundamental physics, such as the internal structure of NSs, the dynamics of binary mergers, and r-process nucleosynthesis (for a recent review see Özel & P. Freire, 2016).

Various observational methods have emerged to measure the macroscopic properties of NSs, which promise to increase our knowledge of the EOS. The gravitational wave (GW) observation of a binary NS merger with LIGO/Virgo offers the possibility of measuring the tidal deformability (B. P. Abbott et al., 2017; B. P. Abbott et al., 2018). X-ray observations of emissions from the hot regions on NS surface with NICER (Watts et al., 2016) allows a joint mass-radius estimation (Riley et al., 2019; Miller et al., 2019).

The largest number of known NSs, however, can be observed as radio pulsars. Currently about 3000 pulsars are known, and the ability of radio astronomers to measure pulsar properties precisely via a technique known as “pulsar timing”, suggests that important information about the EOS of NSs can also be derived from such measurements. This is indeed the case. The most direct and best known route is to measure the masses of NSs precisely. This is possible in binary pulsars using relativistic orbital effects, potentially combined with other information. The mass range, especially the maximum

mass observed, must obviously be consistent with the range of masses supported by a proposed EOS. In addition, there are other orbital effects that also offer the possibility of measuring the moment of inertia (MOI) in binary pulsars via relativistic spin-orbit coupling, as was first suggested by Damour & Schäfer (1988). The MOI of a NS depends crucially on the EOS and hence allows us to constrain or even identify it (Morrison et al., 2004; Lattimer & Schutz, 2005; Greif et al., 2020). Accessing the MOI of isolated NSs, in contrast, may be possible if one can reliably derive or measure the total loss in rotational energy, $\dot{E}$, which relates the MOI with the observed period and period derivative.

In this work, we provide insight into the various methods using binary pulsars and their current status in Section 3.2, before we focus specifically on the possibility of using the Double Pulsar (Burgay et al., 2003; A. G. Lyne et al., 2004) for MOI measurements. We will provide an in-depth study of the relevant factors in Section 3.3, where we explain how Lense-Thirring (LT) precession affects the periastron advance. Section 3.4 describes the intrinsic and extrinsic contributions to the orbital period decay. We describe how we simulate future timing observations in Section 3.5 and evaluate how the Double Pulsar can measure the MOI and constrain the EOS in Section 3.6. Prospects of testing LT precession and constraining theories of gravity is discussed in Section 3.7 by assuming the EOS is known. We investigate potential constraints on next-to-leading-order GW damping in Section 3.8, and potential constraints from future discoveries of more relativistic binary pulsars in Section 3.9. Finally, we conclude in Section 3.10.

3.2 Methods to constrain the EOS via pulsar timing

3.2.1 Mass measurements

A given EOS i can only sustain a NS up to a certain maximum mass, $M_i^{\max}$. Finding a massive NS of mass M_j, consequently excludes all EOS with $M_i^{\max} < M_j$. This was, for instance possible, by using a Shapiro delay measurement in PSR J1614−2230, where P. B. Demorest et al. (2010) determined a mass $M = 1.97 \pm 0.04\,\mathrm{M}_\odot$. We note that a recent update on continued timing observations (Arzoumanian et al., 2018), implies a significantly lower mass of $1.908 \pm 0.016\,\mathrm{M}_\odot$ for this pulsar. As pointed out by Cromartie et al. (2019), a Shapiro delay measurement and the determined uncertainty can be affected by the exact orbital sampling (see also Hu et al., 2022).

In 2013, Antoniadis et al. (2013) could determine the mass of PSR J0348+0432 without using a Shapiro delay measurement. They combined radio timing measurements of the orbit of the pulsar with precise spectroscopy data of the white dwarf companion in the optical regime to derive a mass of $2.01 \pm 0.04\,\mathrm{M}_\odot$, confirming the existence of 2-$\mathrm{M}_\odot$ NSs via a complementary method.

Recently, Cromartie et al. (2019) used a Shapiro delay measurement in PSR J0740+6620 to determine a pulsar mass of $2.14^{+0.10}_{-0.09}\,\mathrm{M}_\odot$. We can use the masses of these latter two most massive pulsars, J0348+0432 (fully accounting for the rather asymmetric probability density distribution found by Antoniadis et al. (2013)) and J0740+6620, to obtain a 99% confidence lower limit for the maximum mass of a NS, $1.98\,\mathrm{M}_\odot < M^{\max}$. Such a constraint already rules out a number of soft EOSs as shown in Figure 3.1.[1]

We can compare this lower limit derived from pulsar timing with an upper limit placed by the NS-NS merger GW170817 observed by LIGO (B. P. Abbott et al., 2017). Assuming that the NS-NS merger resulted in the formation of a black hole, one finds an upper limit of about $2.3\,\mathrm{M}_\odot$ for the maximum mass of a NS (Rezzolla et al., 2018; Shibata et al., 2019).

[1] Note that in Figure 3.6, we show a different but overlapping set of EOSs. Here, we also show EOSs that have been excluded by the maximum mass measurement, while at the same time making the plot not too crowded.

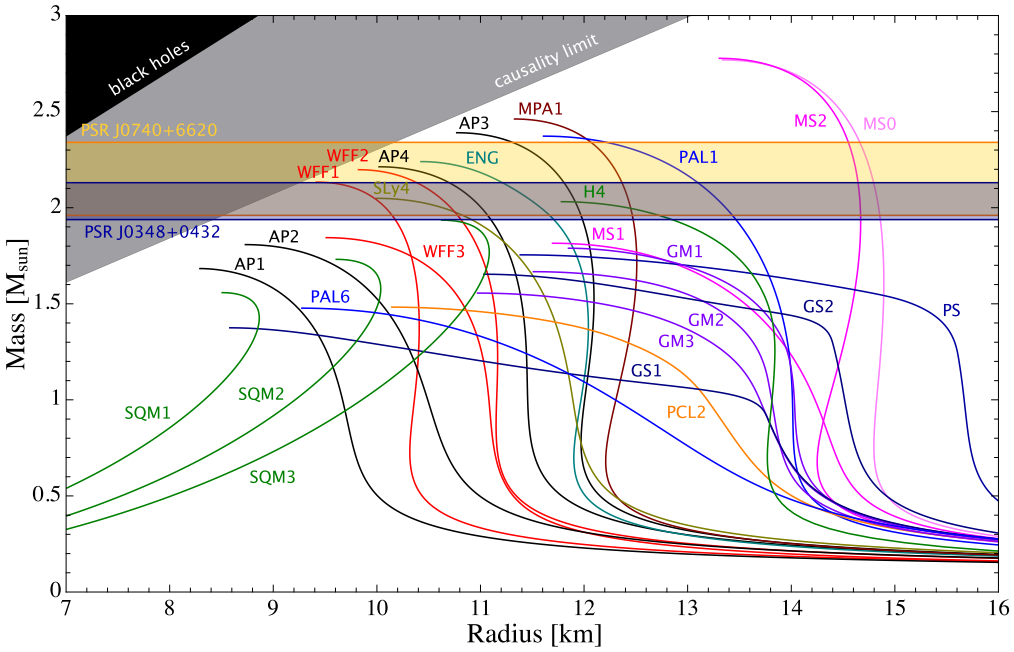

Figure 3.1: The mass of a NS as function of its radius for different EOS (Lattimer & Prakash, 2001). The horizontal bands indicate the 2-σ range for the masses of the two most massive radio pulsars known to date, PSR J0348+0432 (Antoniadis et al., 2013) in blue and PSR J0740+6620 (Cromartie et al., 2019) in yellow.

3.2.2 Relativistic spin-orbit coupling

Unlike in Newtonian gravity, the gravitational field of a body in general relativity (GR) has contributions from the mass currents related to the body's proper rotation. Lense & Thirring (1918) — with substantial help from Albert Einstein (see Pfister, 2007) — have shown that the rotation of the Sun has, in principle, an effect on the planetary orbits. This relativistic spin-orbit coupling, also known as LT precession, has since been well tested in the gravitational field of the rotating Earth with the help of satellite laser ranging (Ciufolini & Pavlis, 2004; Ciufolini et al., 2019). Similarly, in relativistic binaries, the spin of a compact rotating body is expected to couple gravitationally with the orbital motion of the system (Barker & O'Connell, 1975), leading to a precession of the orbit, while the total angular momentum is conserved.[2] This LT precession of the orbit is potentially observable, hence providing a route to access the MOI of the pulsar (Damour & Schäfer, 1988). An MOI measurement, even with an accuracy of ~10%, would offer important constraints of the EOS (Morrison et al., 2004; Lattimer & Schutz, 2005).

The LT precession of the orbit may be detected via the variation in the orbital inclination angle, i, and hence in the (observable) projected semi-major axis of the pulsar obit, $x = a_{\rm p} \sin i/c$ ($a_{\rm p}$ is the semi-major axis, and c the speed of light). However, for this to be detectable, the misalignment angle between pulsar spin and angular momentum vector must be sufficiently large. Also, the orbital inclination angle must not be too close to 90 degrees ("edge-on" geometry), since the precession leads to a contribution to the rate of change of the projected semi-major axis given by

$$\dot{x}^{\rm LT} = x \cot i \left(\frac{{\rm d}i}{{\rm d}t}\right)_{\rm LT}, \tag{3.1}$$

where $({\rm d}i/{\rm d}t)_{\rm LT}$ is given by Eq.(3.27) in Damour & Taylor (1992). For nearly edge-on systems, i.e.

[2] The loss of orbital angular momentum due to the emission of GWs is of higher post-Newtonian order and can be neglected here.

$i \approx 90$ deg, this contribution becomes small and most likely undetectable since $\cot i \ll 1$. However, in relativistic binary systems with smaller inclination angles, such as PSR J1757−1854, this measurement appears to be possible by Cameron et al. (2018). To achieve this, two challenges will have to be addressed successfully. Firstly, the precession is expected to cause a variation in the pulse profile with time due to a change in the viewing geometry (e.g. Kramer, 1998). Special care in the timing procedure is then needed to obtain sufficient precision and to properly account for possible systematic errors (e.g. Stairs et al., 2002; Bhat et al., 2008; van Leeuwen et al., 2015). Moreover, since we require access to the direction of the pulsar spin vector (Damour & Schäfer, 1988; Damour & Taylor, 1992), the geometry of the binary system and the pulsar needs also to be measured. This is, however, possible via polarisation measurements, as shown previously (e.g. Kramer, 1998; Stairs et al., 2004; Desvignes et al., 2019; Venkatraman Krishnan et al., 2020).

Alternatively, rather than using a contribution to $\dot{x}$, one can exploit LT precession also via its contribution to the advance of periastron. If it is possible to isolate the contribution of $\dot{\omega}^{\rm LT}$ from the total periastron advance, then the MOI can be determined (Damour & Schäfer, 1988). This method was suggested for the Double Pulsar, PSR J0737−3039A/B (A. G. Lyne et al., 2004; Kramer et al., 2006b). Kramer & Wex (2009) concluded that an MOI measurement of ∼10% accuracy is possible by ∼2030, with the timing accuracy achievable at the time. Later, Kehl et al. (2017) simulated timing data from emerging telescopes, i.e., the Square Kilometer Array (SKA; e.g. Kramer & B. Stappers, 2015) and its precursor MeerKAT (Bailes et al., 2016; Camilo, 2018), which greatly improve the timing precision, and predict an MOI measurement with an accuracy well below 10% by 2030. However, the timeline of the nominal operation of the SKA assumed by Kehl et al. (2017) was optimistic compared to the current estimates. With MeerKAT in operation since about 2018 (albeit initially with limited capability), operations of the first phase of the SKA (SKA 1, initially expected to have about 10% of the full SKA's sensitivity) are not expected before 2027. However, first useful data from commissioning observations may be already available in 2025.[3] In addition, compared to Kehl et al. (2017), we now already have about two years of Double Pulsar timing observations with MeerKAT, and therefore have more realistic numbers for the timing precision and cadence of observations, not only for the current MeerKAT configuration but also for future extensions. Moreover, Kehl et al. (2017) did not incorporate the contribution of spin-down mass loss of pulsar A to the orbital period derivative into the simulations. As we will show below, considering this effect is important, and its impact on our ability to measure the MOI needs to be studied in a fully consistent analysis. Hence, more complete simulations of the MOI measurement in the Double Pulsar should give us a more realistic estimate of the system's (near) future capability to constrain the EOS of ultra-dense matter inside a NS.

Consequently, in what follows, we present new and important details of how to measure the MOI of radio pulsars using the method of isolating the LT contribution to the advance of periastron. Using the Double Pulsar as the most promising system for this kind of experiment, we simulate timing data of PSR J0737−3039A that can be expected from MeerKAT and future extensions, to assess our ability to measure its MOI in the next 10 years.

3.3 Lense-Thirring effect in the Double Pulsar

The Double Pulsar is the only system to-date where both NSs have been observed as pulsars (Burgay et al., 2003; A. G. Lyne et al., 2004), with an orbital period of only 2.4 h. Breton et al. (2008) used the system to provide a 13%-test of spin-orbit interaction of strongly self-gravitating bodies using the relativistic spin precession in pulsar B. The compact, relativistic nature of the system also allows the

[3] See skatelescope.org for updates.

measurement of several post-Keplerian (PK) parameters to an unparalleled level of accuracy. This not only enables some of the most stringent tests of GR related to strong-field gravity (Kramer et al., 2006b; Kramer & Wex, 2009; Will, 2018), but it is also crucial for the efforts to measure the MOI and to constrain the EOS of a NS.

3.3.1 Spin-orbit coupling contribution to the periastron advance

To simplify the problem, we neglect the LT contribution of pulsar B, since it spins about 122 times slower than pulsar A. Such a simplification is well justified, as will become clear below. In addition, the long term observations of the pulse profile of PSR J0737−3039A shows that the misalignment angle between the spin axis of pulsar A and the orbital angular momentum has an upper limit of 3.2° (Ferdman et al., 2008; Ferdman et al., 2013). Therefore, for all practical purposes, we can assume that the spin of pulsar A is parallel to the orbital angular momentum, which is consistent with evolutionary considerations for the Double Pulsar system and a low-kick supernova formation (e.g. Stairs et al., 2006; Tauris et al., 2017). Pol et al. (2018) confirmed that pulsar A is indeed rotating prograde in its orbit, using the modulation of pulsar B's radio emission by the interaction with the wind of pulsar A. Consequently, the spin of pulsar A only induces a change to the advance of periastron, and does not lead to a change in the orbital inclination, more specifically, the projected semi-major axis. Following Damour & Schäfer (1988), the total intrinsic contribution to the periastron advance in the Double Pulsar system can be written, with sufficient precision, as

$$\begin{aligned}\dot{\omega}^{\rm intr} &= \dot{\omega}^{\rm 1PN} + \dot{\omega}^{\rm 2PN} + \dot{\omega}^{\rm LT,A} \\ &= \frac{3\,\beta_{\rm O}^2\, n_{\rm b}}{1-e_{\rm T}^2}\left[1 + f_{\rm O}\,\beta_{\rm O}^2 - g^{\parallel}_{\rm S_A}\beta_{\rm O}\,\beta_{\rm S_A}\right], \end{aligned} \tag{3.2}$$

where $n_{\rm b}$ is the orbital frequency, and $e_{\rm T}$ is the proper-time eccentricity used as the observed eccentricity in the standard timing model (D. Nice et al., 2015) and defined in Damour & Deruelle (1986). The factor in front of the right-hand side of Eq. (4.13) is the first post-Newtonian (1PN) contribution; the higher order corrections due to 2PN effects and LT precession caused by pulsar A are indicated by the second and third term in the square brackets respectively. The following notations are used to simplify Eq. (4.13),

$$\beta_{\rm O} = \frac{(GMn_{\rm b})^{1/3}}{c}, \tag{3.3}$$

$$\beta_{\rm S_A} = \frac{cI_{\rm A}\Omega_{\rm A}}{Gm_{\rm A}^2}, \tag{3.4}$$

$$f_{\rm O} = \frac{1}{1-e_{\rm T}^2}\left(\frac{3}{2}x_{\rm A}^2 + \frac{3}{2}x_{\rm A} + \frac{27}{4}\right) + \left(\frac{5}{6}x_{\rm A}^2 - \frac{23}{6}x_{\rm A} - \frac{1}{4}\right), \tag{3.5}$$

$$g^{\parallel}_{\rm S_A} = \frac{1}{(1-e_{\rm T}^2)^{1/2}}\left(\frac{1}{3}x_{\rm A}^2 + x_{\rm A}\right). \tag{3.6}$$

The subscript A stands for pulsar A. G is the Newtonian gravitational constant, and $M = m_{\rm A} + m_{\rm B}$ is the total mass defined as the sum of the (inertial) masses of pulsar A and B, and $x_{\rm A} = m_{\rm A}/M$. $I_{\rm A}$ denotes the MOI and $\Omega_{\rm A}$ the angular spin frequency.[4]

[4] Since pulsar A is slowly rotating (~ 2.5% of break-up velocity), for the purpose of this paper we do not have to distinguish between rotating and non-rotating quantities when it comes to (gravitational) mass, moment of inertia, etc. (see e.g. Berti et al., 2005)

Table 3.1: Contributions to the rate of periastron advance in the Double Pulsar calculated using Eq. (4.13), with the Keplerian parameters and masses ($m_A = 1.3381\,M_\odot$, $m_B = 1.2489\,M_\odot$) measured in Kramer et al. (2006b). $I_A^{(45)} = I_A/(10^{45}\,\mathrm{g\,cm^2})$. The current measurement precision for $\dot{\omega}$ is already $\sim 10^{-5}$ deg yr^{-1} (Kramer et al., 2021a), which is about 40 times smaller than $\dot{\omega}^{\mathrm{LT,A}}$.

Contribution	[deg yr^{-1}]
$\dot{\omega}^{\mathrm{1PN}}$	16.898703
$\dot{\omega}^{\mathrm{2PN}}$	0.000439
$\dot{\omega}^{\mathrm{LT,A}}$	$-0.000377\times I_A^{(45)}$

Table 3.1 lists the values of each term contributing to $\dot{\omega}^{\mathrm{intr}}$, using the Keplerian parameters and masses ($m_A = 1.3381\,M_\odot$, $m_B = 1.2489\,M_\odot$) measured in Kramer et al. (2006b). We note that the contribution due to the LT precession $\dot{\omega}^{\mathrm{LT,A}}$ depends on the MOI, whereby is written as a function of $I_A^{(45)}$ defined as $I_A^{(45)} = I_A/(10^{45}\,\mathrm{g\,cm^2})$. Typical values of $I_A^{(45)}$ are around unity for realistic EOSs. It is evident that the contribution from the LT effect is comparable to that of 2PN, but with opposite signs.

The analysis of timing data from relativistic binary pulsars is based on a particularly simple and elegant solution of the post-Newtonian equations of motion, the so called Damour-Deruelle (DD) model (Damour & Deruelle, 1985; Damour & Deruelle, 1986; D. Nice et al., 2015). In the quasi-Keplerian parametrization of the DD model one can see that the advance of periastron is proportional to the true anomaly. This behaviour is modified by two periodic terms as part of the generalised quasi-Keplerian parametrization, which is a natural extension of the DD model when including 2PN and spin-orbit terms (Damour & Schäfer, 1988; Schäfer & Wex, 1993; Wex, 1995). However, these periodic terms will remain well below measurability for the foreseeable future, for any of the known binary pulsars. For that reason, we will ignore them in our analysis.

Besides the coupling to the orbital angular momentum (spin-orbit coupling), the spin of pulsar A also couples to the spin of pulsar B (spin-spin coupling) (Barker & O'Connell, 1975). However, the spin of pulsar B is about a factor of 3×10^6 smaller than the orbital angular momentum. Hence, spin-spin coupling is totally irrelevant here.

Finally there are, at least in principle, also contributions from the rotationally induced mass quadrupole moments of pulsars A and B to the orbital dynamics (Barker & O'Connell, 1975). These spin-squared contributions give rise to an additional change in the advance of periastron (Smarr & Blandford, 1976; Wex, 1998). The contribution from the quadrupole moment of pulsar A is estimated to be $\sim 3 \times 10^{-8}$ deg yr^{-1}, where we have used the relations in Bauböck et al. (2013) to calculate the mass quadrupole. This is four orders of magnitude smaller than the second order effects. The contribution from pulsar B is even smaller (about 10^4 times) due to its slower rotation. Hence we can totally ignore such contributions in this study.

3.3.2 The proper motion contribution to the observed periastron precession

Apart from the intrinsic contributions to the periastron advance, the proper motion of a binary system also can change the apparent geometrical orientation of the orbit, and hence the observed periastron advance (Kopeikin, 1996). As a consequence, the observed value of periastron advance is shifted from its intrinsic value by

$$\dot{\omega}^{\mathrm{obs}} = \dot{\omega}^{\mathrm{intr}} + \dot{\omega}^{\mathrm{K}}\,. \tag{3.7}$$

Here, $\dot{\omega}^{\rm K}$ is the *Kopeikin term* that satisfies

$$\dot{\omega}^{\rm K} = 2.78 \times 10^{-7} \csc i \, (\mu_\alpha \cos\Omega + \mu_\delta \sin\Omega) \ \mathrm{deg\,yr^{-1}}\,, \tag{3.8}$$

where i is the orbital inclination as defined in Damour & Taylor (1992), μ_α and μ_δ are the proper motion in right ascension and declination, and Ω is the longitude of the ascending node (measured from East, in the sense of rotation towards North). Using the parameters measured by Kramer et al. (2006b) and the estimated $\Omega = 25(2)^\circ$ by Rickett et al. (2014),[5] we obtain $\dot{\omega}^{\rm K} = -4.0(3) \times 10^{-7}\,\mathrm{deg\,yr^{-1}}$. Given the current measurement precision $\Delta\dot{\omega} \sim 10^{-5}\,\mathrm{deg\,yr^{-1}}$ (Kramer et al., 2021a), the *Kopeikin term* is a small correction to the intrinsic periastron advance that we use in this study. However, since it is three orders of magnitude smaller than $\dot{\omega}^{\rm LT,A}$ (see Table 3.1), it does not have a significant influence on the LT measurement.

3.3.3 Challenges on extracting the Lense-Thirring contribution and measuring the MOI

Although the current measurement precision $\Delta\dot{\omega}$ is already ~ 40 times smaller than $\dot{\omega}^{\rm LT,A}$, it is not that straightforward to extract the LT contribution from $\dot{\omega}^{\rm obs}$ with Eqs. (4.13) and (3.7), as the two masses ($m_{\rm A}$, $m_{\rm B}$) are needed to calculate $\dot{\omega}^{\rm 1PN}$ and $\dot{\omega}^{\rm 2PN}$. The masses need to be obtained from any other two PK parameters, where the best two here are the Shapiro delay shape parameter s and the orbital period derivative $\dot{P}_{\rm b}$ (see Figure 3.2). For the Double Pulsar, we already have sufficient precision for s, so the limitation is mainly from $\dot{P}_{\rm b}$ (Kramer et al., 2021a). The measurement precision of $\dot{P}_{\rm b}$ will improve over time, especially with the addition of MeerKAT and the SKA. However, the observed value of $\dot{P}_{\rm b}$ is influenced by extrinsic acceleration effects, which depend on the distance of the pulsar and the Galactic gravitational potential. Moreover, the spin-down mass loss of the pulsars also have an impact on $\dot{P}_{\rm b}$, which itself depends on the MOI, meaning the masses can not be determined independently from $I_{\rm A}$. These are the challenges for measuring the MOI. An alternative option to $\dot{P}_{\rm b}$ could be the time dilation amplitude γ, whose fractional error is about one order of magnitude larger than $\dot{P}_{\rm b}$ (see Figure 3.2). However, based on the assumptions of observing plan in Section 3.5, it would take at least two decades from now to obtain a 1σ-measurement of $\dot{\omega}^{\rm LT,A}$ using only γ, s and $\dot{\omega}$, a precision that is already reached now with $\dot{P}_{\rm b}$ (Kramer et al., 2021a). Hence, a comprehensive understanding of the individual contributions to $\dot{P}_{\rm b}$ is needed, which will be discussed in detail in the following section.

3.4 The intrinsic and extrinsic contributions to the orbital period decay

The observed value of the orbital period decay comprises several effects (Damour & Taylor, 1991). For the purpose of this study, we only consider the dominant terms

$$\left(\frac{\dot{P}_{\rm b}}{P_{\rm b}}\right)^{\rm obs} = \left(\frac{\dot{P}_{\rm b}}{P_{\rm b}}\right)^{\rm GR} + \left(\frac{\dot{P}_{\rm b}}{P_{\rm b}}\right)^{\dot{m}_{\rm A}} + \left(\frac{\dot{P}_{\rm b}}{P_{\rm b}}\right)^{\rm Gal} + \left(\frac{\dot{P}_{\rm b}}{P_{\rm b}}\right)^{\rm Shk}\,, \tag{3.9}$$

where gravitational wave damping (GR) and mass loss of pulsar A ($\dot{m}_{\rm A}$) are intrinsic contributions, and Galactic acceleration (Gal) and Shklovskii effect (Shk) are extrinsic contributions. Thereby, the intrinsic orbital period decay can be extracted from the observed value using

$$\dot{P}_{\rm b}^{\rm\ intr} = \dot{P}_{\rm b}^{\rm\ obs} - \dot{P}_{\rm b}^{\rm\ Gal} - \dot{P}_{\rm b}^{\rm\ Shk}\,. \tag{3.10}$$

[5] Note, Rickett et al. (2014) use a different definition for the longitude of the ascending node Ω, which we have accounted for.

Table 3.2: Contributions to the rate of orbital period decay in the Double Pulsar, calculated with Keplerian parameters and masses measured in Kramer et al. (2006b). The Galactic acceleration is computed using Galactic measurements by Gravity Collaboration (2019) and slope in Reid et al. (2014), and a distance of 0.80 kpc is assumed. $I_{\rm B}^{(45)}$ is defined in the same way as $I_{\rm A}^{(45)}$. The current measurement precision for $\dot{P}_{\rm b}$ is below 0.1 fs/s (Kramer et al., 2021a).

Contribution	[fs/s]
$\dot{P}_{\rm b}^{\rm 2.5PN}$	-1248
$\dot{P}_{\rm b}^{\rm Gal}$	-0.38
$\dot{P}_{\rm b}^{\rm Shk}$	0.21
$\dot{P}_{\rm b}^{\rm 3.5PN}$	-0.017
$\dot{P}_{\rm b}^{\dot{m}_{\rm A}}$	$0.023 \times I_{\rm A}^{(45)}$
$\dot{P}_{\rm b}^{\dot{m}_{\rm B}}$	$6.3 \times 10^{-6} \times I_{\rm B}^{(45)}$

Consequently, the uncertainty in the intrinsic orbital period decay also depends on the error in the pulsar distance and the uncertainty in the Galactic gravitational potential at the location of the pulsar and the Earth.

3.4.1 Gravitational wave damping

The binary system loses energy in the form of GW emission, which shrinks the orbit of the system, and in turn gradually reduces the orbital period. The post-Newtonian approximation is employed to describe the orbital dynamics of the binary system (see e.g. Damour, 1987; Blanchet, 2014), i.e. the equations of motion are expanded with respect to v/c, where v denotes a typical orbital velocity. The change of the orbital period due to GW damping enters at order $(v/c)^5$, i.e. the 2.5PN approximation. The corresponding change in the orbital period is given by (Peters & Mathews, 1963; Esposito & Harrison, 1975; Wagoner, 1975)

$$\dot{P}_{\rm b}^{\rm 2.5PN} = -\frac{192\pi}{5} \frac{\eta \beta_{\rm O}^5}{(1-e_{\rm T}^2)^{7/2}} \left(1 + \frac{73}{24} e_{\rm T}^2 + \frac{37}{96} e_{\rm T}^4\right) , \tag{3.11}$$

where $\eta = m_{\rm A} m_{\rm B}/M^2$ is the symmetric mass ratio. Later, Blanchet & Schäfer (1989) extended the expression to the next-to-leading order (3.5PN),

$$\begin{aligned} \dot{P}_{\rm b}^{\rm GR} = -\frac{192\pi}{5} \frac{\eta \beta_{\rm O}^5}{(1-e_{\rm T}^2)^{7/2}} \Bigg\{ 1 + \frac{73}{24} e_{\rm T}^2 + \frac{37}{96} e_{\rm T}^4 + \frac{\beta_{\rm O}^2}{336\,(1-e_{\rm T}^2)} \Bigg[1273 + \frac{16495}{2} e_{\rm T}^2 + \frac{42231}{8} e_{\rm T}^4 + \frac{3947}{16} e_{\rm T}^6 \\ - \left(924 + 3381 e_{\rm T}^2 + \frac{1659}{4} e_{\rm T}^4 - \frac{259}{4} e_{\rm T}^6\right) \eta + \left(3297 e_{\rm T}^2 + 4221 e_{\rm T}^4 + \frac{2331}{8} e_{\rm T}^6\right) \frac{\delta m}{M} \Bigg] \Bigg\}, \end{aligned} \tag{3.12}$$

where δm denotes the mass difference of the timed pulsar and its companion, in our case, $\delta m = m_{\rm A} - m_{\rm B}$. Eq. (3.12) can be written in a simplified form as

$$\dot{P}_{\rm b}^{\rm GR} = \dot{P}_{\rm b}^{\rm 2.5PN} \left(1 + X_{\rm 3.5PN}\right) , \tag{3.13}$$

where the relative correction of the 3.5PN order, $X_{\rm 3.5PN}$, is 1.40×10^{-5} for the Double Pulsar. To date, only the leading order contribution to the orbital period decay is considered in the analysis and

interpretation of any of the known binary pulsars. The higher order correction, however, will need to be included in the future, when we reach the necessary timing precision with emerging powerful radio telescopes such as the SKA. We will evaluate future measurability of the 3.5PN contribution to $\dot{P}_{\rm b}$ in Section 3.8.

Besides the damping of the binary period, the emission of GWs in principle has an additional effect on the observed $\dot{P}_{\rm b}$. Junker & Schäfer (1992) have shown that a double NS system with asymmetric masses in an eccentric orbit becomes accelerated due to the GW recoil. Since any acceleration along the line of sight leads to an apparent change in the orbital period (Damour & Taylor, 1991), the GW recoil at 3.5PN order will also affect the observed orbital period at some level. As Junker & Schäfer (1992) have pointed out, the recoil acceleration changes its direction with the advance of periastron, in our case on a timescale of about 21 years. However, using Eq. (103) in Junker & Schäfer (1992) we find a maximum shift in the observed $\dot{P}_{\rm b}$ due to GW recoil of 4.6×10^{-24}, which is seven orders of magnitude below the current measurement precision.

3.4.2 Galactic acceleration and Shklovskii effect

The contribution of Galactic acceleration can be calculated with (Damour & Taylor, 1991; D. J. Nice & Taylor, 1995; Lazaridis et al., 2009)

$$\left(\frac{\dot{P}_{\rm b}}{P_{\rm b}}\right)^{\rm Gal} = -\frac{K_z |\sin b|}{c} - \frac{\Theta_0^2}{c R_0} \times \left\{ \cos l + \frac{\beta}{\sin^2 l + \beta^2} \left[1 + b_0 \left(1 - \sqrt{\sin^2 l + \beta^2} \right) \right]^2 \right\} \cos b \,, \tag{3.14}$$

where $\beta = (d/R_0)\cos b - \cos l$. For the Double Pulsar, the Galactic longitude l is 245.2° and the Galactic latitude b is −4.5°. As for the distance to the Double Pulsar (d), the VLBI observations made by Deller et al. (2009) implied a distance of $1.15^{+0.22}_{-0.16}$ kpc, whereas the dispersion measure (DM) favours a distance of about 0.52 kpc (Cordes & Lazio, 2002). We note that new, preliminary timing and VLBI measurements indicate a distance closer to the DM distance (Kramer et al., 2021a). Hence, for our simulation, we consider an intermediate distance of 0.8 kpc with a 10% error. We will see in Section 3.6, using a different distance does not have a big influence on our results. The vertical contribution of the Galactic acceleration K_z for Galactic height $z \equiv |d \sin b| \lesssim 1.5$ kpc can be approximated with the expression (Holmberg & Flynn, 2004; Lazaridis et al., 2009)

$$K_z [10^{-9}\,{\rm cm\,s^{-2}}] \simeq 2.27\, z_{\rm kpc} + 3.68 \left[1 - \exp(-4.31\, z_{\rm kpc}) \right], \tag{3.15}$$

where $z_{\rm kpc} \equiv z[{\rm kpc}]$. For K_z, we consider a typical error of about 10% (Holmberg & Flynn, 2004; L. Zhang et al., 2013). The Galactic parameters R_0 is the distance from the Sun to the Galactic center, and Θ_0 is the Galactic circular velocity at the location of the Sun. In our calculation, we adopt the recent result in Gravity Collaboration (2019), where $R_0 = 8.178 \pm 0.026$ kpc and $\Theta_0 = 236.9 \pm 4.2\,{\rm km\,s^{-1}}$.[6] The slope parameter at the radius of the Sun is defined as (Damour & Taylor, 1991):

$$b_0 \equiv \left(\frac{R}{v} \frac{{\rm d}v}{{\rm d}R} \right)_{R=R_0} . \tag{3.16}$$

[6] We note that the latest measurement of R_0 shows a 2σ difference (Gravity Collaboration, 2020), which will not affect our results.

We note this term is often ignored in other studies, as the rotation curve is nearly flat in the vicinity of the Sun. Its uncertainty, however, could be relevant for measuring the MOI, and as such is included in our study. The slope of the Galactic rotation curve at the location of the Sun estimated by Reid et al. (2014) is $-0.2 \pm 0.4\,\mathrm{km\,s^{-1}\,kpc^{-1}}$, corresponding to $b_0 = 0.007 \pm 0.014$. Lately, Eilers et al. (2019) found a slope significantly different from zero, i.e. $-1.7 \pm 0.1\,\mathrm{km\,s^{-1}\,kpc^{-1}}$ ($b_0 = 0.0603 \pm 0.0035$), with a systematic uncertainty of $0.46\,\mathrm{km\,s^{-1}\,kpc^{-1}}$. Both results will be employed later in our simulation, but for Eilers et al. (2019) we only consider the statistical error and assume that the systematic error can be well understood in the future.

Besides the Galactic acceleration, there are additional accelerations due to masses in the vicinity of the Sun or the pulsar, primarily giant molecular clouds (GMCs), but also stars, black holes, and other external masses (Damour & Taylor, 1991; Kehl, 2015). These have most likely, if at all, only a small influence on the result, which should not limit our ability of measuring the MOI with a precision lower than 10% (Kehl, 2015). The influence of these masses mostly depends on the distance to the Double Pulsar, with which we can, for instance, trace and restrict the presence and influence of GMCs using Galactic carbon monoxide (CO) surveys (Neininger et al., 1998; Glover & Mac Low, 2011). We expect that a more firmly established distance measurement in the future will allow a refined analysis to confirm our conclusions.

Finally, the transverse motion of a pulsar leads to an apparent change in the orbital period. This is known as the Shklovskii effect (Shklovskii, 1970), and is given as

$$\left(\frac{\dot{P}_\mathrm{b}}{P_\mathrm{b}}\right)^\mathrm{Shk} = \frac{\mu^2 d}{c}, \quad \text{with} \quad \mu^2 = \mu_\alpha^2 + \mu_\delta^2\,. \tag{3.17}$$

3.4.3 Mass loss

A pulsar loses mass due to its energy emission, which changes the orbital period by (Jeans, 1924; Jeans, 1925)

$$\left(\frac{\dot{P}_\mathrm{b}}{P_\mathrm{b}}\right)^{\dot{m}} = -2\,\frac{\dot{m}_\mathrm{A} + \dot{m}_\mathrm{B}}{M}\,. \tag{3.18}$$

Although the emission process of pulsars is not fully understood, the mass-energy loss can be calculated (with sufficient precision) from the loss in rotational kinetic energy, i.e., $\dot{E}_j^\mathrm{rot} \simeq \dot{m}_j c^2$ (Damour & Taylor, 1991), where $\dot{E}_j^\mathrm{rot} = I_j \Omega_j \dot{\Omega}_j$, with Ω_j the angular velocity of the (proper) rotation of body j (j = A or B), given in terms of the spin period by $\Omega_j = 2\pi/P_j$. Hence,

$$\left(\frac{\dot{P}_\mathrm{b}}{P_\mathrm{b}}\right)^{\dot{m}_j} = \frac{8\pi^2 \dot{P}_j I_j}{c^2 M P_j^3}\,. \tag{3.19}$$

Clearly, the mass-loss correction to the rate of orbital period decay also depends on the MOI, and therefore on the EOS. Table 3.2 lists the predicted value of each contribution to $\dot{P}_\mathrm{b}^\mathrm{obs}$, where the mass-loss contributions are written as a function of $I_\mathrm{j}^{(45)}$. The contribution due to the mass loss of pulsar A is one order of magnitude smaller than that of the Galactic acceleration and the Shklovskii effect, and of the same order of magnitude as the current measurement precision (Kramer et al., 2021a), hence must be considered. The mass-loss contribution of pulsar B, however, is nearly four orders of magnitude smaller than that of pulsar A and thus can be safely ignored.

3.5 Simulations

In order to investigate the capability of measuring the MOI and testing GR with radio pulsars, we developed a simulation framework to generate and analyse time of arrivals (TOAs) for binary pulsars. In this section, we will describe how we simulate TOAs from emerging telescopes for PSR J0737−3039A based on realistic assumptions, and how to measure PK parameters and timing parallax.

To simulate TOAs of PSR J0737−3039A from current and future telescopes, knowledge of the sensitivity of the telescopes, as well as (realistic) assumptions about a future observing plans are needed. We consider the best telescopes for observing this pulsar, i.e., MeerKAT and its future arrays. Unfortunately, this pulsar is not in the field of view of the Five-hundred-meter Aperture Spherical radio Telescope (FAST; Nan et al., 2011), the largest radio telescope today and in the near future.

MeerKAT is a precursor for the mid-frequency array of the SKA, which comprises 64 dishes, each with a diameter of 13.5 m. This corresponds to an effective diameter ($\varnothing_{\rm eff}$) of 108 m. Regular timing observations for the Double Pulsar started in 2019 as a part of the MeerTIME project (Bailes et al., 2016). The MeerKAT extension, hereafter MeerKAT+, is a joint collaboration of the South African Radio Astronomy Observatory (SARAO) and the Max-Planck-Society (MPG) to extend MeerKAT by the addition of 20 SKA-type dishes, each 15 m in diameter, to MeerKAT. MeerKAT+ is expected to operate from 2022, providing an increase in sensitivity by 50% (Kramer, priv. comm.) The first phase of the SKA mid-frequency array, SKA 1-mid, is planned to build 112 additional dishes with 15 m diameter, extending MeerKAT+ further, with first data from 2025 and full operation after 2027. We summarise the observing plans and the effective diameters of these telescopes in Table 3.3.

In order to estimate the TOA uncertainty of each observing phase, we need to consider noise contributions for pulsar A. The TOA uncertainty of pulsar A with real MeerKAT observations at L-band is about 1.06 μs for a 5 minutes integration over the full bandwidth (Bailes et al., 2020). Since the system performance of MeerKAT+ and SKA 1-mid are expected to be similar to that of MeerKAT, and the radiometer noise $\sigma_{\rm rn}$ reduces in reverse proportional to the effective collection area of the telescope $A_{\rm eff}$, we can therefore calculate the radiometer noise using the relation

$$\sigma_{\rm rn}^{\rm tel} = \frac{A_{\rm eff}^{\rm MK}}{A_{\rm eff}^{\rm tel}} \sigma_{\rm rn}^{\rm MK}, \tag{3.20}$$

where the superscript "MK" stands for MeerKAT. We are not considering noise budgets other than the radiometer noise, because: 1) The phase jitter has not been detected in the current MeerKAT observations and must be rather small (Hu et al., 2022; Bailes et al., 2020). It may become important in the future observing phase as the radiometer noise reduces, but the influence of jitter can potentially be reduced using Bayesian methods (Imgrund et al., 2015) or binning and combining the data in orbital phase. 2) The contributions from scintillation and other effects are expected to be one or more orders of magnitude smaller than the radiometer noise of SKA 1-mid, hence are neglected. As a result, in our simulation, we adopt the TOA uncertainties solely based on the radiometer noise estimation for each observing phase, which can be found in Table 3.3.

Based on the above assumptions, we generate TOAs of PSR J0737−3039A that mimic observations with MeerKAT, MeerKAT+, and SKA 1-mid from 2019 to 2030 covering two full orbits per month (∼5 h), and combine them with the existing TOAs from multiple telescopes (Kramer et al., 2021a) to form a long-range data set (2003–2030). Technically speaking, we only use the observing cadence and TOA uncertainties from the existing TOAs, since the data analysis by Kramer et al. (2021a) is still ongoing, and in the next steps all TOAs will be simulated to fit our model, under the assumption of Gaussian white noise.

Table 3.3: Telescope observing plans, effective diameters and TOA uncertainties (L-band, 5 minute integration time) used for simulation. For 2003 – 2019, $\sigma_{\rm TOA}$ are based on observations from multiple telescopes, where the best data are from the GBT. Its typical uncertainty at L-band is shown in the table, whereas the TOAs from the UHF band are expected to be 1.25 times better (Kramer et al., 2021a). The TOA uncertainty for MeerKAT is scaled to 5 minute integration based on real observations (Bailes et al., 2020),[7] and for MeerKAT+ and SKA 1-mid are scaled referring to MeerKAT.

Year	Telescope	$\varnothing_{\rm eff}$ [m]	$\sigma_{\rm TOA}$ [μs]
2003 – 2019	GBT	100	2.5
2019 – 2022	MeerKAT	108	1.06
2022 – 2025	MeerKAT+	127	0.76
2025 – 2030	SKA 1-mid	203	0.30

The first step is to create a parameter file (model) for pulsar A. For this, we take precisely measured masses from Kramer et al. (2006b), $m_{\rm A} = 1.3381\,{\rm M}_\odot$, $m_{\rm B} = 1.2489\,{\rm M}_\odot$, and assume EOS AP4 see Lattimer & Prakash, 2001. This particular choice of EOS satisfies the current lower limit of $1.98\,{\rm M}_\odot$ (99% confidence level, hereafter C.L.) for the maximum mass of a NS (see Section 3.1 for details), and also lies in the MOI ranges obtained for pulsar A by Gorda (2016), Lim et al. (2019) and Greif et al. (2020). The MOI of pulsar A, under this assumption, is therefore $I_{\rm A}^{\rm AP4} = 1.24 \times 10^{45}\,{\rm g\,cm^2}$. We create a parameter file by taking the well measured Keplerian parameters of the Double Pulsar (Kramer et al., 2006b) and the PK parameters computed from $m_{\rm A}$, $m_{\rm B}$, and $I_{\rm A}$. For the advance of periastron $\dot{\omega}$, we consider first and second order PN terms and the LT contribution. As for the orbital period decay $\dot{P}_{\rm b}$, we consider leading order (2.5PN) GW emission, Galactic acceleration, Shklovskii effect and mass loss in pulsar A. The 3.5PN GW term is only considered in Section 3.8.

We then adjust the TOAs to perfectly match with our model, and add a Gaussian white noise to each TOA, according to its $\sigma_{\rm TOA}$. The red noise from DM variations is not considered in our simulation, since it can be in principle corrected for with multi-frequency data. In a final step, we use the pulsar timing software TEMPO to fit for the timing parameters and obtain their uncertainties, including the PK parameters, which are of particular importance here. From 2018 to 2030, the data set is split with a step size of 6 months, so as to demonstrate how the measurements improve with time. The predicted fractional errors of the PK parameters are shown in Figure 3.2.

As part of the simulation, we also measure the timing parallax π_x, which gives an idea of the precision of future distance measurement from timing parallax. The predicted uncertainty of π_x is shown in Figure 3.3. For the uncertainty of pulsar distance, which enters the Galactic acceleration and the Shklovskii effect, we adopt the value calculated from timing parallax when its uncertainty is smaller than what we assumed in Section 3.4.2, which is from mid-2021. Aside from timing parallax measurement, in the future, the VLBI parallax measurements with the SKA can potentially provide an accurate distance measurement (Smits et al., 2011).

3.6 Measuring the MOI and constraining the EOS

Based on our TOA simulation, we predict the future timing measurement of PK parameters (Figure 3.2). The three best measured parameters, $\dot{P}_{\rm b}^{\rm obs}$, $\dot{\omega}^{\rm obs}$ and s, are promising for the determination of $I_{\rm A}$. With Eqs. (3.7) and (3.10), we obtain the intrinsic periastron advance $\dot{\omega}^{\rm intr}(m_{\rm A}, m_{\rm B}, I_{\rm A})$ and the intrinsic orbital period decay $\dot{P}_{\rm b}^{\rm intr}(m_{\rm A}, m_{\rm B}, I_{\rm A})$. Since both now $\dot{\omega}^{\rm intr}$ and $\dot{P}_{\rm b}^{\rm intr}$ depend on the MOI, we can not

[7] The TOA uncertainty obtained from a series of real MeerKAT observations are presented later in Table 4.4.

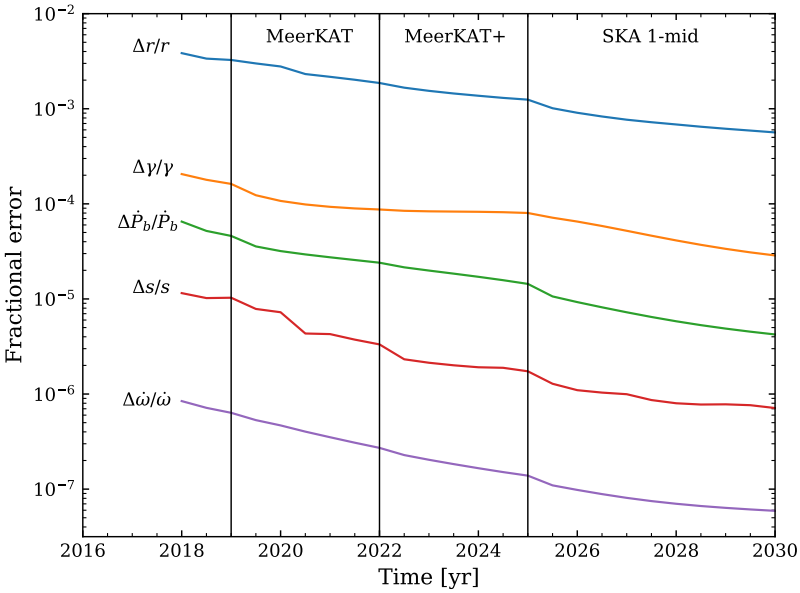

Figure 3.2: Improvement in the fractional errors of five PK parameters with time, based on the simulation described in Section 3.5. From top to bottom are: the Shapiro delay range parameter r (blue), the time dilation amplitude γ (orange), the orbital period derivative $\dot{P}_\mathrm{b}$ (green), the Shapiro delay shape parameter s (red), and the relativistic advance of periastron $\dot{\omega}$ (purple). The vertical lines mark the observing phase of MeerKAT, MeerKAT+, and SKA 1-mid.

directly use $\dot{P}_\mathrm{b}^{\mathrm{intr}}$ and s to determine the masses and hence measure I_A from $\dot{\omega}^{\mathrm{intr}}$ as in Kehl et al. (2017). Instead, a self-consistent method is employed to solve for the masses $(m_\mathrm{A}, m_\mathrm{B})$ and I_A jointly from $\dot{P}_\mathrm{b}^{\mathrm{intr}}(m_\mathrm{A}, m_\mathrm{B}, I_\mathrm{A})$, $s\,(m_\mathrm{A}, m_\mathrm{B})$ and $\dot{\omega}^{\mathrm{intr}}\,(m_\mathrm{A}, m_\mathrm{B}, I_\mathrm{A})$. To estimate the probability distribution function for I_A, we perform a Monte Carlo simulation to randomise the observed parameters according to their uncertainties. This process is repeated for the measurements from 2018 to 2030.

Figure 3.4 shows the predicted measurements of I_A with time, where the new telescopes clearly help to narrow down the uncertainty of I_A. Here we adopt the Galactic measurements (R_0, Θ_0) by Gravity Collaboration (2019) and the slope measurement by Reid et al. (2014). The predicted uncertainty of I_A with time is also illustrated as the blue line in Figure 3.5. In this case, we expect to achieve an MOI measurement with 25% precision at 68% C.L. by the year 2030. Our simulation shows that, although the uncertainty of $\dot{P}_\mathrm{b}^{\mathrm{obs}}$ is initially higher than the Galactic acceleration, it decreases with additional years of precise timing observations (see Figure 3.2), and by 2030, the error in the Galactic acceleration is three times higher than the error in $\dot{P}_\mathrm{b}^{\mathrm{obs}}$, which becomes the limiting factor for measuring the MOI.

However, the measurements of the Galactic potential is expected to improve through various observational methods, such as Gaia mission (Gaia Collaboration, 2016) and ongoing observations of Galactic masers (Reid et al., 2014). A recent study by Eilers et al. (2019) provides a precise measurement of the circular velocity curve of the Milky Way from 5 to 25 kpc. With the distance from the Sun to the Galactic center $R_0 = 8.122 \pm 0.031$ kpc (Gravity Collaboration, 2018), they determine the rotation speed of the local standard of rest $\Theta_0 = 229.0 \pm 0.2\,\mathrm{km\,s^{-1}}$, with a slope of $-1.7 \pm 0.1\,\mathrm{km\,s^{-1}\,kpc^{-1}}$ (statistical errors), corresponding to $b_0 = 0.0603 \pm 0.0035$. The total uncertainties (including systematic errors) given by Eilers et al. (2019) are similar to the measurements used in the previous case (blue line), but here we assume the systematic errors can be well understood in the near future, and only consider the statistical errors. With this assumption, we expect to measure the MOI with 11% precision at 68% C.L. in 2030. This is nearly the same as using an error-free Galactic model, which is indicated by the red line in Figure 3.5. Therefore, with future measurements of the Galactic potential and a better understanding of

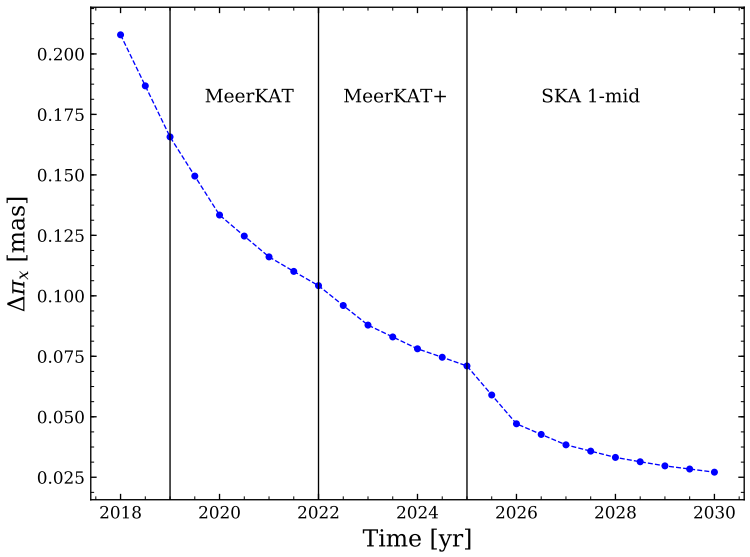

Figure 3.3: Predicted uncertainty of the timing parallax $\Delta\pi_x$ as a function of time. The corresponding uncertainty in distance is smaller than our assumed value from mid-2021, and is therefore used for future corrections of extrinsic acceleration effects.

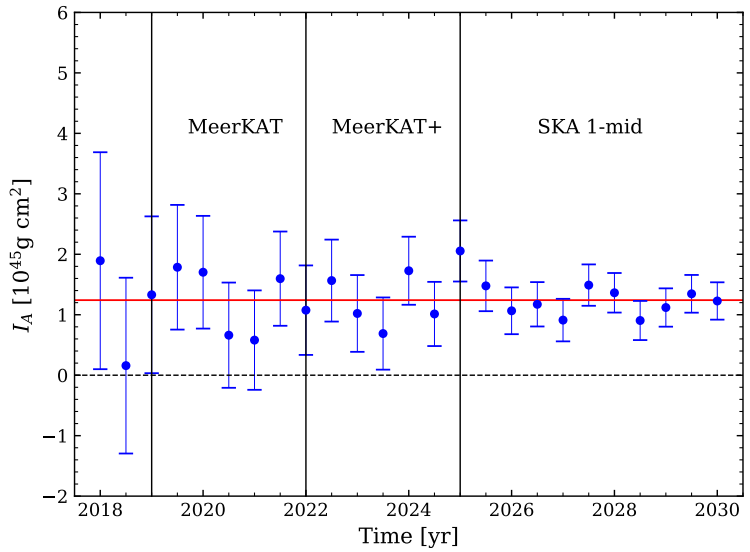

Figure 3.4: Simulated measurements of the MOI of PSR J0737−3039A with time, where two full orbits observation per month are assumed. The red line indicates the theoretical value of the MOI for the chosen EOS AP4 ($I_{\rm A}^{\rm AP4}$).

the systematic errors, an MOI measurement with 11% precision from the Double Pulsar seems realistic.

One important factor for the result is the influence of the mass loss in pulsar A, which was neglected in the previous study by Kehl et al. (2017). Without considering this contribution, the uncertainty of $I_{\rm A}$ significantly reduces and reaches 7% by 2030 (see the grey line in Figure 3.5), in contrast to the red line. In addition, we find that increasing the observing cadence does not significantly improve the precision of MOI measurements.

As mentioned in Section 3.4.2, different approaches provide very different measurement of the distance of the Double Pulsar, and a compromise distance of 0.8 kpc is thereby employed in our study. To investigate how distance influences the MOI measurement, we consider two extreme cases, $d = 0.4$ kpc

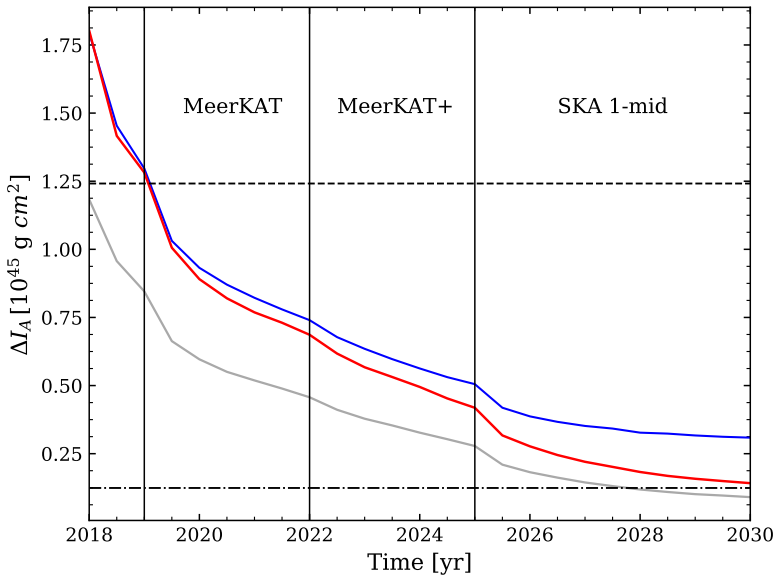

Figure 3.5: Predicted uncertainty of I_A as a function of time. The blue line adopts the Galactic measurements (R_0, Θ_0) by Gravity Collaboration (2019) and slope measurement by Reid et al. (2014), whereas the red line assumes no errors in the Galactic model. The grey line is same as the red line but ignores the influence of mass loss to the orbital period change. The theoretical value I_A^{AP4} is indicated by the dashed black line, whereas the dash-dotted line is 10% of the theoretical value.

and $d = 1.6$ kpc, with the same setups as in the $d = 0.8$ kpc simulations. Using the current Galactic measurements, we find that the uncertainty of the MOI measurement reaches 17% by 2030 when $d = 0.4$ kpc, and has a much higher uncertainty (43%) when $d = 1.6$ kpc. However, with negligible error in the Galactic potential, both predict ∼11% measurements by 2030, same as for the case of $d = 0.8$ kpc. Since an improved Galactic model is expected in the near future, the value we employ for the distance should not have a significant impact on the prediction of the MOI uncertainty.

An 11% precision measurement of the MOI would further improve the constraints of the EOS of NSs (Lattimer & Schutz, 2005; Greif et al., 2020). Figure 3.6 shows the MOIs of a number of EOSs, which are scaled by a factor of $M^{3/2}$ in order to reduce the range of the ordinate (cf. Lattimer & Schutz, 2005). The 11% measurement predicted from our simulation is illustrated by the red bar centered at the assumed EOS AP4, and located at the precisely measured mass of pulsar A. To compare with the constraints from other methods, we mark the curves in different styles. The observations of the binary neutron-star merger event GW170817 by LIGO/Virgo (B. P. Abbott et al., 2018) placed a constraint for the radii of both NSs, 11.9 ± 1.4 km (90% C.L.), which excludes the EOSs in grey dashed curves. Recently, a more stringent constraint combining GW170817 with nuclear theory was obtained by Capano et al. (2020), where they found the radius for a $1.4M_\odot$ NS is $11.0^{+0.9}_{-0.6}$ km (90% C.L.). This further excludes the EOSs in blue dashed curves. The remaining promising EOSs from this constraint are marked in blue solid curves, which is already very close to our 11% prediction from the MOI measurement in 2030. With more and more binary NS mergers expected to be detected in the coming years, tighter constraints on the EOS are likely to be achieved. Meanwhile, recent NICER observation delivered a joint mass-radius measurement for PSR J0030+0451 from two independent analyses. Riley et al. (2019) found an inferred mass and equatorial radius of $1.34^{+0.15}_{-0.16}M_\odot$ and $12.71^{+1.14}_{-1.19}$ km (68% C.L.), while Miller et al. (2019) found $1.44^{+0.15}_{-0.14}M_\odot$ and $13.02^{+1.24}_{-1.06}$ km. This is a weak constraint on the EOS, but is expected to improve with more observations in the near future. The upcoming X-ray missions, such as eXTP (S. N. Zhang et al., 2016) and ATHENA (Barret et al., 2013), are also promising to improve our understanding of the

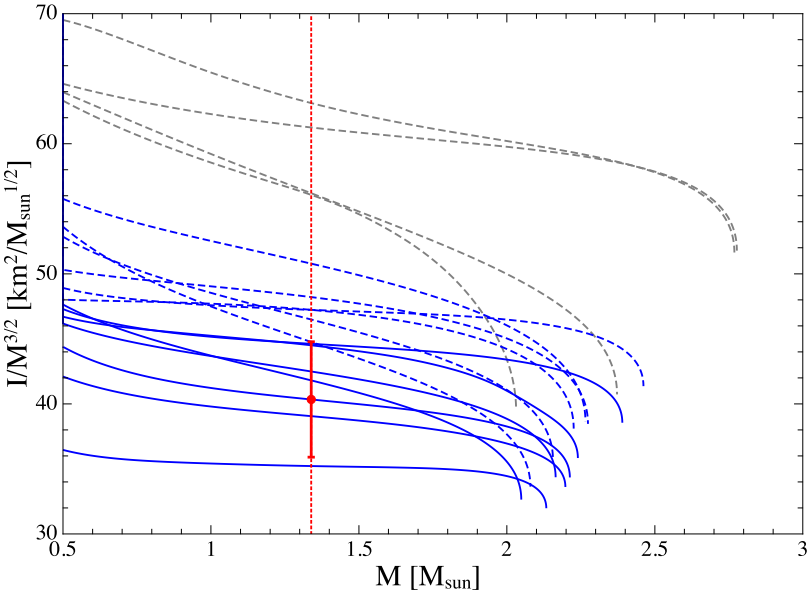

Figure 3.6: Constraints of EOSs from an 11% measurement of the MOI of PSR J0737−3039A (red). EOS AP4 was assumed in the simulation (curve through red dot). The grey dashed curves indicate EOSs that are disfavoured by the LIGO/Virgo observations of the GW170817 binary neutron-star merger (B. P. Abbott et al., 2018). The blue dashed curves are additionally excluded by the refined (combined with nuclear theory) GW170817 analysis by Capano et al. (2020). The following EOSs have been plotted (ascending in their intersection with the left border): WFF1, WFF2, AP4, BSk20, AP3, SLy4, BSk25, MPA1, BSk21, SLy9, BL, BSk22, H4, PAL1, MS2, MS0 (`https://compose.obspm.fr`). All these EOSs are able to support a NS of 1.98 $M_\odot$, the current lower limit for the maximum mass (see Section 3.1 for details).

mass-radius relation for NSs.

Therefore, it is fair to assume that the GWs and X-ray observations will place a more stringent constraint on the EOS within the next 10 years, and if the EOS can be known with sufficient precision, we can in turn use this information as an input to our analysis, test the LT precession and constrain theories of gravity with the Double Pulsar. We will discuss this scenario in detail in the next section.

3.7 Testing Lense-Thirring precession

As discussed in the previous section, the MOI measurement of PSR J0737−3039A is expected to reach 11% accuracy by 2030, whereas GWs and X-ray observations are likely to give a better constraint on the EOS. In this section, we discuss the prospects of testing LT precession and constraining theories of gravity using the Double Pulsar, if the EOS is known.

We again adopt EOS AP4 and this time assume that a precision of 5% could be achieved when calculating the MOI of pulsar A, based on a (hypothesized) future improvement in our understanding of super-dense matter. Given I_A as an input to our simulations, only the masses are unknown for the intrinsic orbital period decay $\dot{P}_b^{intr}$ and the Shapiro shape parameter s. With the masses measured from ($\dot{P}_b^{intr}$, s) and the given I_A, we can directly test the LT contribution to the periastron advance $\dot{\omega}^{LT,A}$. To discuss the physical meaning of such a test, we use the generic framework for relativistic gravity theories introduced by Damour & Taylor (1992), which is fully conservative and based on a Lagrangian that includes a generic term L_{SO} for spin-orbit interaction. As in Damour & Taylor (1992), we will make no assumption about the (strong-field) coupling function Γ_A^B, which enters L_{SO}. Since the spin axis of pulsar A has been found to be practically parallel to the orbital angular momentum, the general form of

the LT contribution to the periastron advance can be written as

$$\dot{\omega}^{\mathrm{LT,A}} = -\frac{2n_{\mathrm{b}}^2 I_{\mathrm{A}} \Omega_{\mathrm{A}}}{(1-e_{\mathrm{T}}^2)^{3/2} M} \frac{\sigma_{\mathrm{A}}}{\mathcal{G}} , \tag{3.21}$$

where σ_{A} is a generic strong-field spin-orbit coupling constant, defined by

$$\sigma_{\mathrm{A}} = \frac{1}{c^2}\left[\Gamma_{\mathrm{A}}^{\mathrm{B}} + \left(\Gamma_{\mathrm{A}}^{\mathrm{B}} - \frac{1}{2}\mathcal{G}\right)\frac{m_{\mathrm{B}}}{m_{\mathrm{A}}}\right] . \tag{3.22}$$

In GR, the generalised gravitational constant $\mathcal{G}$ equals G, and the coupling function $\Gamma_{\mathrm{A}}^{\mathrm{B}}$ equals $2G$ (Damour & Taylor, 1992), so that

$$\sigma_{\mathrm{A}}^{\mathrm{GR}} = \frac{G}{c^2}\left(2 + \frac{3}{2}\frac{m_{\mathrm{B}}}{m_{\mathrm{A}}}\right) . \tag{3.23}$$

But in other theories, $\Gamma_{\mathrm{A}}^{\mathrm{B}}$ is expected to deviate from $2G$, including modifications by self-gravity contributions from the strongly self-gravitating masses in the system.

We define a parameter δ_{LT} to measure the relative deviation of the theory-independent parameter $\sigma_{\mathrm{A}}/\mathcal{G}$ from its GR prediction,

$$\delta_{\mathrm{LT}} = \left(\frac{\sigma_{\mathrm{A}}}{\mathcal{G}}\right)\left(\frac{\sigma_{\mathrm{A}}^{\mathrm{GR}}}{G}\right)^{-1} - 1 . \tag{3.24}$$

By inserting Eq. (3.22) into the above definition, one obtains for the spin-orbit coupling function

$$\frac{\Gamma_{\mathrm{A}}^{\mathrm{B}}}{2\mathcal{G}} - 1 = \left(\frac{3+x_{\mathrm{A}}}{4}\right)\delta_{\mathrm{LT}} , \tag{3.25}$$

To assess potential constraints on a non-GR spin-orbit coupling, we multiply the expression of $\dot{\omega}^{\mathrm{LT,A}}$ in GR (last term in Eq. (4.13)) by $(1+\delta_{\mathrm{LT}})$, and solve for the parameter δ_{LT} using the three PK parameters $\dot{P}_{\mathrm{b}}^{\mathrm{intr}}(m_{\mathrm{A}}, m_{\mathrm{B}})$, $s\,(m_{\mathrm{A}}, m_{\mathrm{B}})$, and $\dot{\omega}^{\mathrm{intr}}(m_{\mathrm{A}}, m_{\mathrm{B}}, \delta_{\mathrm{LT}})$. One has to keep in mind that, for simplicity, we make here the assumption that the non-spin related parts of the orbital dynamics and signal propagation are (to sufficient approximation) given by their GR expressions. It goes without saying, that in practice one has to conduct a fully self-consistent analysis within a given class of alternative gravity theories. For a discussion that purely focuses on the measurability of a potential deviation in the LT contribution, our approach is sufficient.

Figure 3.7 shows the expected decrease in the uncertainty of δ_{LT} with future observations. With R_0 and Θ_0 measurements from Gravity Collaboration (2019) and the slope measurement from Reid et al. (2014), we expect to measure δ_{LT} with 18% precision at 68% C.L. by 2030, which is indicated by the blue line. The red line adopts the Galactic measurements from Eilers et al. (2019), where we expect to achieve a 9% precision by 2030. In the ideal case, we assume that the Galactic potential, the distance to the Double Pulsar, and the MOI can be precisely measured in the future, so that we could leave out the errors. In this scenario, we expect to measure δ_{LT} with 7% precision by 2030 (green line). We have seen in Section 3.6 that change from the Galactic measurements by Eilers et al. (2019) to an error-free Galactic model has little enhancement on the measurements of the MOI, and the uncertainty of the timing parallax is relatively small, therefore, the improvement from 9% (red line) to 7% (green line) is to a fair fraction (nearly half) related to the uncertainty of the MOI.

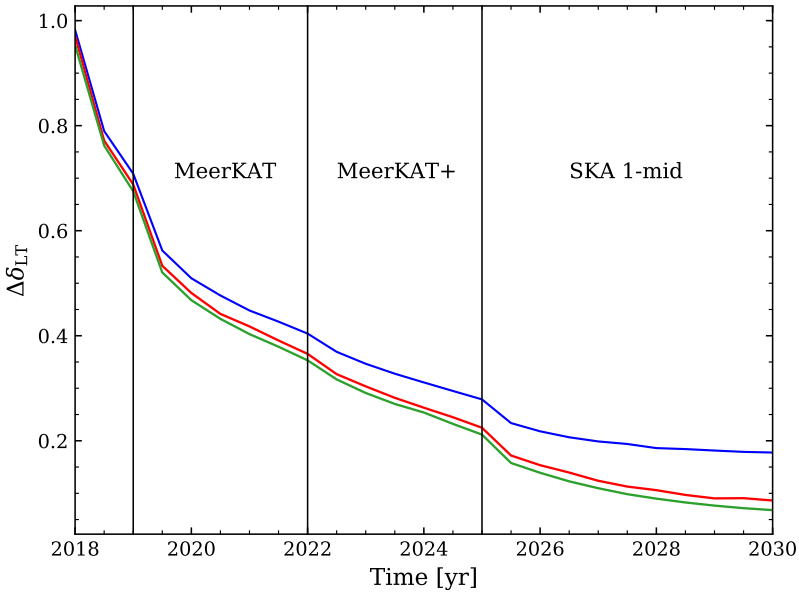

Figure 3.7: Predicted uncertainty of $\delta_{\rm LT}$ as a function of time. The blue line adopts Galactic measurements (R_0, Θ_0) by Gravity Collaboration (2019) and slope measurement by Reid et al. (2014), the red line adopts Galactic and slope measurements by Eilers et al. (2019), and the green line assumes no errors in the Galactic model, the distance and the MOI.

Breton et al. (2008) have conducted a different experiment for spin-orbit coupling in the Double Pulsar system. Studying the geodetic precession of pulsar B, they were able to show that $\sigma_{\rm B}/\mathcal{G}$ is in agreement with GR, with a precision of about 13%. Analogously to Eq. (3.22), $\sigma_{\rm B}$ is related to $\Gamma_{\rm B}^{\rm A}$. A priori there is no reason to assume that $\Gamma_{\rm B}^{\rm A}$ and $\Gamma_{\rm A}^{\rm B}$ are equal (see discussion in Damour & Taylor, 1992). Consequently, a LT test with pulsar A would nicely complement the geodetic precession test of Breton et al. (2008), when investigating the relativistic interaction between the proper rotation of the two NSs and their orbital motion.

Finally, short range modifications of gravity, related to the strong gravitational field of a NS, could significantly change the structure of the star and therefore its MOI, without any "direct" impact on the orbital dynamics or the signal propagation in a binary pulsar system. Examples of such theories are scalar-tensor theories with a massive scalar field having a sufficiently short Compton wavelength (see e.g. Ramazanoğlu & Pretorius, 2016; Yazadjiev et al., 2016). While in such a scenario, PK parameters related to time dilation, GW damping, and Shapiro delay remain (practically) unaffected (see e.g. Alsing et al., 2012), one could still expect a deviation in the precession of periastron of the Double Pulsar. The reason is that due to the modification of the MOI the spin of pulsar A and therefore the spin-orbit coupling is modified. Testing the LT precession in the Double Pulsar can therefore be used to constrain such deviations from GR. It is important to note, that $\dot{P}_{\rm b}^{\dot{m}}$ would also be modified accordingly, and therefore has to be accounted for. Hence, limits on $\delta_{\rm LT}$ would consequently be somewhat weaker than given above (cf. Section 3.6). In such a scenario it could generally be difficult to disentangle uncertainties in the EOS and deviations from GR by astronomical observations. For this, a combination of various experiments, like GWs from binary neutron-star mergers, X-ray observations, and radio pulsar timing might turn out to be necessary. Nonetheless, the future measurement of the LT precession in the Double Pulsar is expected to provide important contributions when constraining such deviations from GR.

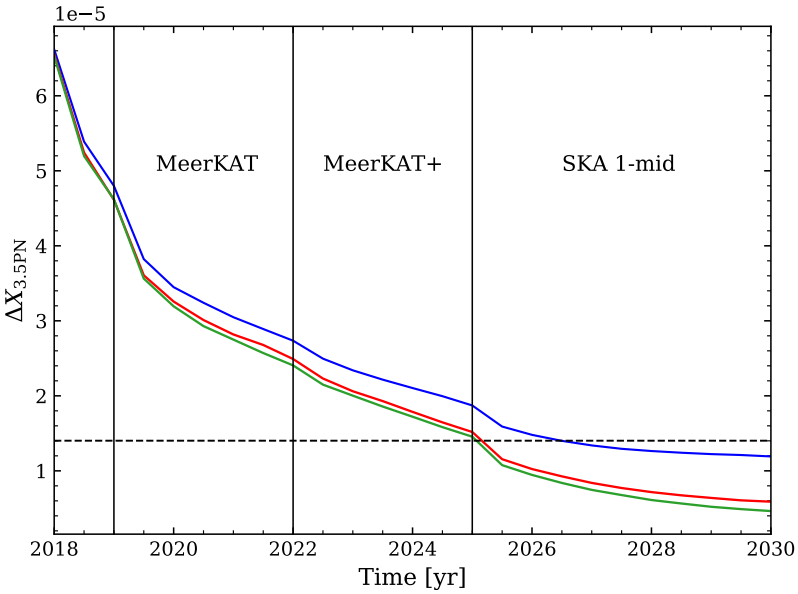

Figure 3.8: Same as Figure 3.7 but for the uncertainty of the 3.5PN order GW correction $X_{3.5\mathrm{PN}}$. The dashed line denotes the theoretical value of $X_{3.5\mathrm{PN}}$.

3.8 Next-to-leading-order gravitational wave damping

In GR, the loss of energy of a material system due to GWs is to leading order sourced by a time-dependent mass quadrupole (Einstein, 1918; Eddington, 1922). This also holds for binary systems where a change in the mass quadrupole is driven by gravity itself. It enters the two-body equations of motion at the 2.5PN order (see e.g. Damour, 1987). When computing the next-to-leading-order contribution to GW damping, one also has to account for the mass-octupole and the current quadrupole moments (Thorne, 1980). Next-to-leading-order contributions enter the equations of motion at 3.5PN ($\mathcal{O}(c^{-7})$), and therefore correspond to the 1PN corrections in the radiation reaction force (Iyer & Will, 1995; Pati & Will, 2002; Königsdörffer et al., 2003; Nissanke & Blanchet, 2005). The corresponding change in the orbital period of a binary system has been determined out by Blanchet & Schäfer (1989) and is given by Eq. (3.12). In this section we will investigate if next-to-leading-order corrections to the GW damping are expected to become important in the near future for the timing observation of the Double Pulsar.

Again we assume EOS AP4 and a 5% error in the knowledge of the MOI I_{A}. We implement the 3.5PN contribution into our model by using Eq. (3.12), and adjust the TOAs accordingly. After running simulations as described in Section 3.5, we obtain the measured PK parameters. We use Eq. (3.13) to solve for the relative correction of the 3.5PN order $X_{3.5\mathrm{PN}}$ using the three PK parameters $\dot{P}_{\mathrm{b}}^{\mathrm{intr}}(m_{\mathrm{A}}, m_{\mathrm{B}}, X_{3.5\mathrm{PN}})$, $s\,(m_{\mathrm{A}}, m_{\mathrm{B}})$, and $\dot{\omega}^{\mathrm{intr}}(m_{\mathrm{A}}, m_{\mathrm{B}})$.

Figure 3.8 illustrates the predicted uncertainty of $X_{3.5\mathrm{PN}}$ with observing phase, which will fall below its theoretical value $X_{3.5\mathrm{PN}}^{\mathrm{theo}}$ in the SKA1-mid era. The colours of the lines represent the same conditions as in Figure 3.7. The blue line shows the improvements in $\Delta X_{3.5\mathrm{PN}}$ with Galactic parameters from Gravity Collaboration (2019) and the slope measurement by Reid et al. (2014), which will reach a precision of 85% at 68% C.L. by 2030. Adopting the Galactic measurements (statistical errors) by Eilers et al. (2019), the red line shows that $X_{3.5\mathrm{PN}}$ can be constrained with a precision of 42% by 2030. By contrast, in the ideal case where there are no errors in the Galactic model, the distance and the MOI, $X_{3.5\mathrm{PN}}$ can be constrained with a precision of 33% by 2030, where nearly half of the improvement is contributed from the MOI.

3.9 Potential new discoveries

Large pulsar surveys with MeerKAT, FAST and the forthcoming SKA, such as TRAPUM (B. Stappers & Kramer, 2016) and CRAFTS (Li et al., 2018), can potentially discover more relativistic double neutron star (DNS) systems, preferably with a more compact orbit than PSR J0737−3039. An example of such a system, PSR J1946+2052, with a more relativistic orbit than the Double Pulsar ($P_{\rm b} \simeq 1.88$ h) and larger periastron advance ($\dot{\omega} \approx 26\,{\rm deg\,yr^{-1}}$) and LT precession ($\dot{\omega}_{\rm LT} \approx 0.001\,{\rm deg\,yr^{-1}}$), was recently discovered in the PALFA survey (Stovall et al., 2018). In its orbital parameters, the PSR J1946+2052 system resembles a system similar to the Double Pulsar, but that has evolved further due to GW damping, by about 40 Myr. While it is still unclear, if for PSR J1946+2052 the necessary precision in the mass determination can be reached to rival the Double Pulsar in the tests proposed here,[8] it certainly adds confidence to the hope of finding more relativistic "cousins" of the Double Pulsar in the coming years. Such binary pulsars would quite likely enable MOI measurements with superior precision within a comparably short period of time, and improve the constraints of the EOS.

Here we consider two scenarios, one with an orbital period of 100 minutes and one with 50 minutes, which are within the expected acceleration searches by MeerKAT. Assuming such systems can be found in 2020 and we start timing them regularly from 2021, with two orbits per month, we run our simulation again to predict the measurements of the MOI. To simplify the simulation, we assume these systems satisfy the conditions of the Double Pulsar (inclination i close to 90 degrees, similar distance and brightness, etc.) but with modified orbital parameters, assuming that these systems had an orbit like the Double Pulsar some time in the past, and then evolved by GW damping to an orbital period of 100 or 50 minutes. In reality, these systems are likely to be further away. Nonetheless, it is also possible that such systems are bright and nearby, but were missed in the past surveys due to their high acceleration (see Johnston & Kulkarni, 1991; Ransom, 2001; Jouteux et al., 2002; Ng et al., 2014; Cameron et al., 2018).

We calculate the evolved semi-major axis using Kepler's third law and the evolved eccentricity using the $a - e$ relation in Peters (1964), for the orbital period of 100 minutes and 50 minutes, respectively. Then we calculate the PK parameters and run simulations as described in Section 3.5 and 3.6. Assuming the same distance as the Double Pulsar, we convert the uncertainty of timing parallax into an uncertainty for the distance. The Galactic measurement by Eilers et al. (2019) is adopted in the simulation and, as before, we assume the systematic uncertainties can be well understood in the future.

Our results show that, for the DNS system with an orbital period of 100 minutes, we could measure the MOI with 12% precision by 2030 and with 4.5% by 2035 at 68% C.L. As for an orbital period of 50 minutes, we expect an MOI measurement with 1.5% precision by 2030 and with 0.5% by 2035 at 68% C.L. Such measurements would probably be comparable to the by then available constraints from other methods (GWs and X-ray observations, nuclear physics, etc.) and help for determining the EOS of NSs.

Furthermore, LISA has the potential to discover ultra relativistic DNS systems with a characteristic orbital frequency of 0.8 mHz (Lau et al., 2020). Thrane et al. (2020) suggested that following up such systems with SKA for 10 years could potentially measure the mass-radius relation with a precision <1%. To this end, we perform a simulation for a DNS system with 20 minute orbital period, and find an MOI precision of ~0.2% (68% C.L.) may be possible with 10 years of timing with SKA 1-mid.

However, there is a low chance that the new discovered DNS systems will be edge-on to our line-of-sight, as is the case for PSR J0737−3039, hence a precise measurement of s might not be possible. Instead, we may need to use γ to constrain the masses and MOI, whose fractional error is usually a few orders of magnitude larger than s (see Figure 3.2). This is indeed the case for PSR J1946+2052, despite its relativistic nature, determining the masses with sufficient precision will be challenging.

[8] Since PSR J1946+2052 is less luminous compared to the Double Pulsar, and s is not measurable due to its orientation.

Moreover, not all DNS systems are ideal to test the Lense–Thirring precession in terms of periastron advance $\dot{\omega}^{\rm LT}$. Systems like the aforementioned PSR J1757−1854 have a large eccentricity most likely caused by a large kick (Tauris et al., 2017) causing a significant misalignment between the spin of pulsar and the orbital angular momentum, and hence $\dot{\omega}^{\rm LT}$ can not be determined as straightforwardly as in the Double Pulsar. However, as pointed out in Section 3.2.2, this allows an alternate test using the contribution of LT precession to the rate of change of the projected semi-major axis $\dot{x}^{\rm LT}$ (Cameron et al., 2018) if profile changes due to geodetic precession can be accounted for in the timing process and the spin orientation can be determined with sufficient precision.

3.10 Conclusion

In this paper, we have developed a consistent method to measure the MOI of radio pulsars, which has been applied to mock data for the Double Pulsar. We simulated TOAs of PSR J0737−3039A assuming future observations with MeerKAT, MeerKAT+ and SKA 1-mid which cover two orbits per month. We found an MOI measurement with 11% accuracy (68% C.L.) could be achievable by the end of this decade, if we have sufficient knowledge of the Galactic gravitational potential (e.g., from Gaia mission (Gaia Collaboration, 2016)). We also found that the mass loss of pulsar A has a considerable impact on the measurement of the MOI. Neglecting this contribution to the orbital period change leads to an overoptimistic prediction. This is the main reason why, even with the better timing precision used in this paper as compared to Kramer & Wex (2009), by ∼2030 we would still only reach the same accuracy level as predicted by Kramer & Wex (2009). Additionally, the assumptions made in this paper are more realistic compared to Kehl et al. (2017), with timing precision from MeerKAT observation, as well as updated timeline and size of upcoming telescopes.

In the second part of the paper, Section 3.7 and 3.8, we have assumed that a better constraint on the EOS might be achieved with GWs and X-ray observations in the future, so as to investigate the capability of testing LT precession and 3.5PN order contributions to the GW damping. This assumption coincides with Landry et al. (2020) where they found that constraints from GWs and X-ray observations are likely to have larger contributions in constraining the EOS than the MOI measurement of J0737−3039A. Assuming a 5% error in the determination of the MOI, we simulated measurements of the relative deviation of the theory-independent spin-orbit coupling parameter $\sigma_{\rm A}/\mathcal{G}$ from GR's prediction. We found a 9% precision measurement is possible by 2030 with an improved Galactic model, whereas a 7% precision measurement in the ideal case — no errors in the Galactic model, the distance, and the MOI. This test is a complement to Breton et al. (2008), where they found a 13% constraint on $\sigma_{\rm B}/\mathcal{G}$. This measurement would enable a constraint for the coupling function $\Gamma_{\rm A}^{\rm B}$ that enters the spin-orbit Lagrangian of the two-body interaction for strongly self-gravitating masses. Such a measurement could be sensitive to short range deviations from GR, which otherwise would not show up in the orbital dynamics of such systems.

We have also studied the measurability of GR's next-to-leading-order (3.5PN) GW-damping contribution. We predicted that the uncertainty of the 3.5PN order correction $X_{\rm 3.5PN}$ will fall below its theoretical value at the beginning of SKA 1-mid (∼2026) and a measurement of $X_{\rm 3.5PN}$ with 3σ-significance is possible in ∼10 years, if by then we have sufficient knowledge of the Galactic gravitational potential, pulsar distance, and the EOS. This means that from the SKA 1-mid era, we will have to include the 3.5PN term in our analysis in order to avoid any bias. Binary mergers detected by LIGO/Virgo do provide constraints on post-Newtonian (PN) terms (B. P. Abbott et al., 2016b). Their way of counting the PN contributions is relative to the Einstein quadrupole formula, i.e. the order they enter the radiation reaction force (Blanchet, 2014). Their 1PN term therefore contains 3.5PN contributions from the

equations of motion. As a comparison to our 3.5PN 3-σ result, (B. P. Abbott et al., 2019) provide a ∼10% measurement (90% C.L.) of the (radiative) 1PN coefficient with GW170817. Future merger events will most likely lead to even more precise measurements of this term. While at the 2.5PN (0PN radiative) level, the Double Pulsar is still many orders of magnitude more precise than LIGO/Virgo mergers (Kramer, 2016; Kramer et al., 2021a). When it comes to higher order PN contributions, we conclude that binary pulsars are not expected to be competitive, simply because of the much smaller orbital velocity.

Finally, we discussed potential new discoveries of DNS systems with radio telescopes like MeerKAT, FAST, and SKA, as well as the space-based future GW observatory LISA. We demonstrated that for a DNS system which mimics the evolved PSR J0737−3039 with an orbital period of 50 minutes, the MOI measurement is expected to reach 1.5% precision (68% C.L.) after 10 years observation with MeerKAT, MeerKAT+ and SKA 1-mid, and 0.5% precision after 15 years. Moreover, LISA is expected to find DNS systems with a characteristic orbital period of 20 minutes in the near future (Lau et al., 2020). Such discoveries can significantly tighten the constraints for the EOS.

To conclude, although the EOS constraints resulting from a future MOI measurement with the Double Pulsar are not likely to exceed those with LIGO/Virgo mergers and X-ray observations in the coming years, we still anticipating other aspects of science coming from this unique gravity laboratory in future studies based on an improved understanding of the NS EOS as an input. Furthermore, the discovery of more relativistic binary pulsars, possible with the unprecedented surveying capabilities of new and upcoming radio telescopes and advances in data analysis (e.g. Lentati et al., 2018), could ultimately lead to EOS constraints quite competitive with other methods.

Acknowledgements

We are grateful to Vivek Venkatraman Krishnan and Aditya Parthasarathy for helpful discussions, and Paulo Freire for carefully reading the manuscript. We would also like to thank our reviewer, Gerhard Schäfer, for his helpful comments. HH is a member of the International Max Planck Research School for Astronomy and Astrophysics at the Universities of Bonn and Cologne. NW and MK gratefully acknowledge support from ERC Synergy Grant “BlackHoleCam” Grant Agreement Number 610058. This work has been supported by the Chinese Academy of Sciences (CAS) and the Max-Planck Society (MPG) in the framework of LEGACY cooperation on low-frequency gravitational wave astronomy.

CHAPTER 4

Gravitational signal propagation in the Double Pulsar studied with the MeerKAT telescope

- **H. Hu**, M. Kramer, D. J. Champion, N. Wex, A. Parthasarathy, T. T. Pennucci, N. K. Porayko, W. van Straten, V. Venkatraman Krishnan, M. Burgay, P. C. C. Freire, R. N. Manchester, A. Possenti, I. H. Stairs, M. Bailes, S. Buchner, A. D. Cameron, F. Camilo, and M. Serylak, Gravitational signal propagation in the double pulsar studied with the MeerKAT telescope, *Astronomy & Astrophysics*, Volume 667, 2022, A149, DOI: 10.1051/0004-6361/202244825

Summary

The Double Pulsar, PSR J0737−3039A/B, has offered a wealth of gravitational experiments in the strong-field regime, all of which general relativity (GR) has passed with flying colours. In particular, among current gravity experiments that test photon propagation, the Double Pulsar probes the strongest spacetime curvature. Observations with the MeerKAT telescope and, in future, the Square Kilometre Array (SKA) can greatly improve the accuracy of current tests and facilitate tests of next-to-leading-order (NLO) contributions in both orbital motion and signal propagation.

In this work, we presented our timing analysis of new observations of PSR J0737−3039A, made using the MeerKAT telescope over the last three years. The increased timing precision offered by MeerKAT already yielded improved measurements on the Shapiro delay, where the precision of the Shapiro shape parameter s is two times better compared to the previous study based on 16-yr data (Kramer et al., 2021a). This also resulted in improved mass measurements. In particular, we studied the NLO signal propagation effects including the lensing correction to Shapiro delay, the retardation effect due to the movement of pulsar B while the signal of pulsar A propagates across the system, and the deflection of the signal of pulsar A by the gravitational field of pulsar B. The significance of lensing, the retardation effect, and the gravitational deflection in the longitudinal direction can be tested using a common factor $q_{\rm NLO}$ by scaling these corrections collectively, where $q_{\rm NLO} = 1$ in GR. Based on the 3-yr MeerKAT data, our results provided an independent confirmation of these NLO signal propagation effects with $q_{\rm NLO} = 0.999(79)$, which is 1.65 times more precise than the measurement from the 16-yr data (Kramer et al., 2021a).

We also investigated novel effects which are expected but have not been observed in pulsars. The gravitational deflection not only results in a time shift in the longitudinal direction but can also lead to a change in the colatitude of the emission direction towards us. This latitudinal deflection can potentially

cause profile variations near superior conjunction as our line-of-sight (LOS) cuts a different region of the pulsar beam (Rafikov & Lai, 2006a; Rafikov & Lai, 2006b). To search for such profile variations, we folded the search mode data of PSR J0737−3039A that are near superior conjunction (orbital phase $89° < \psi < 91°$) and added profiles together for every $\Delta\psi = 0.25°$. The added profiles were compared to a standard profile but no significant evidence of variation were found. In addition, we investigated the measurability of latitudinal deflection time delay due to unaccounted profile variation using simulations and found that this time delay effect can be mostly absorbed by Shapiro parameters and is challenging to be measured with timing.

Furthermore, we explored the prospects of measuring the lensing correction to Shapiro delay independently from other NLO effects. With the simulated data, we found that the lensing signature vanished after fitting for the Shapiro shape parameter. We simulated the timing data for MeerKAT and its future extensions up to 2030 and fitted for a scaling factor $q^{\rm len}$ for the lensing correction ($q^{\rm len} = 1$ in GR), but the uncertainty of $q^{\rm len}$ is larger than 1, making it difficult to be measured with this precision. However, if an instrument with similar performance to the full SKA becomes available in the future, we found that lensing may be measurable with just a few years of timing.

With continued observations with MeerKAT and its future extensions, the accuracy of tests for signal propagation effects will be further improved, and a 50-σ detection of $q_{\rm NLO}$ can be expected by 2030. For that, we also provided an improved analytical description for the signal propagation in the Double Pulsar system that meets the timing precision expected from future instruments such as the full SKA.

As the lead author of this publication, I reduced and analysed the MeerKAT data for PSR J0737−3039A, produced the figures, interpreted the results and wrote the manuscript. Exceptions are Figure 4.3 and Section 4.5.4 (an improved lensing model for the future), which were contributed by NW.

4.1 Introduction

The Double Pulsar PSR J0737−3039A/B is a rich laboratory for strong-field gravity experiments. The system consists of a 23-ms recycled pulsar ('A') and a 2.8-s 'normal' pulsar ('B') in a nearly edge-on and slightly eccentric 2.45-hr orbit (Burgay et al., 2003; A. G. Lyne et al., 2004). Various relativistic effects have been precisely measured in previous work (Kramer et al., 2006b; Kramer et al., 2021a), including periastron precession, time dilation (gravitational redshift and second-order Doppler effect), Shapiro delay due to light propagation in the curved spacetime of the companion, and the orbital period decay, which currently provides the most precise test of quadrupolar gravitational waves predicted by general relativity (GR). In addition, the relativistic spin precession of B was measured by Breton et al. (2008) and the relativistic deformation of the orbit was newly detected in this system (Kramer et al., 2021a). All these make it a still unique system for gravity experiments.

Comparing with other gravity experiments, the Shapiro delay measured in the Double Pulsar probes the strongest spacetime curvature ($\sim 10^{-21}$ cm^{-2}) in a precision experiment with photons, that is, the interaction between gravitational and electromagnetic fields (Wex & Kramer, 2020). In addition, with 16 yr of data, Kramer et al. (2021a) were able, for the first time, to measure higher-order effects of signal propagation in the strong gravitational field of a neutron star, which are currently not accessible via any other method. These include the retardation effect due to the movement of the companion (B) and aberrational light deflection by the gravitation of the companion. The latter confirms the prograde rotation of A, which is consistent with the results measured by Pol et al. (2018) using the emission properties of B and is in line with the expectations from binary evolution models.

In this work, we present observations of PSR J0737−3039A with the MeerKAT telescope, a precursor for the Square Kilometre Array (SKA) at mid-frequency range. Thanks to its location in the Southern

Hemisphere, it permits a timing precision more than two times better than that of the Green Bank Telescope for this pulsar (Bailes et al., 2020; Kramer et al., 2021b). This superior precision enables an independent and improved measurement of signal propagation effects within a very short time span. We also investigate effects that have been expected but not been studied in detail before. These include potential profile variations due to latitudinal deflection, the detectability of latitudinal deflection delay, and the prospects of measuring the effect of lensing on the propagation time separately.

This paper is organised as follows. Section 4.2 describes the MeerKAT observations on the Double Pulsar and data processing. In Section 4.3, we introduce the concepts of gravitational signal propagation effects, including higher-order contributions to the Shapiro and aberration delay. The timing results and mass measurements are presented in Section 4.4. We then provide an in-depth study on the higher-order signal propagation effects in Section 4.5, with a focus on latitudinal deflection and lensing. In addition, we provide an improved analytical description for the signal propagation in the Double Pulsar. Finally, we discuss the results and future prospects in Section 4.6.

4.2 Observations and data processing

4.2.1 MeerKAT observations

The observations presented in this paper come from the MeerKAT telescope as part of the MeerTIME project (Bailes et al., 2020), which performs timing of known pulsars with various scientific themes. Observations on PSR J0737−3039A are conducted under the Relativistic Binary theme (RelBin, Kramer et al., 2021b), which focuses on testing the relativistic effects in binary pulsars to achieve measurements of neutron star masses and tests of theories of gravity. MeerTime observations are generally recorded using the Pulsar Timing User Supplied Equipment (PTUSE) signal processor. This processor receives channelised tied-array beamformed voltages from the correlator-beamformer engine of the MeerKAT observing system and is capable of producing coherently de-dispersed full-Stokes data in both the filterbank (search) mode and the fold (timing) mode, where the data are folded at the topocentric period of the pulsar. Details on the pulsar observing setup with MeerTime are explained by Bailes et al. (2020).

PSR J0737−3039A is regularly observed with a typical cadence of one month and duration of 3 hr. As the orbital period of this pulsar is $\sim$ 2.45 hr, the observations are scheduled to start shortly before an eclipse and finish after the second eclipse, in order to observe the eclipses twice in one observing session. The session is typically composed of a 30-min observation with the fold mode and search mode in parallel, followed by a 2-hr fold-mode observation and another 30-min fold-search dual-mode observation. This specific arrangement is designed to maximise our sensitivity in detecting signal propagation effects, as well as in studying the magnetosphere of pulsar B (Lower et al. in prep.). Observations are performed with two receivers: the L-band receiver that covers the frequency range 856–1712 MHz, and the UHF receiver that covers the frequency range 544–1088 MHz, both with 1024 channels. The data presented here started in March 2019 and ran until May 2022. For the analysis in this paper, we use 29 full-orbit timing observations and 62 search-mode eclipse data sets, which amounts to a total of $\sim$ 87 hr.

4.2.2 Timing data reduction

The raw timing data from the PTUSE machines are folded every eight seconds, which are then processed with the MEERPIPE data reduction pipeline. MEERPIPE carries out radio frequency interference (RFI) removal using a modified COASTGUARD algorithm (Lazarus et al., 2016), followed by flux and polarisation calibration. Details on polarisation and flux calibration are described in Serylak et al. (2021) and Spiewak et al. (2022), respectively.

Table 4.1: Information on the MeerKAT observations and data set[a] for PSR J0737−3039A.

Receiver	Centre Frequency (MHz)	Bandwidth (MHz)	Number of channels[b]	Number of sub-bands	Time span (MJD)[1]	Number of TOAs
L-band	1283.582	775.75	928	16	58568 – 59721	83930
UHF-band	815.734	493	928	32	58936 – 59663	137451

[a] Information presented here is for the trimmed data set, see Section 4.4.1.
[b] Effective usable channels.

After processing with MEERPIPE, the calibrated data products are reduced using the pulsar software package PSRCHIVE (Hotan et al., 2004).[2] We first correct for the rotation measure (RM) with the value measured in Kramer et al. (2021b), that is, RM=120.84 rad m^{-2}. As the L-band observations between March 2019 and February 2020 were restricted to 928 frequency channels (dropping 48 channels each from the top and bottom bands), to maintain consistency throughout the analysis, we reduce the later L-band data to the same frequency channels. We treat the UHF-band data in the same way, as the roll-off adversely affects sensitivity of the top and bottom bands.

For this system, a complete timing model is only available in the pulsar timing software TEMPO (D. Nice et al., 2015, more details are given in Section 4.4). Therefore, to fold the data more accurately, all data are supplied with a `polyco`-format ephemeris with the values measured in Kramer et al. (2021a). Since the Double Pulsar rapidly changes its orbital phase, the time span (TSPAN) of a predicted pulse phase solution has to be as small as possible to retain good precision.[3] With the PSRCHIVE version 2022-01-14, we set TSPAN to the minimum possible value, which is 3 min.

There is a known data processing issue with this pulsar, which is that the pulsar moves rapidly to a different orbital phase during the dispersion delay time. Thus, the pulses received at the same time at different frequencies correspond to different orbital phases and cannot be folded with the same phase prediction. If not properly accounted for, this folding issue will cause frequency-dependent orbital smearing. Standard pulsar software such as PSRCHIVE do not take this effect fully into consideration, even with the frequency-resolved TEMPO2 predictor.[4] To avoid this issue, we first de-disperse the total intensity data so that all frequencies correspond to the same orbital phase, then average the data, first in frequency and then in time.[5] Because of the profile frequency evolution and scintillation effects, data are sub-banded in frequency, with 32 sub-bands for the UHF-band and 16 sub-bands for the L-band.

As for the time-averaging, the integration time needs to be short enough in order to properly resolve the Shapiro delay and the next-to-leading-order (NLO) signal propagation contributions ($q_{\rm NLO}$, see Section 4.3), which are largest at superior conjunction. We perform a simulation to test the measurability of these NLO contributions with different integration times. The results show that a good measurement of Shapiro delay and $q_{\rm NLO}$ can be achieved if the integration time is $\lessapprox 32$ s, but it becomes significantly worse if the integration time is longer than 1 min for $q_{\rm NLO}$ and 2 min for Shapiro delay. Therefore, we average all data with a 32-s integration time, consistent with the analysis by Kramer et al. (2021a). After frequency and time averaging, data are re-dispersed to allow measurements of dispersion measure (DM) in the timing analysis.

[1] Modified Julian Date, subtracting 2400000.5 days from the Julian Date (JD).
[2] http://psrchive.sourceforge.net/
[3] Our analysis suggests that the choice of TSPAN has a significant impact on the Shapiro parameters: a larger TSPAN leads to a large deviation from the expected values.
[4] This issue is going to be addressed in PSRCHIVE 2.0, which is under development.
[5] The order of processing matters. If reversed, the pulse phase appears to be different and phase offsets may be introduced.

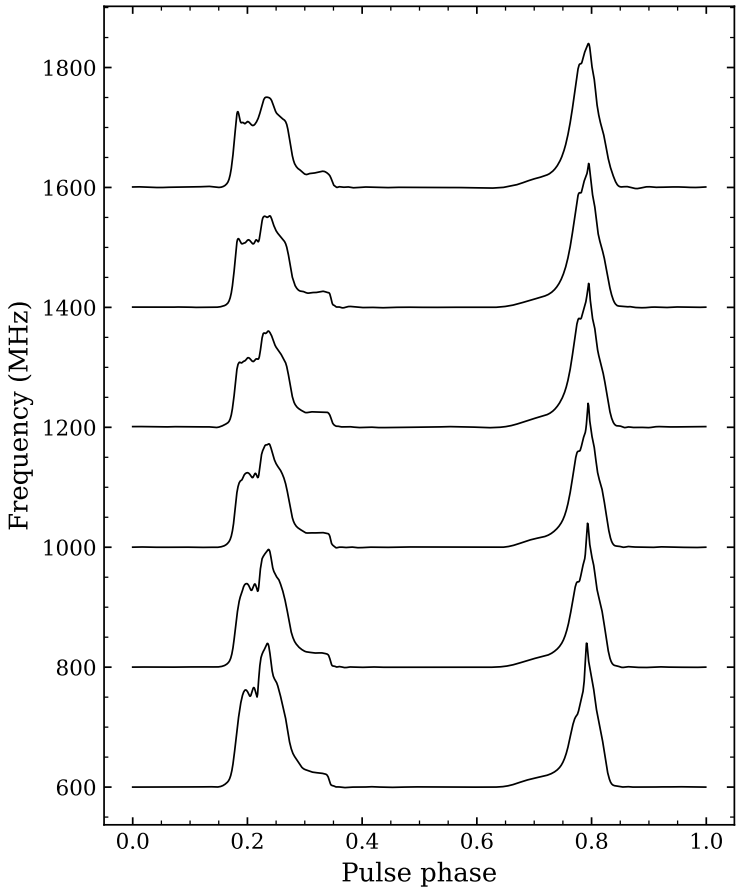

Figure 4.1: Pulse profile of PSR J0737−3039A observed at multiple frequencies with the MeerKAT UHF- and L-band receivers.

4.2.3 Wide-band templates and TOA extraction

Wide-band observations such as MeerTIME can suffer significant profile evolution in frequency, and thus the traditional 1D template is not favoured. To best determine the pulse time of arrivals (TOAs) at multiple frequencies, we employ frequency-dependent 2D templates. With this technique, DM measurements are dependent on the DM value used to align (de-disperse) the 2D template. Due to the correlation between the DM and profile evolution, DM measurements are to some extent frequency dependent, which can lead to a DM offset between L-band and UHF-band data. This could potentially be solved with a simultaneous observation with L-band and UHF-band receivers, which is missing in our case. Therefore, to avoid this problem, we choose a bright observation from each band for making 2D templates, and measure DM using data from their overlapping frequencies. Then, we use these DM values to de-disperse the corresponding full-bandwidth data. This minimises the DM offset between L-band and UHF-band data, which can be seen in Figure 4.2. These data are then sub-banded and averaged in time. Finally, by smoothing the profiles with `psrsmooth`/PSRCHIVE, we obtain 2D templates, with 16 sub-bands at L-band and 32 sub-bands at UHF-band. These templates are then used to measure frequency-resolved TOAs by cross-correlating with the reduced data using `pat`/PSRCHIVE. The pulse profile of PSR J0737−3039A at multiple frequencies is shown in Figure 4.1. More information on the observing systems and data sets is given in Table 4.1.

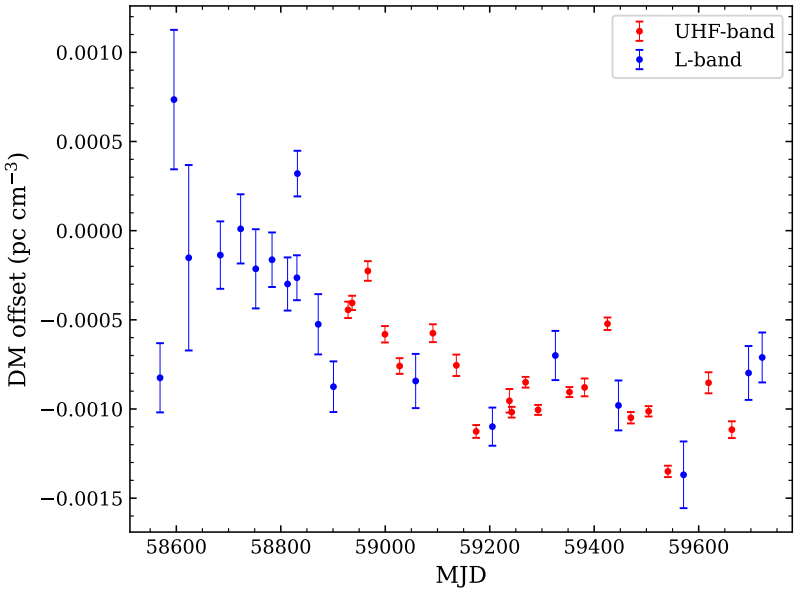

Figure 4.2: DM measurement per observing epoch relative to the reference value 48.913 pc cm^{-3} (see Section 4.2.4).

4.2.4 DM variation

The wide-band observation and high precision of MeerKAT telescope make it possible to obtain an accurate DM measurement on a per-epoch basis so as to minimise the influence of DM noise in the data. To do so, we fit for only DM and spin frequency ν for each observing epoch using 4-min TOAs, and keep the other parameters fixed. The DM measurements are shown in Figure 4.2. Following Kramer et al. (2021a), we use a modified version of TEMPO for our timing analysis, which corrects dispersive delays for each TOA based on the exact DM measurement of that epoch.

One should note that our data set does not show the apparent DM variation as a function of orbital phase, as was seen in Ransom et al. (2004). It had been demonstrated that this effect occurs due to an unaccounted Doppler shift of the observational frequency as the pulsar moves in a binary system,[6] and this will be revisited by Hu, Porayko et al. (in prep.). A more thorough investigation of this effect, as well as the frequency-dependent orbital smearing (see Section 4.2.2), is ongoing and will be presented in detail in the future publication.

4.3 Signal propagation effects at superior conjunction

In this section, we recapitulate the necessary concepts of signal propagation effects in the Double Pulsar, including the NLO contributions in the Shapiro delay and aberration delay. These concepts were described in greater detail in Kramer et al. (2021a).

Being a nearly edge-on binary system (i.e. $i \sim 90°$), the curved spacetime of the companion star (pulsar B) has a significant effect on the propagation of the pulsar's signal. To leading-order this is the well-known Shapiro delay (I. I. Shapiro, 1964), which is expressed in the following form for binary

[6] https://arxiv.org/e-print/astro-ph/0406321v2

pulsars (Blandford & Teukolsky, 1976; Damour & Deruelle, 1986):

$$\Delta_{\rm S}^{(\rm LO)} = -2r \ln \Lambda_u \,, \tag{4.1}$$

$$\Lambda_u = 1 - e_{\rm T} \cos u - s \left[\sin\omega \,(\cos u - e_{\rm T}) + (1 - e_{\rm T}^2)^{1/2} \cos\omega \sin u \right] . \tag{4.2}$$

Here, u denotes the eccentric anomaly (from Kepler's equation with eccentricity $e_{\rm T}$), and ω denotes the longitude of periastron measured from the ascending node. The time eccentricity $e_{\rm T}$ corresponds to the eccentricity parameter in the Damour-Deruelle (DD) timing model (Damour & Deruelle, 1986) that can be fitted in the pulsar timing software TEMPO or TEMPO2 (G. B. Hobbs et al., 2006). The two post-Keplerian (PK) parameters r and s represent the 'range' and 'shape' of Shapiro delay, respectively. The shape parameter is generally identified with the sine of the orbital inclination i as $s \equiv \sin i$, whereas the range parameter is linked to the mass of the companion $m_{\rm B}$, which in GR follows $r = T_\odot m_{\rm B}$. The constant $T_\odot \equiv (\mathcal{G}\mathcal{M})^{\rm N}_\odot / c^3$, where c is the speed of light in vacuum and $(\mathcal{G}\mathcal{M})^{\rm N}_\odot \equiv 1.327\,124\,4 \times 10^{26}\,\mathrm{cm^3\,s^{-2}}$ is the nominal solar mass parameter defined by the IAU 2015 Resolution B3 (Prša et al., 2016). Throughout the paper, all masses expressed in solar mass $\mathrm{M}_\odot$ are referred to the nominal solar mass by taking the ratio $Gm_i/(\mathcal{G}\mathcal{M})^{\rm N}_\odot$ $(i = A, B)$, where G is the gravitational constant.

The leading-order expression Eqs. (4.1) and (4.2) were obtained by integrating along a straight line (in harmonic coordinates) and assuming a static mass distribution when the pulsar's signal propagates through the system (Blandford & Teukolsky, 1976). In reality, the pulsar's signal propagates along a curved path due to the deflection in the gravitational field of the companion and leads to a *lensing correction* to the Shapiro delay. This actually results in a reduced propagation time as a consequence of Fermat's principle (Perlick, 2004). The effect of lensing is not yet observable in any pulsar systems, but for completeness, one can extend Eq. (4.2) by an adapted version of the approximation in Klioner & Zschocke (2010, Eq. (73)): $\Lambda_u \to \Lambda_u + \delta\Lambda_u^{\rm len}$ with

$$\delta\Lambda_u^{\rm len} = 2rc/a_{\rm R} \,, \tag{4.3}$$

where the semi-major axis of the relative orbit $a_{\rm R} = (x + x_{\rm B})/s$, with x and $x_{\rm B}$ being the projected semi-major axes of pulsar A and pulsar B, respectively.[7] For the Double Pulsar, one needs to account for the fact that the companion star moves while the pulsar's signal propagates across the system. This effect is known as the *retardation effect* or 1.5PN correction to the Shapiro delay (Kopeikin & Schäfer, 1999; Rafikov & Lai, 2006a). To sufficient approximation, the signal propagation delay can be extended to

$$\Delta_{\rm S} = -2r \ln \left(\Lambda_u + \delta\Lambda_u^{\rm len} + \delta\Lambda_u^{\rm ret} \right) , \tag{4.4}$$

where the retardation correction $\delta\Lambda_u^{\rm ret}$ can be taken directly from Kopeikin & Schäfer (1999, Eq. (130)) as

$$\delta\Lambda_u^{\rm ret} = \frac{2\pi}{s} \frac{x}{P_{\rm b}} \frac{m_{\rm A}}{m_{\rm B}} e_{\rm T} \sin u - \frac{2\pi\, s}{(1 - e_{\rm T}^2)^{1/2}} \frac{x}{P_{\rm b}} \frac{m_{\rm A}}{m_{\rm B}} \left[\sin\omega \,(\cos u - e_{\rm T}) + (1 - e_{\rm T}^2)^{1/2} \cos\omega \sin u \right] \left[e_{\rm T} \cos\omega + \frac{(\cos u - e_{\rm T}) \cos\omega - (1 - e_{\rm T}^2)^{1/2} \sin\omega \sin u}{1 - e_{\rm T} \cos u} \right] . \tag{4.5}$$

[7] $x_{\rm B}$ had been observed in Kramer et al. (2006b).

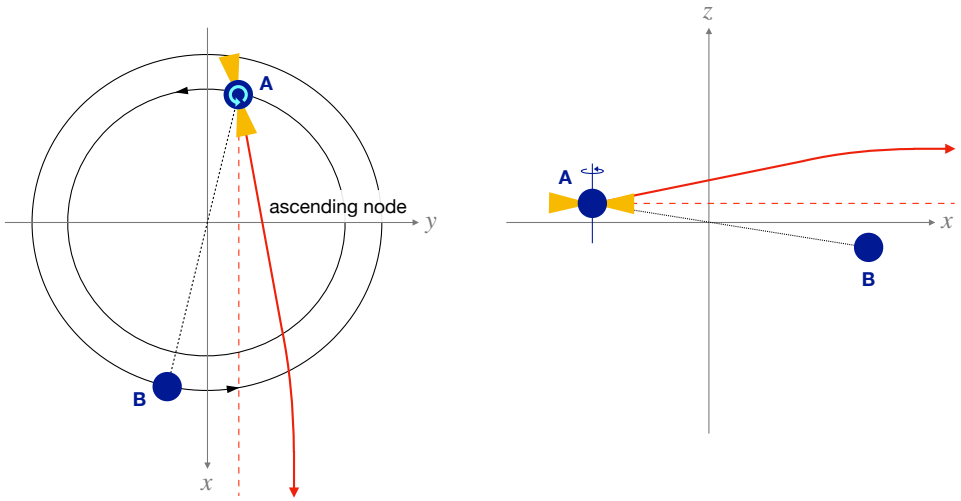

Figure 4.3: Simplified illustration of effects related to the deflection of A's radio signals (solid red) in the gravitational field of B (top down and side perspective). The observer is located at a large distance along the x-axis. Apart from modifications in the propagation time due to a curved path in the gravitational field of B (lensing), one has a longitudinal deflection delay ($\delta_{\rm A}^{\rm londef}$) due to the fact that the pulsar has to rotate by more than 360° between two pulses while approaching the conjunction. After conjunction, it is less than 360°, which makes pulsar signals arrive earlier at the observer. In addition, there is a latitudinal effect, due to a latitudinal shift in the emission direction towards the observer. This can lead to changes in the pulse profile since the line of sight cuts a different part of the emission region, which can also be accompanied by changes in the pulse arrival times (more details in Sections 4.5.1 and 4.5.2).

The quantity $P_{\rm b}$ denotes the orbital period and $m_{\rm A}$ denotes the mass of pulsar A. It should be noted that in the Double Pulsar, the mass ratio $m_{\rm A}/m_{\rm B}$ can be obtained in a theory-independent way (Kramer et al., 2006b; Damour, 2007). Hence, apart from the Shapiro shape parameter s, Eq. (4.5) contains only Keplerian parameters.

Moreover, the classical aberration expression (Smarr & Blandford, 1976) assumes a flat spacetime for the propagation of the pulsar signals, which is no longer sufficient for describing the observations of the Double Pulsar, particularly near the superior conjunction of pulsar A. One needs to account for the gravitational deflection of the pulsar's signal caused by its companion (Doroshenko & Kopeikin, 1995; Rafikov & Lai, 2006b), which adds a lensing correction to the classical aberration. For pulsar A the misalignment angle between its spin vector and the orbital angular momentum is very small (< 3.2°, Ferdman et al., 2008; Ferdman et al., 2013), which is in line with a low-kick birth event (cf. Piran & Shaviv, 2004; Willems & Kalogera, 2004; Willems et al., 2006; Stairs et al., 2006; Tauris et al., 2017). Since the spin of A is practically parallel to the orbital angular momentum, the aberration delay can be simplified as

$$\Delta_{\rm A} = \mathcal{A}\left(\sin\psi + e_{\rm T}\sin\omega\right) + \delta_{\rm A}^{\rm londef}\,. \tag{4.6}$$

The first term on the right-hand side of Eq. (4.6) is the classical aberration delay, where $\psi = \omega + \theta$ is the longitude of the pulsar with respect to the ascending node (θ is the true anomaly, which defines the angle between the direction of the pulsar and the periastron), and the aberration coefficient

$$\mathcal{A} = \frac{x}{\nu P_{\rm b}(1-e_{\rm T}^2)^{1/2}\sin^2 i} \simeq 3.65\,\mu{\rm s}\,. \tag{4.7}$$

As $\mathcal{A}$ is practically not observable and can be absorbed by a shift in various timing parameters (see

discussions in Damour & Deruelle, 1986; Damour & Taylor, 1992), we a priori add the aberration coefficient $\mathcal{A}$ as a fixed parameter in our timing model with the value given in Eq. (4.7).

The second term $\delta_{\rm A}^{\rm londef}$ in Eq. (4.6) is the higher-order correction originating from the *longitudinal deflection delay*, and can be written as (Doroshenko & Kopeikin, 1995)

$$\delta_{\rm A}^{\rm londef} = \mathcal{D}\,\frac{\cos\left(\psi + \delta\psi^{\rm ret}\right)}{\Lambda_u + \delta\Lambda_u^{\rm ret}}\,, \text{with } \mathcal{D} = \frac{1}{\pi\nu}\frac{r}{x + x_{\rm B}}\,. \tag{4.8}$$

Just as in the Shapiro delay, retardation correction is also accounted for here. As a sufficiently good approximation, the position of B when the signal reaches its minimum distance from B can be used (retardation corrected position; cf. Kopeikin & Schäfer, 1999; Rafikov & Lai, 2006a). The angle $\delta\psi^{\rm ret}$ denotes the retardation related correction for the angle between the (coordinate) vector from B to A and the ascending node.

As already discussed in Kramer et al. (2021a), the NLO contributions in the Shapiro and aberration delays cannot be tested separately in the Double Pulsar due to the similarity of their effects on signal propagation. In addition, the lensing correction to the propagation delay (Eq. (4.3)) is challenging to measure as it can be absorbed in the fit of Shapiro shape s (see Section 4.5.3 and discussions in Kramer et al., 2021a). Therefore, to test the significance of the NLO contributions and to obtain an unbiased timing result, a common factor $q_{\rm NLO}$ is multiplied by these contributions and can be fitted for in our timing model:

$$\Lambda_u^{\rm ret} = \Lambda_u^{\rm ret} \times q_{\rm NLO}\,, \tag{4.9}$$

$$\Lambda_u^{\rm len} = \Lambda_u^{\rm len} \times q_{\rm NLO}\,, \tag{4.10}$$

$$\delta_{\rm A}^{\rm londef} = \delta_{\rm A}^{\rm londef} \times q_{\rm NLO}\,. \tag{4.11}$$

In GR, the scaling factor $q_{\rm NLO} = 1$. Figure 4.3 illustrates the different effects related to signal deflection in the Double Pulsar system.

4.4 Timing results

For the timing analysis, we use the timing model in TEMPO known as DDS, which is a modification of the DD model (Damour & Deruelle, 1986) that uses a different parameterisation of the Shapiro delay. In DDS, the Shapiro shape parameter s is replaced by the logarithmic Shapiro shape parameter z_s via

$$z_s \equiv -\ln\left(1 - s\right), \tag{4.12}$$

which is more suitable when s is very close to one (see Kramer et al., 2006a; Kramer et al., 2021a). The NLO contributions in the Shapiro and aberration delays are also implemented in the latest DDS model, which can be measured through a common factor $q_{\rm NLO}$. Because the analytic inversion of the timing model developed in Damour & Deruelle (1986) is no longer sufficient for the Double Pulsar, primarily due to the NLO contributions, a numerical inversion of the timing model was also implemented in the latest DDS model in TEMPO (see Kramer et al., 2021a).

4.4.1 Timing parameters

In our analysis, the full MeerKAT data set shows a large deviation in the Shapiro range parameter r compared to the 16-yr result (Kramer et al., 2021a). We perform a drop-out analysis by removing each

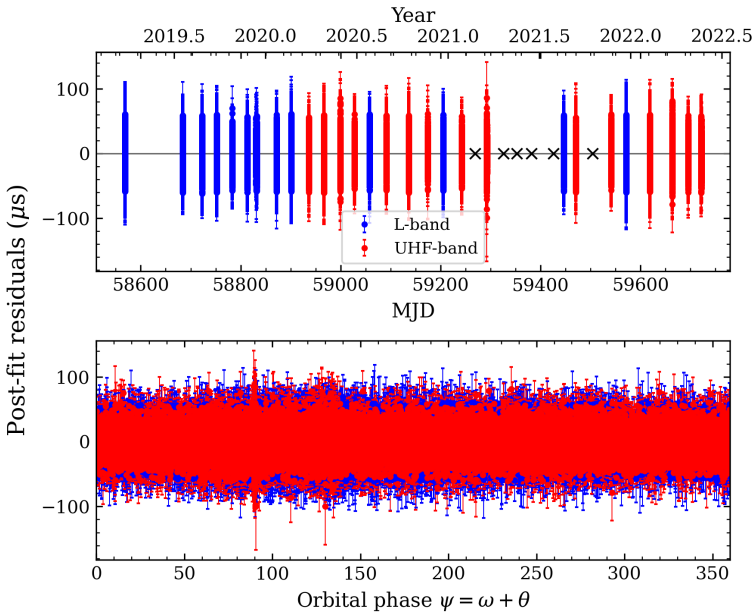

Figure 4.4: Post-fit residuals of PSR J0737−3039A using the DDS binary model as a function of time (top panel) and the orbital phase of pulsar A with respect to the ascending node ψ (bottom panel). The MeerKAT L-band data are plotted in blue, whereas the UHF-band data are in red. The epochs of the excluded six observations are marked as black crosses.

observing epoch and fitting the parameters. We find that r is dependent on specific observing epochs, where six epochs affect r by a significant amount while the rest of the epochs do not. These six epochs are marked as black crosses in Figure 4.4. After excluding all these six epochs, r is consistent with the 16-yr result and the mass measurement in GR (Kramer et al., 2021a). Even though a number of tests and simulations have been made, we are still unclear about the cause of this problem. Possible reasons could be systematic errors in the observations or folding techniques. It should be noted that all data were folded with the TEMPO2 phase predictor during observations, which has shown outliers in this pulsar and has been doubly confirmed by our simulations. These outliers disappear after reinstalling a TEMPO `polyco` ephemeris in data processing (see Section 4.2.2), but we cannot rule out underlying problems due to the folding technique. The results shown here are based on data processed with the `polyco` scheme.[8] In any case, this issue should not affect the measurement of NLO signal propagation effects, which is the main focus of this paper. Therefore, we leave this question to future studies. In the following analysis, we use a trimmed data set that excludes these six epochs.

Table 4.2 and Figure 4.4 present the results obtained from fitting the TEMPO DDS model to the trimmed MeerKAT data set. We fix the proper motion (μ_α, μ_δ) and parallax π_x to the more precise values determined from the 16-yr timing and the VLBI measurements (see Kramer et al., 2021a). As the time span of our data is not sufficient to obtain a reliable measurement of the orbital period derivative $\dot{P}_b$ and the orientation of the orbit ($\omega_0 \approx 0^\circ$) is not at a favourable position for a precise measurement of the Einstein delay amplitude γ_E, we choose to fix these parameters to the more precise measurements from 16-yr data (Kramer et al., 2021a). Fixing the above parameters has no impact on the measurements of signal propagation effects and masses. The two PK parameters that describe the relativistic deformation of the orbit, δ_r and δ_θ (Damour & Deruelle, 1986), are also held fixed at the GR value in our analysis, as δ_r cannot be measured (see Kramer et al., 2021a) and δ_θ is not yet measurable with the current

[8] With the same set of observations, data processed with TEMPO `polyco` and TEMPO2 `predictor` show a noticeable difference ($\sim 3\sigma$) in the Shapiro parameters, where the result with `polyco` is closer to the 16-yr results and shows a smaller χ^2.

Table 4.2: Timing parameters for PSR J0737−3039A using the TEMPO DDS binary model. Numbers in parentheses are 1σ uncertainties applicable to the last digits, obtained from the standard deviation of 1000 MC runs or maximum error from TEMPO, whichever is larger. The overall reduced χ^2 is 0.99.

Parameter	**Value**
Solar System ephemeris	DE436
Terrestrial time standard	UTC(NIST)
Timescale	TDB
Position epoch (MJD)	55045.0
Timing epoch, t_0	55700.0
Astrometric parameters	
Right ascension (R.A.), α (J2000)	07:37:51.248 121(26)
Declination (Dec.), δ (J2000)	−30:39:40.705 36(42)
Proper motion R.A., μ_α (mas yr^{-1})	−2.567(30)*
Proper motion Dec., μ_δ (mas yr^{-1})	2.082(38)*
Parallax, π_x (mas)	1.36(+0.12,−0.10)*
Spin parameters	
Rotational frequency (freq.), ν (Hz)	44.054 068 642 001(56)
First freq. derivative, $\dot{\nu}$ (Hz s^{-1})	$-3.415\,92(37) \times 10^{-15}$
Second freq. derivative, $\ddot{\nu}$ (Hz s^{-2})	$-9.5(12) \times 10^{-27}$
Binary parameters	
Orbital period, P_b (days)	0.102 251 559 297 2(29)
Projected semi-major axis, x (s)	1.415 028 299(88)
Eccentricity, e_T	0.087 777 036(48)
Epoch of periastron, T_0 (MJD)	55700.233 017 54(10)
Longitude of periastron, ω (deg)	204.753 72(36)
Periastron advance, $\dot{\omega}$ (deg yr^{-1})	16.899 321(37)
Orbital period derivative (10^{-12}), $\dot{P}_b$	−1.247 920(78)*
Einstein delay amplitude, γ_E (ms)	0.384 045(94)*
Logarithmic Shapiro shape, z_s	9.669(77)
Range of Shapiro delay, r (μs)	6.163(16)
NLO factor for signal prop., q_{NLO}	0.999(79)
Derived parameters	
$s \equiv \sin i = 1 - e^{-z_s}$	0.999 936 9(+46/ -51)
Orbital inclination, i (deg)	89.36(3) or 90.64(3)
Mass of pulsar A, m_A ($M_\odot$)	1.338 186(10)
Mass of pulsar B, m_B ($M_\odot$)	1.248 866(7)
Total mass, M ($M_\odot$)	2.587 052(11)

* Values adopted from Kramer et al. (2021a).

MeerKAT data.

The values shown in Table 4.2 are the result of 1000 Monte Carlo (MC) runs, where in each run, a random realisation of proper motion, parallax, DM, γ_E, and $\dot{P}_b$ is selected. The DM value is selected according to the DM measurements and uncertainties shown in Figure 4.2. We use the aforementioned

Table 4.3: Mass measurements with a new modified DDGR model that accounts for NLO contributions in the orbital motion and signal propagation in this system. The MOI has been chosen to be $I_A = 1.28 \times 10^{45}\,\mathrm{g\,cm^2}$ in the fit.

Parameter	Value
Mass of pulsar A, m_A ($M_\odot$)	1.338 186(10)
Mass of pulsar B, m_B ($M_\odot$)	1.248 886(5)
Total mass, M ($M_\odot$)	2.587 050(8)

modified version of TEMPO to correct the DM for each TOA and fit for all other timing parameters in each run. The numbers shown in Table 4.2 are the mean values of the distribution of each parameter after 1000 MC runs, whereas the uncertainties are taken from the larger one among the standard deviation of the distributions and the maximum error from TEMPO in all MC runs.

In order to allow direct comparisons with previous publications, parameters shown in Table 4.2 are measured with respect to the same epochs and the same terrestrial time standard UTC(NIST) within the 'Barycentric Dynamical Time' (TDB) timescale as implemented in TEMPO.[9] Even though TDB runs at a slower rate than "Barycentric Coordinate Time (TCB)", which was recommended by IAU 2006 Recolution B3 (see also Soffel et al., 2003),[10] this choice does not have any impact on the results presented in this paper (see discussions in Kramer et al., 2021a). To transfer the topocentric TOAs to the Solar System Barycentre (SSB), the DE436 Solar System ephemeris published by the Jet Propulsion Laboratory is used.[11]

All binary parameters in Table 4.2 are consistent with the 16-yr data, except for x being different by $\sim 3\sigma$. This is because x is highly correlated with γ_E, which is kept fixed in our fit. This should be improved in the future, once we have enough MeerKAT data to fit for x and γ_E simultaneously. In our fit, the root mean square (RMS) is very close to the mean TOA uncertainty, and the reduced χ^2 of the individual observation is close to one, suggesting that our result is not affected by jitter noise. We also perform simulations and single-pulse analysis following the methods in Parthasarathy et al. (2021) and find little evidence of jitter noise.

The RMS of the MeerKAT data shown in Table 4.4 is more than two times better than that of the Green Bank Telescope (see Kramer et al., 2021b). Thanks to this much improved precision, the measurements of the Shapiro parameters improve quickly. Compared to Kramer et al. (2021a), the shape parameter s improves by a factor of two and the range parameter r improves by a factor of 1.3 (see Table 4.2).

4.4.2 Mass measurements

The standard approach for measuring the masses of a binary pulsar system is using two PK parameters. Assuming GR, one can calculate the two a priori unknown masses based on the measurements of Keplerian parameters. For the Double Pulsar, the two most precisely measured PK parameters are periastron advance $\dot{\omega}$ and the Shapiro shape parameter s.

For the advance of periastron, in addition to the 1PN contribution, we also need to account for higher-order corrections due to 2PN effects and Lense-Thirring (LT) precession caused by spin-orbit coupling of pulsar A, as they are much larger than the measurement error of $\dot{\omega}$ see Hu et al., 2020; Kramer et al., 2021a. For the analysis of this paper, the total intrinsic contribution to the periastron

[9] https://www.nist.gov/pml/time-and-frequency-division/time-realization/utcnist-time-scale-0
[10] https://www.iau.org/static/resolutions/IAU2006_Resol3.pdf
[11] https://ssd.jpl.nasa.gov/planets/eph_export.html

advance can be expressed, with sufficient precision, as (Damour & Schäfer, 1988)

$$\dot{\omega} = \dot{\omega}^{\rm 1PN} + \dot{\omega}^{\rm 2PN} + \dot{\omega}^{\rm LT,A} \,. \tag{4.13}$$

The first and second post-Newtonian (PN) terms $\dot{\omega}^{\rm 1PN}$ and $\dot{\omega}^{\rm 2PN}$ are functions of masses and observed Keplerian parameters. The situation is more complicated for the LT contribution $\dot{\omega}^{\rm LT,A}$, as it requires the knowledge of the moment of inertia (MOI) of pulsar A, which is still not very constrained because of our limited knowledge of the equation of state (EOS) of neutron stars. As discussed in detail in Hu et al. (2020), one could measure the masses and the MOI simultaneously by introducing a third PK parameter $\dot{P}_{\rm b}$ into the $\dot{\omega} - s$ test. Such a test has already been carried out by Kramer et al. (2021a) using the 16-yr data with an upper limit obtained: $I_{\rm A} < 3.0 \times 10^{45}$ g cm^2 with 90% confidence. This measurement is expected to improve with the combination of the 16-yr data with MeerKAT data in a forthcoming paper, and should improve considerably in the coming years as more data becomes available. This promises an important complementary constraint on the EOS (Hu et al., 2020). For the calculations here, we take the value of $\dot{\omega}^{\rm LT,A}$ from Eq. (35) in Kramer et al. (2021a), which uses the constraints on the EOS from Dietrich et al. (2020):

$$\dot{\omega}^{\rm LT,A} = -4.83(+29, -35) \times 10^{-4} \text{ deg yr}^{-1} \,. \tag{4.14}$$

The Shapiro shape parameter s is the sine of the orbital inclination i. In Newtonian gravity, the orbital inclination is linked to the projected semi-major axis x via the binary mass function (e.g. Lorimer & Kramer, 2004):

$$\sin i = \frac{(n_{\rm b} M)^{2/3} x}{T_\odot^{1/3} m_{\rm B}} \,, \tag{4.15}$$

where x and the orbital frequency $n_{\rm b} \equiv 2\pi/P_{\rm b}$ are both measured Keplerian parameters. Equation (4.15) gets modified by a 1PN term in the 1PN approximation for Kepler's third law (see Eq. (3.7) in Damour & Deruelle 1985 and Eq. (3.9) in Damour & Taylor 1992):

$$\sin i = \frac{(n_{\rm b} M)^{2/3} x}{T_\odot^{1/3} m_{\rm B}} \left[1 + \left(3 - \frac{m_{\rm A} m_{\rm B}}{3M^2} \right) \left(T_\odot M n_{\rm b} \right)^{2/3} \right] \,. \tag{4.16}$$

Taking the measurements of $P_{\rm b}$, x, and masses from Table 4.2, one can calculate that the 1PN correction is approximately 1.27×10^{-5}. This correction was considered for the first time in pulsar analysis by Kramer et al. (2021a), where the significance was about 1.3σ. Now with MeerKAT data, this 1PN correction is 2.5σ significant and cannot be ignored in the analysis. We hereby use the full 1PN mass function Eq. (4.16) to measure the masses.

Combining the PK parameters $\dot{\omega}$ and s, one obtains the (Doppler-shifted) masses, which are listed in Table 4.2. These measurements are fully consistent with those obtained with 16-yr data (Kramer et al., 2021a), and the precision of $m_{\rm A}$ and $m_{\rm B}$ are also better.

Alternatively, one can fit for masses using the timing model known as DDGR (Taylor & Weisberg, 1989), which is based on the DD model where the PK parameters are explicitly calculated from the masses and the Keplerian parameters, assuming GR. Beside the Keplerian parameters, it fits explicitly for the total mass M and the companion mass $m_{\rm B}$. To make the measurements, we modify the DDGR model so that it incorporates all NLO contributions that need to be accounted for in this system, including NLO signal propagation effects, LT contribution $\dot{\omega}^{\rm LT,A}$, NLO gravitational wave damping and mass-loss contribution to $\dot{P}_{\rm b}$ (see Hu et al., 2020; Kramer et al., 2021a). An MOI needs to be provided to the

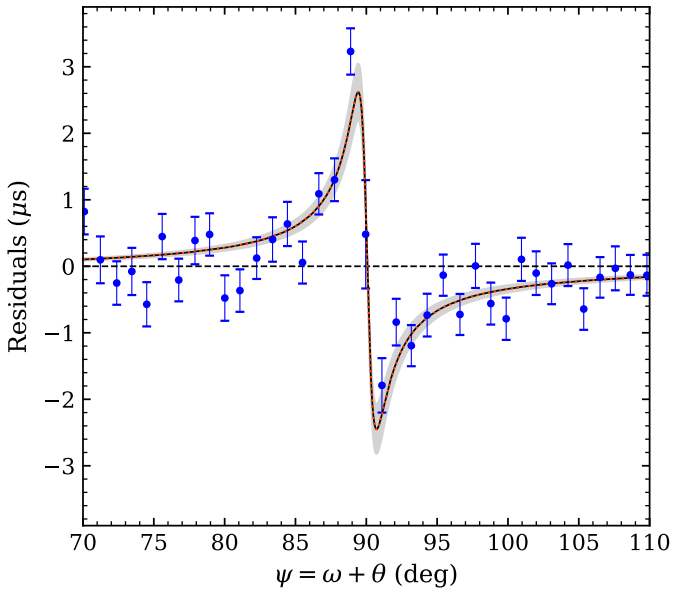

Figure 4.5: Aggregated residuals (blue) due to NLO contributions in Shapiro and aberration delay, shown in the orbital phase ψ. Residuals are re-scaled by $(1 + e_T \cos\theta)^{-1}$ to account for secular variations in amplitude due to the precession of periastron. The black curve indicates the fitted q_{NLO} (see Table 4.2) with the 2σ range shown by the grey shaded areas, which agrees very well with the theoretical prediction indicated by the red dotted line.

model for the calculation of $\dot{\omega}^{LT,A}$ and the mass loss contribution to $\dot{P}_b$. For periastron advance $\dot{\omega}$, the uncertainty from the MOI is still smaller than that from MeerKAT observations (see Eq. (4.14) and Table 4.2). Therefore, based on the EOS constraint from Dietrich et al. (2020), we fix the MOI to $I_A = 1.28 \times 10^{45}\,\mathrm{g\,cm^2}$ in our fit. Table 4.3 shows the mass measurements obtained using the DDGR model. The results are fully consistent with the measurements derived from the DDS model, with smaller uncertainties in m_B and M.

Following Kramer et al. (2021a), one could test the agreement of r in GR by comparing $m_B^{(r)} = r/T_\odot = 1.2512(33)\,M_\odot$ (cf. Table 4.2) with the companion mass determined here, which gives

$$r^{obs}/r^{GR} = 1.0019(26)\,. \tag{4.17}$$

This leads to a 5.3×10^{-3} (95% confidence) test of GR.

4.5 Studying NLO signal propagation effects

Because the Double Pulsar system is nearly edge-on to our line of sight (LOS, see i in Table 4.2), it is ideal for measuring signal propagation effects caused by the gravitational field of the companion near superior conjunction. The leading-order expression Eq. (4.1) is no longer sufficient for describing the signal propagation in the Double Pulsar. Such a model would result in significant residuals near superior conjunction when aggregating residuals in the orbital phase, as shown in Figure 4.5. These residuals agree very well with the expected NLO contributions discussed in Section 4.3, which are shown by the red curve. The significance of the NLO corrections can be tested by scaling these corrections collectively by a common factor q_{NLO} (cf. Eqs. 4.9-4.11; q_{NLO}=1 in GR) and fitting for it. We find, with the trimmed

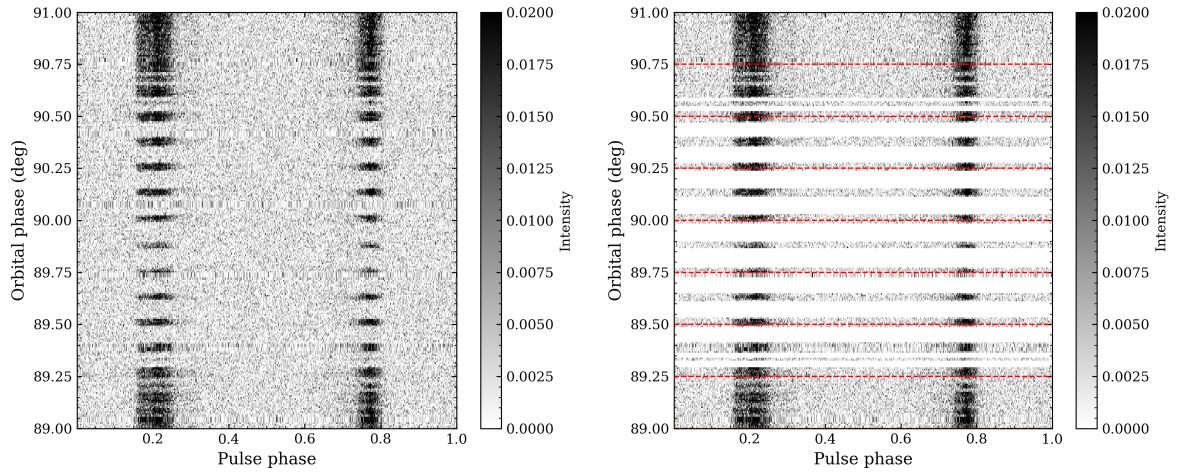

Figure 4.6: Left: Example of one eclipse observation at UHF band, plotted in intensity against orbital phase ψ and pulse phase. The intensity modulation occurs when pulsar A is eclipsed by the magnetosphere of pulsar B. Each integration is a sum of eight pulses. When plotting, the discontinuities between recordings are patched with the previous sub-integration. Right: Same as for Figure 4.6(a), but masking out the regions without pulses (blocked by the magnetosphere of pulse B). The dashed red lines indicate the orbital phase bins used in Figures 4.7 and 4.8.

data set,

$$q_{\rm NLO} = 0.999(79)\,, \tag{4.18}$$

which has surpassed the 16-yr result by 1.65 times with only ~3 yr of data, thanks to the much improved precision offered by MeerKAT.

Following the definition of $q_{\rm NLO}$ in Section 4.3, a fit for this parameter involves two aspects of gravity: a 1.5PN correction of the Shapiro delay due to the movement of the companion $\delta\Lambda_u^{\rm ret}$, and corrections related to the signal deflection in the gravitational field of the companion $\delta\Lambda_u^{\rm len}$ and $\delta_{\rm A}^{\rm londef}$. Even though these contributions cannot be tested individually in a simultaneous fit because of their similarity, one can still test one at a time while keeping the other one fixed (cf. Kramer et al., 2021a). We find

$$q_{\rm NLO}[\text{deflection}] = 1.00(15)\,, \tag{4.19}$$

$$q_{\rm NLO}[\text{retardation}] = 1.00(17)\,. \tag{4.20}$$

4.5.1 Searching for profile variation at eclipse

The lensing correction to the aberration delay may not only lead to a shift in time in the longitudinal aspect but can also result in a change of the co-latitude of the emission direction towards Earth, namely the *latitudinal deflection delay*. This would cause profile variations as the LOS cuts a different region of the pulsar beam (Rafikov & Lai, 2006a; Rafikov & Lai, 2006b). An illustration of the latitudinal deflection effect is shown in the right panel of Figure 4.3. Various analyses have confirmed that pulsar A is an orthogonal rotator (Guillemot et al., 2013; Ferdman et al., 2013; Kramer et al., 2021b), meaning that the main pulse and the interpulse come from opposite magnetic poles. Therefore, we do not expect shifts of pulse components in phase, as discussed in Rafikov & Lai (2006b), based on the (incorrect) assumption of an aligned rotator suggested by P. Demorest et al. (2004).

The profile variation is expected to be maximum at the superior conjunction and symmetric around

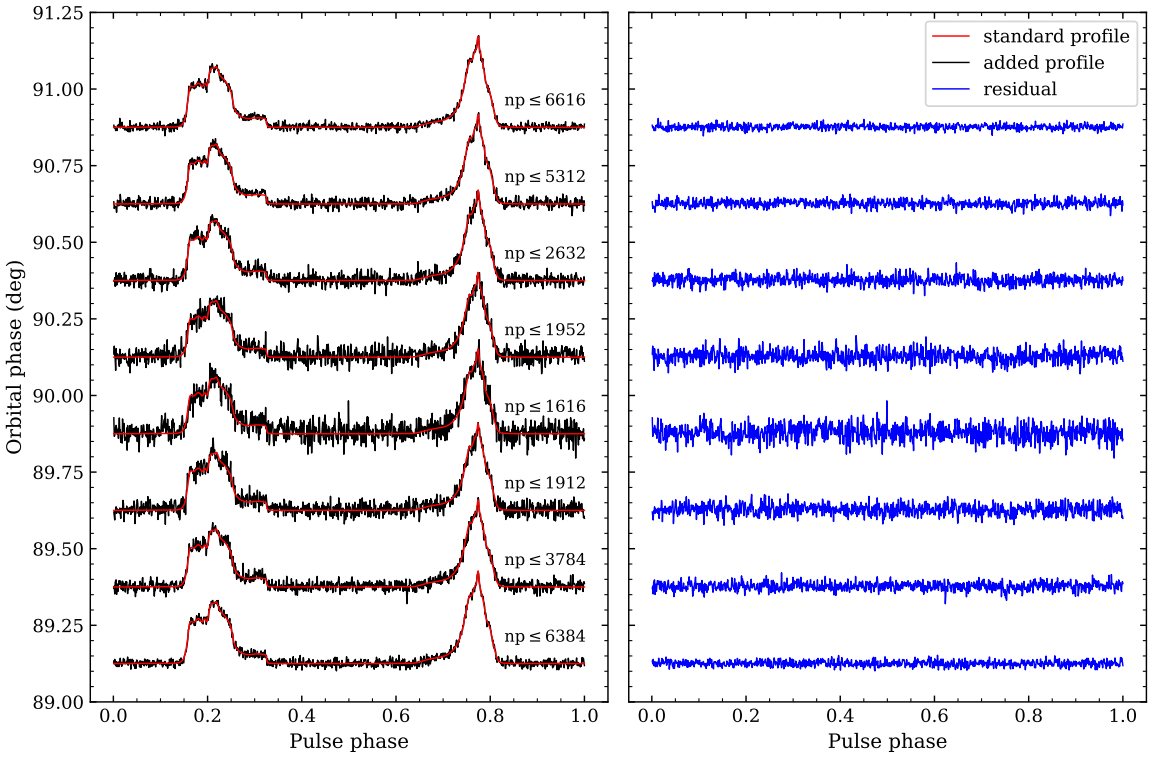

Figure 4.7: Profile variation with respect to orbital phase. Left: Black lines indicate the integrated profile of L-band data summed from 25 eclipses for orbital phases $89° < \psi < 91°$ with an interval of $\Delta\psi = 0.25°$. The baseline of the profile is placed at the centre of each interval, and the numbers on the right side of the profiles (np) indicate the estimated upper limit for the number of pulses in that interval. The red curves indicate the reference (standard) profile integrated over a 2-hr observation excluding the eclipse part. Right: Residuals of the added profile with respect to the reference profile.

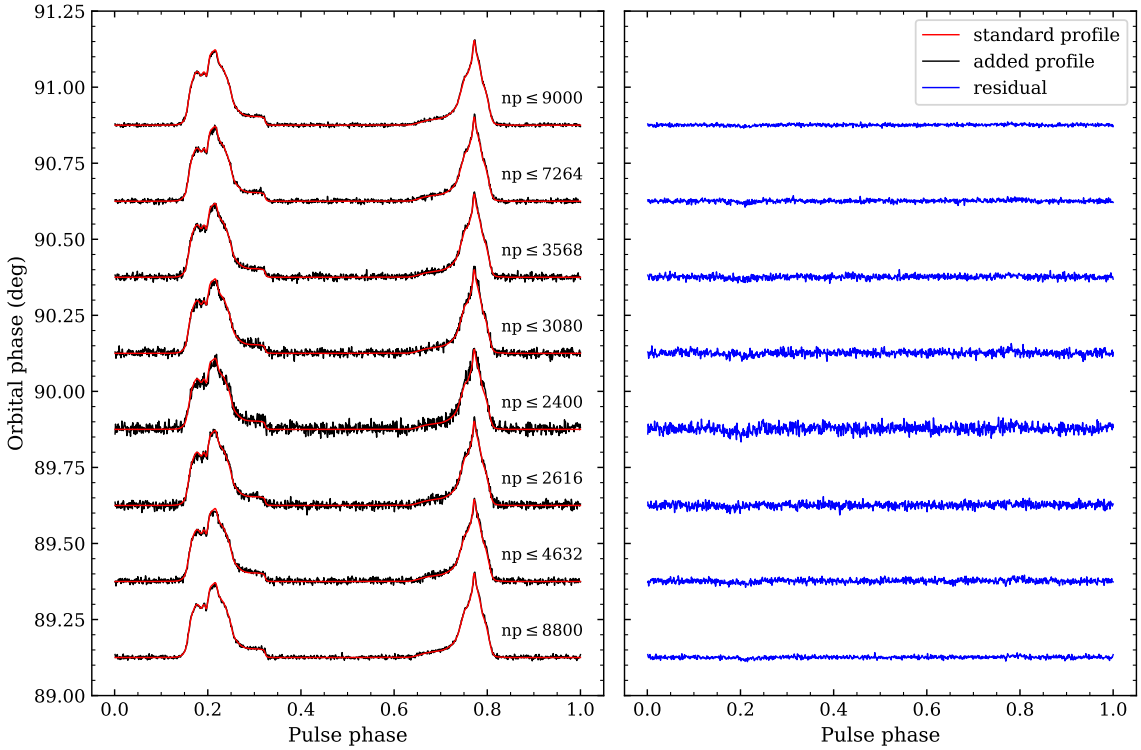

Figure 4.8: Same as for Figure 4.7, but for the UHF-band data summed from 37 eclipses.

$\psi = 90°$ (retardation corrected). This study requires high time resolution, for which we use the search mode data. We select the data that are near the eclipses and fold them into single pulses using TEMPO `polyco` (with TSPAN=1min). Data are then combined, cleaned, and polarisation calibrated before integrated into total intensity and averaged in frequency. As the single pulses are still very weak, we average over every eight pulses to increase the signal-to-noise ratio (S/N). An example of eclipse data is shown in Figure 4.6(a).

In order to get a high S/N profile, we first mask the regions where pulsar A's emission is blocked by pulsar B (see Figure 4.6(b)) and split the data into orbital phases with a step of $\Delta\psi = 0.25°$ for $89° < \psi < 91°$. Then for each phase interval, we integrate pulses from all observations of a given band (L or UHF) together to increase the S/N. The resulting profiles are shown in Figure 4.7 for the L-band data and in Figure 4.8 for the UHF-band data, which are summed from 25 and 37 eclipses respectively. The difference between the added profiles at the eclipse and a 2-hr integrated profile at the non-eclipse part of the orbit is insignificant. The subtle residual structures in these figures can result from interstellar medium effects (DM variation and scintillation) based on our simulations. Therefore, we conclude that the current data are not (yet) sensitive to profile variations caused by the latitudinal aberration delay, or are not significant in the region that is seen by our LOS. These profiles will be used in a subsequent study on the geometry of the system.

4.5.2 Simulation for latitudinal deflection delay

To investigate whether the deflection delay caused by latitudinal deflection is measurable from pulsar timing, we perform a simulation based on a simple emission model, which consists of a set of circular cones. Following Doroshenko & Kopeikin (1995) and Rafikov & Lai (2006b), the latitudinal deflection delay for pulsar A can be written as

$$\delta_{\rm A}^{\rm latdef} = -\mathcal{D}\,\frac{\cos i \sin\left(\psi + \delta\psi^{\rm ret}\right)}{\left(\Lambda_u + \delta\Lambda_u^{\rm ret}\right)\tan\chi_0}\,, \tag{4.21}$$

where χ_0 is the angle between the arc connecting the LOS and spin axis and the arc connecting LOS and magnetic axis. It should be noted that Eq. (4.21) is based on the approximation of Doroshenko & Kopeikin (1995) for the deflection angle, and therefore assumes that the impact parameter is (sufficiently) large compared to the Einstein radius. While this is sufficient, at least until full SKA becomes operational, we present an improved description further below in Section 4.5.4.

We include this deflection time delay in our test model assuming $\chi_0 = 45°$ (i.e. a relatively large latitudinal deflection delay) and scale it with a factor $q^{\rm latdef}$.[12] We simulate high-precision TOAs using this test model and fit for the scaling factor. The pre-fit residuals show an advance signature with an amplitude of $-2.8\ \mu$s and symmetric to $\psi = 90°$, which is in a similar shape to Shapiro delay but with the opposite sign and a smaller amplitude. However, after fitting for Shapiro parameters, the signature gets mostly absorbed and leaves residuals below 42 ns at superior conjunction.

4.5.3 Prospects of lensing measurement

Even though the retardation and deflection effects can be tested separately while keeping the other one fixed, as shown in Eqs. (4.19) and (4.20), measuring the lensing correction to Shapiro delay $\delta\Lambda_u^{\rm len}$

[12] It should be noted that χ_0 is not a constant, but our purpose here is to get a feeling for the measurability of the effect in timing rather than a proper account of the effect, which requires knowledge of the latitudinal variation in the emission pattern of the pulsar. Furthermore, as discussed at the beginning of Section 4.5.1, the beam geometry adopted by Rafikov & Lai (2006b) is not the correct one anyway.

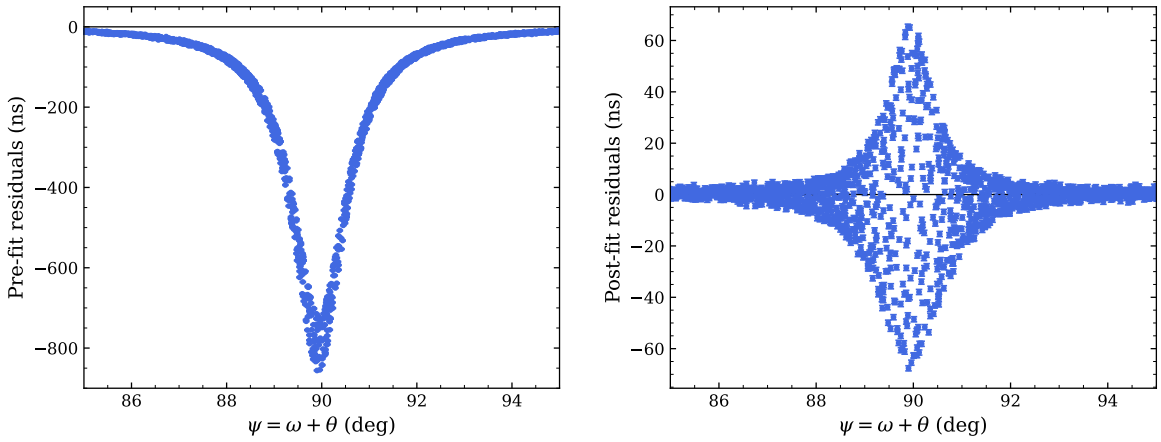

Figure 4.9: (a) Lensing simulation: pre-fit residual plotted against orbital phase ψ. Data displayed here are centred on $\omega = 180°$ and span a decade. The scattering at the lower end of the curve is due to the precession of periastron. (b) Lensing simulation: post-fit residual plotted against orbital phase ψ.

independently is challenging. As already pointed out by Kramer et al. (2021a), this effect is difficult to observe because of its strong covariance with s, or equivalently z_s. Our simulation also confirms that the lensing signature can be mostly absorbed by z_s in timing due to its symmetry with respect to conjunction. For demonstration purposes, we simulate 1-ns TOAs, which model all NLO signal propagation contributions, then keep the retardation and deflection delay fixed in the model and fit for the scaling factor attached to the lensing correction, q^{len} (corresponding to q_{NLO} in Eq. (4.10)). Figure 4.9(a) shows the residuals when lensing correction is not taken into account, leading to a reduced propagation time of about 850 ns as a result of Fermat's principle. However, after fitting for z_s, the lensing signature gets absorbed and leaves the residuals to be below 70 ns (Figure 4.9(b)), making a detection with the current timing precision certainly impossible.

To investigate whether lensing can be measured separately in the near future, we simulate TOAs for MeerKAT, MeerKAT extension, and the first phase of the SKA (SKA 1) until 2030 based on similar assumptions made in Hu et al. (2020). In addition, as the TOA precision reduces significantly due to the intermittent signals during the eclipse (see Figure 4.6(a)), we account for this in our simulations by increasing the uncertainty of these TOAs based on MeerKAT observations. As a simple estimate, we assume GR and perform the simulation using the modified DDGR model with a grid fit to q^{len}. If lensing is measurable, the value of q^{len} should be close to one. However, it turns out that with the observed and simulated data from 2019 to 2030, the uncertainty of q^{len} is still larger than one.

To further push the precision, we assume that an instrument will be available in the future that is capable of providing a timing accuracy one order of magnitude better than that of the SKA 1 (i.e. 100 ns for an integration time of 30 s), for example, a future full SKA. As a rough estimate, here we only consider radiometer noise and ignore any other noise sources, such as jitter noise or scintillation noise. The uncertainty of q^{len} against the time span of the simulated data is shown in Figure 4.10. With such precision, one would expect to get a 5-σ test of lensing with $\sim$ 4 yr of data.

From the simulation, we also obtain an estimated uncertainty for the common factor of NLO contributions q_{NLO} in the near future. Assuming no jitter noise, with MeerKAT and the SKA 1, we can expect a 50-σ detection by 2030.

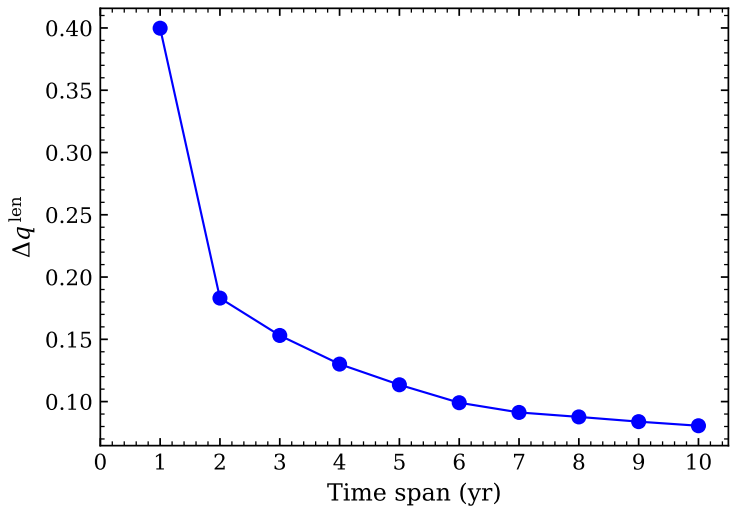

Figure 4.10: Uncertainty of factor q^{len} as a function of time span for the simulated data assumed to be ten times better than the SKA 1.

4.5.4 Improvements in the timing model for $\lesssim 50$ ns precision

Equations (4.8) and (4.21) are based on the approximation for the signal deflection used by Doroshenko & Kopeikin (1995). As discussed in detail in Kramer et al. (2021a), this is still sufficient for the analysis of current timing data. For that reason, the analysis in this paper is still based on Doroshenko & Kopeikin (1995), which (including corrections for retardation) is already part of the TEMPO distribution. However, in the future we can expect to obtain a timing precision of better than ~ 50 ns near conjunction ($\pm 1^\circ$), so that an improved treatment of the deflection is required. In a series of papers, Rafikov and Lai used the standard lensing equation to treat the signal propagation in the Double Pulsar near conjunction (Lai & Rafikov, 2005; Rafikov & Lai, 2006a; Rafikov & Lai, 2006b). This allowed them to drop the assumption that the impact parameter is much larger than the Einstein radius. The standard lensing equation, however, is based on the assumption of small angles (see e.g. Schneider et al. 1992). Therefore, strictly speaking, Lai and Rafikov's calculations are only valid near conjunction. Similar to the calculations of I. I. Shapiro, 1967 and Ward (1970), Wucknitz (2008) studied the deflection of photons in the gravitational field of a 'point mass' for general lensing scenarios not limited to regions close to the optical axis. Based on these results, we give an analytic expression for the signal deflection that is valid for the whole orbit, and recovers the calculations by Lai and Rafikov near conjunction, and those of Doroshenko & Kopeikin (1995) if the impact parameter is large compared to the Einstein radius.

In the following paragraphs, Θ is the angle between $\vec{r}_{\mathrm{AB}'}$ and the direction towards the observer, where $\vec{r}_{\mathrm{AB}'}$ denotes the vector from the position of pulsar A at emission to the (retardation corrected) position of pulsar B (the underlying geometry for our calculations is illustrated in Figure 4.11). The deflection $\Delta\Theta$ of A's radio signal by pulsar B can be obtained from Eq. (24) in Wucknitz (2008), with the replacements $\alpha \to \Delta\Theta$, $\theta \to \Theta + \Delta\Theta$, and $m \to \alpha_{\mathrm{E}}^2$, where the quantity α_{E} is the angle corresponding to the Einstein radius, and is given by

$$\alpha_{\mathrm{E}} = \frac{2}{c}\sqrt{\frac{G m_{\mathrm{B}}}{|\vec{r}_{\mathrm{AB}'}|}} \ll 1\,. \tag{4.22}$$

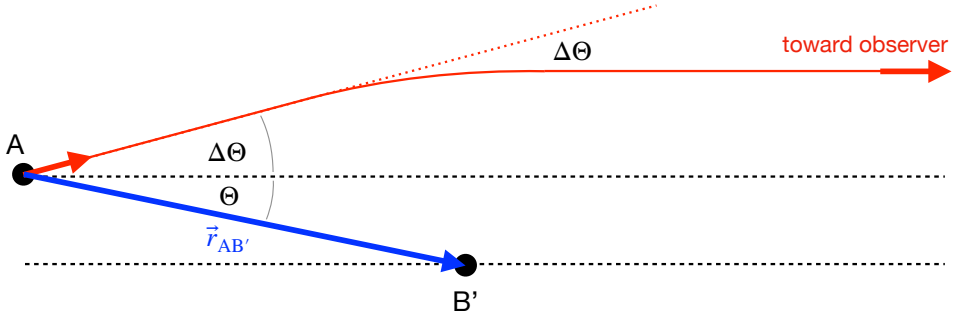

Figure 4.11: Schematic picture of the lensing geometry as used in Section 4.5.4. B' denotes the retardation corrected position of B (cf. Klioner & Kopeikin 1992; Kopeikin & Schäfer 1999). In principle there is a second photon path towards the observer (below B'). However, for the Double Pulsar, this signal is not only significantly weaker, but the path also comes so close to pulsar B that the photons are absorbed by the plasma-filled magnetosphere of B (cf. Lai & Rafikov 2005; Rafikov & Lai 2006b).

This is the maximum value $\Delta\Theta$ can assume. The distance $D_{\rm d}$ in Wucknitz (2008) corresponds to $|\vec{r}_{AB'}|$.[13] Consequently, one obtains

$$\Delta\Theta \sin(\Theta + \Delta\Theta) - \frac{\alpha_{\rm E}^2}{2}\left[1 + \cos(\Theta + \Delta\Theta)\right] = 0\,. \tag{4.23}$$

Since $\Delta\Theta \leq \alpha_{\rm E} \ll 1$ for all angles of Θ, we can expand the equation above in $\Delta\Theta$ while keeping terms only up to order $\alpha_{\rm E}^2$. This leads to a quadratic equation:

$$\Delta\Theta^2 + \Delta\Theta\, \sin\Theta - \frac{\alpha_{\rm E}^2}{2}(1 + \cos\Theta) \simeq 0\,, \tag{4.24}$$

which has, under the assumptions made, one solution:

$$\Delta\Theta \simeq \frac{1}{2}\left(\sqrt{\sin^2\Theta + 2\alpha_{\rm E}^2(1+\cos\Theta)} - \sin\Theta\right)\,. \tag{4.25}$$

For $\Theta \ll 1$ this agrees with the standard lensing equation (see e.g. Schneider et al. 1992).

The angle $\Theta \in [0, \pi]$ needs to be computed from the retardation-corrected orbital phase via $\cos\Theta = \sin i \sin(\psi + \delta\psi^{\rm ret})$. The longitudinal and latitudinal deflection delay are given by

$$\delta_{\rm A}^{\rm londef} = \frac{\Delta\Theta}{2\pi\nu}\,\frac{\cos(\psi + \delta\psi^{\rm ret})}{\sin\Theta \sin i}\,, \tag{4.26}$$

$$\delta_{\rm A}^{\rm latdef} = -\frac{\Delta\Theta}{2\pi\nu}\,\frac{\sin(\psi + \delta\psi^{\rm ret})}{\sin\Theta \tan i \tan\chi_0}\,, \tag{4.27}$$

respectively (cf. Eqs. (10) and (24) in Rafikov & Lai (2006b), with $\zeta = \pi - i$ and $\eta = -\pi/2$ spin of A aligned with orbital angular momentum). If Θ is much larger than $\alpha_{\rm E}$, one has $\Delta\Theta \simeq \alpha_{\rm E}^2(1+\cos\Theta)/(2\sin\Theta)$. This corresponds to the approximation of Doroshenko & Kopeikin (1995) for the deflection angle, and one recovers Eqs. (4.8) and (4.21).

[13] We note that the $D_{\rm d}$ in Eq. (24) of Wucknitz (2008) is a typo and should not be there since it is already part of the definition of m.

4.6 Discussion

In this paper, we have presented results from 3-yr timing observations of the Double Pulsar using the MeerKAT telescope, with a specific focus on studying higher-order signal propagation effects in the gravitational field of the companion. In order to minimise the effects from profile evolution and DM variation, we used frequency-dependent 2D templates to generate TOAs and a DM model to correct dispersive delay in TOAs.

Thanks to its high inclination and orbital compactness, the Double Pulsar is a unique pulsar system for testing NLO signal propagation effects in strong fields. The significantly increased precision offered by MeerKAT permits an independent verification of NLO signal propagation effects and has already surpassed the 16-yr result with only ∼3 yr of data. In our analysis, the Shapiro shape parameter s has been improved by a factor of two compared to the previous result (Kramer et al., 2021a), which also leads to a better mass measurement. The Shapiro range parameter r agrees with GR at 5.3×10^{-3} (95% confidence). The precision of the measurement of NLO signal propagation effects $q_{\rm NLO}$ has been improved by a factor of 1.65. In this work, we investigated the potential profile variation due to latitudinal deflection delay and the possibility of measuring lensing correction to the Shapiro delay, which has never been studied in detail before in pulsar analysis. With the current MeerKAT data, we found little evidence of profile variation at superior conjunction. It could be that the profile variation is not significant at the region we are looking at, or our current data are not sensitive enough to identify it. We also performed simulations on latitudinal deflection delay based on a simple emission model and found it unlikely to be detected because of its correlation with Shapiro delay. As for the lensing correction $\delta\Lambda_u^{\rm len}$, we found it can be mostly absorbed by the Shapiro shape parameter. Our simulation showed that lensing is unlikely to be measured separately from timing before the full SKA or similarly powerful instruments, and may then be measurable with a few years of timing observations if noises such as phase jitter and scintillation do not limit our precision.

However, our analysis also showed that adding certain epochs has a significant impact on the measured Shapiro parameters, but not on $q_{\rm NLO}$. This could be due to the fact that the phase predicted using the `polyco` scheme is particularly worse at the superior conjunction, which caused the discrepancies in the Shapiro parameters. Comparison of `polyco` with different TSPAN values showed residuals oscillating near the superior conjunction, and we may already be limited by the precision of `polyco` scheme. Of course, there may exist other unknown systematic errors in the data.

To support our timing analysis and study of profile variations at eclipse due to latitudinal deflection, we also checked profiles from all observations. We found variations in the total profile from epoch to epoch. The differences in the profiles are more prominent at lower frequencies and broadband. Our simulation suggested that these profile variations are likely to be associated with DM variation and scintillation. Even though we have sub-banded data into 16/32 frequency bands and used 2D templates, profile variations may still have an impact on timing. The study of profile variations will be continued in a subsequent work to improve the constraint on the geometry of the system.

Moreover, although not discussed in this paper, we found evidence of red noise in the spectrum of timing residuals with an amplitude two orders of magnitude larger than for typical millisecond pulsars. If not taken into account, it may strongly affect astrometric parameters, as well as influence binary parameters, according to our simulations. This makes it more difficult to combine the 3-yr MeerKAT data set and the 16-yr data set. Given that the timing precision of the former significantly outperforms the latter, the weighting of MeerKAT data already exceeds the 16-yr data and can dominate noise modelling. For the purpose of this paper, we did not include 16-yr data because of their minor contribution to the $q_{\rm NLO}$ measurement (∼10% improvement). However, for studying secular relativistic effects, an appropriate noise modelling may be required to combine these data. We will investigate this in further

Table 4.4: Comparison of the MeerKAT timing precision $\sigma_{\rm RMS}$ assumed in Hu et al. (2020) and from real observations with L-band and UHF-band receivers, scaled to a 5-min integration time over the full bandwidth.

Telescope / receiver	Reference	$\sigma_{\rm RMS}$ (μs)
MeerKAT L band	Hu et al. (2020)	1.06
MeerKAT L band	this work	0.90
MeerKAT UHF band	this work	0.55

ongoing studies.

In the future, continuing observations with MeerKAT and the SKA will further improve the precision of tests on signal propagation effects, and a 50-σ detection of $q_{\rm NLO}$ can be expected by 2030. For that, we have also provided an improved analytical description of the signal propagation in the Double Pulsar. Furthermore, as demonstrated by Hu et al. (2020), the precision of secular relativistic effects will also be greatly improved and will eventually enable the measurement of the MOI of pulsar A and the NLO gravitational wave damping in the near future. The timing precision of the MeerKAT data used in this work is even better than that assumed in Hu et al. (2020), which is based on early L-band data from MeerKAT (see Table 4.4). This makes their predictions conservative and we are likely to achieve even better measurements with future observations.

Acknowledgements

We acknowledge Kuo Liu for helpful discussions on data processing and analysis, and Olaf Wucknitz for carefully reading the manuscript and discussions on gravitational lensing which were particularly helpful in Section 4.5.4. The MeerKAT telescope is operated by the South African Radio Astronomy Observatory, which is a facility of the National Research Foundation, an agency of the Department of Science and Innovation. MeerTime data is housed on the OzSTAR supercomputer at Swinburne University of Technology. HH is a member of the International Max Planck Research School for Astronomy and Astrophysics at the Universities of Bonn and Cologne. This work is supported by the Max-Planck Society as part of the "LEGACY" collaboration with the Chinese Academy of Sciences on low-frequency gravitational wave astronomy. Pulsar research at UBC is supported by an NSERC Discovery Grant and by the Canadian Institute for Advanced Research. Part of this work has been funded using resources from the research grant "iPeska" (P.I. Andrea Possenti) funded under the INAF national call Prin-SKA/CTA approved with the Presidential Decree 70/2016.

CHAPTER 5

Application of a new timing model for testing Damour–Esposito-Farèse gravity

Parts of the work presented in this chapter are included in the following publication:

- A. Batrakov, **H. Hu**, N. Wex, P. C. C. Freire, V. Venkatraman Krishnan, M. Kramer, Y. J. Guo, L. Guillemot, J. W. McKee, I. Cognard, and G. Theureau, A new pulsar timing model for scalar-tensor gravity: with applications to PSR J2222−0137 and pulsar-black hole binaries, *Astronomy & Astrophysics*, 2023, DOI: 10.1051/0004-6361/202245246

As the second author of this paper, I am responsible for simulating the timing data for PSR J2222−0137 and pulsar-black hole systems as applications of the newly developed timing model for scalar-tensor gravity. I wrote Sections 5.1, 5.2 and 6.1 of this paper and provided discussions and edits as important contributions to the paper. In this chapter, I will briefly introduce the necessary background for this new timing model and present my simulation work (including details that are not in the paper), and discuss results based on these simulations. More details can be found in the above paper, which is included at the end of the dissertation.

5.1 Introduction

Einstein's general relativity (GR) is a geometrical theory of gravity, building upon a rank-2 tensor field, the metric of the spacetime. To date, predictions by GR has been successfully tested in various experiments, in and beyond the Solar System (Will, 2014). Presently it is regarded as the standard theory of gravitation. Despite the broadly acknowledged success of GR, many alternative theories have been proposed which predict deviations from GR that can not be tested in the weak-field regime of gravity. Among these, the scalar-tensor gravity (STG) theories are probably the best studied alternatives to GR. Like GR, the STG theories are metric theories of gravity, but have additional fields, for instance a scalar field φ. A theory that for many years was seen as the only natural competitor of GR is Jordan-Fierz-Brans-Dicke (JFBD) gravity (Jordan, 1955; Fierz, 1956; Jordan, 1959; Brans & Dicke, 1961). This theory contains one free parameter, the Brans-Dicke parameter $\omega_{\rm BD}$, which is tightly constrained by timing observations of a pulsar in a triple star system (Archibald et al., 2018; Voisin et al., 2020). For the scope of this work, we focus on the mono-scalar-tensor theory $T_1(\alpha_0, \beta_0)$ of Damour–Esposito-Farèse (DEF) gravity (Damour & Esposito-Farèse, 1992; Damour & Esposito-Farèse, 1993; Damour & Esposito-Farèse, 1996). Besides the spacetime metric, it contains a massless scalar field φ with the asymptotic value φ_0 at spatial infinity. The theory parameters α_0 and β_0 define the two-dimensional space of DEF gravity. GR corresponds to the case where $\alpha_0 = \beta_0 = 0$, and JFBD gravity corresponds to the case that $\beta_0 = 0$ and

$\alpha_0^2 = (2\omega_{\rm BD} + 3)^{-1}$. Note that for all β_0, α_0 is well constrained by the Solar System experiments with Cassini Spacecraft: $|\alpha_0| \lesssim 0.003$ (Bertotti et al., 2003). The so-called "gravitational form factors" of a body i with mass m_i and moment of inertia I_i that enter the PK parameters in DEF gravity are

$$\alpha_i \equiv \left.\frac{\partial \ln m_i}{\partial \varphi_0}\right|_{\bar{m}_i}, \quad \beta_i \equiv \left.\frac{\partial \alpha_i}{\partial \varphi_0}\right|_{\bar{m}_i}, \quad k_i \equiv -\left.\frac{\partial \ln I_i}{\partial \varphi_0}\right|_{\bar{m}_i}, \tag{5.1}$$

where the baryonic mass $\bar{m}_i$ is kept fixed when taking the partial derivatives. The parameter α_i describes the effective coupling strength of the body to the scalar field, and the parameter β_i describes the derivative of the effective coupling strength in the scalar field. The last parameter k_i describes the field dependence of I_i. For a weakly self-gravitating body, such as a white dwarf (WD), the gravitational form factors can be approximated by their weak-field expressions:

$$\alpha_{\rm WD} \simeq \alpha_0, \quad \beta_{\rm WD} \simeq \beta_0, \quad k_{\rm WD} \simeq 0\,. \tag{5.2}$$

In the case of a neutron star (NS), if its mass exceeds the critical mass, the effective scalar coupling can reach the order unity ($\alpha_{\rm NS} \simeq O(1)$) due to spontaneous scalarization, even if $|\alpha_0| << 1$. The critical mass depends on β_0 and the equation of state (EOS) of dense matter. For black holes (BHs), they are not scalarized in DEF gravity as a consequence of the "no-hair" theorem (Hawking, 1972; Damour & Esposito-Farèse, 1992), therefore

$$\alpha_{\rm BH} = 0, \quad \beta_{\rm BH} = 0, \quad k_{\rm BH} = 0\,. \tag{5.3}$$

5.2 Dipolar gravitational wave damping

Neutron stars and white dwarfs are quite different in terms of compactness. This asymmetry in compactness makes PSR-WD systems ideal laboratories for testing gravity theories that violate the strong equivalence principle (Will, 2014; Wex, 2014; Wex & Kramer, 2020). A common consequence of such alternative theories is the emission of dipolar gravitational waves (GWs). Unlike in GR, the leading contributions in the loss of orbital energy due to GWs are not from quadrupolar radiation but from dipolar radiation, which enters the equation of motion already at the 1.5 post-Newtonian (PN) level (i.e. order v^3/c^3). The observed orbital period derivative consists of many contributions, here we consider

$$\dot{P}_{\rm b}^{\rm obs} = \dot{P}_{\rm b}^{\rm GR} + \dot{P}_{\rm b}^{\rm D} + \dot{P}_{\rm b}^{\rm Gal} + \dot{P}_{\rm b}^{\rm Shk}\,. \tag{5.4}$$

The term $\dot{P}_{\rm b}^{\rm GR}$ denotes the contribution due to GW damping predicted by GR, which to leading order enters the equation of motion at the 2.5PN level (i.e. quadrupolar GWs) and is given by Eq. (2.24). In specific cases, one may need to consider other intrinsic contributions, such as the spin-down mass loss of pulsar or companion (e.g. in the Double Pulsar, see discussions in Section 3.4.3), the next-to-leading-order GW damping (3.5PN, see Section 3.4.1), tidal effects, and a possible temporal variation of the gravitational constant G. Besides, one also needs to consider external contributions due to the relative motion between pulsar binary barycentre and the Solar System barycentre, i.e., Galactic differential acceleration $\dot{P}_{\rm b}^{\rm Gal}$ and Shklovskii effect $\dot{P}_{\rm b}^{\rm Shk}$. Calculations of these kinematic contributions can be found in Section 3.4.2. For DEF gravity, one finds the contribution of the dipolar radiation follows (Damour & Esposito-Farèse, 1992)

$$\dot{P}_{\rm b}^{\rm D} = -2\pi n_{\rm b} \frac{G_*}{c^3} \frac{m_{\rm p} m_{\rm c}}{m_{\rm p} + m_{\rm c}} \frac{1 + e_{\rm T}^2/2}{(1 - e_{\rm T}^2)^{5/2}} (\alpha_{\rm p} - \alpha_{\rm c})^2 + O(v^5/c^5)\,, \tag{5.5}$$

where $n_b = 2\pi/P_b$ is the orbital frequency, c is the speed of light in vacuum, and e_T is the time eccentricity used as the eccentricity parameter in the Damour-Deruelle (DD) timing model (Damour & Deruelle, 1986). m_p and m_c are the masses of the pulsar and the companion. G_* is the bare gravitational coupling constant and is related to the Newtonian gravitational constant G (as measured by a Cavendish-type experiment) via $G = G_*(1 + \alpha_0^2)$. α_p and α_c are the effective scalar couplings of the pulsar and the companion, respectively. One can see that $\dot{P}_b^D$ depends strongly on the difference in the effective scalar coupling of two bodies, i.e. $\alpha_p - \alpha_c$. In addition to the dipole contribution, there are also monopole and quadrupole contributions related to the scalar field that enter at 2.5PN level $O(v^5/c^5)$. Usually these contributions are negligible even when compared to the GR contribution $\dot{P}_b^{GR}$. Their expressions can be found in Damour & Esposito-Farèse (1992).

In order to test dipolar GWs, one needs to measure other contributions in Eq. (5.4) with a good precision, as

$$\dot{P}_b^D = \dot{P}_b^{obs} - \dot{P}_b^{GR} - \dot{P}_b^{Gal} - \dot{P}_b^{Shk} . \tag{5.6}$$

The GR contribution $\dot{P}_b^{GR}$ can be calculated using mass measurements and orbital parameters measured from timing. To account for kinematic contributions $\dot{P}_b^{Gal}$ and $\dot{P}_b^{Shk}$, good knowledge of Galactic gravitational potential and distance and proper motion of the pulsar are required.

5.3 DDSTG: a new pulsar timing model for scalar-tensor gravity

In Batrakov et al. (2023), a new timing model "DDSTG" has been developed as a direct extension of the DDGR model (Taylor & Weisberg 1989, see also Section 4.4.2) for STG theories. It has been implemented into an independent version of the standard timing software TEMPO (D. Nice et al., 2015). With the DDSTG model, four new parameters need to be provided in the ephemeris file: the theory parameters $\{\alpha_0, \beta_0\}$, the EOS ID (e.g. MPA1), and the type of the companion {NS, WD, BH}.[1] The DD model fits for all PK parameters and could suffer strong correlations between parameters. In contrast, the DDSTG model works in a similar way to the DDGR model: it fits directly for the total mass of the system m_{tot} and the companion mass m_c from timing data and calculates the five PK parameters for an assumed theory based on these masses, which then breaks the correlation between PK parameters. With the measured masses, TEMPO reads the gravitational form factors $\{\alpha_i, \beta_i, k_i\}$ for the selected EOS from pre-calculated 3D grids. As it is computationally expensive to calculate the neutron star structure for a given mass on the fly, 3D grids of gravitational form factors have been pre-calculated for eleven EOSs that are not ruled out by the maximum mass of neutron stars, i.e. $M_{max} > 2M_\odot$. Once $\{\alpha_i, \beta_i, k_i\}$ are known, the model computes PK parameters according to their expressions in DEF gravity (see Damour & Esposito-Farèse, 1992; Damour & Esposito-Farèse, 1996). Details of the DDSTG model are explained in Batrakov et al. (2023).

Binary pulsars with high asymmetry in compactness, such as PSR-WD systems and PSR-BH systems, are particularly interesting for constraining STG theories, as these systems are expected to lose orbital energy at a much higher rate due to dipolar GW emission (Will, 1993; Damour & Esposito-Farèse, 1996; Damour & Esposito-Farèse, 1998). As a demonstration of the DDSTG model, we apply this model to existing and simulated data of the PSR-WD system J2222−0137 in Section 5.4 and to the simulated data of hypothetical PSR-BH systems in Section 5.5. In all these studies, we assume the stiff EOS MPA1 (Müther et al., 1987) for the pulsar, which allows a maximum neutron star mass of 2.461 $M_\odot$. Such a stiff EOS generally yields more conservative limits in most parts of DEF gravity parameter space (see

[1] Note, "WD" can be selected for any weakly self-gravitating body, hence also including a non-degenerate companion such as a main-sequence star.

Table 5.1: Effective diameter of telescopes $\varnothing_{\rm eff}$, observing bandwidth, and TOA uncertainty $\sigma_{\rm TOA}$ of PSR J2222−0137 used in the simulations. All information are based on the L-band data from real observations, and are scaled to 15-min integration time over the full bandwidth.

Telescope	$\varnothing_{\rm eff}$ (m)	Bandwidth (MHz)	$\sigma_{\rm TOA}$ (μs)
Effelsberg	100	200/400	2.67
Nançay	94	512	2.02
Lovell	76	400	3.66
MeerKAT	108	856	0.84
FAST	300	500	0.12

however Shibata et al. 2014; Shao et al. 2017; Zhao et al. 2022).

5.4 Application to PSR J2222−0137, a pulsar-white dwarf binary

PSR J2222−0137 is a 32.8 ms pulsar discovered in the Green Bank Telescope (GBT) 350 MHz drift-scan pulsar survey (Boyles et al., 2013). The pulsar is accompanied by a heavy WD with mass $m_{\rm c} = 1.319(4)\mathrm{M}_\odot$, forming a binary system with an orbital period of 2.4 days (Guo et al., 2021). The pulsar has an intermediate mass of $m_{\rm p} = 1.831(10)\mathrm{M}_\odot$ (Guo et al., 2021), which helps to constrain spontaneous scalarization of DEF gravity, yielding strong limits on this highly non-linear phenomenon (Shao et al., 2017; Zhao et al., 2022). The asymmetry in its compactness makes it a useful tool to constrain dipolar GWs which are predicted in DEF gravity. As one of the closest pulsars known, it has an excellent timing precision with a distance well measured by VLBI (see Deller et al. 2013). A significant Shapiro delay and the rate of periastron advance $\dot{\omega}$ has been detected in this system, which yields precise mass measurements and $\sim 1\%$ test of GR for the Shapiro delay (Guo et al., 2021). Because of these properties, PSR J2222−0137 allows a robust test of dipolar GWs.

Since 2012, PSR J2222−0137 has been regularly observed with the three largest European Radio Telescopes: the 100-m Effelsberg radio telescope (EFF), 94-m Nançay Radio Telescope (NRT), and 76-m Lovell telescope (LT). For convenience, we refer to the combination of these telescopes as "3ERT". Based on the GBT and 3ERT follow-up data from 2009 to 2021, Guo et al. (2021) obtained a precise measurement of the orbital period derivative $\dot{P}_{\rm b}$. After accounting for contributions from GR and kinematic effects, Guo et al. (2021) found an upper limit $|\alpha_{\rm p} - \alpha_{\rm c}| < 0.005$ (95% C.L.).

In addition, PSR J2222−0137 has been observed with the MeerKAT telescope since September 2019 (Kramer et al., 2021b) and with the Five-hundred-meter Aperture Spherical radio Telescope (FAST) since October 2020. The timing precision of PSR J2222−0137 is much improved with these telescopes. To estimate how the timing parameters of this system will improve in the near future, in the next section we simulate realistic timing data, i.e. the time of arrivals (TOAs), based on the timing properties of these telescopes.

5.4.1 Simulation for "3ERT", MeerKAT, and FAST

We simulate TOAs for PSR J2222−0137 spanning 10 years from 2021 to 2030 based on the TOA precision obtained with 3ERT (EFF+NRT+LT), FAST and MeerKAT, where we take the median TOA uncertainties ($\sigma_{\rm TOA}$) from Effelsberg, Nançay, and Lovell data sets (Guo et al., 2021) as well as the ongoing observations from MeerKAT and FAST. These simulations are conservative since they assume no improvement in the existing capabilities of these telescopes.

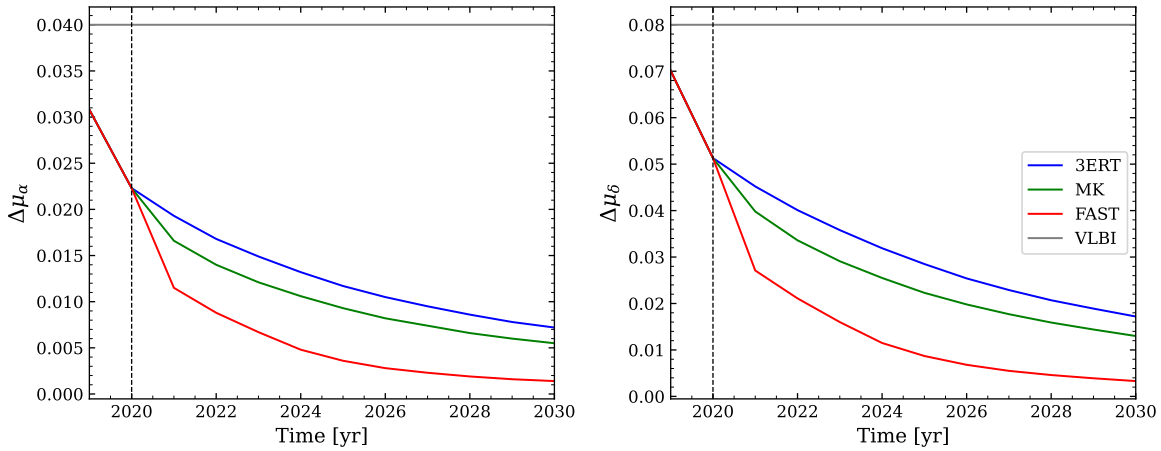

Figure 5.1: Predicted uncertainties of proper motion in right ascension (left) and declination (right) with simulated data from 3ERT (blue), MeerKAT (MK, green), and FAST (red) in combination with the existing data. The grey line indicates the measurement from VLBI observations (Deller et al., 2013) and the vertical dashed line indicates the start of simulations.

For TOAs from FAST, the radiometer noise reduces significantly thanks to its large collecting area, while the jitter noise becomes a limitation of timing precision. We find, however, that increasing the integrating time to 15 min can largely reduce the jitter noise and eliminate its contribution to the timing precision, as it scales with the number of averaged pulses N_p as $\sigma_{\rm J} \propto 1/\sqrt{N_p}$ (Lorimer & Kramer, 2004). Therefore, the median TOA uncertainty from 15-min TOAs is adopted in the simulation.

Table 5.1 lists the telescopes assumed in our simulation, with the information on their effective diameter $\varnothing_{\rm eff}$, observing bandwidth, and TOA uncertainties at L-band. All TOA uncertainties are scaled to an integration time of 15 min over the full bandwidth. For each telescope, we assume a full orbit observation (~60 h) per year, and split the observation into monthly cadence, i.e. 5 h per month,[2] to allow a good estimation of the timing parallax (which requires a good coverage of the Earth's orbit). This is important for the estimation of the uncertainties in the external $\dot{P}_{\rm b}$ contributions, which is discussed in the next section.

The simulation is performed using the program developed in Hu et al. (2020). First, we simulate TOAs based on the above assumptions, and add the TOAs from Effelsberg, Nançay, and Lovell telescopes together as "3ERT" to be compared with MeerKAT and FAST. For each group, the simulated TOAs are combined with the existing TOAs in Guo et al. (2021). Then we adjust the TOAs to perfectly match with the parameters published in Guo et al. (2021), and add a Gaussian white noise to each TOA based on its $\sigma_{\rm TOA}$. Finally, we fit for the timing parameters and obtain their uncertainties, among which $\dot{P}_{\rm b}$ and timing parallax are of most important here. The whole process is done with the DDSTG model, with the DD model as a comparison.

5.4.2 Contributions in the change of orbital period $\dot{P}_{\rm b}$

The predicted uncertainties of the observed $\dot{P}_{\rm b}$ with time are shown in Figure 5.3, where the blue, green and red lines denote the results based on the simulated data from 3ERT, MeerKAT and FAST, respectively. As discussed in Section 5.2, we also need to account for external effects caused by Galactic acceleration

[2] This may be unrealistic as telescopes may be oversubscribed. However, we found, e.g. for FAST, that with a more realistic assumption of 30 minutes per month, the uncertainty in the observed $\dot{P}_{\rm b}$ is only 5% worse than observing 5 hours per month after 10-yr timing.

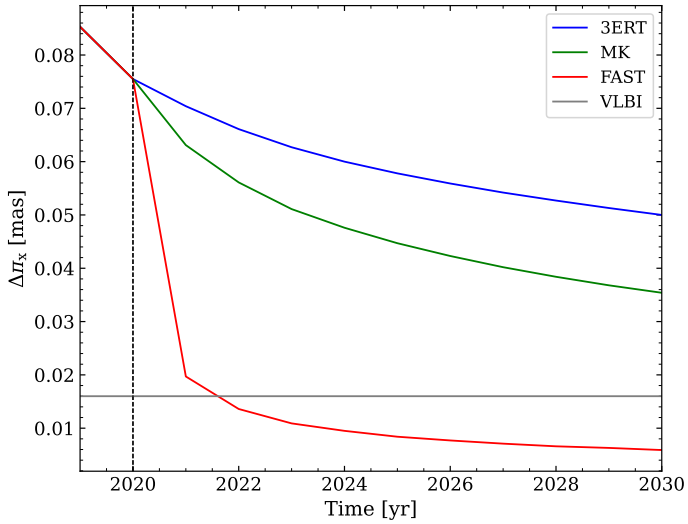

Figure 5.2: Same as Figure 5.1 but for timing parallax π_x. The simulated FAST data in combination with existing data is expected to yield a better measurement than the VLBI parallax (Deller et al., 2013) from 2022 onwards.

and Shklovskii effect: $\dot{P}_{\rm b}^{\rm ext} = \dot{P}_{\rm b}^{\rm Gal} + \dot{P}_{\rm b}^{\rm Shk}$. The uncertainties of these effects depend on our knowledge of the Galactic gravitational potential and the measurement errors in the proper motion and distance of the pulsar, which are expected to become more precise in the future with observations. For proper motion and distance of the pulsar d, we can estimate their future uncertainties from timing with our simulations. The results are shown in Figure 5.1 for the proper motion of the pulsar in right ascension μ_α (left panel) and declination μ_δ (right panel), and in Figure 5.2 for timing parallax $\pi_x({\rm mas}) = 1/d({\rm kpc})$. With the simulated FAST data, the uncertainty of the timing parallax is expected to be smaller than that of the VLBI parallax measurement (Deller et al., 2013) from 2022.

For the Shklovskii effect, the current proper motion measurements are already very precise, and its uncertainty is dominated by the uncertainty in the distance, which comes from VLBI parallax or timing parallax measurement, whichever is smaller. With the predicted timing parallax measurement with FAST, the uncertainty of $\dot{P}_{\rm b}^{\rm Shk}$ will decrease quickly with time as indicated by the brown line in Figure 5.3. Compared to the predicted uncertainty of the observed $\dot{P}_{\rm b}$ with FAST (red line), $\Delta\dot{P}_{\rm b}^{\rm Shk}$ is always smaller except when approaching 2030. Since future VLBI parallax measurements are also expected to be improved, the uncertainty in the Shklovskii effect will likely not be a limiting factor for $\dot{P}_{\rm b}$.

As for the contribution from Galactic acceleration, a typical uncertainty in its vertical component (ΔK_z) is about 10% (Holmberg & Flynn, 2004; L. Zhang et al., 2013), which contributes the most in the uncertainty of $\dot{P}_{\rm b}^{\rm Gal}$ and shown as the cyan dashed line in Figure 5.3. With FAST, $\dot{P}_{\rm b}$ will then be limited by ΔK_z from 2024 onwards, if there is no improvement for this quantity. We find that ΔK_z needs to be improved to $\lesssim 3\%$ to not limit the precision of $\dot{P}_{\rm b}$ before 2030. The orange and magenta dashed lines indicate the cases for $\Delta K_z = 3\%$ and $\Delta K_z = 1\%$, respectively. This may be possible with *Gaia* (Gaia Collaboration, 2016) in the near future.

With Eq. (5.6), one could obtain a limit on the leading-order contribution from dipolar GWs shown in Eq. (5.5), and consequently an upper limit for $|\alpha_{\rm p} - \alpha_{\rm c}|$. Figure 5.4 shows the upper limit of $|\alpha_{\rm p} - \alpha_{\rm c}|$ expected from FAST observations with $\Delta K_z = 10\%, 3\%, 1\%$. For these three cases, the upper limits are expected to be 0.0020, 0.0015 and 0.0014 (95% C.L) in 2030, which are more than 2.5 times better than the current limit from PSR J2222−0137 (Guo et al., 2021) and will likely surpass the current best limit from PSR J1738+0333, i.e., $|\alpha_{\rm p} - \alpha_{\rm c}| < 2 \times 10^{-3}$ (95% C.L.) (Antoniadis et al., 2012).

For the scope of this work, we assume that with future timing and VLBI observations and measurements

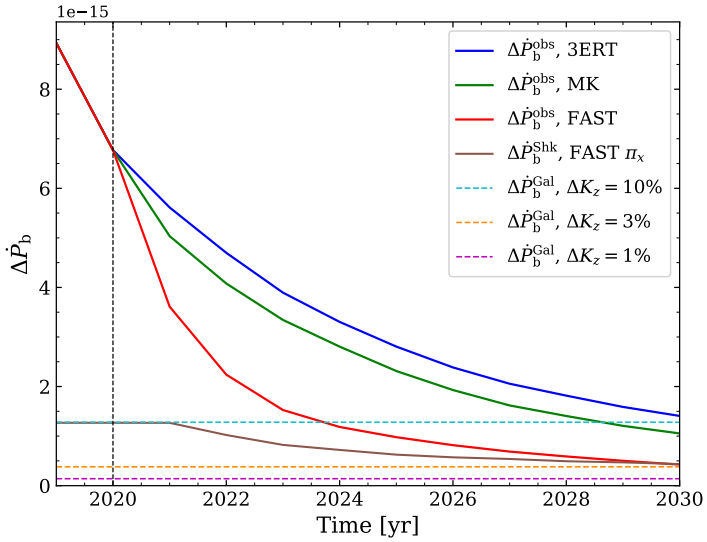

Figure 5.3: Comparison of contributions in the uncertainty of $\dot{P}_b$ measurement for simulated data from 2021 to 2030. The blue, green and red lines denote the uncertainty of $\dot{P}_b^{obs}$ with simulated data from 3ERT, MeerKAT (MK) and FAST, respectively. The brown line indicates the uncertainty of $\dot{P}_b^{Shk}$ when using the timing parallax measured from simulated FAST data. The horizontal dashed lines indicate the uncertainties of $\dot{P}_b^{Gal}$ when assuming 10% (cyan), 3% (orange) and 1% (pink) uncertainties in the vertical component of the Galactic acceleration K_z.

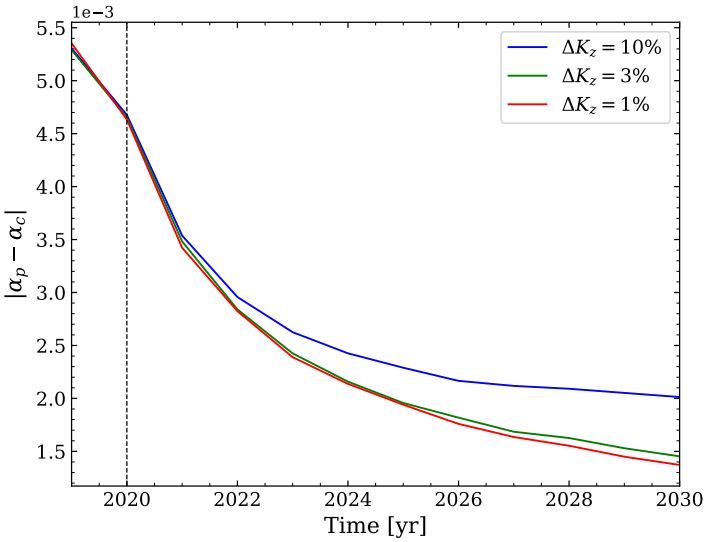

Figure 5.4: Upper limit of $|\alpha_p - \alpha_c|$ (95% C.L.) as a function of time with simulated FAST data. The blue, green and red lines indicate the cases when $\Delta K_z = 10\%, 3\%, 1\%$, respectively.

of the Galactic acceleration (especially the vertical component), the precision of $\dot{P}_b$ will not be limited by external effects, hence we use the observed uncertainty as the uncertainty for the intrinsic $\dot{P}_b$.

5.4.3 Potential future constraints from PSR J2222−0137

To constrain the DEF gravity parameters $\{\alpha_0, \beta_0\}$ with the DDSTG model, we run TEMPO for every selected pair of $\{\alpha_0, \beta_0\}$ in a 2D grid and obtain the χ^2 value of the fit. To compare these χ^2, we subtract the minimum value χ^2_{min} from them, which results in a quantity $\Delta\chi^2 = \chi^2 - \chi^2_{min}$. Then, a $\Delta\chi^2$ map can

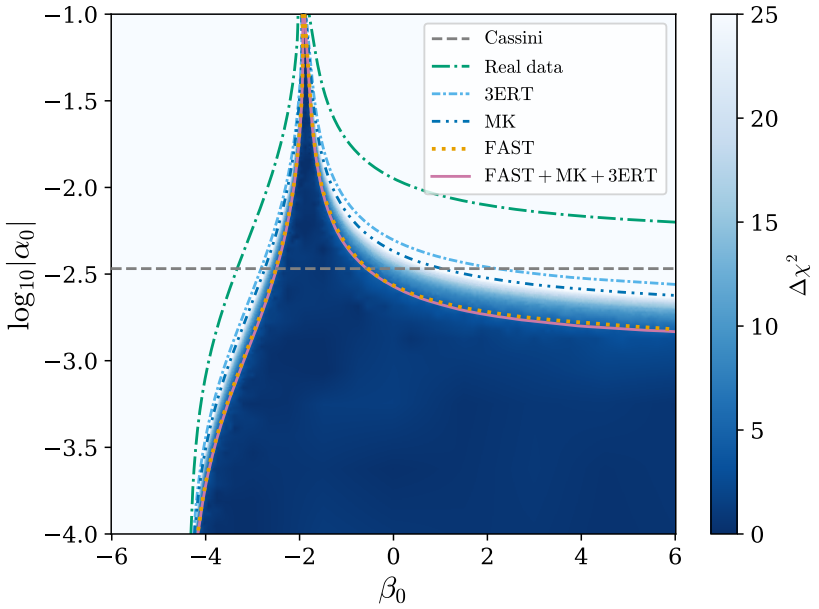

Figure 5.5: Predicted limits on DEF gravity parameters (90% C.L.) for PSR J2222−0137 with simulated data (2021–2030) from different telescopes. The curves indicate the upper limit obtained with 3ERT (light blue), MeerKAT (MK, dark blue), FAST (orange), and the combination of three (pink) with its $\Delta\chi^2$ map shown in blue. The limit from FAST alone is almost as good as the combination of FAST, MeerKAT, and 3ERT. The green curve denotes the limit from the existing data set (Guo et al., 2021) and the grey dashed line indicates the limit from the Cassini mission (Bertotti et al., 2003). The EOS MPA1 is assumed. Figure 6 in Batrakov et al. (2023).

be plotted over the $\{\alpha_0, \beta_0\}$ space to display the constraint for a desired confidence level.

Following this technique, we run the DDSTG timing model on the simulated PSR J2222−0137 data for a grid of $\{\alpha_0, \beta_0\}$. During each run, TEMPO fits for spin parameters, astrometric parameters, Keplerian parameters, and masses $m_{\rm tot}$ and $m_{\rm c}$. The external contributions to the change of orbital period $\dot{P}_{\rm b}^{\rm ext}$ is held fixed since, as explained above, its error is negligible. Figure 5.5 shows the $\Delta\chi^2$ map for the combination of 3ERT, MeerKAT and FAST data, where the pink curve is the contour of 90% C.L. limit on the DEF gravity parameters ($\Delta\chi^2 \simeq 4.6$) and the area below is allowed. Compared to the current limit (green curve) based on data from Guo et al. (2021), the limits expected in 2030 are much improved with simulated data from 3ERT (light blue), MeerKAT (dark blue), and in particular, FAST (orange). A significant improvement is expected for large positive β_0, where it is sensitive to dipolar GW emission. While the tightest constraints can be obtained by combining all three observatories (FAST+MeerKAT+3ERT), the high accuracy of FAST is sufficient to place a significant constraint by itself.

5.5 Application to pulsar-black hole systems

Compared to PSR-WD binaries, systems composed of a pulsar and a stellar-mass black hole can be even more asymmetric in terms of effective scalar coupling α_i (Damour & Esposito-Farèse, 1998) because of the "no-hair" theorem for black holes. If discovered, such systems would bring tremendous advances to black hole physics and strong-field gravity tests. It will not only complement the tests using binary black holes with GWs observed by LIGO/Virgo (B. P. Abbott et al., 2016b) or the probes of spacetime of supermassive black holes using interferometric imaging (Event Horizon Telescope Collaboration et al., 2019; Event Horizon Telescope Collaboration et al., 2022), but it can also provide a novel way to

Table 5.2: Properties of pulsar-black hole systems assumed in the simulation.

Parameters	Values
Right ascension (R.A.), α (J2000)	21:20:01.2
Declination (Dec.), δ (J2000)	12:10:38.2
Dispersion measure, DM (pc cm^{-3})	67.1
Pulsar mass, $m_{\rm p}$ ($M_\odot$)	1.4
BH mass, $m_{\rm BH}$ ($M_\odot$)	10.0
Eccentricity, $e_{\rm T}$	0.6
Orbital period, $P_{\rm b}$	8 h, 1 d, 3 d
TOA uncertainty, $\sigma_{\rm TOA}$ (μs)	10, 1
Number of TOAs	3144

measure the spin and the quadruple moment of a black hole, by this testing cosmic censorship conjecture and no-hair theorem (Wex & Kopeikin, 1999; Liu et al., 2014a). More relevant for this work, PSR-BH systems are promising to place strong constraints on alternative gravity theories, such as the STG theories (Damour & Esposito-Farèse, 1998; Liu et al., 2014a).

Although not yet discovered, new-generation radio telescopes such as MeerKAT, FAST and the SKA are capable of finding them in the near future (Liu et al., 2014a). Therefore, as a further application of the new timing model, we investigate the potential limits on DEF gravity that may be obtained from PSR-BH systems using simulations.

5.5.1 Simulation for pulsar-black hole systems

In order to simulate TOAs for PSR-BH binaries, we have to assume some characteristics of these systems first. We assume that they are composed of a 1.4 $M_\odot$ pulsar and a 10.0 $M_\odot$ black hole in a highly eccentric orbit ($e = 0.6$). As PSR-BH systems are more likely to reside in globular clusters, we assume them to be located in the globular cluster M15 and take the position (right ascension and declination) and dispersion measure (DM) of PSR B2127+11C (Jacoby et al., 2006) for our simulation. To investigate the effect of orbital period on the capacity of constraining DEF gravity, we consider three cases, with orbital periods of 3 days, 1 day, and 8 hours, respectively. The selected parameters for PSR-BH systems are presented in Table 5.2.

Due to our lack of knowledge about the real observational properties of PSR-BH systems, we simulate data sets with two different TOA uncertainties (for 15-min integration time): a moderate case of 10 μs which is typical for pulsars in globular clusters (with the precision of 3ERT, e.g.), and a precise case of 1 μs which might be possible with FAST. We assume that these systems are observed 6 hours every two weeks and starts from a random orbital phase each time. All simulations cover a time span of 5 years and have the same number of TOAs, i.e. $n_{\rm TOA} = 3144$.

5.5.2 Potential future constraints from PSR-BH systems

For our tests, the external contributions $\dot{P}_{\rm b}^{\rm ext}$ and their uncertainties are not included as we are short of this information. Table 5.3 shows the comparison of $\dot{P}_{\rm b}^{\rm GR}$ and the observed uncertainty $\Delta\dot{P}_{\rm b}^{\rm obs}$ for PSR-BH systems with different orbital periods $P_{\rm b}$ and TOA uncertainties $\sigma_{\rm TOA}$.

By applying the same method discussed in Section 5.4.3, with the DDSTG model, we obtain potential future constraints on DEF gravity parameters from PSR-BH systems, which are shown in Figure 5.6.

Table 5.3: Comparison of $\dot{P}_{\rm b}^{\rm GR}$ and $\Delta\dot{P}_{\rm b}^{\rm obs}$ for PSR-BH systems with three different orbital periods, given in unit of 10^{-12} s s^{-1}.

$P_{\rm b}$	$\dot{P}_{\rm b}^{\rm GR}$	$\Delta\dot{P}_{\rm b}^{\rm obs}$ ($\sigma_{\rm TOA} = 10\,\mu$s)	$\Delta\dot{P}_{\rm b}^{\rm obs}$ ($\sigma_{\rm TOA} = 1\,\mu$s)
3 d	−0.22220	0.08031	0.00827
1 d	−1.38661	0.01723	0.00185
8 h	−8.65279	0.00532	0.00055

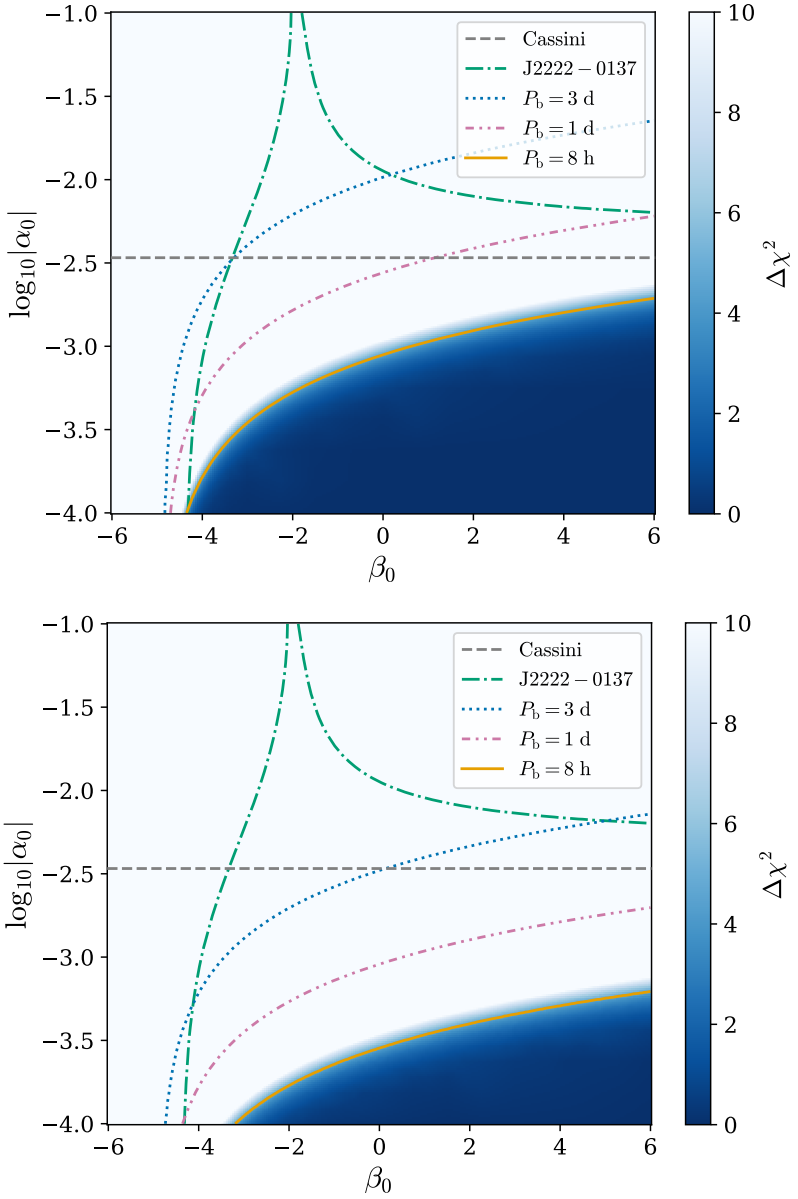

Figure 5.6: Same as Figure 5.5 but for the simulated 5-yr data of PSR-BH systems. The top panel assumes a TOA uncertainty of 10 μs, whereas the bottom panel assumes a more precise case of 1 μs. The blue, pink, and orange lines indicate the 90% C.L. limits obtained from PSR-BH systems with orbital period of 3 days, 1 days, and 8 hours, respectively. The blue area shows the $\Delta\chi^2$ map for the case that $P_{\rm b}$ = 8 h. Figure 7 in Batrakov et al. (2023).

One can see that more relativistic systems, i.e. with shorter orbital periods, provide more stringent limits on DEF gravity as more areas of the parameter space are excluded. For a moderate timing precision of $\sigma_{\rm TOA} = 10\,\mu$s, the orbital period of the PSR-BH system should be a fraction of a day in order to place new limits on DEF gravity (see the top panel of Figure 5.6). By comparing the top ($\sigma_{\rm TOA} = 10\,\mu$s) and bottom ($\sigma_{\rm TOA} = 1\,\mu$s) panels of Figure 5.6, one finds that increasing the precision of TOAs can significantly improve the constraining power on DEF gravity and potentially place the tightest limits.

However, it has been discussed in Batrakov et al. (2023) that the quality of these tests would be degraded if the PSR-BH system is in a globular cluster, as $\dot{P}_{\rm b}$ can be contaminated by a large kinematic contribution due to the acceleration of the system in the gravitational field of the globular cluster $a_{\rm GC}$:

$$\dot{P}_{\rm b}^{\rm GC} = \frac{a_{\rm GC}}{c} P_{\rm b}\,. \tag{5.7}$$

As shown in Table 5.3, for a 8-h PSR-BH system timed with a precision of 10 μs, the significance of the radiative test ($\dot{P}_{\rm b}^{\rm GR}/\Delta\dot{P}_{\rm b}^{\rm obs}$) is more than 1600σ if $\dot{P}_{\rm b}$ is not contaminated. But if the system is at the location of PSR B2127+11C where $|a_{\rm GC}/c| \lesssim 6\times10^{-18}{\rm s}^{-1}$, only a 50-$\sigma$ test of the radiative properties is possible. It becomes even worse if the system is closer to the cluster centre.

5.6 Conclusion

A new timing model "DDSTG" has been developed by Batrakov et al. (2023) for testing STG theories with binary pulsars and has been implemented into an independent version of the pulsar timing software TEMPO. A specific class of STG theories, the DEF gravity, has been studied using this timing model. To fit for parameters with the DDSTG model, one need to provide the theory parameters $\{\alpha_0, \beta_0\}$, the EOS ID of neutron star, and the type of the companion {NS, WD, BH}. As a demonstration of the DDSTG model, we applied it to two scenarios with high asymmetry in effective scalar coupling α_i: the PSR-WD system PSR J2222−0137 and hypothetical PSR-BH systems.

For PSR J2222−0137, the asymmetry in its compactness results in the prediction of a very strong dipolar GW contribution to the orbital period derivative ($\dot{P}_{\rm b}^{\rm D}$) for some areas in the DEF gravity parameter space. The precise distance measurement from VLBI, excellent timing precision, and well measured relativistic effects offered by this system allow a precise constraint on dipolar GWs and hence the DEF gravity parameter space. We applied the DDSTG model to the existing data of PSR J2222−0137 and simulated realistic TOAs from 2021 to 2030 for large telescopes including 3ERT, MeerKAT and FAST based on the precision of real observations. The simulation showed that the timing parallax offered by FAST will soon provide a better distance measurement than the VLBI parallax, so that the uncertainty in the Shklovskii effect would not limit the precision of $\dot{P}_{\rm b}$. The main limiting factor to $\dot{P}_{\rm b}$ comes from the uncertainty in the Galactic acceleration, which mostly originates from the uncertainty in its vertical component ΔK_z. We found that if ΔK_z can be improved to $\lesssim 3\%$, which is likely the case in the near future, in particular with the available *Gaia* data (Gaia Collaboration et al., 2022),[3] then ΔK_z will no longer limit the precision of $\dot{P}_{\rm b}$. Compared to the current limit based on existing data from Guo et al. (2021), the simulations indicated that future observations can significantly improve the constraints on DEF gravity, especially with the observations of FAST.

We then investigated the prospects of constraining DEF gravity with PSR-BH systems, which hopefully will be discovered in the near future from pulsar surveys. We simulated artificial TOAs for eccentric PSR-BH systems with presumed realistic parameters and different orbital periods (3 days, 1 day and 8 hours) for 5 years. Two timing precision were considered: a moderate case of 10 μs that are typical

[3] https://www.cosmos.esa.int/web/gaia/data

for pulsars in globular clusters, and a precise case of 1 μs that may be possible with FAST. PSR-BH systems with smaller orbital periods and better timing precision can place the most stringent limits for a large part of the DEF gravity parameter space. However, depending on the location, it may be challenging to obtain a precise constraint for the dipolar GW contribution $\dot{P}_{\rm b}^{\rm D}$. For example, if such a system resides in a globular cluster, $\dot{P}_{\rm b}$ is likely to be contaminated by a large kinematic contribution due to the acceleration of the system in the gravitational field of the globular cluster, and therefore the precision might be reduced.

With this work, we demonstrated that the DDSTG model can be applied to binary pulsar systems with different compactness. To obtain the best limits on DEF gravity, one shall combine the constraints from various experiments as their constraining power differs in the DEF gravity space. Note that the limits on DEF gravity obtained from binary pulsars are EOS-dependent and are further weakened by the uncertainty in the neutron star EOS due to our imperfect knowledge. Therefore, improving our knowledge of the EOS is of great importance for testing gravity theories. Such an improvement might come through a future moment of inertia measurement of PSR J0737−3039A, or observations with GW detectors such as LIGO/Virgo and X-ray telescopes such as NICER (see Chapter 3 for detailed discussions).

CHAPTER 6

Towards nanohertz gravitational wave detection: improving clock accuracy and telescope sensitivity

This chapter summarises my work that help to facilitate nanohertz gravitational wave (GW) detection using pulsar timing arrays (PTAs). This is achieved in two ways: improving the accuracy of clocks for Effelsberg observations while also increasing the sensitivity of telescopes by expanding the collection area. Section 6.1 provides some background on the detection of GWs with various experiments, and Section 6.2 introduces the basics of PTAs and discusses some recent progress on nanohertz GW detection, as well as my contributions on the data combination of PSR J1713+0747, which forms the longest PTA data set and plays a major role in the GW analysis. Section 6.3 documents my work on the Effelsberg clock corrections, which rescued over two years of timing data and improved the timing accuracy of the studied pulsars. The accuracy of clock corrections is essential for high precision pulsar timing, both for the PTA experiment and for the studies of individual pulsars. Finally, Section 6.4 presents an ongoing project on building the most powerful pulsar telescope through phased-array observations with the largest radio telescopes in Europe and China. The increased telescope sensitivity will enhance the timing precision that fulfils the requirement for GW detection and therefore the sensitivity of PTAs.

6.1 Introduction

Just half a year after Albert Einstein published his field equations and completed general relativity (GR), he predicted the existence of GWs within his new theory of gravitation (Einstein, 1916b). This marked the first description of GWs within a complete field theory of gravity (Kennefick, 2007). GWs are disturbances of spacetime generated by accelerated masses which propagate in all directions at the speed of light. As a GW propagates, the space is alternatively stretched and compressed, therefore changing the distance between objects rhythmically at the same frequency of the GW. The amplitude of GWs is characterised by a dimensionless spatial strain (h). However, this minuscule effect is challenging to detect and separate from background vibrations that are everywhere on Earth.

The first experimental attempts at GW detection were pioneered by Joseph Weber in the 1960s using resonant antennas (Weber, 1960). These large metal bars were isolated from external vibrations and expected to vibrate at a resonant frequency of 1660 Hz when a GW of a similar frequency passes through. GW bursts, e.g. from supernova explosions, were expected to be detected by such instruments. Even though detections were reported (Weber, 1968), it turned out that GWs were too weak to be measured in this way and the claimed detections were most likely noise. Later, the discovery of the first binary pulsar by Russell Hulse and Joseph Taylor (Hulse & Taylor, 1975) and subsequent observations of the

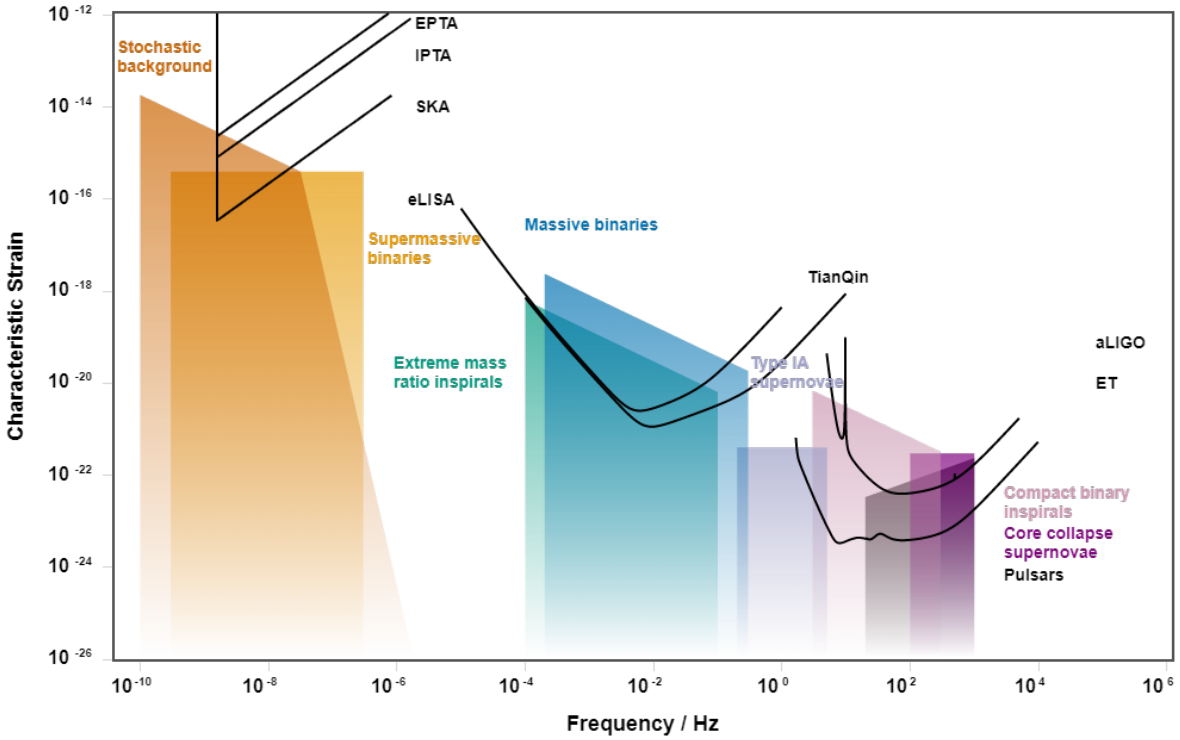

Figure 6.1: Noise curves for a selection of GW detectors as a function of frequency. At very low frequencies are pulsar timing arrays: the European Pulsar Timing Array (EPTA), the International Pulsar Timing Array (IPTA), and the future Square Kilometre Array (SKA); at low frequencies are space-borne detectors: the evolved Laser Interferometer Space Antenna (eLISA) and the Chinese mission TianQin; and at high frequencies are ground-based detectors: the advanced Laser Interferometer Gravitational-Wave Observatory (aLIGO) and the future Einstein Telescope (ET). The characteristic strain h_c of potential astrophysical sources is shown in coloured regions. The figure is generated using GWPLOTTER developed by Moore et al. (2015).

decay in its orbital period provided the first evidence of the existence of GWs (Taylor & Weisberg, 1989). The discovery of such a unique laboratory opened up new windows for gravity experiments and earned Hulse and Taylor the 1993 Nobel Prize in Physics. This motivated further GW searches and substantial efforts had been made, in particular with laser interferometers such as the Laser Interferometer Gravitational-Wave Observatory (LIGO, Drever et al., 1989; Abramovici et al., 1992) and Virgo detector (Brillet et al., 1989; Bradaschia et al., 1990). These detectors are modified Michelson interferometers that measures the GW strain h as a length difference of the orthogonal arms divided by the total length of one arm, i.e. $h = (\Delta L_1 - \Delta L_2)/L$. Their primary targets are GWs produced by compact binary coalescences, supernova explosions, and non-axisymmetric neutron stars in the frequency range of 10 Hz to 10 kHz (Riles, 2013). After years of non-detection, LIGO went through an upgrade to the much improved "advanced LIGO" (aLIGO) and recorded the first GW-like signal when it was back online in September 2015. This signal was later confirmed as the first GW detection by the LIGO-Virgo collaboration (B. P. Abbott et al., 2016a), and subsequently the 2017 Nobel Prize in Physics was awarded to Rainer Weiss, Kip Thorne, and Barry Barish for their key contributions.

Both aLIGO and Virgo are terrestrial GW detectors with arm lengths of $L \sim 10^3$ m and are sensitive to GWs from merging stellar-mass binaries. However, they are limited by seismic noise at low GW frequencies and one has to get off the Earth to overcome it. Several space-based detectors have been proposed and are expected to be operational in the 2030s, including the Laser Interferometer Space Antenna (LISA, Amaro-Seoane et al., 2017), TianQin (Luo et al., 2016), and Taiji (Ruan et al., 2018).

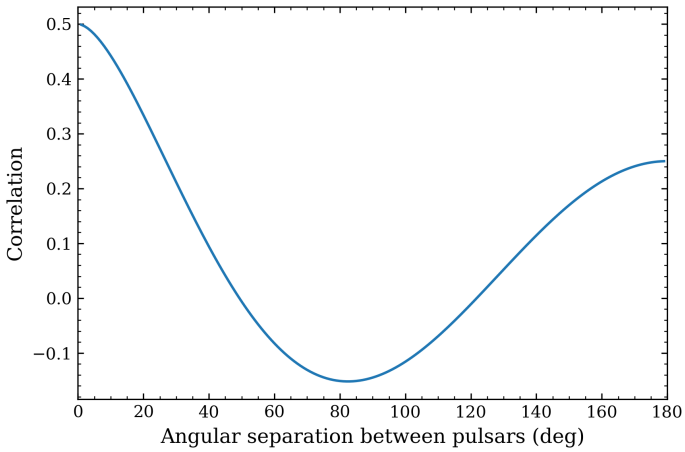

Figure 6.2: Hellings & Downs curve that describes the degree of correlation between pairs of pulsars as a function of angular separation between pulsars.

Such detectors are composed of three spacecraft separated by $10^8 \sim 10^9$ m and are sensitive to GWs with frequencies from 0.1 mHz to 1 Hz, e.g. from massive binaries with $\sim 10^6$ $M_\odot$. However, the loudest GW sources in the Universe — the inspiraling supermassive black hole binaries (SMBHBs, $>10^7 M_\odot$) — are expected to generate GWs in the nanohertz band which can be detected using an ensemble of millisecond pulsars (Sazhin, 1978; Detweiler, 1979) called a *pulsar timing array* (PTA, Foster & Backer, 1990). This experiment monitors a selection of MSPs at diverse sky positions and with a typical distance of kiloparsecs from the Earth. GWs distort the spacetime between pulsars and the Earth, altering their proper distance and resulting in a measurable deviation in the time of arrival (TOA) of pulsar signals on a timescale of decades.

The limiting factor for GW detectors is the noise (either external or instrumental) that competes with the signals to be detected, which differs in frequency for each detector. In order to detect the signal, the characteristic strain h_c (see Moore et al., 2015) of the noise curve must be lower than that of the target source. A summary of the noise curves for selected GW detectors and the characteristic strain for potential GW sources is shown in Figure 6.1.

6.2 Pulsar Timing Array

The primary motivating physical sources of GWs in the nanohertz band is inspiraling SMBHBs. The incoherent superposition of a large number of SMBHB GW signals form a stochastic GW background (GWB) which can be detected with PTAs by searching for spatially correlated signals (Rajagopal & Romani, 1995; Jaffe & Backer, 2003; Wyithe & Loeb, 2003; Sesana et al., 2004). In addition, cosmic strings (Kibble, 1976; Sanidas et al., 2012) or relic GW from the early Universe (Grishchuk, 2005) could also be detected using this technique. A detection in the PTA band will enable novel tests of gravity theories and provide unique insights into galaxy formation and evolution (Sesana, 2013).

The stochastic GWB can be parameterised by a power law which describes the dependence of the characteristic strain h_c induced by the GWB on the GW frequency f (see e.g. Maggiore, 2000; F. A. Jenet et al., 2006):

$$h_c = A \left(\frac{f}{f_c} \right)^{\alpha} , \tag{6.1}$$

where A is the strain amplitude of the GWB at reference frequency f_c (typically set to $1\,\mathrm{yr}^{-1}$), and $\alpha = (3 - \gamma)/2$ is the spectral index, which depends on the astrophysical origin of the GWB. In the case

of circular-orbit SMBHBs, the spectral index is expected to be $\alpha = -2/3$, i.e. $\gamma = 13/3$ (Phinney, 2001).

The isotropic GWB induces a spatially correlated signal in the timing residuals of pulsars, which is comprised of the pulsar term and the Earth term, due to the spacetime distortion at the positions of the pulsars and the Earth, respectively. Only the Earth term is fully coherent across all pulsars. In GR, GWs have a quadrupolar spatial correlation, and the correlation between the timing residuals of all pulsar pairs is expected to follow the Hellings & Downs (HD) relation (Hellings & Downs, 1983). The mathematical expression of the HD curve follows (F. A. Jenet et al., 2005)

$$r(\theta) = \frac{1}{2} - \frac{1}{4}\left(\frac{1-\cos\theta}{2}\right) + \frac{3}{2}\left(\frac{1-\cos\theta}{2}\right)\ln\left(\frac{1-\cos\theta}{2}\right), \tag{6.2}$$

where θ is the angular separation of pulsars on the sky. An illustration of the HD correlation is shown in Figure 6.2. To search for GWBs with PTAs, the basic idea is to look for a common red noise signal with this characteristic spatial correlation in an array of pulsars. This is what distinguishes it from other red noise sources.

The sensitivity of GW detection with PTAs relies on the span of observation time and the number of pulsars (Siemens et al., 2013), as well as their directional position on the sky. Therefore, the European Pulsar Timing Array (EPTA, B. W. Stappers et al., 2006; Janssen et al., 2008; Kramer & Champion, 2013), the Parkes Pulsar Timing Array (PPTA, Manchester, 2006), the North-American Nanohertz Observatory for Gravitational Waves (NANOGrav, F. Jenet et al., 2009), and the recently joined Indian PTA (InPTA) have formed the International Pulsar Timing Array (IPTA, Manchester & IPTA, 2013) to assemble all the PTA data (Verbiest et al., 2016; Perera et al., 2019) and carry out GW searches with the combined data set (Antoniadis et al., 2022). The new PTAs with highly sensitive telescopes, such as the Chinese PTA (CPTA, Lee, 2016) based on FAST and the MeerTIME PTA based on the MeerKAT telescope (Bailes et al., 2020), will also make important contributions to the IPTA over the coming years. The EPTA makes use of the five largest radio telescopes in Europe: the Effelsberg 100-m Radio Telescope (EFF) in Germany, the 76-m Lovell Telescope (LT) in Britain, the Nançay Radio Telescope (NRT) in France, the Westerbork Synthesis Radio Telescope (WRST) in the Netherlands, and the 64-m Sardinia Radio Telescope (SRT) in Italy. These five telescopes also operate together as a tied-array telescope known as the *Large European Array for Pulsars* (LEAP), where data are coherently combined to form a telescope with an equivalent diameter of 195 m (Bassa et al., 2016). LEAP serves as the sixth telescope of the EPTA and provides a significant improvement in the sensitivity of pulsar timing observations.

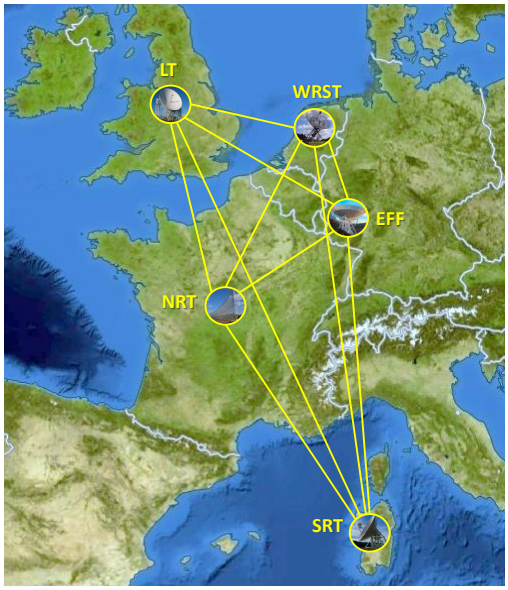

Figure 6.3: The five largest radio telescopes in Europe that make up LEAP.

In the past few years, I have been actively involved in the EPTA and LEAP collaborations, conducting observations and data processing. In particular, I processed Effelsberg data for PSR J1713+0747 during 2011-2019 and combined them with EPTA first data release (DR1, Desvignes et al., 2016) and new data from other EPTA telescopes. This extends the data set from 17.7 yr to 24 yr spanning from 1996 to 2019, which is the longest among all PTA data sets. The residuals of the combined data set for PSR J1713+0747 are shown in Figure 6.4, where the left panel has no noise model and the right panel

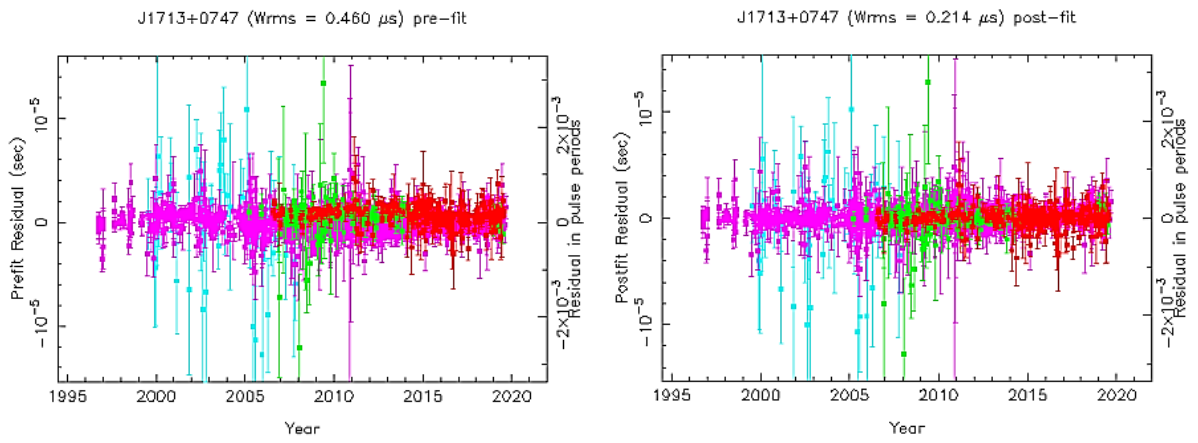

Figure 6.4: Timing residuals of PSR J1713+0747 for the combined EPTA data. The left panel does not include noise modelling, whereas the right panel includes EFAC, EQUAD, and has subtracted DM and red noise. With a noise model considered, the weighted RMS of residuals reduces from 0.460 μs to 0.214 μs.

includes noise models for EFAC and EQUAD, and subtracts DM and red noise. The weighted root mean square (RMS) of residuals of the latter is approximately half that of the former. PSR J1713+0747 is one of the most precisely timed MSPs and is ranked as one of the top pulsars in PTAs for nanohertz GW detection. Therefore, this data set plays an critical role in the EPTA second data release (DR2) analysis performed by Chen et al. (2021) and Chalumeau et al. (2022), and impacts all of the pulsar pairs that involves it. Moreover, the precision of binary parameters for this pulsar have improved by at least a factor of two compared to the previous data sets (Zhu et al., 2015; Desvignes et al., 2016; Zhu et al., 2019), which can deliver more stringent tests of gravitational symmetries, such as for a temporal variation of the gravitational constant G.

Thus far, PTAs have already collected more than two decades of data. A common red noise has been detected in the EPTA DR2 six-pulsar data set (Chen et al., 2021), the NANOGrav 12.5-year data set (Arzoumanian et al., 2020), the PPTA DR2 (Goncharov et al., 2021), and the IPTA DR2 (Antoniadis et al., 2022). The amplitudes of common red noise measured from these data sets are shown in Figure 6.5, where they are broadly consistent and in line with theoretical expectations. However, little evidence has been found yet to support the existence of an HD correlation, which would be required to claim a detection. The significance of the correlation power of the pulsar pairs is still insufficient to distinguish between different spatial correlations, including a monopolar correlation — a uniform correlation for any angular separation, $r(\theta) = 1$. In addition, monopolar correlations appear to exist in selected data sets. Possible sources of such signals are errors in the time standard and clocks. Tiburzi et al. (2016) found that clock errors can lead to large values of GWB amplitude, resulting in false GWB detections. Therefore, the accuracy of clock correction is important for GWB searches. In the following section, I will present my contributions on improving the accuracy of clock corrections for pulsar observations with the Effelsberg telescope, which helps to reduce clock errors and improve the timing precision.

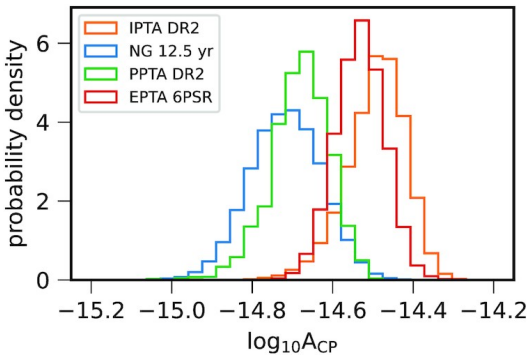

Figure 6.5: Comparison of common red noise amplitude $A_{\rm CP}$ from various data sets for a fixed spectral index $\gamma = 13/3$. Figure 10 in Antoniadis et al. (2022).

6.3 Improving clock accuracy for Effelsberg pulsar observations

Critical to pulsar timing is the accuracy of the timestamp of observations. The observation time is determined by a local atomic clock, typically a hydrogen maser, which is constantly compared to the Coordinated Universal Time (UTC) via the Global Positioning System (GPS). The time offsets between the maser and the GPS are recorded and later used as a "clock correction file" in pulsar timing to transfer the time tagging of observations to the international time standards, and eventually to the Solar System barycentre (see Section 2.3.1 for details).

The accuracy of the time tagging of observations depends on the stability of the maser used at each telescope and accuracy of clock corrections. The long-term instability of masers could induce red noise in the pulsar timing data, whereas the systematic offsets introduced by tuning or changing of the maser can result in a monopolar spatial correlation stronger than the HD correlation. Both of them, if not properly corrected for, may contaminate the signature of nanohertz GWs. Therefore, the stability of masers and accuracy of clock corrections need to be studied, which is the focus of this work.

6.3.1 Maser-GPS offset measurements

For pulsar observations with the Effelsberg telescope, the observatory instrument used for measuring the time offsets between the maser and the GPS broke down in 2017 and remained unnoticed until 2019. A new instrument was later available from May 2019 (see Section 6.3.2), but in order to use the data taken during the breakdown period, the maser-GPS offsets need to be determined.

Fortunately, a separate instrument used for VLBI observations also measures maser-GPS offsets but at a more frequent rate. However, there are steps in the VLBI offset measurements due to firmware changes associated with VLBI observations, and there is also a constant delay compared to observatory offset measurements. In order to use these data, I checked an overlap span of data for both measurements starting from MJD 57400 and the comparison is shown in Figure 6.6. The orange line indicates the measurements with the observatory instrument and the blue line indicates the measurements with the VLBI instrument (with jumps removed). In order to make the VLBI measurements usable for pulsar timing data taken during the breakdown period, I searched for, fitted and removed the steps in the VLBI measurements, then aligned these measurements to the observatory measurements at the starting point (MJD 57400). This results in a smooth green curve ("VLBI postfit") shown in Figure 6.6.

The difference of the green and the orange lines is shown in Figure 6.7. For the measurements before MJD 57790, the residuals are mostly below 35 ns. But at MJD 57790, a 50 ns offset suddenly appears and increases with time. This offset in the residuals is purely due to the behaviour of the observatory instrument, which became very unstable from MJD 57830 and eventually broke down around MJD 58040. Therefore, starting from MJD 57790 (February 2017) I used the post-fit curve of the VLBI offset measurements to extend the clock file for pulsar timing. Since there are outliers from the GPS, maser-GPS measurements are usually taken every 15 min. In order to create a smooth clock file that can be used in pulsar timing software, I removed the outliers and took the running median value for each day as the clock correction. The resulting clock file (red dots in Figure 6.8) allowed me to rescue more than 27 months of data for at least 40 pulsars, which is important for PTA experiments and a number of timing projects.

A new instrument for maser-GPS offset measurements has been available since May 2019 (MJD 58611). The running median of this recording (green line) is taken to be compared with the VLBI measurements (red dots) in Figure 6.8, where they agree very well in the overlapping region. Therefore, starting from MJD 58611, the offsets measured by the new instrument are used for making Effelsberg clock file.

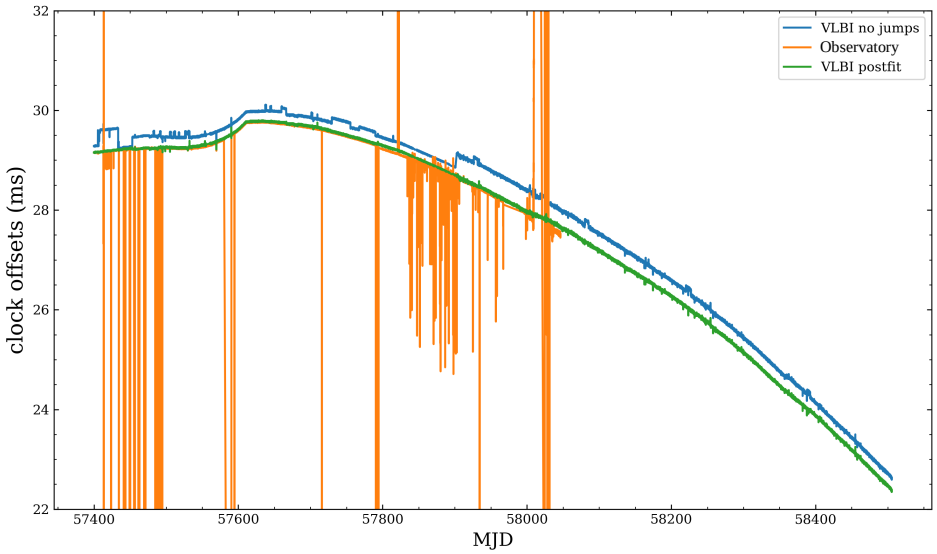

Figure 6.6: Comparison of maser-GPS offsets recorded by the observatory instrument (orange) and the VLBI instrument (blue, with jumps removed). The green curve is the post-fit of the VLBI measurements, where the steps are fitted and removed, and the whole curve is aligned with the orange curve from the starting point.

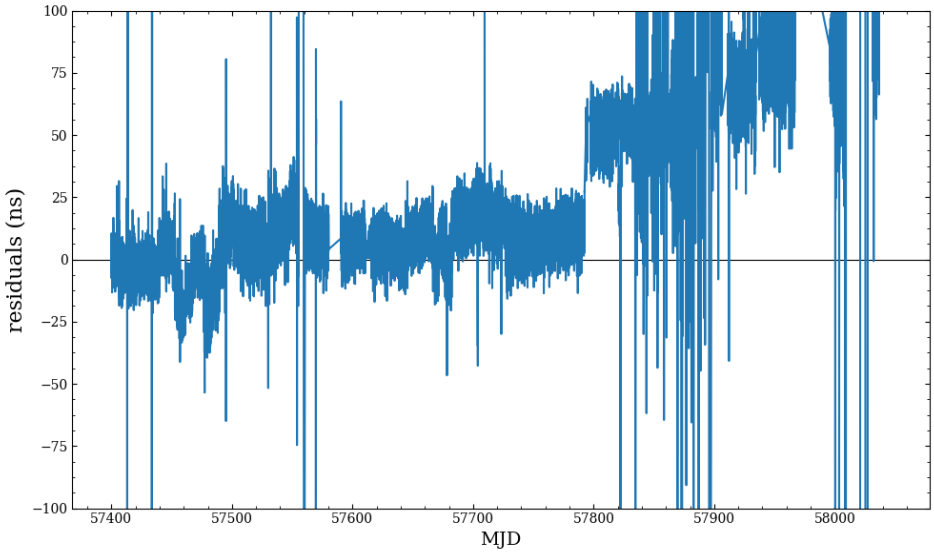

Figure 6.7: Residuals of the VLBI offset measurements and the observatory offset measurements (i.e. difference of the green line and the orange line in Figure 6.6).

6.3.2 Stability of masers at Effelsberg

The stability of hydrogen masers depends primarily on temperature control, which shall be kept stable and uniform. In addition, they should be shielded from vibrations and perturbing magnetic fields. Hydrogen masers have excellent short-term stability, but their stability decreases on a longer timescale. A new maser (i3000) has been available at Effelsberg since MJD 58670, and the time offsets between the new maser and the GPS have been constantly recorded. Before switching to the new maser, the old maser (i45)-GPS and the new maser (i3000)-GPS measurements were monitored for a year in order to compare their stability. I fitted each of the two measurements with a cubic curve and subtract it from the data,[1] and the residuals are shown in Figure 6.9. For a time span of ~1 yr, the old maser-GPS

[1] Polynomial functions of higher degree were fitted, but did not lead to better results.

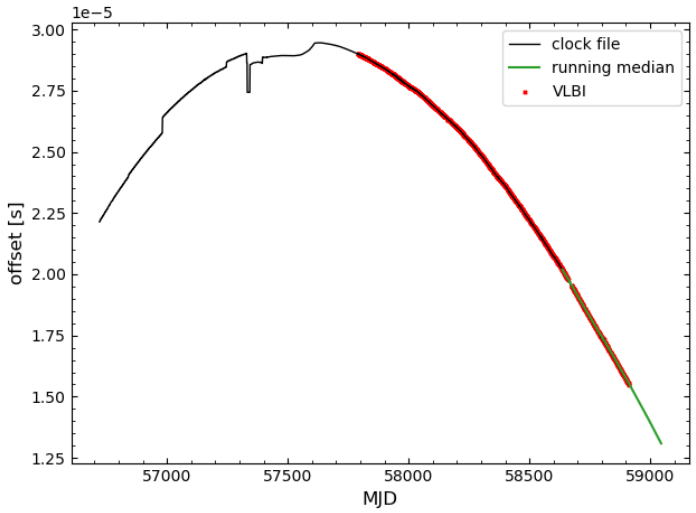

Figure 6.8: Comparison of time offset recordings. The black line shows the clock file generated using the old observatory instrument (before MJD 57790) and VLBI instrument (after MJD 57790). The VLBI instrument data are also marked in red, whereas the running median of the new observatory instrument data is shown in green. They match well in the overlapping region.

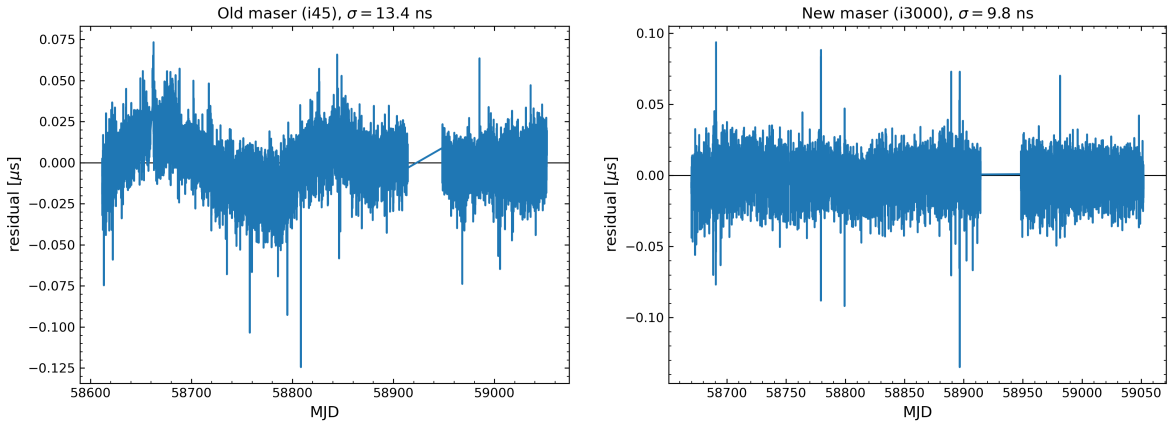

(a) (b)

Figure 6.9: Residuals of 1-yr maser-GPS measurements after cubic fitting. Panel (a) shows the measurements for the old maser (i45), which has a strong red noise signal and a standard deviation of 13.4 ns. Panel (b) shows the measurements for the new maser (i3000), where the standard deviation is 9.8 ns.

measurements (left panel) shows strong red noise and has a standard deviation of 13.4 ns. In contrast, the new maser-GPS measurements (right panel) looks quite flat and has a standard deviation of 9.8 ns. Therefore, the new maser is more stable on longer timescales and has less red noise than the old maser, which is more favourable for pulsar timing and in particular for GW detection. Therefore, starting from MJD 59297, the new maser began to be used for pulsar observations.

6.3.3 Measuring clock offsets using LEAP

I also looked back to the earlier maser-GPS measurements in the pulsar clock file, and found unexpected offsets during MJD 56720–57400 that are not present in the VLBI offset measurements (see the grey and the cyan line in Figure 6.10). LEAP offers a unique way to verify these offsets because it operates phased-array observations using multiple telescopes. To correlate the baseband data from different telescopes, one has to find the time difference of the recorded data between the pairs of telescopes. For

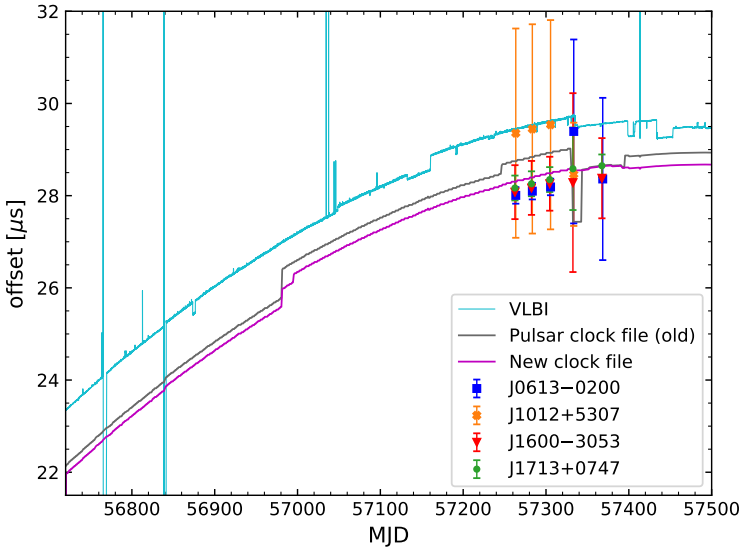

Figure 6.10: Comparison of clock offset measurements. The cyan line shows the VLBI offset measurements and the grey line shows the pulsar clock file made with the observatory offset measurements. The coloured data points are time offsets measured by the timing of four pulsars observed by LEAP, suggesting that the three jumps in the grey line are not real. The new clock file is shown in purple which corrects the offsets between MJD 56720–57000 using LEAP skipbin numbers and removes the jumps between MJD 57240–57400 based on LEAP timing.

Table 6.1: Time offsets in the EFF clock file measured using the WRST skipbin number from LEAP observations.

MJD	offset (s)
56720 – 56981	-1.111×10^{-6}
56981 – 57000	-5.45×10^{-7}
57000 – now	-3.74×10^{-7}

LEAP, this measurement is referenced to the Effelsberg telescope and the timing analysis is based on the Effelsberg clock and its corrections. After accounting for the light travelling time delay between observatories, there remains instrumentation delays at each observatory, measured as a 'skipbin' number. The skipbin steps the data through an integer number of time samples and one skipbin corresponds to 62.5 ns. In principle, the skipbin number should be invariant, therefore changes in the skipbin number would indicate possible errors in the clock. Apart from the two major clock jumps at Effelsberg between MJD 56230 and 56720, the skipbin number for Effelsberg is set to 0 by default.

To examine these time offsets in the Effelsberg clock file, the skipbin numbers measured during MJD 56720–57400 were checked. The skipbin numbers of the WRST were taken as a reference, as they are found to be relatively stable during that period of time. In addition, the skipbin numbers of the NRT were used as a second reference for confirming the existence of the offsets. It cannot be used for measurements as it drifts very quickly due to the type of clock used. In total, three offsets were spotted between MJD 56720 and 57000. These offsets were measured by taking the average of the WRST skipbin numbers from a couple of pulsars over several epochs and then converted into time offsets, as shown in Table 6.1. I added these offsets to the pulsar clock file and tested it against several pulsars, all of which showed improvements in their RMS values. The original pulsar clock file is plotted as the grey line in Figure 6.10, whereas the new clock file with offsets measured from LEAP is shown as the purple line. These two lines are consistent before MJD 56720. The new clock file has two different offset measurements at MJD 56720 and MJD 56981, and a new offset measurement at MJD 57000.

Apart from these unexplained "persistent" offsets, there are also temporary jumps in the MJD range

Table 6.2: RMS residual of five pulsars using LEAP data. The second and third column show the RMS before and after correcting the clock jump at MJD 57330. The forth column lists the improvements in the RMS.

Pulsar	RMS before (μs)	RMS after (μs)	RMS improvement
J1713+0747	0.329	0.305	7.3%
J1600−3053	0.647	0.637	1.5%
J1012+5307	0.904	0.817	9.6%
J0613−0200	0.686	0.673	1.9%
J1744−1134	0.362	0.314	13.3%

57240–57400 in the pulsar clock file that are not in the VLBI offset measurements (see Figure 6.10). Unfortunately, WRST was not available for the observations during this period, hence a reliable measurement of skipbin numbers is not possible. However, one can use pulsar timing to fit for the best clock offset for a giving epoch. To do this, I used the LEAP data on four high-ranking pulsars: J0613−0200, J1012+5307, J1600−3053, and J1713+0747, which were the only available data at the time. I divided the MJD range into three parts where the jumps are present: 57246–57332, 57332–57343, and 57343–57395. Then in the fit for each MJD range, I added a time offset to the TOAs within this range and obtained χ^2 by fitting a timing model to all TOAs. The time offset was taken from a fine grid for a reasonable range ($\pm 5\mu$s). The optimal time offset is where χ^2 reaches minimum, and is plotted in Figure 6.10 with 1-σ error bar (blue, orange, red, and green). One can see that the majority of the measurements from pulsar timing favours a smooth curve between MJD 57240–57400, suggesting that the three jumps in the grey line are not real, in particular the 1 μs jump at MJD 57330. A comparison of the RMS values of five LEAP pulsars before and after correction for this jump is shown in Table 6.2. In all cases, the RMS value reduces after removing this jump in the clock file, and the improvement can be $\gtrsim 10\%$ for some of the pulsars. Therefore, I removed these jumps and created a new clock file for pulsar timing, which is shown as the purple line in Figure 6.10).

6.3.4 Summary

In this section, I summarised my work on extending and correcting the Effelsberg clock file for pulsar timing. As the instrument used for maser-GPS offset measurements broke in 2017, I extended the clock file from February 2017 to May 2019 (MJD 57790–58611) by adapting the VLBI offset measurements, so that the pulsar timing data collected during this period of time can still be used. I then extended the clock file using the new instrument which has been available since May 2019 (MJD 58611). In addition, I checked the unexpected offsets and jumps in the clock file using LEAP. The skipbin numbers measured for correlating multiple telescope data were used to determine the offsets and pulsar timing with LEAP TOAs were helpful to confirm the false jumps in the clock file. These helped to reduce the clock errors in Effelsberg and LEAP timing data, which otherwise can result in a monopolar correlation in GW searches. To conclude, a reliable, more accurate, and up-to-date clock file for pulsar timing with Effelsberg and LEAP data was produced, which can help to eliminate possible monopolar correlation in the data.

This work improves the accuracy of the Effelsberg clock file and reduces the RMS of residuals for all five pulsars. Thanks to this clock file, the GW analysis and noise analysis of the six pulsars (including the five pulsars mentioned in Table 6.2) in EPTA DR2 performed by Chen et al. (2021) and Chalumeau et al. (2022) are possible. This clock file will continue to be useful for the ongoing EPTA DR2 analysis of 25 pulsars and for future IPTA work. Apart from PTA experiments, it also benefits many other timing projects, such as the timing analysis of PSR J2222−0137 by Guo et al. (2021) and the study of TOA

creation methods by J. Wang et al. (2022). Further investigation into the impact of clock stability and accuracy on GW detection is planned and will be discussed in Section 7.

6.4 Pan-EurAsia Pulsar Array: the largest pulsar telescope on Earth

Over the last few years, LEAP has proven its strength in terms of data quality (Bassa et al., 2016; Chen et al., 2021) and its unique application in measuring clock offsets (Section 6.3.3) because of the phased-array observation mode. The increased sensitivity offered by LEAP not only facilitates the PTA analysis in Chen et al. (2021) and Chalumeau et al. (2022), but also permits a number of other pulsar projects that are otherwise limited by the sensitivity of smaller telescopes, such as studies of single pulses (Liu et al., 2016; McKee et al., 2019), scintillation (Main et al., 2020; Mall et al., 2022), and quasi-periodic micro-structure of MSPs (Liu et al., 2022). Following the success of LEAP, a collaboration between the Max-Planck-Gesellschaft (MPG) and the Chinese Academy of Sciences (CAS) was established a few years ago to conduct the LEAP-type observations by involving FAST and the upcoming Xinjiang Qitai 110-m Radio Telescope (QTT, N. Wang, 2014; Xie et al., 2022) within the framework of MPG-CAS Low-Frequency Gravitational Wave consortium (LEGACY).

The *Pan-EurAsia Pulsar Array* (PEAPA), formerly known as *Über-LEAP*, was proposed to coherently combine LEAP, FAST, and eventually QTT in a phased-array mode to deliver the largest collection area, a 374-m equivalent dish three times larger than the SKA 1.[2] It will not rival the sensitivity of the full SKA, but both LEAP and FAST are readily available and QTT will be available in a few years, while the full SKA is only expected on a somewhat longer timescale. The PEAPA gains an extra 50% sensitivity compared to FAST and will become the largest radio telescope in the world, offering the longest baseline and the highest precision for pulsar timing observations. This unprecedented high precision can greatly decrease the level of radiometer noise which is currently the dominant source of noise in most PTA pulsars. Consequently, it will allow more pulsars to be timed with an accuracy <100 ns and therefore advance the detection of nanohertz GWs through the PTA, which is the primary goal of this project.

As the data are stored in baseband format, it can be processed flexibly to high-time or high-frequency resolution as required. Therefore, in addition to pulsar timing, the PEAPA enables many other scientific projects. One of these is to reveal the nature of radio emissions from MSPs in the single-pulse domain. Potential new algorithms may be developed to correct for pulse jitter (see Section 2.4) via single pulse studies, which will be greatly valuable for pulsar timing experiments both with FAST itself and with the SKA. Moreover, the PEAPA will improve our understanding of the variation of interstellar weather. More specifically, it can help to resolve scattering screens and DM variations, which can be used to reduce noises related to the interstellar medium (ISM). Furthermore, using an imaging VLBI-like observation mode, the PEAPA can measure the position, proper motion and parallax of pulsars with high accuracy. These are useful for breaking the degeneracy between timing parameters and for calculating the external contributions to the change of orbital period $\dot{P}_{\rm b}$ (see e.g. Section 3.4). Finally, given its high sensitivity, the PEAPA is an ideal tool for targeted pulsar searches, for example in globular clusters where exotic systems like pulsar-black hole binaries may exist.

In January 2019, FAST performed the first joint experimental VLBI observation with the 65-m Tianma radio telescope and successfully obtained fringes, validating the capability of FAST for VLBI observations. In the past few years, several proposals have been submitted to FAST for trial observations with FAST and Effelsberg. The main goal is to obtain the first fringe between FAST and Effelsberg before involving other LEAP telescopes. In the following, I will present the progress made on this project.

[2] The maximum illuminated aperture for FAST is 300 m.

Table 6.3: List of selected sources that can be observed simultaneously with FAST and Effelsberg. Columns 4 and 5 show the overlapping observable time (in hours) when the zenith angle of FAST is set to 30° and 40°, respectively.

Name	RA	DEC	Overlap time (30°)	Overlap time (40°)
B0531+21	05:34:31.97	+22:00:52.06	0:51	1:36
J0621+1002	06:21:22.11	+10:02:38.74	0:10	0:57
J0751+1807	07:51:09.16	+18:07:38.49	0:40	1:24
J1012+5307	10:12:33.44	+53:07:02.26	2:12	3:43
J1022+1001	10:22:57.99	+10:01:52.68	0:09	0:56
B1237+25	12:39:40.46	+24:53:49.29	1:00	1:44
J1640+2224	16:40:16.75	+22:24:08.82	0:52	1:36
J1713+0747	17:13:49.53	+07:47:37.48	0:00	0:34
J1911+1347	19:11:55.20	+13:47:34.36	0:26	1:11
B1933+16	19:35:47.83	+16:16:39.99	0:18	1:03
B1937+21	19:39:38.56	+21:34:59.12	0:50	1:34
B1957+20	19:59:36.77	+20:48:15.12	0:48	1:32

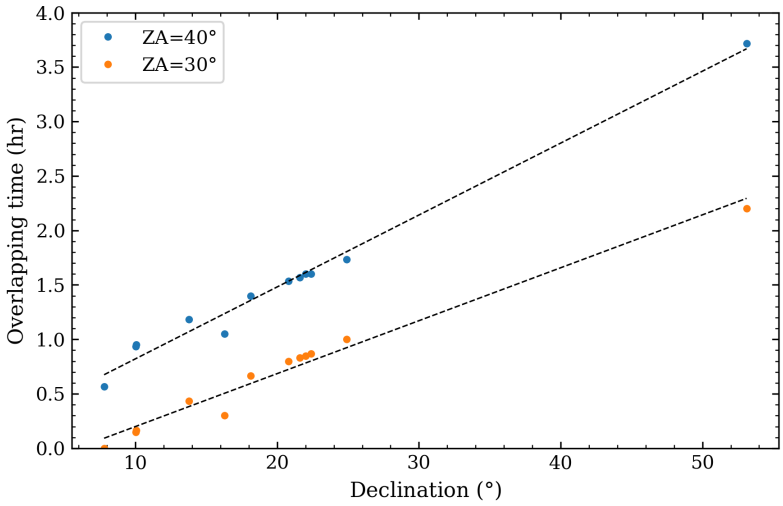

Figure 6.11: Relation between the overlapping observation time of FAST and Effelsberg and the declination of pulsars. The orange and blue dots represent the cases where the zenith angle (ZA) of FAST is 30° and 40° respectively. The black dashed lines are linear fits to the data.

6.4.1 Source lists

Before planning the observations, one needs to work out which sources can be observed simultaneously with FAST and Effelsberg, as they have 6:40 hr difference in local sidereal time. To do this, I calculated the rise and set time of selected sources at FAST and Effelsberg that suit the science cases, mainly MSPs but also 'slow' pulsars that emit giant pulses, such as PSR B1237+25, PSR B1937+21, and the Crab pulsar B0531+21. The overlapping observation time is the difference between the rise time at Effelsberg and the set time at FAST, and therefore depends on the zenith angle allowed by FAST. The maximum zenith angle for FAST is 40°, while for best performance, a zenith angle of less than 30° is recommended (Jiang et al., 2019). Table 6.3 summarises the overlapping time calculated for selected sources in both cases. Due to the relative geographical position of FAST and Effelsberg, the low declination pulsars like PSR J1713+0747, PSR J0621+1002 and PSR J1022+1001 can only be observed for a short time. The relation of the declination of pulsars and the overlapping observation time is plotted in Figure 6.11. One

Table 6.4: List of joint observations with FAST and Effelsberg. The first observation was only successfully carried out by FAST.

Epoch	Name	Type	UTC start	UTC end
1	J0521+2112	calibrator	2019-07-26 03:30:00	2019-07-26 03:35:00
	B0531+21	pulsar	2019-07-26 03:45:00	2019-07-26 04:00:00
2	J1240+2405	calibrator	2019-08-20 09:00:00	2019-08-20 09:05:00
	B1237+25	pulsar	2019-08-20 09:15:00	2019-08-20 09:30:00
3	J1900+2722	calibrator	2021-01-14 05:42:00	2021-01-14 05:47:00
	J1911+1347	pulsar	2021-01-14 06:00:00	2021-01-14 06:12:00
	B1937+21	pulsar	2021-01-14 06:25:00	2021-01-14 06:52:00
	J1956+2820	calibrator	2021-01-14 07:03:00	2021-01-14 07:08:00

can see that for the pulsars on our list (declination 7°–53°), the overlapping observation time increases almost linearly with the declination of the pulsar.

6.4.2 Observations and prospects

So far, three observations (including four pulsars) have been carried out and are summarised in Table 6.4. For each pulsar, a 5-min scan of a phase calibrator was performed to obtain a sufficiently close initial estimate for correlating the pulsar data. Due to operational difficulties at Effelsberg, the first observation on 2019-07-26 was conducted successfully by FAST only. Nevertheless, preliminary processing of FAST data on the Crab pulsar was carried out. Figure 6.12 shows the pulse profile (left) and the intensity in time against the pulse phase (right), and the quality of data is excellent. The other two observations were carried out jointly by FAST and Effelsberg on 2019-08-20 and 2021-01-14. The Effelsberg data have been preliminary processed, and an example on PSR B1237+25 is shown in Figure 6.13, where mode changing can be clearly seen in the right panel and can be used to study pulsar emission geometries.

The project has been delayed due to data transfer issues, but eventually all Effelsberg data have been transferred to China and data processing is underway. Once the data are coherently combined, at least two papers are expected based on the existing observations: one on the design and technical aspects of the PEAPA and others on the scientific aspects, as the pulsars observed are suitable for studying single/giant pulses and ISM effects.

Based on the performance of LEAP and FAST, one can estimate the expected timing precision of the PEAPA observations using Eq. (2.7). For the same pulsar, the TOA uncertainty scales as $\sigma_{\rm TOA} \propto T_{\rm sys}/\left(\mathtt{G}\sqrt{t_{\rm int}\Delta f}\right)$, where the system temperature $T_{\rm sys}$ of these telescopes are similar (20-35K). Assuming that the system temperature, integration time $t_{\rm int}$ and bandwidth Δf are the same in the observations, $\sigma_{\rm TOA}$ is only inversely proportional to telescope gain $\mathtt{G}$. The total gain of LEAP is about 6 K/Jy where Effelsberg has a gain of 1.5 K/Jy (Bassa et al., 2016), and the gains of FAST and QTT are 16 K/Jy (Jiang et al., 2019) and 2 K/Jy (estimated), respectively. The gains of EFF+FAST and the

Table 6.5: Comparison of telescope gain and RMS of PSR J1737+0747 for EPTA, LEAP, EFF+FAST, and the PEAPA.

	EPTA	LEAP	EFF+FAST	PEAPA
Telescope gain G (K/Jy)	1.2 (average)	6	17.5	24
RMS (ns) of PSR J1713+0747	680 Desvignes et al. (2016)	180 Bassa et al. (2016)	60	45

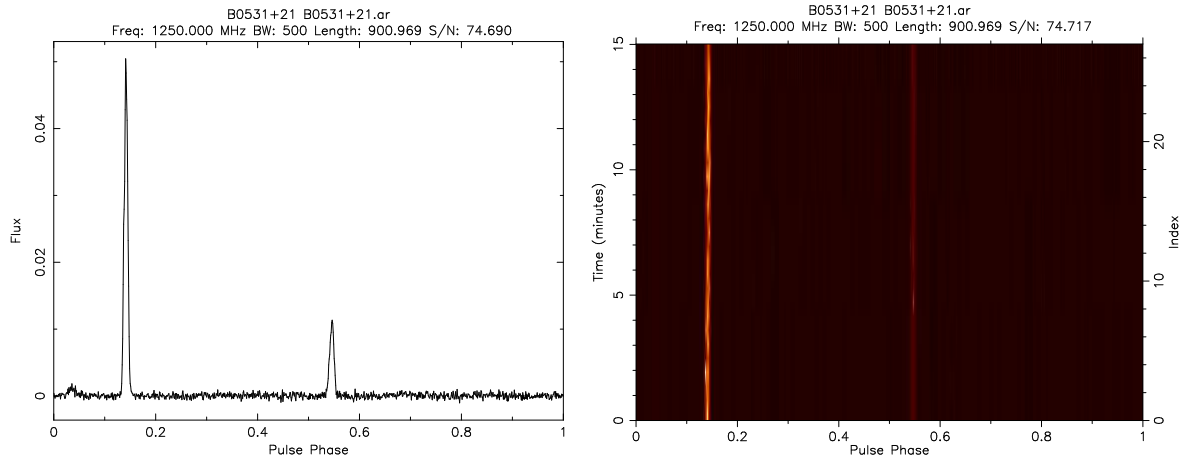

(a) pulse profile

(b) intensity in time versus pulse phase

Figure 6.12: FAST observation of the Crab pulsar B0531+21 on 2019-07-26.

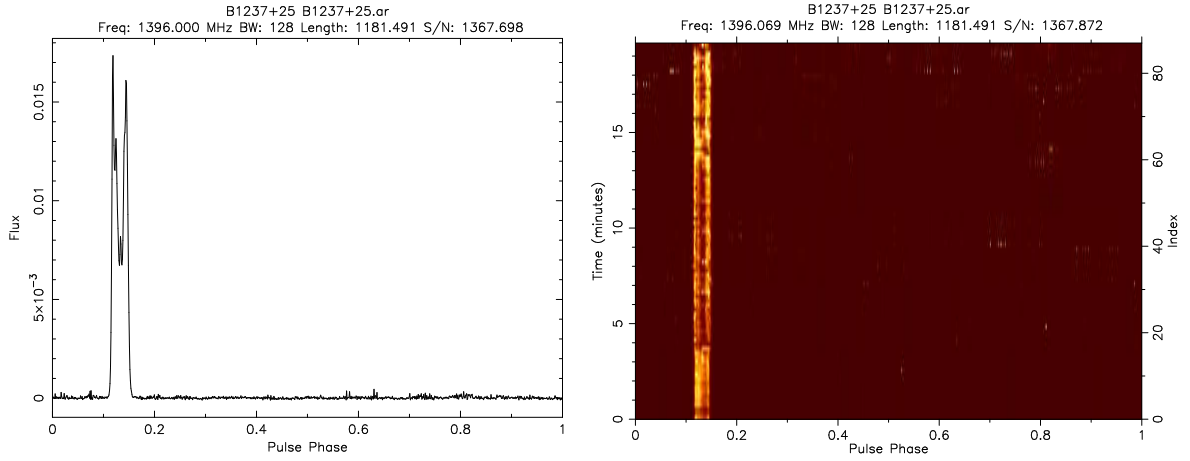

(a) pulse profile

(b) intensity in time versus pulse phase

Figure 6.13: Effelsberg observation of PSR B1237+25 on 2019-08-20. Mode changing can be clearly seen in panel (b).

PEAPA are listed in Table 6.5, which are three and four times larger than LEAP respectively. This makes the PEAPA the most sensitive pulsar telescope. Taking PSR J1713+0747 as an example, the RMS residual expected from EFF+FAST and the PEAPA observations can be estimated from the scaling relation $\sigma_{\mathrm{TOA}} \propto 1/\mathtt{G}$ (assuming only radiometer noise) based on LEAP observations (Bassa et al., 2016). Table 6.5 shows a comparison of telescope gain and RMS residual of PSR J1713+0747 with EPTA, LEAP, EFF+FAST, and the PEAPA. Because of the large gains of EFF+FAST and the PEAPA, the RMS residual of PSR J1713+0747 can be reduced to 60 ns and 45 ns, which is better than any other radio telescope currently available. Similarly, with this observing mode, more pulsars can be timed with an accuracy below 100 ns, thereby significantly advancing the detection of nanohertz GWs. This could also save observation time as a very short integration time is sufficient to obtain high accuracy data.

Overall, the PEAPA project is expected to provide high precision data that will benefit nanohertz GW detection and allow us to carry out other interesting studies. The data analysis will be continued and future observations are planned, which are subject to further work.

CHAPTER 7

Discussion

This dissertation explored a range of questions in fundamental physics using pulsar timing. The time of arrivals (TOAs) of pulsar signals carry information about some of the most extreme objects in the Universe and provide unique insights into the fundamental properties of the densest matter and two fundamental interactions — electromagnetism and gravity. New-generation radio telescopes such as the MeerKAT telescope, the Five-hundred-meter Aperture Spherical radio Telescope (FAST), and the future Square Kilometre Array (SKA) promise important contributions to our understanding of the Universe.

In the first two projects, we studied the unique Double Pulsar system, PSR J0737−3039A/B. It provides rich tests of relativistic effects in a strong gravitational field, more than any other known binary pulsar. The excellent sensitivity of new-generation radio telescopes allows us to study various higher-order contributions to orbital motion and signal propagation that have not been tested in any other binary pulsar before.

The first study focused on the higher-order effects in the orbital motion of the Double Pulsar, including the periastron precession ($\dot{\omega}$) caused by the Lense-Thirring effect, and the change of orbital period ($\dot{P}_{\rm b}$) due to spin-down mass loss and next-to-leading-order (NLO) gravitational wave (GW) damping. We developed a consistent method to measure the moment of inertia (MOI) of radio pulsars using three post-Keplerian (PK) parameters ($\dot{\omega}$, s, $\dot{P}_{\rm b}$) and applied it to the simulated data of PSR J0737−3039A. Based on this method, Kramer et al. (2021a) obtained an upper limit for the MOI of pulsar A with 16-yr data: $I_{\rm A} < 3.0\times10^{45}\,{\rm g\,cm^2}$ (90% confidence). Observations with MeerKAT and its future extensions are expected to improve this measurement considerably and we found an 11% accuracy (68% confidence and hereafter) could be achievable by 2030. Such a measurement can provide complementary constraints on the equation of state (EOS) of nuclear matter to other experiments, such as neutron star mergers observed by GW detectors (LIGO/Virgo, etc.) and X-ray observations by NICER and future missions such as eXTP. Moreover, discoveries of more relativistic "cousins" of the Double Pulsar could place stringent constraints on the EOS that are an order of magnitude better than the Double Pulsar and competitive with other methods. Therefore, we can expect advances in our knowledge of neutron star EOS in the near future. This in turn would allow a 7% test of Lense-Thirring precession in the Double Pulsar by 2030 and constraining on the gravity theories, or a 3σ-measurement of the NLO GW damping which has not been tested in any binary pulsar.

The second study concentrated on the signal propagation effects in the strong gravitational field of the Double Pulsar, i.e. the interaction between electromagnetic and gravitational fields. We analysed 3-yr wideband MeerKAT data of PSR J0737−3039A using modern techniques, i.e. frequency-dependent (2D) templates and epoch-dependent dispersion measure (DM) modelling, which helped to improve the accuracy of TOAs. Compared to the 16-yr results, the excellent precision of MeerKAT data already

allowed better measurements of Shapiro delay and masses, as well as an independent confirmation of NLO signal propagation effects, which is 1.65 times more significant than before. In particular, we studied the retardation effect caused by the movement of pulsar B and the deflection of the signal by the gravitational field of B. In addition, we investigated novel effects that have been expected but not yet observed, including latitudinal signal deflection and lensing correction to Shapiro delay. We searched for potential profile changes near superior conjunctions caused by latitudinal deflection and found no evidence for it, which could be useful to constrain the geometry of the system in a subsequent study. The expected profile variations, if not taken into account, could affect the determination of TOAs, but we found this latitudinal deflection delay can be mostly absorbed by the Shapiro delay. Furthermore, our simulations suggested that the lensing correction to Shapiro delay may be measurable within a few years with the full SKA or equivalent instruments.

The third study explored the prospects of testing a class of alternative gravity theories, the Damour–Esposito-Farèse (DEF) gravity, using the recently developed timing model for scalar-tensor gravity — the DDSTG model. Due to asymmetry in their compactness, pulsar-white dwarf systems such as PSR J2222−0137 and pulsar-black hole systems are useful tools to constrain dipolar GWs predicted in many alternative theories due to a violation of the strong equivalence principle (Wex, 2014; Liu et al., 2014a). By simulating realistic data of PSR J2222−0137 and hypothetical pulsar-black hole systems for a number of large telescopes such as FAST, we found that future observations will significantly improve the constraints on DEF gravity. In particular, if pulsar-black hole systems can be discovered, they have the potential to set the most stringent limits for a large part of the DEF gravity parameter space and enhance our understanding of gravity.

Finally, the fourth study involved two projects that are conducive to the detection of nanohertz GWs with pulsar timing arrays (PTAs). Firstly, I extended the clock correction file for Effelsberg from February 2017 to May 2019, which allowed us to still use the data collected during this period in our analysis. In addition, I corrected the errors in the clock correction file using the information from phased-array observations with the Large European Array for Pulsars (LEAP) and timing a handful of most precisely timed pulsars. Since clock errors are a possible source of the monopolar correlation present in the current gravitational wave analysis, this work improved the accuracy of clock corrections and can potentially help to eliminate possible monopolar correlation in Effelsberg and LEAP data. Secondly, the Pan-EurAsia Pulsar Array (PEAPA) has been proposed to coherently combine LEAP, FAST, and the upcoming 110-m Qitai Radio Telescope (QTT) to deliver the world's largest pulsar telescope. Phased-array observations have been carried out with Effelsberg and FAST, and we expect a dramatically increase in the telescope sensitivity and TOA accuracy, which will greatly advance GW detection.

Of course, to make some of these experiments possible, we also need advances in the knowledge of other branches of astronomy. For instance, to perform the gravity experiments that involves the orbital period derivative $\dot{P}_{\rm b}$, such as in the first and third studies, good knowledge of the astrometric information of pulsars and the relative acceleration of pulsars and the Solar System in the gravitational field of the Galaxy is required. The former can be improved from complementary VLBI observations, while the latter is expected to improve in the near future with e.g. *Gaia* data (Gaia Collaboration et al., 2022).

Data combination of the Double Pulsar

Even though the 3-yr MeerKAT data have already shown better measurements of Shapiro delay and NLO signal propagation effects, the precision of the secular parameters has not yet caught up with the results of the 16-yr data. To improve the precision on the secular parameters and to perform the tests proposed in Chapter 3, one needs to combine the two data sets. In fact, we have made extensive efforts trying to combine these two data sets. The uncertainties of PK parameters are much reduced, but the

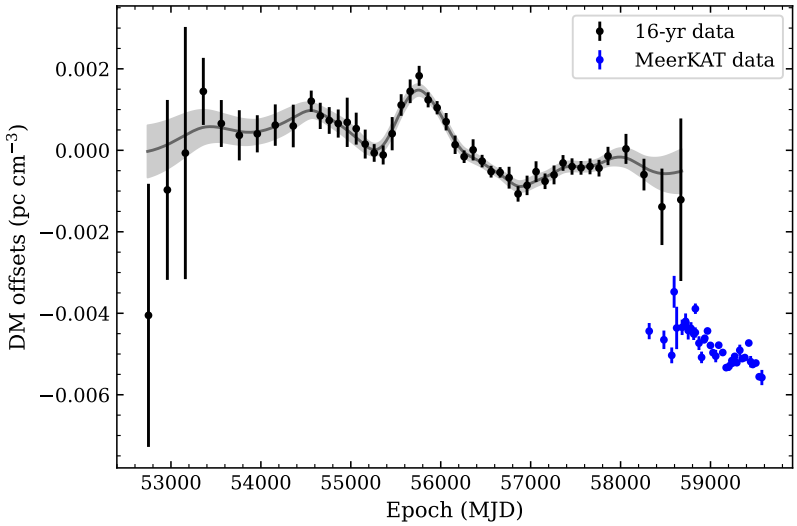

Figure 7.1: DM measurements from the 16-yr data (black) and MeerKAT data (blue) with respect to the reference value 48.917 208 pc cm^{-3}. The solid curve resulted from a Gaussian learning process with uncertainties in grey.

secular parameters appear to deviate from the result obtained from the individual data sets. This is of course unexpected and suggests that we have issues in the processing techniques or the analysis software.

This problem can be reproduced also with simulations. We adjusted TOAs of MeerKAT and 16-yr data separately using the same ephemeris and added only white noise. For each data set we obtained measurements consistent with the input values, but when combining the two data sets together, the secular parameters again showed deviations. The precision of MeerKAT data helps to reduce the uncertainties of parameters quite significantly, but it also skews the derived secular parameters due to their large relative weight giving their small uncertainties. One possible solution could therefore be to reduce the weighting of MeerKAT data by a factor of ~ 5. This is approximately the ratio of the data span of the 16-yr data to the 3-yr MeerKAT data, which is feasible for obtaining consistent measurements but more studies are needed. Moreover, in this case the uncertainty of the parameters would increase and the advantage of MeerKAT precision is depreciated.

The situation is more complicated still as there are also DM noise and red noise in the data. For DM, the model of the 16-yr data was made by fitting multiple frequency data at 100-d intervals (see Kramer et al. 2021a for detail), whereas for MeerKAT we used 2D templates and fitted for DM independently at every observing epoch. As mentioned in Chapter 4, DM measurements depend on the DM to which the 2D template is referenced. As shown in Figure 7.1, one of the problems we encountered is that the two sets of data have different reference DM values and they have overlapping data. This can potentially be solved by changing the reference DM of MeerKAT 2D templates, or by correcting TOAs to infinite frequency before fitting to the timing model. The situation is even more complicated with the addition of red noise, which is highly correlated with astrometric parameters and DM models. With simulations, we found that astrometric parameters and some of the binary parameters can be strongly influenced by red noise. To properly model red noise and account for correlations between parameters, it is common to use Bayesian approach, e.g. with TEMPONEST. However, running TEMPONEST analysis for the Double Pulsar is computationally expensive ($> 10^6$ TOAs compared to typically $\sim 10^3$ TOAs for PTA pulsars) and a more efficient technique may be required. Moreover, as TEMPONEST is based on TEMPO2, the aberration and orbital deformation parameters are missing in its DD model, as well as the consideration of NLO effects in the Double Pulsar. These are to be incorporated into the ongoing upgrade of the TEMPO2 DD model.

To sum up, our findings suggest that the data combination of a long-span less-precision data set and a

short-span high-precision data set is challenging. This could be a common problem for other pulsars, especially when combining with high-precision data from MeerKAT and FAST as PTA experiments. Since the orbital parameters of the Double Pulsar are known so precisely, it is probably the best system to solve any problem in data combination. We are continuing this study and hope to solve this problem in the near future.

Impact of clock accuracy on low-frequency gravitational wave detection

As discussed in Chapter 6, a possible source of correlated common red noise seen in PTAs is errors in Terrestrial Time (TT) to which all TOAs are referred. Any imperfections in this timescale will affect the TOAs of all pulsars in a fully correlated manner — a monopolar correlation. This effect has been discussed extensively in Guinot & Petit (1991), G. Hobbs et al. (2012) and G. Hobbs et al. (2020), and it has been used to create pulsar-based timescales that can complement the atomic timescales. Tiburzi et al. (2016) also showed that various spatially correlated noise, including errors in the TT standard and a stochastic clock-like signal, can induce false detections of GWs. Our work on measuring clock offsets with LEAP and pulsar timing also demonstrated that errors in maser-GPS measurements can reduce the timing precision and can be corrected with the techniques used in Section 6.3.3. However, more studies are needed to understand the impact of the stability of local masers and the accuracy of clock offset measurements on PTA precision and GW detection.

To further investigate this problem, we plan to simulate different types of noises and errors in the clock offset measurements (white noise, red noise, constant offsets, temporal jumps, etc.) and study how the different noise/error affect the correlation curve. With simulations, we also expect to find solutions to minimise the effect of clock noise/error and eliminate possible monopolar correlation in the PTA analysis. In addition, we can study the impact of combining data from multiple telescopes with different clock errors on GW detection and find the best way to boost its precision. Moreover, for high sensitivity telescopes, such as FAST and the SKA, timing accuracy may be already limited by the stability of atomic clocks, which can also be found out with simulations. Obviously, much more further work is needed.

Future timing: beyond the sensitivity of FAST

FAST is currently the most sensitive radio telescope and has already showed excellent timing precision (see e.g. Chapter 5). To go beyond the sensitivity of FAST, the PEAPA project has been purposed to coherently combine the largest radio telescopes in Europe and China. In Chapter 6, the potential of the PEAPA has been demonstrated and joint observations with FAST and Effelsberg have been conducted. In addition, two large fully steerable radio telescopes are being planned in China and will be available in the coming years: the 100-m QTT and the 120-m Jingdong Pulsar Radio Telescope (JRT, M. Wang et al., 2022). Construction of QTT has started recently and is expected to take six years to complete. It is located in northwestern China, between FAST and the Europe, which is in particular helpful in finding fringes for VLBI-mode observations and improving the capability of VLBI network. JRT, on the other hand, is dedicated to pulsar science and will be built in the southwest of FAST (24.5°N 101.0°E). Thanks to its excellent location, it can cover 90% of the sky and is capable of observing many Southern sky sources that are not accessible to many telescopes in the Northern Hemisphere. Moreover, more than 6000 h of observation time can be allocated to millisecond pulsar timing every year which can greatly advance the nanohertz GW detection (M. Wang et al., 2022). Overall, by combining the power of these large radio telescopes in VLBI-mode observations, the future is bright for GW detection at nanohertz frequencies and for many interesting gravity experiments with pulsars.

Bibliography

Abbott, B. P. et al. (2016a), *Observation of Gravitational Waves from a Binary Black Hole Merger*, Phys. Rev. Lett. **116** 061102, arXiv: 1602.03837 [gr-qc] (cit. on pp. 2, 84).

Abbott, B. P. et al. (2016b), *Tests of General Relativity with GW150914*, Phys. Rev. Lett. **116** 221101, arXiv: 1602.03841 [gr-qc] (cit. on pp. 47, 78).

Abbott, B. P. et al. (2017), *GW170817: Observation of Gravitational Waves from a Binary Neutron Star Inspiral*, Phys. Rev. Lett. **119** 161101, arXiv: 1710.05832 [gr-qc] (cit. on pp. 27, 28).

Abbott, B. P. et al. (2018), *GW170817: Measurements of Neutron Star Radii and Equation of State*, Phys. Rev. Lett. **121** 161101, arXiv: 1805.11581 [gr-qc] (cit. on pp. 27, 41, 42).

Abbott, B. P. et al. (2019), *Tests of General Relativity with GW170817*, Phys. Rev. Lett. **123** 011102, arXiv: 1811.00364 [gr-qc] (cit. on p. 48).

Abramovici, A. et al. (1992), *LIGO: The Laser Interferometer Gravitational-Wave Observatory*, Science **256** 325 (cit. on p. 84).

Alsing, J., Berti, E., Will, C. M. & Zaglauer, H. (2012), *Gravitational radiation from compact binary systems in the massive Brans-Dicke theory of gravity*, Phys. Rev. D **85** 064041, arXiv: 1112.4903 [gr-qc] (cit. on p. 44).

Amaro-Seoane, P. et al. (2017), *Laser Interferometer Space Antenna*, arXiv e-prints, arXiv: 1702.00786 [astro-ph.IM] (cit. on p. 84).

Andersson, N., Glampedakis, K., Ho, W. C. G. & Espinoza, C. M. (2012), *Pulsar Glitches: The Crust is not Enough*, Phys. Rev. Lett. **109** 241103, arXiv: 1207.0633 [astro-ph.SR] (cit. on p. 8).

Antoniadis, J. et al. (2012), *The relativistic pulsar-white dwarf binary PSR J1738+0333 - I. Mass determination and evolutionary history*, MNRAS **423** 3316, arXiv: 1204.3948 [astro-ph.HE] (cit. on p. 76).

Antoniadis, J. et al. (2022), *The International Pulsar Timing Array second data release: Search for an isotropic gravitational wave background*, MNRAS **510** 4873, arXiv: 2201.03980 [astro-ph.HE] (cit. on pp. 2, 25, 86, 87).

Antoniadis, J. et al. (2013), *A Massive Pulsar in a Compact Relativistic Binary*, en, Science **340** 448, ISSN: 0036-8075, URL: https://ui.adsabs.harvard.edu/abs/2013Sci...340..448A/abstract (visited on 26/11/2019) (cit. on pp. 8, 28, 29).

Archibald, A. M. et al. (2018), *Universality of free fall from the orbital motion of a pulsar in a stellar triple system*, Nature **559** 73, arXiv: 1807.02059 [astro-ph.HE] (cit. on p. 71).

Arzoumanian, Z., Brazier, A., Burke-Spolaor, S., Chamberlin, S., Chatterjee, S. et al. (2018), *The NANOGrav 11-year Data Set: High-precision Timing of 45 Millisecond Pulsars*, ApJS **235** 37, arXiv: 1801.01837 [astro-ph.HE] (cit. on p. 28).

Arzoumanian, Z. et al. (2020), *The NANOGrav 12.5 yr Data Set: Search for an Isotropic Stochastic Gravitational-wave Background*, ApJ **905** L34, arXiv: 2009.04496 [astro-ph.HE] (cit. on p. 87).

Baade, W. & Zwicky, F. (1934a), *Cosmic Rays from Super-novae*, Proceedings of the National Academy of Science **20** 259 (cit. on p. 3).

Baade, W. & Zwicky, F. (1934b), *On Super-novae*, Proceedings of the National Academy of Science **20** 254 (cit. on p. 3).

Baade, W. & Zwicky, F. (1934c), *Remarks on Super-Novae and Cosmic Rays*, Physical Review **46** 76 (cit. on p. 3).

Bailes, M. et al. (2016), *MeerTime - the MeerKAT Key Science Program on Pulsar Timing*, 11, arXiv: 1803.07424 [astro-ph.IM] (cit. on pp. 30, 37).

Bailes, M. et al. (2020), *The MeerKAT telescope as a pulsar facility: System verification and early science results from MeerTime*, PASA **37** e028, arXiv: 2005.14366 [astro-ph.IM] (cit. on pp. 16, 37, 38, 51, 86).

Barker, B. M. & O'Connell, R. F. (1975), *Gravitational two-body problem with arbitrary masses, spins, and quadrupole moments*, Phys. Rev. D **12** 329 (cit. on pp. 29, 32).

Barret, D. et al. (2013), "Athena+: The first Deep Universe X-ray Observatory", *SF2A-2013: Proceedings of the Annual meeting of the French Society of Astronomy and Astrophysics*, ed. by L. Cambresy, F. Martins, E. Nuss & A. Palacios 447, arXiv: 1310.3814 [astro-ph.HE] (cit. on p. 41).

Bassa, C. G. et al. (2016), *LEAP: the Large European Array for Pulsars*, MNRAS **456** 2196, arXiv: 1511.06597 [astro-ph.IM] (cit. on pp. 15, 86, 93, 95, 96).

Batrakov, A. et al. (2023), *A new pulsar timing model for scalar-tensor gravity with applications to PSR J2222-0137 and pulsar-black hole binaries*, A&A, arXiv: 2303.03824 [astro-ph.HE] (cit. on pp. 73, 78, 80, 81).

Bauböck, M., Berti, E., Psaltis, D. & Özel, F. (2013), *Relations between Neutron-star Parameters in the Hartle-Thorne Approximation*, ApJ **777** 68, arXiv: 1306.0569 [astro-ph.HE] (cit. on p. 32).

Berti, E., White, F., Maniopoulou, A. & Bruni, M. (2005), *Rotating neutron stars: an invariant comparison of approximate and numerical space-time models*, MNRAS **358** 923, arXiv: gr-qc/0405146 [gr-qc] (cit. on p. 31).

Bertotti, B., Iess, L. & Tortora, P. (2003), *A test of general relativity using radio links with the Cassini spacecraft*, Nature **425** 374 (cit. on pp. 2, 72, 78).

Bhat, N. D. R., Bailes, M. & Verbiest, J. P. W. (2008), *Gravitational-radiation losses from the pulsar white-dwarf binary PSR J1141 6545*, Phys. Rev. D **77** 124017, arXiv: 0804.0956 [astro-ph] (cit. on p. 30).

Bhattacharya, D. & van den Heuvel, E. P. J. (1991), *Formation and evolution of binary and millisecond radio pulsars*, Phys. Rep. **203** 1 (cit. on p. 7).

Blanchet, L. (2014), *Gravitational Radiation from Post-Newtonian Sources and Inspiralling Compact Binaries*, Living Reviews in Relativity **17** 2, arXiv: 1310.1528 [gr-qc] (cit. on pp. 34, 47).

Blanchet, L. & Schäfer, G. (1989), *Higher order gravitational radiation losses in binary systems.*, MNRAS **239** 845 (cit. on pp. 34, 45).

Blandford, R. & Teukolsky, S. A. (1976), *Arrival-time analysis for a pulsar in a binary system.*, ApJ **205** 580 (cit. on pp. 17, 22, 55).

Bowyer, S., Byram, E. T., Chubb, T. A. & Friedman, H. (1964), *Lunar Occultation of X-ray Emission from the Crab Nebula*, Science **146** 912 (cit. on p. 4).

Boyles, J. et al. (2013), *The Green Bank Telescope 350 MHz Drift-scan survey. I. Survey Observations and the Discovery of 13 Pulsars*, ApJ **763** 80, arXiv: 1209.4293 [astro-ph.HE] (cit. on p. 74).

Bradaschia, C. et al. (1990), *The VIRGO Project: A wide band antenna for gravitational wave detection*, Nuclear Instruments and Methods in Physics Research Section A: Accelerators, Spectrometers, Detectors and Associated Equipment **289** 518, ISSN: 0168-9002, URL: https://www.sciencedirect.com/science/article/pii/016890029091525G (cit. on p. 84).

Brans, C. & Dicke, R. H. (1961), *Mach's Principle and a Relativistic Theory of Gravitation*, **124** 925 (cit. on p. 71).

Breton, R. P. et al. (2008), *Relativistic Spin Precession in the Double Pulsar*, Science **321** 104, arXiv: 0807.2644 [astro-ph] (cit. on pp. 8, 27, 30, 44, 47, 50).

Brillet, A., Giazotto, A. & al., et (1989), *Virgo Project Technical Report No. VIR-0517A-15*, URL: https://tds.ego-gw.it/?content=3&r=12122 (cit. on p. 84).

Burgay, M. et al. (2003), *An increased estimate of the merger rate of double neutron stars from observations of a highly relativistic system*, Nature **426** 531, arXiv: astro-ph/0312071 [astro-ph] (cit. on pp. 8, 28, 30, 50).

Caballero, R. N. et al. (2018), *Studying the Solar system with the International Pulsar Timing Array*, MNRAS **481** 5501, arXiv: 1809.10744 [astro-ph.EP] (cit. on p. 25).

Cameron, A. D. et al. (2018), *The High Time Resolution Universe Pulsar Survey - XIII. PSR J1757-1854, the most accelerated binary pulsar*, MNRAS **475** L57, arXiv: 1711.07697 [astro-ph.HE] (cit. on pp. 30, 46, 47).

Camilo, F. (2018), *African star joins the radio astronomy firmament*, Nature Astronomy **2** 594 (cit. on p. 30).

Capano, C. D. et al. (2020), *Stringent constraints on neutron-star radii from multimessenger observations and nuclear theory*, Nature Astron. **4** 625, arXiv: 1908.10352 [astro-ph.HE] (cit. on pp. 41, 42).

Chadwick, J. (1932), *Possible Existence of a Neutron*, Nature **129** 312 (cit. on p. 3).

Chalumeau, A. et al. (2022), *Noise analysis in the European Pulsar Timing Array data release 2 and its implications on the gravitational-wave background search*, MNRAS **509** 5538, arXiv: 2111.05186 [astro-ph.HE] (cit. on pp. 87, 92, 93).

Chandrasekhar, S. (1931), *The highly collapsed configurations of a stellar mass*, MNRAS **91** 456 (cit. on p. 3).

Chen, S. et al. (2021), *Common-red-signal analysis with 24-yr high-precision timing of the European Pulsar Timing Array: inferences in the stochastic gravitational-wave background search*, MNRAS **508** 4970, arXiv: 2110.13184 [astro-ph.HE] (cit. on pp. 25, 87, 92, 93).

Ciufolini, I. & Pavlis, E. C. (2004), *A confirmation of the general relativistic prediction of the Lense-Thirring effect*, Nature **431** 958 (cit. on pp. 2, 29).

Ciufolini, I. et al. (2019), *An improved test of the general relativistic effect of frame-dragging using the LARES and LAGEOS satellites*, European Physical Journal C **79** 872, arXiv: 1910.09908 [gr-qc] (cit. on pp. 2, 29).

Clifton, T., Ferreira, P. G., Padilla, A. & Skordis, C. (2012), *Modified gravity and cosmology*, Phys. Rep. **513** 1, arXiv: 1106.2476 [astro-ph.CO] (cit. on p. 3).

Cordes, J. M. & Lazio, T. J. W. (2002), *NE2001.I. A New Model for the Galactic Distribution of Free Electrons and its Fluctuations*, arXiv e-prints astro, arXiv: astro-ph/0207156 [astro-ph] (cit. on p. 35).

Cromartie, H. T. et al. (2019), *Relativistic Shapiro delay measurements of an extremely massive millisecond pulsar*, Nature Astronomy **4** 72, ISSN: 2397-3366, URL: http://dx.doi.org/10.1038/s41550-019-0880-2 (cit. on pp. 28, 29).

Damour, T. (1987), "The problem of motion in Newtonian and Einsteinian gravity.", *Three Hundred Years of Gravitation*, Cambridge University Press 128 (cit. on pp. 34, 45).

Damour, T. & Deruelle, N. (1985), *General relativistic celestial mechanics of binary systems. I. The post-Newtonian motion.*, Ann. Inst. Henri Poincaré Phys. Théor **43** 107 (cit. on pp. 21, 32, 61).

Damour, T. & Esposito-Farèse, G. (1992), *Tensor-multi-scalar theories of gravitation*, Classical and Quantum Gravity **9** 2093 (cit. on pp. 71–73).

Damour, T. & Schäfer, G. (1988), *Higher-order relativistic periastron advances and binary pulsars.*, Nuovo Cimento B Serie **101B** 127 (cit. on pp. 26, 28–32, 61).

Damour, T. (2007), *Binary Systems as Test-beds of Gravity Theories*, arXiv e-prints, arXiv: 0704.0749 [gr-qc] (cit. on p. 56).

Damour, T. & Deruelle, N. (1986), *General relativistic celestial mechanics of binary systems. II. The post-newtonian timing formula*, Annales de l'institut Henri Poincaré (A) Physique théorique **44** 263, URL: http://www.numdam.org/item?id=AIHPA_1986__44_3_263_0 (visited on 08/07/2014) (cit. on pp. 20–23, 31, 32, 55, 57, 58, 73).

Damour, T. & Esposito-Farèse, G. (1993), *Nonperturbative strong-field effects in tensor-scalar theories of gravitation*, Phys. Rev. Lett. **70** (15) 2220, URL: https://link.aps.org/doi/10.1103/PhysRevLett.70.2220 (cit. on p. 71).

Damour, T. & Esposito-Farèse, G. (1996), *Tensor-scalar gravity and binary-pulsar experiments*, Phys. Rev. D **54** 1474, arXiv: gr-qc/9602056 [gr-qc] (cit. on pp. 71, 73).

Damour, T. & Esposito-Farèse, G. (1998), *Gravitational-wave versus binary-pulsar tests of strong-field gravity*, Phys. Rev. D **58** 042001, arXiv: gr-qc/9803031 [gr-qc] (cit. on pp. 73, 78, 79).

Damour, T. & Taylor, J. H. (1991), *On the Orbital Period Change of the Binary Pulsar PSR 1913+16*, ApJ **366** 501 (cit. on pp. 33, 35, 36).

Damour, T. & Taylor, J. H. (1992), *Strong-field tests of relativistic gravity and binary pulsars*, Phys. Rev. D **45** 1840 (cit. on pp. 2, 20, 29, 30, 33, 42–44, 57, 61).

Degenaar, N. & Suleimanov, V. F. (2018), "Testing the Equation of State with Electromagnetic Observations", *Astrophysics and Space Science Library*, ed. by L. Rezzolla, P. Pizzochero, D. I. Jones, N. Rea & I. Vidaña, vol. 457, Astrophysics and Space Science Library 185 (cit. on p. 5).

Deller, A. T., Bailes, M. & Tingay, S. J. (2009), *Implications of a VLBI Distance to the Double Pulsar J0737-3039A/B*, Science **323** 1327, arXiv: 0902.0996 [astro-ph.SR] (cit. on p. 35).

Deller, A. T. et al. (2013), *VLBI Astrometry of PSR J2222-0137: A Pulsar Distance Measured to 0.4% Accuracy*, ApJ **770** 145, arXiv: 1305.4865 [astro-ph.SR] (cit. on pp. 74–76).

Demorest, P. et al. (2004), *Orientations of Spin and Magnetic Dipole Axes of Pulsars in the J0737-3039 Binary Based on Polarimetry Observations at the Green Bank Telescope*, ApJ **615** L137, arXiv: astro-ph/0402025 [astro-ph] (cit. on p. 63).

Demorest, P. B., Pennucci, T., Ransom, S. M., Roberts, M. S. E. & Hessels, J. W. T. (2010), *A two-solar-mass neutron star measured using Shapiro delay*, Nature **467** 1081, arXiv: 1010.5788 [astro-ph.HE] (cit. on p. 28).

Demorest, P. B. et al. (2013), *Limits on the Stochastic Gravitational Wave Background from the North American Nanohertz Observatory for Gravitational Waves*, ApJ **762** 94, arXiv: 1201.6641 [astro-ph.CO] (cit. on p. 17).

Desvignes, G. et al. (2016), *High-precision timing of 42 millisecond pulsars with the European Pulsar Timing Array*, MNRAS **458** 3341, arXiv: 1602.08511 [astro-ph.HE] (cit. on pp. 86, 87, 95).

Desvignes, G. et al. (2019), *Radio emission from a pulsar's magnetic pole revealed by general relativity*, Science **365** 1013, arXiv: 1909.06212 [astro-ph.HE] (cit. on p. 30).

Detweiler, S. (1979), *Pulsar timing measurements and the search for gravitational waves*, ApJ **234** 1100 (cit. on pp. 8, 85).

Dicke, R. H. (1946), *The Measurement of Thermal Radiation at Microwave Frequencies*, Review of Scientific Instruments **17** 268 (cit. on p. 17).

Dietrich, T. et al. (2020), *Multimessenger constraints on the neutron-star equation of state and the Hubble constant*, Science **370** 1450, arXiv: 2002.11355 [astro-ph.HE] (cit. on pp. 61, 62).

Doroshenko, O. V. & Kopeikin, S. M. (1995), *Relativistic effect of gravitational deflection of light in binary pulsars*, MNRAS **274** 1029, arXiv: astro-ph/9505065 [astro-ph] (cit. on pp. 22, 56, 57, 65, 67, 68).

Drever, R. W. P., Raab, F., Thorne, K., Vogt, R. & R., W. (1989), *Laser Interferometer Gravitational-wave Observatory (LIGO) Technical Report*, URL: https://dcc.ligo.org/LIGO-M890001/public/main (cit. on p. 84).

Dyson, F. W., Eddington, A. S. & Davidson, C. (1920), *A Determination of the Deflection of Light by the Sun's Gravitational Field, from Observations Made at the Total Eclipse of May 29, 1919*, Philosophical Transactions of the Royal Society of London Series A **220** 291 (cit. on p. 1).

Eddington, A. S. (1922), *The propagation of gravitational waves*, Proc. Roy. Soc. Lond. A **A102** 268 (cit. on p. 45).

Edwards, R. T., Hobbs, G. B. & Manchester, R. N. (2006), *TEMPO2, a new pulsar timing package - II. The timing model and precision estimates*, MNRAS **372** 1549, arXiv: astro-ph/0607664 [astro-ph] (cit. on p. 19).

Eilers, A.-C., Hogg, D. W., Rix, H.-W. & Ness, M. K. (2019), *The Circular Velocity Curve of the Milky Way from 5 to 25 kpc*, ApJ **871** 120, arXiv: 1810.09466 [astro-ph.GA] (cit. on pp. 36, 39, 43–46).

Einstein, A. (1915a), *Die Feldgleichungen der Gravitation*, Sitzungsberichte der Königlich Preußischen Akademie der Wissenschaften (Berlin) 844 (cit. on p. 1).

Einstein, A. (1915b), *Erklarung der Perihelionbewegung der Merkur aus der allgemeinen Relativitatstheorie*, Sitzungsberichte der Königlich Preußischen Akademie der Wissenschaften (Berlin) 831 (cit. on p. 1).

Einstein, A. (1916a), *Die Grundlage der allgemeinen Relativitätstheorie*, Annalen der Physik **354** 769 (cit. on p. 1).

Einstein, A. (1916b), *Näherungsweise Integration der Feldgleichungen der Gravitation*, Sitzungsberichte der Königlich Preußischen Akademie der Wissenschaften (Berlin 688 (cit. on p. 83).

Einstein, A. (1918), *Über Gravitationswellen*, Sitzungsber. Preuss. Akad. Wiss. Berlin (Math. Phys.) **1918** 154 (cit. on p. 45).

Esposito, L. W. & Harrison, E. R. (1975), *Properties of the Hulse-Taylor binary pulsar system.*, ApJ **196** L1 (cit. on p. 34).

Event Horizon Telescope Collaboration et al. (2019), *First M87 Event Horizon Telescope Results. I. The Shadow of the Supermassive Black Hole*, ApJ **875** L1, arXiv: 1906.11238 [astro-ph.GA] (cit. on p. 78).

Event Horizon Telescope Collaboration et al. (2022), *First Sagittarius A* Event Horizon Telescope Results. I. The Shadow of the Supermassive Black Hole in the Center of the Milky Way*, ApJ **930** L12 (cit. on p. 78).

Everitt, C. W. F. et al. (2011), *Gravity Probe B: Final Results of a Space Experiment to Test General Relativity*, Phys. Rev. Lett. **106** 221101, arXiv: 1105.3456 [gr-qc] (cit. on p. 2).

Ferdman, R. D. et al. (2008), "The double pulsar: evolutionary constraints from the system geometry", *40 Years of Pulsars: Millisecond Pulsars, Magnetars and More*, ed. by C. Bassa, Z. Wang, A. Cumming & V. M. Kaspi, vol. 983, American Institute of Physics Conference Series 474, arXiv: 0711.4927 [astro-ph] (cit. on pp. 31, 56).

Ferdman, R. D. et al. (2013), *The Double Pulsar: Evidence for Neutron Star Formation without an Iron Core-collapse Supernova*, ApJ **767** 85, arXiv: 1302.2914 [astro-ph.SR] (cit. on pp. 31, 56, 63).

Fierz, M. (1956), Helv. Phys. Acta **29** 128 (cit. on p. 71).

Fomalont, E., Kopeikin, S., Lanyi, G. & Benson, J. (2009), *Progress in Measurements of the Gravitational Bending of Radio Waves Using the VLBA*, ApJ **699** 1395, arXiv: 0904.3992 [astro-ph.CO] (cit. on p. 2).

Fonseca, E. et al. (2021), *Refined Mass and Geometric Measurements of the High-mass PSR J0740+6620*, ApJ **915** L12, arXiv: 2104.00880 [astro-ph.HE] (cit. on p. 8).

Foster, R. S. & Backer, D. C. (1990), *Constructing a Pulsar Timing Array*, ApJ **361** 300 (cit. on pp. 8, 85).

Freire, P. C. et al. (2003), *Further results from the timing of the millisecond pulsars in 47 Tucanae*, MNRAS **340** 1359 (cit. on p. 25).

Froeschle, M., Mignard, F. & Arenou, F. (1997), "Determination of the PPN Parameter gamma with the HIPPARCOS Data", *Hipparcos - Venice '97*, ed. by R. M. Bonnet et al., vol. 402, ESA Special Publication 49 (cit. on p. 2).

Gaia Collaboration (2016), *The Gaia mission*, A&A **595** A1, arXiv: 1609.04153 [astro-ph.IM] (cit. on pp. 26, 39, 47, 76).

Gaia Collaboration et al. (2022), *Gaia Data Release 3: Summary of the content and survey properties*, arXiv e-prints, arXiv: 2208.00211 [astro-ph.GA] (cit. on pp. 81, 98).

Giacconi, R., Gursky, H., Paolini, F. R. & Rossi, B. B. (1962), *Evidence for x Rays From Sources Outside the Solar System*, Phys. Rev. Lett. **9** 439 (cit. on p. 4).

Glover, S. C. O. & Mac Low, M. .-. (2011), *On the relationship between molecular hydrogen and carbon monoxide abundances in molecular clouds*, MNRAS **412** 337, arXiv: 1003.1340 [astro-ph.GA] (cit. on p. 36).

Gold, T. (1968), *Rotating Neutron Stars as the Origin of the Pulsating Radio Sources*, Nature **218** 731 (cit. on p. 4).

Goncharov, B. et al. (2021), *On the Evidence for a Common-spectrum Process in the Search for the Nanohertz Gravitational-wave Background with the Parkes Pulsar Timing Array*, ApJ **917** L19, arXiv: 2107.12112 [astro-ph.HE] (cit. on p. 87).

Gorda, T. (2016), *Global Properties of Rotating Neutron Stars with QCD Equations of State*, ApJ **832** 28, arXiv: 1605.08067 [astro-ph.HE] (cit. on p. 38).

Gravity Collaboration (2018), *Detection of the gravitational redshift in the orbit of the star S2 near the Galactic centre massive black hole*, A&A **615** L15, arXiv: 1807.09409 [astro-ph.GA] (cit. on p. 39).

Gravity Collaboration (2019), *A geometric distance measurement to the Galactic center black hole with 0.3% uncertainty*, A&A **625** L10, arXiv: 1904.05721 [astro-ph.GA] (cit. on pp. 34, 35, 39, 41, 43–45).

Gravity Collaboration (2020), *Detection of the Schwarzschild precession in the orbit of the star S2 near the Galactic centre massive black hole*, A&A **636** L5, arXiv: 2004.07187 [astro-ph.GA] (cit. on p. 35).

Greif, S. K., Hebeler, K., Lattimer, J. M., Pethick, C. J. & Schwenk, A. (2020), *Equation of State Constraints from Nuclear Physics, Neutron Star Masses, and Future Moment of Inertia Measurements*, ApJ **901** 155, arXiv: 2005.14164 [astro-ph.HE] (cit. on pp. 28, 38, 41).

Grishchuk, L. P. (2005), *REVIEWS OF TOPICAL PROBLEMS: Relic gravitational waves and cosmology*, Physics Uspekhi **48** 1235, arXiv: gr-qc/0504018 [gr-qc] (cit. on p. 85).

Grosser, M. (1979), *The discovery of Neptune* (cit. on p. 1).

Guillemot, L. et al. (2013), *Fermi LAT Pulsed Detection of PSR J0737-3039A in the Double Pulsar System*, ApJ **768** 169, arXiv: 1303.7352 [astro-ph.HE] (cit. on p. 63).

Guinot, B. & Petit, G. (1991), *Atomic time and the rotation of pulsars.*, A&A **248** 292 (cit. on p. 100).

Guo, Y. J., Lee, K. J. & Caballero, R. N. (2018), *A dynamical approach in exploring the unknown mass in the Solar system using pulsar timing arrays*, MNRAS **475** 3644, arXiv: 1802.05452 [astro-ph.IM] (cit. on p. 25).

Guo, Y. J. et al. (2021), *PSR J2222−0137. I. Improved physical parameters for the system*, A&A **654** A16, arXiv: 2107.09474 [astro-ph.HE] (cit. on pp. 8, 74–76, 78, 81, 92).

Haensel, P., Potekhin, A. Y. & Yakovlev, D. G. (2007), *Neutron Stars 1 : Equation of State and Structure*, vol. 326 (cit. on p. 4).

Han, J. L., Manchester, R. N., Lyne, A. G., Qiao, G. J. & van Straten, W. (2006), *Pulsar Rotation Measures and the Large-Scale Structure of the Galactic Magnetic Field*, ApJ **642** 868, arXiv: astro-ph/0601357 [astro-ph] (cit. on p. 12).

Han, J. L., Manchester, R. N., van Straten, W. & Demorest, P. (2018), *Pulsar Rotation Measures and Large-scale Magnetic Field Reversals in the Galactic Disk*, ApJS **234** 11, arXiv: 1712.01997 [astro-ph.GA] (cit. on pp. 9, 12).

Hankins, T. H. & Rickett, B. J. (1975), *Pulsar signal processing.*, Methods in Computational Physics **14** 55 (cit. on p. 11).

Haskell, B. & Melatos, A. (2015), *Models of pulsar glitches*, International Journal of Modern Physics D **24** 1530008, arXiv: 1502.07062 [astro-ph.SR] (cit. on p. 8).

Hawking, S. W. (1972), *Black holes in the Brans-Dicke: Theory of gravitation*, Communications in Mathematical Physics **25** 167 (cit. on p. 72).

Hawking, S. W. & Israel, W. (1989), *Three Hundred Years of Gravitation* (cit. on p. 3).

Heger, A., Fryer, C. L., Woosley, S. E., Langer, N. & Hartmann, D. H. (2003), *How Massive Single Stars End Their Life*, The Astrophysical Journal **591** 288, URL: https://doi.org/10.1086/375341 (cit. on p. 4).

Hellings, R. W. & Downs, G. S. (1983), *Upper limits on the isotropic gravitational radiation background from pulsar timing analysis.*, ApJ **265** L39 (cit. on p. 86).

Hewish, A., Bell, S. J., Pilkington, J. D. H., Scott, P. F. & Collins, R. A. (1968), *Observation of a Rapidly Pulsating Radio Source*, Nature **217** 709 (cit. on p. 4).

Hobbs, G. et al. (2012), *Development of a pulsar-based time-scale*, MNRAS **427** 2780, arXiv: 1208.3560 [astro-ph.IM] (cit. on pp. 8, 25, 100).

Hobbs, G. et al. (2020), *A pulsar-based time-scale from the International Pulsar Timing Array*, MNRAS **491** 5951, arXiv: 1910.13628 [astro-ph.IM] (cit. on pp. 8, 100).

Hobbs, G. B., Edwards, R. T. & Manchester, R. N. (2006), *TEMPO2, a new pulsar-timing package - I. An overview*, MNRAS **369** 655, arXiv: astro-ph/0603381 [astro-ph] (cit. on pp. 19, 55).

Holmberg, J. & Flynn, C. (2004), *The local surface density of disc matter mapped by Hipparcos*, MNRAS **352** 440, arXiv: astro-ph/0405155 [astro-ph] (cit. on pp. 35, 76).

Hotan, A. W., van Straten, W. & Manchester, R. N. (2004), *PSRCHIVE and PSRFITS: An Open Approach to Radio Pulsar Data Storage and Analysis*, PASA **21** 302, arXiv: astro-ph/0404549 [astro-ph] (cit. on pp. 16, 52).

Hu, H. et al. (2022), *Gravitational signal propagation in the double pulsar studied with the MeerKAT telescope*, A&A **667** A149, arXiv: 2209.11798 [astro-ph.HE] (cit. on pp. 28, 37).

Hu, H., Kramer, M., Wex, N., Champion, D. J. & Kehl, M. S. (2020), *Constraining the dense matter equation-of-state with radio pulsars*, MNRAS **497** 3118, arXiv: 2007.07725 [astro-ph.SR] (cit. on pp. 60, 61, 66, 70, 75).

Hulse, R. A. & Taylor, J. H. (1975), *Discovery of a pulsar in a binary system.*, ApJ **195** L51 (cit. on pp. 2, 8, 83).

Imgrund, M., Champion, D. J., Kramer, M. & Lesch, H. (2015), *A Bayesian method for pulsar template generation*, MNRAS **449** 4162, arXiv: 1501.03497 [astro-ph.IM] (cit. on p. 37).

Iyer, B. R. & Will, C. M. (1995), *Post-Newtonian gravitational radiation reaction for two-body systems: Nonspinning bodies*, Phys. Rev. D **52** 6882 (cit. on p. 45).

Jacoby, B. A. et al. (2006), *Measurement of Orbital Decay in the Double Neutron Star Binary PSR B2127+11C*, ApJ **644** L113, arXiv: astro-ph/0605375 [astro-ph] (cit. on p. 79).

Jaffe, A. H. & Backer, D. C. (2003), *Gravitational Waves Probe the Coalescence Rate of Massive Black Hole Binaries*, ApJ **583** 616, arXiv: astro-ph/0210148 [astro-ph] (cit. on p. 85).

Janssen, G. H. et al. (2008), "European Pulsar Timing Array", *40 Years of Pulsars: Millisecond Pulsars, Magnetars and More*, ed. by C. Bassa, Z. Wang, A. Cumming & V. M. Kaspi, vol. 983, American Institute of Physics Conference Series 633 (cit. on p. 86).

Jeans, J. H. (1924), *Cosmogonic problems associated with a secular decrease of mass*, MNRAS **85** 2 (cit. on p. 36).

Jeans, J. H. (1925), *The effect of varying mass on a binary system*, MNRAS **85** 912 (cit. on p. 36).

Jenet, F. et al. (2009), *The North American Nanohertz Observatory for Gravitational Waves*, arXiv e-prints, arXiv: 0909.1058 [astro-ph.IM] (cit. on p. 86).

Jenet, F. A. et al. (2006), *Upper Bounds on the Low-Frequency Stochastic Gravitational Wave Background from Pulsar Timing Observations: Current Limits and Future Prospects*, The Astrophysical Journal **653** 1571, URL: https://doi.org/10.1086/508702 (cit. on p. 85).

Jenet, F. A., Hobbs, G. B., Lee, K. J. & Manchester, R. N. (2005), *Detecting the Stochastic Gravitational Wave Background Using Pulsar Timing*, ApJ **625** L123, arXiv: astro-ph/0504458 [astro-ph] (cit. on p. 86).

Jiang, P. et al. (2019), *Commissioning progress of the FAST*, Science China Physics, Mechanics, and Astronomy **62** 959502, arXiv: 1903.06324 [astro-ph.IM] (cit. on pp. 15, 94, 95).

Johnston, H. M. & Kulkarni, S. R. (1991), *On the Detectability of Pulsars in Close Binary Systems*, ApJ **368** 504 (cit. on p. 46).

Jones, P. B. (1990), *The generation of timing noise by superfluid rotation in pulsars.*, MNRAS **246** 364 (cit. on p. 25).

Jordan, P. (1955), *Schwerkraft und Weltall*, Die Wissenschaft, Vieweg, URL: https://books.google.de/books?id=VP85AQAAIAAJ (cit. on p. 71).

Jordan, P. (1959), *Zum gegenwärtigen Stand der Diracschen kosmologischen Hypothesen*, **157** 112 (cit. on p. 71).

Jouteux, S., Ramachandran, R., Stappers, B. W., Jonker, P. G. & van der Klis, M. (2002), *Searching for pulsars in close circular binary systems*, A&A **384** 532, arXiv: astro-ph/0111231 [astro-ph] (cit. on p. 46).

Junker, W. & Schäfer, G. (1992), *Binary systems - Higher order gravitational radiation damping and wave emission*, MNRAS **254** 146 (cit. on p. 35).

Kehl, M. S. (2015), *Prospects of measuring the Lense-Thirring precession in the Double Pulsar*, MA thesis: University of Bonn (cit. on p. 36).

Kehl, M. S., Wex, N., Kramer, M. & Liu, K. (2017), "Future measurements of the Lense-Thirring effect in the Double Pulsar", *14th Marcel Grossmann Meeting on Recent Developments in Theoretical and Experimental General Relativity, Astrophysics, and Relativistic Field Theories*, vol. 2 1860, arXiv: 1605.00408 [astro-ph.HE] (cit. on pp. 30, 39, 40, 47).

Keith, M. J. et al. (2013), *Measurement and correction of variations in interstellar dispersion in high-precision pulsar timing*, MNRAS **429** 2161, arXiv: 1211.5887 [astro-ph.GA] (cit. on p. 25).

Kennefick, D. (2007), *Traveling at the Speed of Thought: Einstein and the Quest for Gravitational Waves* (cit. on p. 83).

Kibble, T. W. B. (1976), *Topology of cosmic domains and strings*, Journal of Physics A Mathematical General **9** 1387 (cit. on p. 85).

Klioner, S. A. & Kopeikin, S. M. (1992), *Microarcsecond Astrometry in Space: Relativistic Effects and Reduction of Observations*, AJ **104** 897 (cit. on p. 68).

Klioner, S. A. & Zschocke, S. (2010), *Numerical versus analytical accuracy of the formulae for light propagation*, Classical and Quantum Gravity **27** 075015, arXiv: 1001.2133 [astro-ph.CO] (cit. on pp. 22, 55).

Königsdörffer, C., Faye, G. & Schäfer, G. (2003), *Binary black-hole dynamics at the third-and-a-half post-Newtonian order in the ADM formalism*, Phys. Rev. D **68** 044004, arXiv: gr-qc/0305048 [gr-qc] (cit. on p. 45).

Kopeikin, S. M. (1996), *Proper Motion of Binary Pulsars as a Source of Secular Variations of Orbital Parameters*, ApJ **467** L93 (cit. on p. 32).

Kopeikin, S. M. & Schäfer, G. (1999), *Lorentz covariant theory of light propagation in gravitational fields of arbitrary-moving bodies*, Phys. Rev. D **60** 124002, arXiv: gr-qc/9902030 [gr-qc] (cit. on pp. 22, 55, 57, 68).

Kramer, M. & Wex, N. (2009), *TOPICAL REVIEW: The double pulsar system: a unique laboratory for gravity*, Classical and Quantum Gravity **26** 073001 (cit. on pp. 30, 31, 47).

Kramer, M. (1994), *Geometrical analysis of average pulsar profiles using multi-component Gaussian FITS at several frequencies. II. Individual results.*, A&AS **107** 527 (cit. on p. 17).

Kramer, M. & Stairs, I. H. (2008), *The double pulsar.*, ARA&A **46** 541 (cit. on p. 9).

Kramer, M. & Stappers, B. (2015), "Pulsar Science with the SKA", *Advancing Astrophysics with the Square Kilometre Array (AASKA14)* 36, arXiv: 1507.04423 [astro-ph.IM] (cit. on p. 30).

Kramer, M., Wielebinski, R., Jessner, A., Gil, J. A. & Seiradakis, J. H. (1994), *Geometrical analysis of average pulsar profiles using multi-component Gaussian FITS at several frequencies. I. Method and analysis.*, A&AS **107** 515 (cit. on p. 17).

Kramer, M. et al. (2006a), *Strong-field tests of gravity with the double pulsar*, Annalen der Physik **15** 34 (cit. on p. 57).

Kramer, M. et al. (2006b), *Tests of General Relativity from Timing the Double Pulsar*, Science **314** 97, arXiv: astro-ph/0609417 [astro-ph] (cit. on pp. 2, 8, 30–34, 38, 50, 55, 56).

Kramer, M. et al. (2021a), *Strong-Field Gravity Tests with the Double Pulsar*, Physical Review X **11** 041050, arXiv: 2112.06795 [astro-ph.HE] (cit. on pp. 2, 8, 21, 32–38, 48–50, 52, 54, 57–63, 66, 67, 69, 97, 99).

Kramer, M. et al. (2021b), *The relativistic binary programme on MeerKAT: science objectives and first results*, MNRAS **504** 2094, arXiv: 2102.05160 [astro-ph.HE] (cit. on pp. 51, 52, 60, 63, 74).

Kramer, M. (1998), *Determination of the Geometry of the PSR B1913+16 System by Geodetic Precession*, ApJ **509** 856, arXiv: astro-ph/9808127 [astro-ph] (cit. on p. 30).

Kramer, M. (2016), *Pulsars as probes of gravity and fundamental physics*, International Journal of Modern Physics D **25** 1630029, arXiv: 1606.03843 [astro-ph.HE] (cit. on p. 48).

Kramer, M. & Champion, D. J. (2013), *The European Pulsar Timing Array and the Large European Array for Pulsars*, Classical and Quantum Gravity **30** 224009 (cit. on p. 86).

Kulkarni, S. R. (2020), *Dispersion measure: Confusion, Constants & Clarity*, arXiv e-prints, arXiv: 2007.02886 [astro-ph.HE] (cit. on p. 11).

Lai, D. & Rafikov, R. R. (2005), *Effects of Gravitational Lensing in the Double Pulsar System J0737-3039*, ApJ **621** L41, arXiv: astro-ph/0411726 [astro-ph] (cit. on pp. 67, 68).

Lam, M. T. et al. (2019), *The NANOGrav 12.5 yr Data Set: The Frequency Dependence of Pulse Jitter in Precision Millisecond Pulsars*, ApJ **872** 193, arXiv: 1809.03058 [astro-ph.HE] (cit. on p. 24).

Landau, L. D. (1932), *To the Stars theory*, Phys. Zs. Sowjet **1** 285 (cit. on p. 3).

Landry, P., Essick, R. & Chatziioannou, K. (2020), *Nonparametric constraints on neutron star matter with existing and upcoming gravitational wave and pulsar observations*, arXiv e-prints **101** 123007, arXiv: 2003.04880 [astro-ph.HE] (cit. on p. 47).

Large, M. I., Vaughan, A. E. & Mills, B. Y. (1968), *A Pulsar Supernova Association?*, Nature **220** 340 (cit. on p. 4).

Lattimer, J. M. & Prakash, M. (2001), *Neutron Star Structure and the Equation of State*, The Astrophysical Journal **550** 426, ISSN: 1538-4357, URL: http://dx.doi.org/10.1086/319702 (cit. on pp. 5, 27, 29, 38).

Lattimer, J. M. & Prakash, M. (2016), *The equation of state of hot, dense matter and neutron stars*, Physics Reports **621** 127, ISSN: 0370-1573, URL: http://dx.doi.org/10.1016/j.physrep.2015.12.005 (cit. on pp. 5, 27).

Lattimer, J. M. & Schutz, B. F. (2005), *Constraining the Equation of State with Moment of Inertia Measurements*, ApJ **629** 979, arXiv: astro-ph/0411470 [astro-ph] (cit. on pp. 28, 29, 41).

Lau, M. Y. M. et al. (2020), *Detecting double neutron stars with LISA*, MNRAS **492** 3061, ISSN: 0035-8711, eprint: https://academic.oup.com/mnras/article-pdf/492/3/3061/31907130/staa002.pdf, URL: https://doi.org/10.1093/mnras/staa002 (cit. on pp. 46, 48).

Lazaridis, K. et al. (2009), *Generic tests of the existence of the gravitational dipole radiation and the variation of the gravitational constant*, MNRAS **400** 805, arXiv: 0908.0285 [astro-ph.GA] (cit. on p. 35).

Lazarus, P. et al. (2016), *Prospects for high-precision pulsar timing with the new Effelsberg PSRIX backend*, MNRAS **458** 868, arXiv: 1601.06194 [astro-ph.IM] (cit. on pp. 16, 51).

Le Verrier, U. (1859), *Lettre de M. Le Verrier à M. Faye sur la théorie de Mercure et sur le mouvement du périhélie de cette planète*, Comptes rendus hebdomadaires des séances de l'Académie des sciences (Paris) **49** 379 (cit. on p. 1).

Lebach, D. E. et al. (1995), *Measurement of the Solar Gravitational Deflection of Radio Waves Using Very-Long-Baseline Interferometry*, Phys. Rev. Lett. **75** 1439 (cit. on p. 2).

Lee, K. J. (2016), "Prospects of Gravitational Wave Detection Using Pulsar Timing Array for Chinese Future Telescopes", *Frontiers in Radio Astronomy and FAST Early Sciences Symposium 2015*, ed. by L. Qain & D. Li, vol. 502, Astronomical Society of the Pacific Conference Series 19 (cit. on p. 86).

Lense, J. & Thirring, H. (1918), *Über den Einfluß der Eigenrotation der Zentralkörper auf die Bewegung der Planeten und Monde nach der Einsteinschen Gravitationstheorie*, Physikalische Zeitschrift **19** 156 (cit. on p. 29).

Lentati, L., Champion, D. J., Kramer, M., Barr, E. & Torne, P. (2018), *COBRA: a Bayesian approach to pulsar searching*, MNRAS **473** 5026 (cit. on p. 48).

Lentati, L. et al. (2014), *TEMPONEST: a Bayesian approach to pulsar timing analysis*, MNRAS **437** 3004, arXiv: 1310.2120 [astro-ph.IM] (cit. on p. 24).

Lentati, L. et al. (2017), *Wide-band profile domain pulsar timing analysis*, MNRAS **466** 3706, arXiv: 1612.05258 [astro-ph.IM] (cit. on p. 25).

Li, D. et al. (2018), *FAST in Space: Considerations for a Multibeam, Multipurpose Survey Using China's 500-m Aperture Spherical Radio Telescope (FAST)*, IEEE Microwave Magazine **19** 112, arXiv: 1802.03709 [astro-ph.IM] (cit. on p. 46).

Lim, Y., Holt, J. W. & Stahulak, R. J. (2019), *Predicting the moment of inertia of pulsar J0737-3039A from Bayesian modeling of the nuclear equation of state*, Phys. Rev. C **100** 035802, arXiv: 1810.10992 [nucl-th] (cit. on p. 38).

Liu, K., Eatough, R. P., Wex, N. & Kramer, M. (2014a), *Pulsar-black hole binaries: prospects for new gravity tests with future radio telescopes*, MNRAS **445** 3115, arXiv: 1409.3882 [astro-ph.GA] (cit. on pp. 2, 79, 98).

Liu, K. et al. (2014b), *Measuring pulse times of arrival from broad-band pulsar observations*, MNRAS **443** 3752, arXiv: 1407.3827 [astro-ph.GA] (cit. on p. 17).

Liu, K. et al. (2016), *Variability, polarimetry, and timing properties of single pulses from PSR J1713+0747 using the Large European Array for Pulsars*, MNRAS **463** 3239, arXiv: 1609.00188 [astro-ph.HE] (cit. on p. 93).

Liu, K. et al. (2022), *Detection of quasi-periodic micro-structure in three millisecond pulsars with the Large European Array for Pulsars*, MNRAS **513** 4037, arXiv: 2206.10045 [astro-ph.HE] (cit. on p. 93).

Lorimer, D. R. & Kramer, M. (2004), *Handbook of Pulsar Astronomy*, vol. 4 (cit. on pp. 4, 5, 10, 11, 13, 17, 61, 75).

Lorimer, D. R. (2001), *Binary and Millisecond Pulsars at the New Millennium*, Living Reviews in Relativity **4** 5, arXiv: astro-ph/0104388 [astro-ph] (cit. on p. 7).

Luo, J. et al. (2016), *TianQin: a space-borne gravitational wave detector*, Classical and Quantum Gravity **33** 035010, arXiv: 1512.02076 [astro-ph.IM] (cit. on p. 84).

Lyne, A. G. et al. (2004), *A Double-Pulsar System: A Rare Laboratory for Relativistic Gravity and Plasma Physics*, Science **303** 1153, arXiv: astro-ph/0401086 [astro-ph] (cit. on pp. 8, 28, 30, 50).

Lyne, A., Hobbs, G., Kramer, M., Stairs, I. & Stappers, B. (2010), *Switched Magnetospheric Regulation of Pulsar Spin-Down*, Science **329** 408, arXiv: 1006.5184 [astro-ph.GA] (cit. on p. 24).

Lyne, A. G. & Graham-Smith, F. (2006), *Pulsar Astronomy* (cit. on pp. 4, 6).

Maggiore, M. (2000), *Gravitational wave experiments and early universe cosmology*, Physics Reports **331** 283, ISSN: 0370-1573, URL: https://www.sciencedirect.com/science/article/pii/S0370157399001027 (cit. on p. 85).

Main, R. A. et al. (2020), *Measuring interstellar delays of PSR J0613-0200 over 7 yr, using the Large European Array for Pulsars*, MNRAS **499** 1468, arXiv: 2009.10707 [astro-ph.HE] (cit. on pp. 25, 93).

Mall, G. et al. (2022), *Modelling annual scintillation arc variations in PSR J1643-1224 using the Large European Array for Pulsars*, MNRAS **511** 1104, arXiv: 2201.04245 [astro-ph.HE] (cit. on p. 93).

Manchester, R. N. (2006), *The Parkes Pulsar Timing Array*, Chinese Journal of Astronomy and Astrophysics Supplement **6** 139, arXiv: astro-ph/0604288 [astro-ph] (cit. on p. 86).

Manchester, R. N., Hobbs, G. B., Teoh, A. & Hobbs, M. (2005), *The Australia Telescope National Facility Pulsar Catalogue*, AJ **129** 1993, arXiv: astro-ph/0412641 [astro-ph] (cit. on p. 6).

Manchester, R. N. & IPTA (2013), *The International Pulsar Timing Array*, Classical and Quantum Gravity **30** 224010, arXiv: 1309.7392 [astro-ph.IM] (cit. on p. 86).

Manchester, R. N. & Taylor, J. H. (1972), *Parameters of 61 Pulsars*, Astrophys. Lett. **10** 67 (cit. on p. 11).

McKee, J. W. et al. (2019), *A detailed study of giant pulses from PSR B1937+21 using the Large European Array for Pulsars*, MNRAS **483** 4784, arXiv: 1811.02856 [astro-ph.HE] (cit. on p. 93).

Melatos, A. & Link, B. (2014), *Pulsar timing noise from superfluid turbulence*, MNRAS **437** 21, arXiv: 1310.3108 [astro-ph.HE] (cit. on p. 24).

Miller, M. C. et al. (2019), *PSR J0030+0451 Mass and Radius from NICER Data and Implications for the Properties of Neutron Star Matter*, ApJ **887** L24, arXiv: 1912.05705 [astro-ph.HE] (cit. on pp. 27, 41).

Moore, C. J., Cole, R. H. & Berry, C. P. L. (2015), *Gravitational-wave sensitivity curves*, Classical and Quantum Gravity **32** 015014, arXiv: 1408.0740 [gr-qc] (cit. on pp. 84, 85).

Morrison, I. A., Baumgarte, T. W., Shapiro, S. L. & Pand haripande, V. R. (2004), *The Moment of Inertia of the Binary Pulsar J0737-3039A: Constraining the Nuclear Equation of State*, ApJ **617** L135, arXiv: astro-ph/0411353 [astro-ph] (cit. on pp. 28, 29).

Müther, H., Prakash, M. & Ainsworth, T. L. (1987), *The nuclear symmetry energy in relativistic Brueckner-Hartree-Fock calculations*, Physics Letters B **199** 469 (cit. on p. 73).

Nan, R. et al. (2011), *THE FIVE-HUNDRED-METER APERTURE SPHERICAL RADIO TELESCOPE (FAST) PROJECT*, International Journal of Modern Physics D **20** 989, eprint: https://doi.org/10.1142/S0218271811019335, URL: https://doi.org/10.1142/S0218271811019335 (cit. on p. 37).

Neininger, N., Guélin, M., Ungerechts, H., Lucas, R. & Wielebinski, R. (1998), *Carbon monoxide emission as a precise tracer of molecular gas in the Andromeda galaxy*, Nature **395** 871 (cit. on p. 36).

Newton, I. (1687), *Philosophiae Naturalis Principia Mathematica. Auctore Js. Newton* (cit. on p. 1).

Ng, C. et al. (2014), *The High Time Resolution Universe pulsar survey - X. Discovery of four millisecond pulsars and updated timing solutions of a further 12*, MNRAS **439** 1865, arXiv: 1401.3003 [astro-ph.HE] (cit. on p. 46).

Nice, D. et al. (2015), *Tempo: Pulsar timing data analysis*, ascl: 1509.002 (cit. on pp. 19, 31, 32, 52, 73).

Nice, D. J. & Taylor, J. H. (1995), *PSR J2019+2425 and PSR J2322+2057 and the Proper Motions of Millisecond Pulsars*, ApJ **441** 429 (cit. on p. 35).

Nissanke, S. & Blanchet, L. (2005), *Gravitational radiation reaction in the equations of motion of compact binaries to 3.5 post-Newtonian order*, Classical and Quantum Gravity **22** 1007, arXiv: gr-qc/0412018 [gr-qc] (cit. on p. 45).

Nomoto, K., Thielemann, F. .-. & Yokoi, K. (1984), *Accreting white dwarf models for type I supern. III. Carbon deflagration supernovae.*, ApJ **286** 644 (cit. on p. 4).

Nordtvedt, K. (1999), *30 years of lunar laser ranging and the gravitational interaction*, Classical and Quantum Gravity **16** A101 (cit. on p. 2).

Oppenheimer, J. R. & Volkoff, G. M. (1939), *On Massive Neutron Cores*, Physical Review **55** 374 (cit. on pp. 3, 4).

Özel, F. & Freire, P. (2016), *Masses, Radii, and the Equation of State of Neutron Stars*, ARA&A **54** 401, arXiv: 1603.02698 [astro-ph.HE] (cit. on p. 27).

Pacini, F. (1967), *Energy Emission from a Neutron Star*, Nature **216** 567 (cit. on p. 4).

Parthasarathy, A. et al. (2021), *Measurements of pulse jitter and single-pulse variability in millisecond pulsars using MeerKAT*, MNRAS **502** 407, arXiv: 2101.08531 [astro-ph.HE] (cit. on pp. 24, 60).

Pati, M. E. & Will, C. M. (2002), *Post-Newtonian gravitational radiation and equations of motion via direct integration of the relaxed Einstein equations. II. Two-body equations of motion to second post-Newtonian order, and radiation reaction to 3.5 post-Newtonian order*, Phys. Rev. D **65** 104008, arXiv: gr-qc/0201001 [gr-qc] (cit. on p. 45).

Pennucci, T. T. (2019), *Frequency-dependent Template Profiles for High-precision Pulsar Timing*, ApJ **871** 34, arXiv: 1812.02006 [astro-ph.HE] (cit. on p. 17).

Perera, B. B. P. et al. (2019), *The International Pulsar Timing Array: second data release*, MNRAS **490** 4666, arXiv: 1909.04534 [astro-ph.HE] (cit. on p. 86).

Perlick, V. (2004), *Gravitational Lensing from a Spacetime Perspective*, Living Reviews in Relativity **7** 9 (cit. on p. 55).

Peters, P. C. (1964), *Gravitational Radiation and the Motion of Two Point Masses*, Physical Review **136** 1224 (cit. on p. 46).

Peters, P. C. & Mathews, J. (1963), *Gravitational Radiation from Point Masses in a Keplerian Orbit*, Physical Review **131** 435 (cit. on p. 34).

Pfister, H. (2007), *On the history of the so-called Lense-Thirring effect*, General Relativity and Gravitation **39** 1735 (cit. on p. 29).

Phinney, E. S. (2001), *A Practical Theorem on Gravitational Wave Backgrounds*, arXiv e-prints astro, arXiv: astro-ph/0108028 [astro-ph] (cit. on p. 86).

Piran, T. & Shaviv, N. J. (2004), *On the Low Progenitor Mass of the Binary Pulsar J0737-3039B*, arXiv e-prints, arXiv: astro-ph/0401553 (cit. on p. 56).

Pol, N. et al. (2018), *A Direct Measurement of Sense of Rotation of PSR J0737–3039A*, The Astrophysical Journal **853** 73, URL: https://doi.org/10.3847/1538-4357/aaa1a0 (cit. on pp. 31, 50).

Prša, A. et al. (2016), *Nominal Values for Selected Solar and Planetary Quantities: IAU 2015 Resolution B3*, AJ **152** 41, arXiv: 1605.09788 [astro-ph.SR] (cit. on pp. xii, 23, 55).

Rafikov, R. R. & Lai, D. (2006a), *Effects of gravitational lensing and companion motion on the binary pulsar timing*, Phys. Rev. D **73** 063003, arXiv: astro-ph/0512417 [astro-ph] (cit. on pp. 22, 23, 50, 55, 57, 63, 67).

Rafikov, R. R. & Lai, D. (2006b), *Effects of Pulsar Rotation on Timing Measurements of the Double Pulsar System J0737-3039*, ApJ **641** 438, arXiv: astro-ph/0503461 [astro-ph] (cit. on pp. 23, 50, 56, 63, 65, 67, 68).

Rajagopal, M. & Romani, R. W. (1995), *Ultra–Low-Frequency Gravitational Radiation from Massive Black Hole Binaries*, ApJ **446** 543, arXiv: astro-ph/9412038 [astro-ph] (cit. on p. 85).

Ramazanoğlu, F. M. & Pretorius, F. (2016), *Spontaneous scalarization with massive fields*, Phys. Rev. D **93** 064005, arXiv: 1601.07475 [gr-qc] (cit. on p. 44).

Ransom, S. M. et al. (2004), *Orbital Modulation of the Apparent Dispersion Measure Towards PSR J0737-3039A*, arXiv e-prints, arXiv: astro-ph/0406321 (cit. on p. 54).

Ransom, S. M. (2001), *New search techniques for binary pulsars*, PhD thesis: Harvard University (cit. on p. 46).

Reid, M. J. et al. (2014), *A Parallax Distance to the Microquasar GRS 1915+105 and a Revised Estimate of its Black Hole Mass*, ApJ **796** 2, arXiv: 1409.2453 [astro-ph.GA] (cit. on pp. 34, 36, 39, 41, 43–45).

Rezzolla, L., Most, E. R. & Weih, L. R. (2018), *Using Gravitational-wave Observations and Quasi-universal Relations to Constrain the Maximum Mass of Neutron Stars*, ApJ **852** L25, arXiv: 1711.00314 [astro-ph.HE] (cit. on p. 28).

Richards, D. W. & Comella, J. M. (1969), *The Period of Pulsar NP 0532*, Nature **222** 551 (cit. on p. 4).

Rickett, B. J. et al. (2014), *Interstellar Scintillation of the Double Pulsar J0737-3039*, ApJ **787** 161, arXiv: 1404.1120 [astro-ph.SR] (cit. on p. 33).

Riles, K. (2013), *Gravitational waves: Sources, detectors and searches*, Progress in Particle and Nuclear Physics **68** 1, arXiv: 1209.0667 [hep-ex] (cit. on p. 84).

Riley, T. E. et al. (2019), *A NICER View of PSR J0030+0451: Millisecond Pulsar Parameter Estimation*, ApJ **887** L21, arXiv: 1912.05702 [astro-ph.HE] (cit. on pp. 27, 41).

Ruan, W.-H., Guo, Z.-K., Cai, R.-G. & Zhang, Y.-Z. (2018), *Taiji Program: Gravitational-Wave Sources*, arXiv e-prints, arXiv: 1807.09495 [gr-qc] (cit. on p. 84).

Sana, H. et al. (2012), *Binary Interaction Dominates the Evolution of Massive Stars*, Science **337** 444, arXiv: 1207.6397 [astro-ph.SR] (cit. on p. 7).

Sanidas, S. A., Battye, R. A. & Stappers, B. W. (2012), *Constraints on cosmic string tension imposed by the limit on the stochastic gravitational wave background from the European Pulsar Timing Array*, Phys. Rev. D **85** (12) 122003, URL: https://link.aps.org/doi/10.1103/PhysRevD.85.122003 (cit. on p. 85).

Sazhin, M. V. (1978), *Opportunities for detecting ultralong gravitational waves*, Soviet Ast. **22** 36 (cit. on pp. 8, 85).

Schäfer, G. & Wex, N. (1993), *Second post-Newtonian motion of compact binaries*, Physics Letters A **174** 196 (cit. on p. 32).

Scheuer, P. A. G. (1968), *Amplitude Variations in Pulsed Radio Sources*, Nature **218** 920 (cit. on p. 12).

Schneider, P., Ehlers, J. & Falco, E. E. (1992), *Gravitational Lenses*, Springer-Verlag New York (cit. on pp. 67, 68).

Serylak, M. et al. (2021), *The thousand-pulsar-array programme on MeerKAT IV: Polarization properties of young, energetic pulsars*, MNRAS **505** 4483, arXiv: 2009.05797 [astro-ph.HE] (cit. on p. 51).

Sesana, A. (2013), *Insights into the astrophysics of supermassive black hole binaries from pulsar timing observations*, Classical and Quantum Gravity **30** 224014, arXiv: 1307.2600 [astro-ph.CO] (cit. on p. 85).

Sesana, A., Haardt, F., Madau, P. & Volonteri, M. (2004), *Low-Frequency Gravitational Radiation from Coalescing Massive Black Hole Binaries in Hierarchical Cosmologies*, ApJ **611** 623, arXiv: astro-ph/0401543 [astro-ph] (cit. on p. 85).

Shannon, R. M. et al. (2014), *Limitations in timing precision due to single-pulse shape variability in millisecond pulsars*, MNRAS **443** 1463, arXiv: 1406.4716 [astro-ph.SR] (cit. on p. 24).

Shao, L., Sennett, N., Buonanno, A., Kramer, M. & Wex, N. (2017), *Constraining Nonperturbative Strong-Field Effects in Scalar-Tensor Gravity by Combining Pulsar Timing and Laser-Interferometer Gravitational-Wave Detectors*, Physical Review X **7** 041025, arXiv: 1704.07561 [gr-qc] (cit. on p. 74).

Shapiro, I. I. (1964), *Fourth Test of General Relativity*, Phys. Rev. Lett. **13** 789 (cit. on pp. 1, 54).

Shapiro, I. I. (1967), *New Method for the Detection of Light Deflection by Solar Gravity*, Science **157** 806 (cit. on p. 67).

Shapiro, S. S., Davis, J. L., Lebach, D. E. & Gregory, J. S. (2004), *Measurement of the Solar Gravitational Deflection of Radio Waves using Geodetic Very-Long-Baseline Interferometry Data, 1979 1999*, Phys. Rev. Lett. **92** 121101 (cit. on p. 2).

Shibata, M., Taniguchi, K., Okawa, H. & Buonanno, A. (2014), *Coalescence of binary neutron stars in a scalar-tensor theory of gravity*, Phys. Rev. D **89** (8) 084005, URL: https://link.aps.org/doi/10.1103/PhysRevD.89.084005 (cit. on p. 74).

Shibata, M., Zhou, E., Kiuchi, K. & Fujibayashi, S. (2019), *Constraint on the maximum mass of neutron stars using GW170817 event*, Phys. Rev. D **100** 023015, arXiv: 1905.03656 [astro-ph.HE] (cit. on p. 28).

Shklovskii, I. S. (1970), *Possible Causes of the Secular Increase in Pulsar Periods.*, Soviet Ast. **13** 562 (cit. on p. 36).

Sieber, W. (1982), *Causal relationship between pulsar long-term intensity variations andthe interstellar medium.*, A&A **113** 311 (cit. on p. 12).

Siemens, X., Ellis, J., Jenet, F. & Romano, J. D. (2013), *The stochastic background: scaling laws and time to detection for pulsar timing arrays*, Classical and Quantum Gravity **30** 224015, arXiv: 1305.3196 [astro-ph.IM] (cit. on p. 86).

Smarr, L. L. & Blandford, R. (1976), *The binary pulsar: physical processes, possible companions, and evolutionary histories.*, ApJ **207** 574 (cit. on pp. 22, 32, 56).

Smits, R., Tingay, S. J., Wex, N., Kramer, M. & Stappers, B. (2011), *Prospects for accurate distance measurements of pulsars with the Square Kilometre Array: Enabling fundamental physics*, A&A **528** A108, arXiv: 1101.5971 [astro-ph.IM] (cit. on p. 38).

Soffel, M. et al. (2003), *The IAU 2000 Resolutions for Astrometry, Celestial Mechanics, and Metrology in the Relativistic Framework: Explanatory Supplement*, The Astronomical Journal **126** 2687, ISSN: 1538-3881, URL: http://dx.doi.org/10.1086/378162 (cit. on pp. 19, 60).

Soffel, M. & Langhans, R. (2013), *Space-Time Reference Systems* (cit. on p. 19).

Spiewak, R. et al. (2022), *The MeerTime Pulsar Timing Array: A census of emission properties and timing potential*, PASA **39** e027, arXiv: 2204.04115 [astro-ph.HE] (cit. on p. 51).

Staelin, D. H. & Reifenstein Edward C., I. (1968), *Pulsating Radio Sources near the Crab Nebula*, Science **162** 1481 (cit. on p. 4).

Stairs, I. H., Splaver, E. M., Thorsett, S. E., Nice, D. J. & Taylor, J. H. (2000), *A baseband recorder for radio pulsar observations*, MNRAS **314** 459, arXiv: astro-ph/9912272 [astro-ph] (cit. on p. 14).

Stairs, I. H., Thorsett, S. E. & Arzoumanian, Z. (2004), *Measurement of Gravitational Spin-Orbit Coupling in a Binary-Pulsar System*, Phys. Rev. Lett. **93** 141101, arXiv: astro-ph/0408457 [astro-ph] (cit. on p. 30).

Stairs, I. H., Thorsett, S. E., Dewey, R. J., Kramer, M. & McPhee, C. A. (2006), *The formation of the double pulsar PSR J0737-3039A/B*, MNRAS **373** L50, arXiv: astro-ph/0609416 [astro-ph] (cit. on pp. 31, 56).

Stairs, I. H., Thorsett, S. E., Taylor, J. H. & Wolszczan, A. (2002), *Studies of the Relativistic Binary Pulsar PSR B1534+12. I. Timing Analysis*, ApJ **581** 501, arXiv: astro-ph/0208357 [astro-ph] (cit. on p. 30).

Stappers, B. & Kramer, M. (2016), "An Update on TRAPUM", *MeerKAT Science: On the Pathway to the SKA* 9 (cit. on p. 46).

Stappers, B. W., Kramer, M., Lyne, A. G., D'Amico, N. & Jessner, A. (2006), *The European Pulsar Timing Array*, Chinese Journal of Astronomy and Astrophysics Supplement **6** 298 (cit. on p. 86).

Stovall, K., Freire, P. C. C., Chatterjee, S., Demorest, P. B., Lorimer, D. R. et al. (2018), *PALFA Discovery of a Highly Relativistic Double Neutron Star Binary*, ApJ **854** L22, arXiv: 1802.01707 [astro-ph.HE] (cit. on p. 46).

Tauris, T. M. et al. (2017), *Formation of Double Neutron Star Systems*, ApJ **846** 170, arXiv: 1706.09438 [astro-ph.HE] (cit. on pp. 9, 31, 47, 56).

Taylor, J. H., Fowler, L. A. & McCulloch, P. M. (1979), *Measurements of general relativistic effects in the binary pulsar PSR1913 + 16*, Nature **277** 437 (cit. on pp. 2, 8).

Taylor, J. H. & Weisberg, J. M. (1989), *Further Experimental Tests of Relativistic Gravity Using the Binary Pulsar PSR 1913+16*, ApJ **345** 434 (cit. on pp. 24, 61, 73, 84).

Thorne, K. (1980), *Multipole Expansions of Gravitational Radiation*, Rev. Mod. Phys. **52** 299 (cit. on p. 45).

Thrane, E., Osłowski, S. & Lasky, P. D. (2020), *Ultrarelativistic astrophysics using multimessenger observations of double neutron stars with LISA and the SKA*, MNRAS **493** 5408, arXiv: 1910.12330 [astro-ph.HE] (cit. on p. 46).

Tiburzi, C. et al. (2016), *A study of spatial correlations in pulsar timing array data*, MNRAS **455** 4339, arXiv: 1510.02363 [astro-ph.IM] (cit. on pp. 87, 100).

Tiburzi, C. et al. (2021), *The impact of solar wind variability on pulsar timing*, A&A **647** A84, arXiv: 2012.11726 [astro-ph.HE] (cit. on p. 25).

Tiesinga, E., Mohr, P. J., Newell, D. B. & Taylor, B. N. (2021), *CODATA recommended values of the fundamental physical constants: 2018**, Reviews of Modern Physics **93** 025010 (cit. on p. xii).

Tolman, R. C. (1939), *Static Solutions of Einstein's Field Equations for Spheres of Fluid*, Physical Review **55** 364 (cit. on p. 3).

van Leeuwen, J. et al. (2015), *The Binary Companion of Young, Relativistic Pulsar J1906+0746*, ApJ **798** 118, arXiv: 1411.1518 [astro-ph.SR] (cit. on p. 30).

Venkatraman Krishnan, V. et al. (2020), *Lense–Thirring frame dragging induced by a fast-rotating white dwarf in a binary pulsar system*, Science **367** 577, arXiv: 2001.11405 [astro-ph.HE] (cit. on p. 30).

Verbiest, J. P. W. et al. (2016), *The International Pulsar Timing Array: First data release*, MNRAS **458** 1267, arXiv: 1602.03640 [astro-ph.IM] (cit. on p. 86).

Voisin, G. et al. (2020), *An improved test of the strong equivalence principle with the pulsar in a triple star system*, A&A **638** A24, arXiv: 2005.01388 [gr-qc] (cit. on p. 71).

Wagoner, R. V. (1975), *Test for the existence of gravitational radiation.*, ApJ **196** L63 (cit. on p. 34).

Wang, J. et al. (2022), *A comparative analysis of pulse time-of-arrival creation methods*, A&A **658** A181, arXiv: 2111.13482 [astro-ph.IM] (cit. on p. 93).

Wang, M. et al. (2022), *Jingdong 120-m Pulsar Radio Telescope*, SCIENTIA SINICA Physica, Mechanica & Astronomica -, URL: https://www.sciengine.com/SSPMA/doi/10.1360/SSPMA-2022-0162;JSESSIONID=93023d0d-5002-4917-8880-011b7bc83ece (cit. on p. 100).

Wang, N. (2014), *Xinjiang Qitai 110 m radio telescope*, SCIENTIA SINICA Physica, Mechanica & Astronomica **44** 783, URL: https://www.sciengine.com/SSPMA/doi/10.1360/SSPMA2014-00039;JSESSIONID=a2332298-9cb8-4e9f-8630-cc47caadbde1 (cit. on p. 93).

Ward, W. R. (1970), *General-Relativistic Light Deflection for the Complete Celestial Sphere*, ApJ **162** 345 (cit. on p. 67).

Watts, A. L. et al. (2016), *Colloquium: Measuring the neutron star equation of state using x-ray timing*, Rev. Mod. Phys. **88** (2) 021001, URL: https://link.aps.org/doi/10.1103/RevModPhys.88.021001 (cit. on p. 27).

Webbink, R. F. (1984), *Double white dwarfs as progenitors of R Coronae Borealis stars and type I supernovae.*, ApJ **277** 355 (cit. on p. 4).

Weber, J. (1960), *Detection and Generation of Gravitational Waves*, Phys. Rev. **117** (1) 306, URL: https://link.aps.org/doi/10.1103/PhysRev.117.306 (cit. on p. 83).

Weber, J. (1968), *Gravitational-Wave-Detector Events*, Phys. Rev. Lett. **20** 1307 (cit. on p. 83).

Weisberg, J. M. & Huang, Y. (2016), *Relativistic Measurements from Timing the Binary Pulsar PSR B1913+16*, ApJ **829** 55, arXiv: 1606.02744 [astro-ph.HE] (cit. on p. 21).

Wex, N. & Kopeikin, S. M. (1999), *Frame Dragging and Other Precessional Effects in Black Hole Pulsar Binaries*, ApJ **514** 388, arXiv: astro-ph/9811052 [astro-ph] (cit. on pp. 2, 79).

Wex, N. (1995), *The second post-Newtonian motion of compact binary-star systems with spin*, Classical and Quantum Gravity **12** 983 (cit. on p. 32).

Wex, N. (1998), *A timing formula for main-sequence star binary pulsars*, MNRAS **298** 67, ISSN: 0035-8711, eprint: https://academic.oup.com/mnras/article-pdf/298/1/67/2983068/298-1-67.pdf, URL: https://doi.org/10.1046/j.1365-8711.1998.01570.x (cit. on p. 32).

Wex, N. (2014), *Testing Relativistic Gravity with Radio Pulsars*, arXiv e-prints, arXiv: 1402.5594 [gr-qc] (cit. on pp. 2, 8, 72, 98).

Wex, N. & Kramer, M. (2020), *Gravity Tests with Radio Pulsars*, Universe **6** 156 (cit. on pp. 8, 50, 72).

Will, C. M. (1981), *Theory and experiment in gravitational physics.* (Cit. on p. 1).

Will, C. M. (2018), *Theory and experiment in gravitational physics, Second Edition, Cambridge University Press*, Cambridge, England: Cambridge University Press (cit. on pp. 1, 31).

Will, C. M. (1993), *Theory and Experiment in Gravitational Physics* (cit. on pp. 2, 73).

Will, C. M. (2014), *The Confrontation between General Relativity and Experiment*, Living Reviews in Relativity **17** 4, arXiv: 1403.7377 [gr-qc] (cit. on pp. 8, 71, 72).

Willems, B. & Kalogera, V. (2004), *Constraints on the Formation of PSR J0737-3039: The Most Probable Isotropic Kick Magnitude*, ApJ **603** L101, arXiv: astro-ph/0312426 [astro-ph] (cit. on p. 56).

Willems, B., Kaplan, J., Fragos, T., Kalogera, V. & Belczynski, K. (2006), *Formation and progenitor of PSR J0737-3039: New constraints on the supernova explosion forming pulsar B*, Phys. Rev. D **74** 043003, arXiv: astro-ph/0602024 [astro-ph] (cit. on p. 56).

Woltjer, L. (1964), *X-Rays and Type I Supernova Remnants.*, ApJ **140** 1309 (cit. on p. 5).

Wucknitz, O. (2008), *From planes to spheres: about gravitational lens magnifications*, MNRAS **386** 230, arXiv: 0801.3758 [astro-ph] (cit. on pp. 67, 68).

Wyithe, J. S. B. & Loeb, A. (2003), *Low-Frequency Gravitational Waves from Massive Black Hole Binaries: Predictions for LISA and Pulsar Timing Arrays*, ApJ **590** 691, arXiv: astro-ph/0211556 [astro-ph] (cit. on p. 85).

Xie, J.-T., Wang, J.-B., Wang, N. & Hu, Y. (2022), *Pulsar Survey With the QiTai 110 m Radio Telescope*, Research in Astronomy and Astrophysics **22** 075009 (cit. on p. 93).

Yazadjiev, S. S., Doneva, D. D. & Popchev, D. (2016), *Slowly rotating neutron stars in scalar-tensor theories with a massive scalar field*, Phys. Rev. D **93** 084038, arXiv: 1602.04766 [gr-qc] (cit. on p. 44).

Yunes, N. & Siemens, X. (2013), *Gravitational-Wave Tests of General Relativity with Ground-Based Detectors and Pulsar-Timing Arrays*, Living Reviews in Relativity **16** 9, arXiv: 1304.3473 [gr-qc] (cit. on p. 2).

Zhang, L. et al. (2013), *THE GRAVITATIONAL POTENTIAL NEAR THE SUN FROM SEGUE K-DWARF KINEMATICS*, The Astrophysical Journal **772** 108, ISSN: 1538-4357, URL: http://dx.doi.org/10.1088/0004-637X/772/2/108 (cit. on pp. 35, 76).

Zhang, S. N., Feroci, M., Santangelo, A., Dong, Y. W., Feng, H. et al. (2016), "eXTP: Enhanced X-ray Timing and Polarization mission", *Proc. SPIE*, vol. 9905, Society of Photo-Optical Instrumentation Engineers (SPIE) Conference Series 99051Q, arXiv: 1607.08823 [astro-ph.IM] (cit. on p. 41).

Zhao, J., Freire, P. C. C., Kramer, M., Shao, L. & Wex, N. (2022), *Closing a spontaneous-scalarization window with binary pulsars*, Classical and Quantum Gravity **39** 11LT01, arXiv: 2201.03771 [astro-ph.HE] (cit. on p. 74).

Zhu, W. W. et al. (2015), *Testing Theories of Gravitation Using 21-Year Timing of Pulsar Binary J1713+0747*, ApJ **809** 41, arXiv: 1504.00662 [astro-ph.SR] (cit. on pp. 21, 87).

Zhu, W. W. et al. (2019), *Tests of gravitational symmetries with pulsar binary J1713+0747*, MNRAS **482** 3249, arXiv: 1802.09206 [astro-ph.HE] (cit. on pp. 21, 87).

Acknowledgements

First of all, I would like to thank my scientific advisers who have had an important influence on the work presented here. Many thanks to Michael Kramer for guiding me through knotty scientific problems, for his insights and unfading enthusiasm for science which has been truly inspiring, and for his trust that shaped me into an independent researcher. A big thanks to my day-to-day advisor David Champion, for his standing support over the past four years, for always encouraging me when things did not work out, and for being thoughtful and versatile in tackling problems with observations and data. A special thanks to Norbert Wex, for his invaluable theoretical support in many of these projects, for his rigorous approach to science, and for his patience in explaining every detail and sharing scientific anecdotes.

I would like to express my gratitude to Norbert Langer for being in my TAC, evaluating the progress of my studies, and for being the second reviewer of this thesis. I also wish to thank Marta Burgay for her constant support as a TAC member, and, of course, for the discovery of the Double Pulsar system, which is obviously crucial for the work presented here. Simon Stellmer and Valentin Blomer are acknowledged for kindly joining my doctoral committee, and Claus Lämmerzahl is thanked for reviewing this thesis.

I am grateful to my colleagues, in particular Aditya, Alexander, Kuo, Nataliya, Paulo, Ramesh, Timothy, Vivek, Willem, and Yanjun, for various fruitful discussions. Eleni and Madhuri are thanked for their kind guidance on observations and data processing. I also wish to thank Alex Kraus and the Effelsberg team for coordinating and helping with Effelsberg observations.

I acknowledge all people involved in MeerTIME, EPTA, and LEAP collaborations for their support and valuable discussions. I also wish to thank the MPG-CAS LEGACY collaboration for funding and for connecting researchers in China and Germany. I am grateful to Kejia Lee, Weiwei Zhu, and their teams for coordinating observations with FAST and hosting my stay.

I would like to thank our big family — the Fundi group — for creating such a friendly atmosphere and for the laughs that delighted the corridors. I am indebted to Kira, Silvia, Le, and Barbara, among others, for their kindness and excellent assistance with the paperwork. I am thankful to Rainer, Simone, Gunther, and Arne for coordinating all IMPRS-related activities, and to IMPRS students for sharing memorable moments in these events and in daily life. I also wish to thank the Chinese community at MPIfR, AIfA, and outside for sharing spare time, happiness, and delicious Chinese food together.

I thank my parents, 胡风林 and 万晓红, with all my heart for their unparalleled love, encouragement, and support. Even though we could not meet physically in the past three years because of the pandemic, we have always been close in spirit.

Finally, I would like to thank my soulmate, 杨丹, for his love, accompany, and delicious food that fulfilled my life spiritually and materially. 感谢孙伯熊、万仲熊、霍叔熊（彼得）、熊队长以及所有家庭成员的默默陪伴，你们的微笑让我有家的温暖。

Curriculum Vitae

Personal Details

Family Name	Hu (胡)
Given Name	Huanchen (奂晨)
Date of Birth	29.08.1994
Place of Birth	Tianjin, China
Nationality	Chinese
ORCID iD	https://orcid.org/0000-0002-3407-8071

Education

10.2018 – 04.2023	Ph.D. student, International Max Planck Research School (IMPRS) for Astronomy and Astrophysics at the Universities of Bonn and Cologne ⋄ Research project at Max Planck Institute for Radio Astronomy, Bonn Dissertation: *Gravity tests with pulsars using new-generation radio telescopes* Supervisors: Prof. Dr. Michael Kramer, Dr. David Champion
10.2016 – 09.2018	M.Sc., AstroMundus – Erasmus Mundus Joint Master Degree in Astrophysics S1: University of Innsbruck, Austria S2: University of Padova, Italy S3: University of Rome Tor Vergata, Italy S4: University of Göttingen, Germany ⋄ Research project at Max Planck Institute for Solar System Research, Göttingen Thesis: *Coupling of solar p and g modes* Supervisors: Prof. Dr. Laurent Gizon, Dr. Vincent Böning
09.2012 – 07.2016	B.Sc., Astronomy, Beijing Normal University, China
09.2015 – 01.2016	Exchange semester, National University of Ireland, Maynooth, Ireland

Scientific contributions

First- and second-author papers

1. **H. Hu**, M. Kramer, D. J. Champion, N. Wex et al. (2022), A&A, 667, A149
   Gravitational signal propagation in the double pulsar studied with the MeerKAT telescope
2. **H. Hu**, M. Kramer, N. Wex, D. J. Champion, M. S. Kehl (2020), MNRAS, 497, 3118-3130
   Constraining the dense matter equation-of-state with radio pulsars
3. A. Batrakov, **H. Hu**, N. Wex, P. C. C. Freire, V. Venkatraman Krishnan, M. Kramer et al. (2023), A&A, DOI: 10.1051/0004-6361/202245246
   A new pulsar timing model for scalar-tensor gravity: with applications to PSR J2222−0137 and pulsar-black hole binaries
4. V. G. A. Böning, **H. Hu**, L. Gizon (2019), A&A, 629, A26
   Signature of solar g modes in first-order p-mode frequency shifts

Collaboration papers

1. S. Chen, R. N. Caballero, Y. J. Guo, A. Chalumeau, K. Liu, G. Shaifullah, K. J. Lee, S. Babak, G. Desvignes, A. Parthasarathy, **H. Hu** et al. (2021), MNRAS, 508, 4970–4993
   Common-red-signal analysis with 24-yr high-precision timing of the European Pulsar Timing Array: inferences in the stochastic gravitational-wave background search
2. M. Falxa, ..., **H. Hu** et al. (2023), MNRAS, 521, 5077-5086
   Searching for continuous Gravitational Waves in the second data release of the International Pulsar Timing Array
3. K. Liu, ..., **H. Hu** et al. (2022), MNRAS, 513, 4037-4044
   Detection of quasi-periodic micro-structure in three millisecond pulsars with the Large European Array for Pulsars
4. J. Antoniadis, ..., **H. Hu** et al. (2022), MNRAS, 510, 4873–4887
   The International Pulsar Timing Array second data release: Search for an isotropic Gravitational Wave Background
5. G. Mall, ..., **H. Hu** et al. (2022), MNRAS, 511, 1104-1114
   Modelling annual scintillation arc variations in PSR J1643-1224 using the Large European Array for Pulsars
6. J. Wang, ..., **H. Hu** et al. (2022), A&A, 658, A181
   A comparative analysis of pulse time-of-arrival creation methods
7. M. Kramer, ..., **H. Hu** et al. (2021), MNRAS, 504, 2094-2114
   The relativistic binary programme on MeerKAT: science objectives, first results

8. A. Chalumeau, ..., **H. Hu** et al. (2021), MNRAS, 509, 5538-5558
   Noise analysis in the European Pulsar Timing Array data release 2, its implications on the gravitational-wave background search
9. M. Bailes, ..., **H. Hu** et al. (2020), PASA, 37, e028
   The MeerKAT Telescope as a Pulsar Facility: System verification, early science results from MeerTime
10. R. Main, ..., **H. Hu** et al. (2020), MNRAS, 499, 1468–1479
    Measuring Interstellar Delays of PSR J0613-0200 over 7 years, using the Large European Array for Pulsars
11. B. B. P. Perera, ..., **H. Hu** et al. (2019), MNRAS, 490, 4666-4687
    The International Pulsar Timing Array: second data release

Conference presentations

1. DPG Spring Meeting of the Matter and Cosmos Section, Dresden, March 20-24, 2023
   Talk: *Taking gravity tests with the Double Pulsar to higher orders*
2. WE-Heraeus-Seminar on "Time and Clocks", Bad Honnef, February 27-March 3, 2023
   Poster: *Gravity experiments in strong fields using pulsars as clocks*
3. Annual meeting of the German Astronomical Society, Bremen, September 12-16, 2022
   Talk: *Taking gravity tests with the Double Pulsar to the next level*
4. 23rd International Conference on General Relativity & Gravitation (virtual), July 3-8, 2022
   Talk: *Gravity tests with the Double Pulsar – from MeerKAT to the SKA*
5. MPG-CAS LEGACY meeting (virtual), January 17-19, 2022
   Talk: *Updates on the Double Pulsar*
6. Sixteenth Marcel Grossmann meeting (virtual), July 5-10, 2021
   Talk: *Constraining the dense matter EOS and testing higher-order GR effects with the Double Pulsar*
7. Annual meeting of the German Astronomical Society (virtual), September 21-25, 2020
   Talk: *Constraining the dense matter EOS and testing higher-order GR effects with the Double Pulsar*
8. International Pulsar Timing Array meeting, Pune, India, June 10-21, 2019
   Talk: *Über-LEAP: building the most powerful pulsar telescope*

Books

1. *The Evolution of Physics* (Chinese Edition), Cultural Development Press, 2019
   Authors: Albert Einstein and Leopold Infeld, Translator: **H. Hu**
2. *Ripples in Spacetime: Einstein, Gravitational Waves, and the Future of Astronomy* (Chinese Edition), CITIC Press Corporation, 2018
   Author: Govert Schilling, Translator: **H. Hu**
3. *The Elephant in the Universe: Our Hundred-Year Search for Dark Matter* (Chinese edition), CITIC Press Corporation, 2023 (in press)
   Author: Govert Schilling, Translator: **H. Hu**

Conferences organised

1. EPTA spring meeting (SOC chair), Milan, Italy, March 13-17, 2023
2. 16th Bonn Neutron Star Workshop (SOC and LOC), Bonn, April 19-20, 2023

Paper I: Constraining the dense matter equation-of-state with radio pulsars

---

Monthly Notices
of the
ROYAL ASTRONOMICAL SOCIETY

MNRAS **497,** 3118–3130 (2020)
Advance Access publication 2020 July 20

doi:10.1093/mnras/staa2107

Constraining the dense matter equation-of-state with radio pulsars

Huanchen Hu (胡奂晨)[1]★ Michael Kramer,[1,2] Norbert Wex[1] David J. Champion[1] and Marcel S. Kehl[1]

[1]*Max-Planck-Institut für Radioastronomie, Auf dem Hügel 69, D-53121 Bonn, Germany*
[2]*Jodrell Bank Centre for Astrophysics, The University of Manchester, Oxford Road, Manchester M13 9PL, UK*

Accepted 2020 July 15. Received 2020 July 15; in original form 2020 June 23

ABSTRACT

Radio pulsars provide some of the most important constraints for our understanding of matter at supranuclear densities. So far, these constraints are mostly given by precision mass measurements of neutron stars (NS). By combining single measurements of the two most massive pulsars, J0348+0432 and J0740+6620, the resulting lower limit of 1.98 $M_{\odot}$ (99 per cent confidence) of the maximum NS mass, excludes a large number of equations of state (EOSs). Further EOS constraints, complementary to other methods, are likely to come from the measurement of the moment of inertia (MOI) of binary pulsars in relativistic orbits. The Double Pulsar, PSR J0737−3039A/B, is the most promising system for the first measurement of the MOI via pulsar timing. Reviewing this method, based in particular on the first MeerKAT observations of the Double Pulsar, we provide well-founded projections into the future by simulating timing observations with MeerKAT and the SKA. For the first time, we account for the spin-down mass-loss in the analysis. Our results suggest that an MOI measurement with 11 per cent accuracy (68 per cent confidence) is possible by 2030. If by 2030 the EOS is sufficiently well known, however, we find that the Double Pulsar will allow for a 7 per cent test of Lense–Thirring precession, or alternatively provide a $\sim 3\sigma$-measurement of the next-to-leading order gravitational wave damping in GR. Finally, we demonstrate that potential new discoveries of double NS systems with orbital periods shorter than that of the Double Pulsar promise significant improvements in these measurements and the constraints on NS matter.

Key words: dense matter – equation of state – gravitation – pulsars: general – pulsars: individual: J0737−3039A.

1 INTRODUCTION

Neutron stars (NSs) are among the most compact and exotic objects in nature, comprised of extraordinarily dense matter that is not accessible in laboratory experiments. Determining the properties and structure of the cold dense matter inside NSs is therefore a tremendous challenge in nuclear physics. Thus far, a variety of equations of state (EOSs) have been proposed to describe the pressure–density relation inside NSs (see e.g. Lattimer & Prakash 2001, 2016). Constraining the EOS is crucial for understanding aspects of fundamental physics, such as the internal structure of NSs, the dynamics of binary mergers, and r-process nucleosynthesis (for a recent review see Özel & Freire 2016).

Various observational methods have emerged to measure the macroscopic properties of NSs, which promise to increase our knowledge of the EOS. The gravitational wave (GW) observation of a binary NS merger with LIGO/Virgo offers the possibility of measuring the tidal deformability (Abbott et al. 2017, 2018). X-ray observations of emissions from the hot regions on NS surface with NICER (Watts et al. 2016) allows a joint mass–radius estimation (Miller et al. 2019; Riley et al. 2019).

The largest number of known NSs, however, can be observed as radio pulsars. Currently about 3000 pulsars are known, and the ability of radio astronomers to measure pulsar properties precisely via a technique known as 'pulsar timing', suggests that important information about the EOS of NSs can also be derived from such measurements. This is indeed the case. The most direct and best known route is to measure the masses of NSs precisely. This is possible in binary pulsars using relativistic orbital effects, potentially combined with other information. The mass range, especially the maximum mass observed, must obviously be consistent with the range of masses supported by a proposed EOS. In addition, there are other orbital effects that also offer the possibility of measuring the moment of inertia (MOI) in binary pulsars via relativistic spin-orbit coupling, as was first suggested by Damour & Schäfer (1988). The MOI of a NS depends crucially on the EOS and hence allows us to constrain or even identify it (Morrison et al. 2004; Lattimer & Schutz 2005; Greif et al. 2020). Accessing the MOI of isolated NSs, in contrast, may be possible if one can reliably derive or measure the total loss in rotational energy, $\dot{E}$, which relates the MOI with the observed period and period derivative.

In this work, we provide insight into the various methods using binary pulsars and their current status in Section 2, before we focus specifically on the possibility of using the Double Pulsar (Burgay et al. 2003; Lyne et al. 2004) for MOI measurements. We will provide

★ E-mail: huhu@mpifr-bonn.mpg.de

an in-depth study of the relevant factors in Section 3, where we explain how Lense–Thirring (LT) precession affects the periastron advance. Section 4 describes the intrinsic and extrinsic contributions to the orbital period decay. We describe how we simulate future timing observations in Section 5 and evaluate how the Double Pulsar can measure the MOI and constrain the EOS in Section 6. Prospects of testing LT precession and constraining theories of gravity is discussed in Section 7 by assuming the EOS is known. We investigate potential constraints on next-to-leading order GW damping in Section 8, and potential constraints from future discoveries of more relativistic binary pulsars in Section 9. Finally, we conclude in Section 10.

2 METHODS TO CONSTRAIN THE EOS VIA PULSAR TIMING

2.1 Mass measurements

A given EOS i can only sustain a NS up to a certain maximum mass, $M_i^{\max}$. Finding a massive NS of mass M_j, consequently excludes all EOS with $M_i^{\max} < M_j$. This was, for instance possible, by using a Shapiro delay measurement in PSR J1614−2230, where Demorest et al. (2010) determined a mass $M = 1.97 \pm 0.04\,M_\odot$. We note that a recent update on continued timing observations (Arzoumanian et al. 2018), implies a significantly lower mass of $1.908 \pm 0.016\,M_\odot$ for this pulsar. As pointed out by Cromartie et al. (2019), a Shapiro delay measurement and the determined uncertainty can be affected by the exact orbital sampling (see also Hu et al., in preparation).

In 2013, Antoniadis et al. (2013) could determine the mass of PSR J0348+0432 without using a Shapiro delay measurement. They combined radio timing measurements of the orbit of the pulsar with precise spectroscopy data of the white dwarf companion in the optical regime to derive a mass of $2.01 \pm 0.04\,M_\odot$, confirming the existence of 2-$M_\odot$ NSs via a complementary method.

Recently, Cromartie et al. (2019) used a Shapiro delay measurement in PSR J0740+6620 to determine a pulsar mass of $2.14^{+0.10}_{-0.09}\,M_\odot$. We can use the masses of these latter two most massive pulsars, J0348+0432 (fully accounting for the rather asymmetric probability density distribution found by Antoniadis et al. 2013) and J0740+6620, to obtain a 99 per cent confidence lower limit for the maximum mass of a NS, $1.98\,M_\odot < M^{\max}$. Such a constraint already rules out a number of soft EOSs as shown in Fig. 1.[1]

We can compare this lower limit derived from pulsar timing with an upper limit placed by the NS–NS merger GW170817 observed by LIGO (Abbott et al. 2017). Assuming that the NS–NS merger resulted in the formation of a black hole, one finds an upper limit of about $2.3\,M_\odot$ for the maximum mass of a NS (Rezzolla, Most & Weih 2018; Shibata et al. 2019).

2.2 Relativistic spin-orbit coupling

Unlike in Newtonian gravity, the gravitational field of a body in general relativity (GR) has contributions from the mass currents related to the body's proper rotation. Lense & Thirring (1918) – with substantial help from Albert Einstein (see Pfister 2007) – have shown that the rotation of the Sun has, in principle, an effect on the

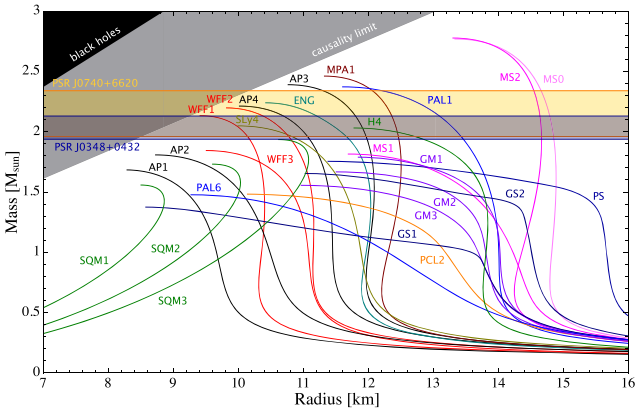

Figure 1. The mass of a NS as function of its radius for different EOS (Lattimer & Prakash 2001). The horizontal bands indicate the 2-σ range for the masses of the two most massive radio pulsars known to date, PSR J0348+0432 (Antoniadis et al. 2013) in blue and PSR J0740+6620 (Cromartie et al. 2019) in yellow.

planetary orbits. This relativistic spin-orbit coupling, also known as LT precession, has since been well tested in the gravitational field of the rotating Earth with the help of satellite laser ranging (Ciufolini & Pavlis 2004; Ciufolini et al. 2019). Similarly, in relativistic binaries, the spin of a compact rotating body is expected to couple gravitationally with the orbital motion of the system (Barker & O'Connell 1975), leading to a precession of the orbit, while the total angular momentum is conserved.[2] This LT precession of the orbit is potentially observable, hence providing a route to access the MOI of the pulsar (Damour & Schäfer 1988). An MOI measurement, even with an accuracy of ∼10 per cent, would offer important constraints of the EOS (Morrison et al. 2004; Lattimer & Schutz 2005).

The LT precession of the orbit may be detected via the variation in the orbital inclination angle, i, and hence in the (observable) projected semimajor axis of the pulsar obit, $x = a_{\rm p} \sin i/c$ ($a_{\rm p}$ is the semimajor axis, and c the speed of light). However, for this to be detectable, the misalignment angle between pulsar spin and angular momentum vector must be sufficiently large. Also, the orbital inclination angle must not be too close to 90 degrees ('edge-on' geometry), since the precession leads to a contribution to the rate of change of the projected semimajor axis given by

$$\dot{x}^{\rm LT} = x \cot i \left(\frac{{\rm d}i}{{\rm d}t}\right)_{\rm LT}, \tag{1}$$

where $({\rm d}i/{\rm d}t)_{\rm LT}$ is given by equation (3.27) in Damour & Taylor (1992). For nearly edge-on systems, i.e. $i \approx 90$ deg, this contribution becomes small and most likely undetectable since $\cot i \ll 1$. However, in relativistic binary systems with smaller inclination angles, such as PSR J1757−1854, this measurement appears to be possible by Cameron et al. (2018). To achieve this, two challenges will have to be addressed successfully. First, the precession is expected to cause a variation in the pulse profile with time due to a change in the viewing geometry (e.g. Kramer 1998). Special care in the timing procedure is then needed to obtain sufficient precision and to properly account for possible systematic errors (e.g. Stairs et al. 2002; Bhat, Bailes & Verbiest 2008; van Leeuwen et al. 2015). Moreover, since we require access to the direction of the pulsar spin vector (Damour & Schäfer

[1] Note that in Fig. 6, we show a different but overlapping set of EOSs. Here, we also show EOSs that have been excluded by the maximum mass measurement, while at the same time making the plot not too crowded.

[2] The loss of orbital angular momentum due to the emission of GWs is of higher post-Newtonian order and can be neglected here.

1988; Damour & Taylor 1992), the geometry of the binary system and the pulsar needs also to be measured. This is, however, possible via polarization measurements, as shown previously (e.g. Kramer 1998; Stairs, Thorsett & Arzoumanian 2004; Desvignes et al. 2019; Venkatraman Krishnan et al. 2019; Venkatraman Krishnan et al. 2020).

Alternatively, rather than using a contribution to $\dot{x}$, one can exploit LT precession also via its contribution to the advance of periastron. If it is possible to isolate the contribution of $\dot{\omega}^{\rm LT}$ from the total periastron advance, then the MOI can be determined (Damour & Schäfer 1988). This method was suggested for the Double Pulsar, PSR J0737−3039A/B (Lyne et al. 2004; Kramer et al. 2006). Kramer & Wex (2009) concluded that an MOI measurement of ∼10 per cent accuracy is possible by ∼2030, with the timing accuracy achievable at the time. Later, Kehl et al. (2017) simulated timing data from emerging telescopes, i.e. the Square Kilometer Array (SKA; e.g. Kramer & Stappers 2015) and its precursor MeerKAT (Bailes et al. 2018; Camilo 2018), which greatly improve the timing precision, and predict an MOI measurement with an accuracy well below 10 per cent by 2030. However, the timeline of the nominal operation of the SKA assumed by Kehl et al. (2017) was optimistic compared to the current estimates. With MeerKAT in operation since about 2018 (albeit initially with limited capability), operations of the first phase of the SKA (SKA 1, initially expected to have about 10 per cent of the full SKA's sensitivity) are not expected before 2027. However, first useful data from commissioning observations may be already available in 2025.[3] In addition, compared to Kehl et al. (2017), we now already have about two years of Double Pulsar timing observations with MeerKAT, and therefore have more realistic numbers for the timing precision and cadence of observations, not only for the current MeerKAT configuration but also for future extensions. Moreover, Kehl et al. (2017) did not incorporate the contribution of spin-down mass-loss of pulsar A to the orbital period derivative into the simulations. As we will show below, considering this effect is important, and its impact on our ability to measure the MOI needs to be studied in a fully consistent analysis. Hence, more complete simulations of the MOI measurement in the Double Pulsar should give us a more realistic estimate of the system's (near) future capability to constrain the EOS of ultradense matter inside a NS.

Consequently, in what follows, we present new and important details of how to measure the MOI of radio pulsars using the method of isolating the LT contribution to the advance of periastron. Using the Double Pulsar as the most promising system for this kind of experiment, we simulate timing data of PSR J0737−3039A that can be expected from MeerKAT and future extensions, to assess our ability to measure its MOI in the next 10 yr.

3 LENSE–THIRRING EFFECT IN THE DOUBLE PULSAR

The Double Pulsar is the only system to-date where both NSs have been observed as pulsars (Burgay et al. 2003; Lyne et al. 2004), with an orbital period of only 2.4 h. Breton et al. (2008) used the system to provide a 13 per cent-test of spin-orbit interaction of strongly self-gravitating bodies using the relativistic spin precession in pulsar B. The compact, relativistic nature of the system also allows the measurement of several post-Keplerian (PK) parameters to an unparalleled level of accuracy. This not only enables some of the most stringent tests of GR related to strong-field gravity (Kramer et al. 2006; Kramer & Wex 2009; Will 2018), but it is also crucial for the efforts to measure the MOI and to constrain the EOS of a NS.

3.1 Spin-orbit coupling contribution to the periastron advance

To simplify the problem, we neglect the LT contribution of pulsar B, since it spins about 122 times slower than pulsar A. Such a simplification is well justified, as will become clear below. In addition, the long-term observations of the pulse profile of PSR J0737−3039A shows that the misalignment angle between the spin axis of pulsar A and the orbital angular momentum has an upper limit of 3.2° (Ferdman et al. 2008, 2013). Therefore, for all practical purposes, we can assume that the spin of pulsar A is parallel to the orbital angular momentum, which is consistent with evolutionary considerations for the Double Pulsar system and a low-kick supernova formation (e.g. Stairs et al. 2006; Tauris et al. 2017). Pol et al. (2018) confirmed that pulsar A is indeed rotating prograde in its orbit, using the modulation of pulsar B's radio emission by the interaction with the wind of pulsar A. Consequently, the spin of pulsar A only induces a change to the advance of periastron, and does not lead to a change in the orbital inclination, more specifically, the projected semimajor axis. Following Damour & Schäfer (1988), the total intrinsic contribution to the periastron advance in the Double Pulsar system can be written, with sufficient precision, as

$$\begin{aligned}\dot{\omega}^{\rm intr} &= \dot{\omega}^{\rm 1PN} + \dot{\omega}^{\rm 2PN} + \dot{\omega}^{\rm LT,A} \\ &= \frac{3\,\beta_{\rm O}^2\, n_{\rm b}}{1-e_{\rm T}^2}\left[1 + f_{\rm O}\,\beta_{\rm O}^2 - g_{\rm S_A}^{\parallel}\beta_{\rm O}\,\beta_{\rm S_A}\right], \end{aligned} \tag{2}$$

where $n_{\rm b}$ is the orbital frequency, and $e_{\rm T}$ is the proper-time eccentricity used as the observed eccentricity in the standard timing model (Manchester et al. 2015) and defined in Damour & Deruelle (1986). The factor in front of the right-hand side of equation (2) is the first post-Newtonian (1PN) contribution; the higher order corrections due to 2PN effects and LT precession caused by pulsar A are indicated by the second and third term in the square brackets, respectively. The following notations are used to simplify equation (2),

$$\beta_{\rm O} = \frac{(GMn_{\rm b})^{1/3}}{c}, \tag{3}$$

$$\beta_{\rm S_A} = \frac{cI_{\rm A}\Omega_{\rm A}}{Gm_{\rm A}^2}, \tag{4}$$

$$f_{\rm O} = \frac{1}{1-e_{\rm T}^2}\left(\frac{3}{2}x_{\rm A}^2 + \frac{3}{2}x_{\rm A} + \frac{27}{4}\right) + \left(\frac{5}{6}x_{\rm A}^2 - \frac{23}{6}x_{\rm A} - \frac{1}{4}\right), \tag{5}$$

$$g_{\rm S_A}^{\parallel} = \frac{1}{(1-e_{\rm T}^2)^{1/2}}\left(\frac{1}{3}x_{\rm A}^2 + x_{\rm A}\right). \tag{6}$$

The subscript A stands for pulsar A. G is the Newtonian gravitational constant, and $M = m_{\rm A} + m_{\rm B}$ is the total mass defined as the sum of the (inertial) masses of pulsar A and B, and $x_{\rm A} = m_{\rm A}/M$. $I_{\rm A}$ denotes the MOI and $\Omega_{\rm A}$ the angular spin frequency.[4]

Table 1 lists the values of each term contributing to $\dot{\omega}^{\rm intr}$,

[3] See skatelescope.org for updates.

[4] Since pulsar A is slowly rotating (∼2.5 per cent of break-up velocity), for the purpose of this paper we do not have to distinguish between rotating and non-rotating quantities when it comes to (gravitational) mass, moment of inertia, etc. (see e.g. Berti et al. 2005)

Table 1. Contributions to the rate of periastron advance in the Double Pulsar calculated using equation (2), with the Keplerian parameters and masses ($m_A = 1.3381\,M_\odot$, $m_B = 1.2489\,M_\odot$) measured in Kramer et al. (2006). $I_A^{(45)} = I_A/(10^{45}\,\mathrm{g\,cm^2})$. The current measurement precision for $\dot{\omega}$ is already $\sim 10^{-5}$ deg yr^{-1} (Kramer et al., in preparation), which is about 40 times smaller than $\dot{\omega}^{\mathrm{LT,A}}$.

Contribution	(deg yr^{-1})
$\dot{\omega}^{\mathrm{1PN}}$	16.898703
$\dot{\omega}^{\mathrm{2PN}}$	0.000439
$\dot{\omega}^{\mathrm{LT,A}}$	$-0.000377\times I_A^{(45)}$

using the Keplerian parameters and masses ($m_A = 1.3381\,M_\odot$, $m_B = 1.2489\,M_\odot$) measured in Kramer et al. (2006). We note that the contribution due to the LT precession $\dot{\omega}^{\mathrm{LT,A}}$ depends on the MOI, whereby it is written as a function of $I_A^{(45)}$ defined as $I_A^{(45)} = I_A/(10^{45}\,\mathrm{g\,cm^2})$. Typical values of $I_A^{(45)}$ are around unity for realistic EOSs. It is evident that the contribution from the LT effect is comparable to that of 2PN, but with opposite signs.

The analysis of timing data from relativistic binary pulsars is based on a particularly simple and elegant solution of the post-Newtonian equations of motion, the so-called Damour-Deruelle (DD) model (Damour & Deruelle 1985; Damour & Deruelle 1986; Manchester et al. 2015). In the quasi-Keplerian parametrization of the DD model one can see that the advance of periastron is proportional to the true anomaly. This behaviour is modified by two periodic terms as part of the generalized quasi-Keplerian parametrization, which is a natural extension of the DD model when including 2PN and spin-orbit terms (Damour & Schäfer 1988; Schäfer & Wex 1993; Wex 1995). However, these periodic terms will remain well below measurability for the foreseeable future, for any of the known binary pulsars. For that reason, we will ignore them in our analysis.

Besides the coupling to the orbital angular momentum (spin-orbit coupling), the spin of pulsar A also couples to the spin of pulsar B (spin–spin coupling) (Barker & O'Connell 1975). However, the spin of pulsar B is about a factor of 3×10^6 smaller than the orbital angular momentum. Hence, spin–spin coupling is totally irrelevant here.

Finally there are, at least in principle, also contributions from the rotationally induced mass quadrupole moments of pulsars A and B to the orbital dynamics (Barker & O'Connell 1975). These spin-squared contributions give rise to an additional change in the advance of periastron (Smarr & Blandford 1976; Wex 1998). The contribution from the quadrupole moment of pulsar A is estimated to be $\sim 3 \times 10^{-8}$ deg yr^{-1}, where we have used the relations in Bauböck et al. (2013) to calculate the mass quadrupole. This is four orders of magnitude smaller than the second-order effects. The contribution from pulsar B is even smaller (about 10^4 times) due to its slower rotation. Hence we can totally ignore such contributions in this study.

3.2 The proper motion contribution to the observed periastron precession

Apart from the intrinsic contributions to the periastron advance, the proper motion of a binary system also can change the apparent geometrical orientation of the orbit, and hence the observed periastron advance (Kopeikin 1996). As a consequence, the observed value of periastron advance is shifted from its intrinsic value by

$$\dot{\omega}^{\mathrm{obs}} = \dot{\omega}^{\mathrm{intr}} + \dot{\omega}^{\mathrm{K}}. \tag{7}$$

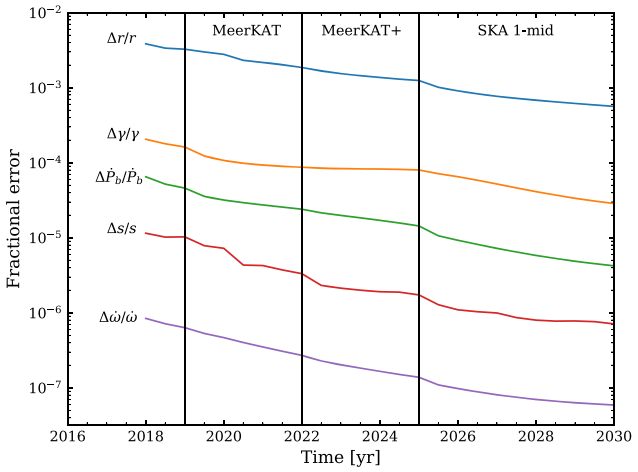

Figure 2. Improvement in the fractional errors of five PK parameters with time, based on the simulation described in Section 5. From top to bottom are: the Shapiro delay range parameter r (blue), the time dilation amplitude γ (orange), the orbital period derivative $\dot{P}_b$ (green), the Shapiro delay shape parameter s (red), and the relativistic advance of periastron $\dot{\omega}$ (purple). The vertical lines mark the observing phase of MeerKAT, MeerKAT+, and SKA 1-mid.

Here, $\dot{\omega}^{\mathrm{K}}$ is the *Kopeikin term* that satisfies

$$\dot{\omega}^{\mathrm{K}} = 2.78 \times 10^{-7}\,\csc i\,(\mu_\alpha \cos\Omega + \mu_\delta \sin\Omega)\,\mathrm{deg\,yr^{-1}}, \tag{8}$$

where i is the orbital inclination as defined in Damour & Taylor (1992), μ_α and μ_δ are the proper motion in right ascension and declination, and Ω is the longitude of the ascending node (measured from East, in the sense of rotation towards North). Using the parameters measured by Kramer et al. (2006) and the estimated $\Omega = 25(2)^\circ$ by Rickett et al. (2014),[5] we obtain $\dot{\omega}^{\mathrm{K}} = -4.0(3) \times 10^{-7}$ deg yr^{-1}. Given the current measurement precision $\Delta\dot{\omega} \sim 10^{-5}$ deg yr^{-1} (Kramer et al., in preparation), the *Kopeikin term* is a small correction to the intrinsic periastron advance that we use in this study. However, since it is three orders of magnitude smaller than $\dot{\omega}^{\mathrm{LT,A}}$ (see Table 1), it does not have a significant influence on the LT measurement.

3.3 Challenges on extracting the Lense–Thirring contribution and measuring the MOI

Although the current measurement precision $\Delta\dot{\omega}$ is already $\sim$ 40 times smaller than $\dot{\omega}^{\mathrm{LT,A}}$, it is not that straightforward to extract the LT contribution from $\dot{\omega}^{\mathrm{obs}}$ with equations (2) and (7), as the two masses (m_A, m_B) are needed to calculate $\dot{\omega}^{\mathrm{1PN}}$ and $\dot{\omega}^{\mathrm{2PN}}$. The masses need to be obtained from any other two PK parameters, where the best two here are the Shapiro delay shape parameter s and the orbital period derivative $\dot{P}_b$ (see Fig. 2). For the Double Pulsar, we already have sufficient precision for s, so the limitation is mainly from $\dot{P}_b$ (Kramer et al., in preparation). The measurement precision of $\dot{P}_b$ will improve over time, especially with the addition of MeerKAT and the SKA. However, the observed value of $\dot{P}_b$ is influenced by extrinsic acceleration effects, which depend on the distance of the pulsar and the Galactic gravitational potential. Moreover, the spin-down mass-loss of the pulsars also have an impact on $\dot{P}_b$, which

[5]Note, Rickett et al. (2014) use a different definition for the longitude of the ascending node Ω, which we have accounted for.

itself depends on the MOI, meaning the masses cannot be determined independently from I_A. These are the challenges for measuring the MOI. An alternative option to $\dot{P}_b$ could be the time dilation amplitude γ, whose fractional error is about one order of magnitude larger than $\dot{P}_b$ (see Fig. 2). However, based on the assumptions of observing plan in Section 5, it would take at least two decades from now to obtain a 1σ-measurement of $\dot{\omega}^{\rm LT,A}$ using only γ, s, and $\dot{\omega}$, a precision that is already reached now with $\dot{P}_b$ (Kramer et al., in preparation). Hence, a comprehensive understanding of the individual contributions to $\dot{P}_b$ is needed, which will be discussed in detail in the following section.

4 THE INTRINSIC AND EXTRINSIC CONTRIBUTIONS TO THE ORBITAL PERIOD DECAY

The observed value of the orbital period decay comprises several effects (Damour & Taylor 1991). For the purpose of this study, we only consider the dominant terms

$$\left(\frac{\dot{P}_b}{P_b}\right)^{\rm obs} = \left(\frac{\dot{P}_b}{P_b}\right)^{\rm GR} + \left(\frac{\dot{P}_b}{P_b}\right)^{\dot{m}_A} + \left(\frac{\dot{P}_b}{P_b}\right)^{\rm Gal} + \left(\frac{\dot{P}_b}{P_b}\right)^{\rm Shk}, \quad (9)$$

where gravitational wave damping (GR) and mass-loss of pulsar A ($\dot{m}_A$) are intrinsic contributions, and Galactic acceleration (Gal) and Shklovskii effect (Shk) are extrinsic contributions. Thereby, the intrinsic orbital period decay can be extracted from the observed value using

$$\dot{P}_b^{\rm intr} = \dot{P}_b^{\rm obs} - \dot{P}_b^{\rm Gal} - \dot{P}_b^{\rm Shk}. \quad (10)$$

Consequently, the uncertainty in the intrinsic orbital period decay also depends on the error in the pulsar distance and the uncertainty in the Galactic gravitational potential at the location of the pulsar and the Earth.

4.1 Gravitational wave damping

The binary system loses energy in the form of GW emission, which shrinks the orbit of the system, and in turn gradually reduces the orbital period. The post-Newtonian approximation is employed to describe the orbital dynamics of the binary system (see e.g. Damour 1987; Blanchet 2014), i.e. the equations of motion are expanded with respect to v/c, where v denotes a typical orbital velocity. The change of the orbital period due to GW damping enters at order $(v/c)^5$, i.e. the 2.5PN approximation. The corresponding change in the orbital period is given by (Peters & Mathews 1963; Esposito & Harrison 1975; Wagoner 1975)

$$\dot{P}_b^{\rm 2.5PN} = -\frac{192\pi}{5}\frac{\eta\,\beta_O^5}{\left(1-e_T^2\right)^{7/2}}\left(1+\frac{73}{24}e_T^2+\frac{37}{96}e_T^4\right), \quad (11)$$

where $\eta = m_A m_B/M^2$ is the symmetric mass ratio. Later, Blanchet & Schäfer (1989) extended the expression to the next-to-leading order (3.5PN),

$$\begin{aligned}\dot{P}_b^{\rm GR} = -\frac{192\pi}{5}\frac{\eta\,\beta_O^5}{\left(1-e_T^2\right)^{7/2}}\Bigg\{1+\frac{73}{24}e_T^2+\frac{37}{96}e_T^4+\frac{\beta_O^2}{336\left(1-e_T^2\right)}\\ \times\left[1273+\frac{16495}{2}e_T^2+\frac{42231}{8}e_T^4+\frac{3947}{16}e_T^6\right.\\ -\left(924+3381e_T^2+\frac{1659}{4}e_T^4-\frac{259}{4}e_T^6\right)\eta\\ \left.+\left(3297e_T^2+4221e_T^4+\frac{2331}{8}e_T^6\right)\frac{\delta m}{M}\right]\Bigg\}, \quad (12)\end{aligned}$$

where δm denotes the mass difference of the timed pulsar and its companion, in our case, $\delta m = m_A - m_B$. Equation (12) can be written in a simplified form as

$$\dot{P}_b^{\rm GR} = \dot{P}_b^{\rm 2.5PN}\left(1+X_{\rm 3.5PN}\right), \quad (13)$$

where the relative correction of the 3.5PN order, $X_{\rm 3.5PN}$, is 1.40×10^{-5} for the Double Pulsar. To date, only the leading order contribution to the orbital period decay is considered in the analysis and interpretation of any of the known binary pulsars. The higher order correction, however, will need to be included in the future, when we reach the necessary timing precision with emerging powerful radio telescopes such as the SKA. We will evaluate future measurability of the 3.5PN contribution to $\dot{P}_b$ in Section 8.

Besides the damping of the binary period, the emission of GWs in principle has an additional effect on the observed $\dot{P}_b$. Junker & Schäfer (1992) have shown that a double NS system with asymmetric masses in an eccentric orbit becomes accelerated due to the GW recoil. Since any acceleration along the line of sight leads to an apparent change in the orbital period (Damour & Taylor 1991), the GW recoil at 3.5PN order will also affect the observed orbital period at some level. As Junker & Schäfer (1992) have pointed out, the recoil acceleration changes its direction with the advance of periastron, in our case on a time-scale of about 21 yr. However, using equation (103) in Junker & Schäfer (1992) we find a maximum shift in the observed $\dot{P}_b$ due to GW recoil of 4.6×10^{-24}, which is seven orders of magnitude below the current measurement precision.

4.2 Galactic acceleration and Shklovskii effect

The contribution of Galactic acceleration can be calculated with (Damour & Taylor 1991; Nice & Taylor 1995; Lazaridis et al. 2009)

$$\begin{aligned}\left(\frac{\dot{P}_b}{P_b}\right)^{\rm Gal} = -\frac{K_z|\sin b|}{c}-\frac{\Theta_0^2}{cR_0}\Bigg\{\cos l+\frac{\beta}{\sin^2 l+\beta^2}\\ \times\left[1+b_0\left(1-\sqrt{\sin^2 l+\beta^2}\right)\right]^2\Bigg\}\cos b, \quad (14)\end{aligned}$$

where $\beta = (d/R_0)\cos b - \cos l$. For the Double Pulsar, the Galactic longitude l is 245.2° and the Galactic latitude b is −4.5°. As for the distance to the Double Pulsar (d), the VLBI observations made by Deller, Bailes & Tingay (2009) implied a distance of $1.15^{+0.22}_{-0.16}$ kpc, whereas the dispersion measure (DM) favours a distance of about 0.52 kpc (Cordes & Lazio 2002). We note that new, preliminary timing and VLBI measurements indicate a distance closer to the DM distance (Kramer et al., in preparation). Hence, for our simulation, we consider an intermediate distance of 0.8 kpc with a 10 per cent error. We will see in Section 6, using a different distance does not have a big influence on our results. The vertical contribution of the Galactic acceleration K_z for Galactic height $z \equiv |d\,\sin b| \lesssim 1.5$ kpc can be approximated with the expression (Holmberg & Flynn 2004; Lazaridis et al. 2009)

$$K_z[10^{-9}\,{\rm cm\,s^{-2}}] \simeq 2.27\,z_{\rm kpc} + 3.68\left[1-\exp(-4.31\,z_{\rm kpc})\right], \quad (15)$$

where $z_{\rm kpc} \equiv z$[kpc]. For K_z, we consider a typical error of about 10 per cent (Holmberg & Flynn 2004; Zhang et al. 2013). The Galactic parameters R_0 is the distance from the Sun to the Galactic centre, and Θ_0 is the Galactic circular velocity at the location of the Sun. In our calculation, we adopt the recent result in Gravity Collaboration (2019), where $R_0 = 8.178 \pm 0.026$ kpc[6] and

[6]We note that the latest measurement of R_0 shows a 2σ difference (Gravity Collaboration 2020), which will not affect our results.

$\Theta_0 = 236.9 \pm 4.2\,\mathrm{km\,s^{-1}}$. The slope parameter at the radius of the Sun is defined as (Damour & Taylor 1991):

$$b_0 \equiv \left(\frac{R}{v}\frac{\mathrm{d}v}{\mathrm{d}R}\right)_{R=R_0}. \tag{16}$$

We note this term is often ignored in other studies, as the rotation curve is nearly flat in the vicinity of the Sun. Its uncertainty, however, could be relevant for measuring the MOI, and as such is included in our study. The slope of the Galactic rotation curve at the location of the Sun estimated by Reid et al. (2014) is $-0.2 \pm 0.4\,\mathrm{km\,s^{-1}\,kpc^{-1}}$, corresponding to $b_0 = 0.007 \pm 0.014$. Lately, Eilers et al. (2019) found a slope significantly different from zero, i.e. $-1.7 \pm 0.1\,\mathrm{km\,s^{-1}\,kpc^{-1}}$ ($b_0 = 0.0603 \pm 0.0035$), with a systematic uncertainty of $0.46\,\mathrm{km\,s^{-1}\,kpc^{-1}}$. Both results will be employed later in our simulation, but for Eilers et al. (2019) we only consider the statistical error and assume that the systematic error can be well understood in the future.

Besides the Galactic acceleration, there are additional accelerations due to masses in the vicinity of the Sun or the pulsar, primarily giant molecular clouds (GMCs), but also stars, black holes, and other external masses (Damour & Taylor 1991; Kehl 2015). These have most likely, if at all, only a small influence on the result, which should not limit our ability of measuring the MOI with a precision lower than 10 per cent (Kehl 2015). The influence of these masses mostly depends on the distance to the Double Pulsar, with which we can, for instance, trace and restrict the presence and influence of GMCs using Galactic carbon monoxide (CO) surveys (Neininger et al. 1998; Glover & Mac Low 2011). We expect that a more firmly established distance measurement in the future will allow a refined analysis to confirm our conclusions.

Finally, the transverse motion of a pulsar leads to an apparent change in the orbital period. This is known as the Shklovskii effect (Shklovskii 1970), and is given as

$$\left(\frac{\dot{P}_\mathrm{b}}{P_\mathrm{b}}\right)^{\mathrm{Shk}} = \frac{\mu^2 d}{c}, \quad \text{with} \quad \mu^2 = \mu_\alpha^2 + \mu_\delta^2. \tag{17}$$

4.3 Mass-loss

A pulsar looses mass due to its energy emission, which changes the orbital period by (Jeans 1924, 1925)

$$\left(\frac{\dot{P}_\mathrm{b}}{P_\mathrm{b}}\right)^{\dot{m}} = -2\,\frac{\dot{m}_\mathrm{A} + \dot{m}_\mathrm{B}}{M}. \tag{18}$$

Although the emission process of pulsars is not fully understood, the mass–energy loss can be calculated (with sufficient precision) from the loss in rotational kinetic energy, i.e. $\dot{E}_j^{\mathrm{rot}} \simeq \dot{m}_j c^2$ (Damour & Taylor 1991), where $\dot{E}_j^{\mathrm{rot}} = I_j \Omega_j \dot{\Omega}_j$, with Ω_j the angular velocity of the (proper) rotation of body j (j = A or B), given in terms of the spin period by $\Omega_j = 2\pi/P_j$. Hence,

$$\left(\frac{\dot{P}_\mathrm{b}}{P_\mathrm{b}}\right)^{\dot{m}_j} = \frac{8\pi^2 \dot{P}_j I_j}{c^2 M P_j^3}. \tag{19}$$

Clearly, the mass-loss correction to the rate of orbital period decay also depends on the MOI, and therefore on the EOS. Table 2 lists the predicted value of each contribution to $\dot{P}_\mathrm{b}^{\mathrm{obs}}$, where the mass-loss contributions are written as a function of $I_\mathrm{j}^{(45)}$. The contribution due to the mass-loss of pulsar A is one order of magnitude smaller than that of the Galactic acceleration and the Shklovskii effect, and of the same order of magnitude as the current measurement precision (Kramer et al., in preparation), hence must be considered. The mass-loss contribution of pulsar B, however, is nearly four orders of magnitude smaller than that of pulsar A and thus can be safely ignored.

Table 2. Contributions to the rate of orbital period decay in the Double Pulsar, calculated with Keplerian parameters and masses measured in Kramer et al. (2006). The Galactic acceleration is computed using Galactic measurements by Gravity Collaboration (2019) and slope in Reid et al. (2014), and a distance of 0.80 kpc is assumed. $I_\mathrm{B}^{(45)}$ is defined in the same way as $I_\mathrm{A}^{(45)}$. The current measurement precision for $\dot{P}_\mathrm{b}$ is below 0.1 fs/s (Kramer et al., in preparation).

Contribution	[fs/s]
$\dot{P}_\mathrm{b}^{\,\mathrm{2.5PN}}$	-1248
$\dot{P}_\mathrm{b}^{\,\mathrm{Gal}}$	-0.38
$\dot{P}_\mathrm{b}^{\,\mathrm{Shk}}$	0.21
$\dot{P}_\mathrm{b}^{\,\mathrm{3.5PN}}$	-0.017
$\dot{P}_\mathrm{b}^{\,\dot{m}_\mathrm{A}}$	$0.023 \times I_\mathrm{A}^{(45)}$
$\dot{P}_\mathrm{b}^{\,\dot{m}_\mathrm{B}}$	$6.3 \times 10^{-6} \times I_\mathrm{B}^{(45)}$

5 SIMULATIONS

In order to investigate the capability of measuring the MOI and testing GR with radio pulsars, we developed a simulation framework to generate and analyse time-of-arrivals (TOAs) for binary pulsars. In this section, we will describe how we simulate TOAs from emerging telescopes for PSR J0737−3039A based on realistic assumptions, and how to measure PK parameters and timing parallax.

To simulate TOAs of PSR J0737−3039A from current and future telescopes, knowledge of the sensitivity of the telescopes, as well as (realistic) assumptions about a future observing plans are needed. We consider the best telescopes for observing this pulsar, i.e. MeerKAT and its future arrays. Unfortunately, this pulsar is not in the field of view of the Five-hundred-meter Aperture Spherical radio Telescope (FAST; Nan et al. 2011), the largest radio telescope today and in the near future.

MeerKAT is a precursor for the mid-frequency array of the SKA, which comprises 64 dishes, each with a diameter of 13.5 m. This corresponds to an effective diameter ($\varnothing_{\mathrm{eff}}$) of 108 m. Regular timing observations for the Double Pulsar started in 2019 as a part of the MeerTIME project (Bailes et al. 2018). The MeerKAT extension, hereafter MeerKAT+, is a joint collaboration of the South African Radio Astronomy Observatory (SARAO) and the Max-Planck-Society (MPG) to extend MeerKAT by the addition of 20 SKA-type dishes, each 15 m in diameter, to MeerKAT. MeerKAT+ is expected to operate from 2022, providing an increase in sensitivity by 50 per cent (Kramer, private communication). The first phase of the SKA mid-frequency array, SKA 1-mid, is planned to build 112 additional dishes with 15 m diameter, extending MeerKAT+ further, with first data from 2025 and full operation after 2027. We summarize the observing plans and the effective diameters of these telescopes in Table 3.

In order to estimate the TOA uncertainty of each observing phase, we need to consider noise contributions for pulsar A. The TOA uncertainty of pulsar A with real MeerKAT observations at L-band is about 1.06 μs for a 5 min integration over the full bandwidth (Bailes et al. 2020). Since the system performance of MeerKAT+ and SKA 1-mid are expected to be similar to that of MeerKAT, and the radiometer noise σ_{rn} reduces in reverse proportional to the effective

Table 3. Telescope observing plans, effective diameters and TOA uncertainties (*L*-band, 5 min integration time) used for simulation. For 2003–2019, $\sigma_{\rm TOA}$ are based on observations from multiple telescopes, where the best data are from the GBT. Its typical uncertainty at *L*-band is shown in the table, whereas the TOAs from the UHF band are expected to be 1.25 times better (Kramer et al., in preparation). The TOA uncertainty for MeerKAT is scaled to 5 min integrations based on real observations (Bailes et al. 2020), and for MeerKAT+ and SKA 1-mid are scaled referring to MeerKAT.

Year	Telescope	$\mathcal{D}_{\rm eff}$ (m)	$\sigma_{\rm TOA}$ (μs)
2003–2019	GBT	100	2.5
2019–2022	MeerKAT	108	1.06
2022–2025	MeerKAT+	127	0.76
2025–2030	SKA 1-mid	203	0.30

collection area of the telescope $A_{\rm eff}$, we can therefore calculate the radiometer noise using the relation

$$\sigma_{\rm rn}^{\rm tel} = \frac{A_{\rm eff}^{\rm MK}}{A_{\rm eff}^{\rm tel}} \sigma_{\rm rn}^{\rm MK}, \tag{20}$$

where the superscript 'MK' stands for MeerKAT. We are not considering noise budgets other than the radiometer noise, because: (1) The phase jitter has not been detected in the current MeerKAT observations and must be rather small (Bailes et al. 2020, Hu et al., in preparation). It may become important in the future observing phase as the radiometer noise reduces, but the influence of jitter can potentially be reduced using Bayesian methods (Imgrund et al. 2015) or binning and combining the data in orbital phase. (2) The contributions from scintillation and other effects are expected to be one or more orders of magnitude smaller than the radiometer noise of SKA 1-mid, hence are neglected. As a result, in our simulation, we adopt the TOA uncertainties solely based on the radiometer noise estimation for each observing phase, which can be found in Table 3.

Based on the above assumptions, we generate TOAs of PSR J0737−3039A that mimic observations with MeerKAT, MeerKAT+, and SKA 1-mid from 2019 to 2030 covering two full orbits per month (∼5 h), and combine them with the existing TOAs from multiple telescopes (Kramer et al., in preparation) to form a long-range data set (2003–2030). Technically speaking, we only use the observing cadence and TOA uncertainties from the existing TOAs, since the data analysis by Kramer et. al (in preparation) is still ongoing, and in the next steps all TOAs will be simulated to fit our model, under the assumption of Gaussian white noise.

The first step is to create a parameter file (model) for pulsar A. For this, we take precisely measured masses from Kramer et al. (2006), $m_{\rm A} = 1.3381\,M_\odot$, $m_{\rm B} = 1.2489\,M_\odot$, and assume EOS AP4 (see Lattimer & Prakash 2001). This particular choice of EOS satisfies the current lower limit of $1.98\,M_\odot$ (99 per cent confidence level, hereafter C.L.) for the maximum mass of a NS (see Section 1 for details), and also lies in the MOI ranges obtained for pulsar A by Gorda (2016), Lim, Holt & Stahulak (2019), Greif et al. (2020). The MOI of pulsar A, under this assumption, is therefore $I_{\rm A}^{\rm AP4} = 1.24 \times 10^{45}\,{\rm g\,cm^2}$. We create a parameter file by taking the well measured Keplerian parameters of the Double Pulsar (Kramer et al. 2006) and the PK parameters computed from $m_{\rm A}$, $m_{\rm B}$, and $I_{\rm A}$. For the advance of periastron $\dot{\omega}$, we consider first- and second-order PN terms and the LT contribution. As for the orbital period decay $\dot{P}_{\rm b}$, we consider leading order (2.5PN) GW emission, Galactic acceleration, Shklovskii effect, and mass-loss in pulsar A. The 3.5PN GW term is only considered in Section 8.

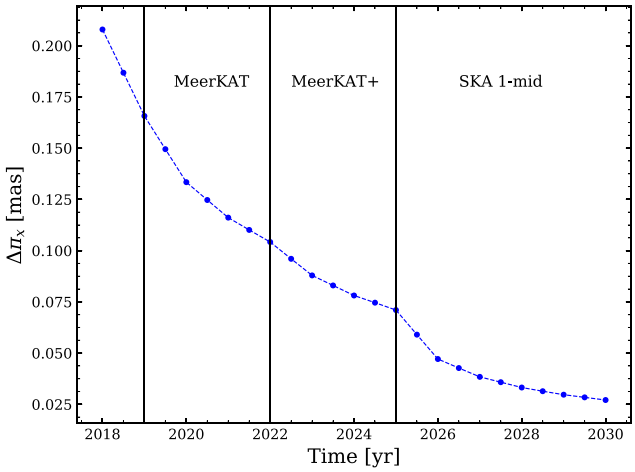

Figure 3. Predicted uncertainty of the timing parallax $\Delta\pi_x$ as a function of time. The corresponding uncertainty in distance is smaller than our assumed value from mid-2021, and is therefore used for future corrections of extrinsic acceleration effects.

We then adjust the TOAs to perfectly match with our model, and add a Gaussian white noise to each TOA, according to its $\sigma_{\rm TOA}$. The red noise from DM variations is not considered in our simulation, since it can be in principle corrected for with multifrequency data. In a final step, we use the pulsar timing software TEMPO[7] to fit for the timing parameters and obtain their uncertainties, including the PK parameters, which are of particular importance here. From 2018 to 2030, the data set is split with a step size of 6 months, so as to demonstrate how the measurements improve with time. The predicted fractional errors of the PK parameters are shown in Fig. 2.

As part of the simulation, we also measure the timing parallax π_x, which gives an idea of the precision of future distance measurement from timing parallax. The predicted uncertainty of π_x is shown in Fig. 3. For the uncertainty of pulsar distance, which enters the Galactic acceleration and the Shklovskii effect, we adopt the value calculated from timing parallax when its uncertainty is smaller than what we assumed in Section 4.2, which is from mid-2021. Aside from timing parallax measurement, in the future, the VLBI parallax measurements with the SKA can potentially provide an accurate distance measurement (Smits et al. 2011).

6 MEASURING THE MOI AND CONSTRAINING THE EOS

Based on our TOA simulation, we predict the future timing measurement of PK parameters (Fig. 2). The three best measured parameters, $\dot{P}_{\rm b}^{\rm obs}$, $\dot{\omega}^{\rm obs}$, and s, are promising for the determination of $I_{\rm A}$. With equations (7) and (10), we obtain the intrinsic periastron advance $\dot{\omega}^{\rm intr}(m_{\rm A}, m_{\rm B}, I_{\rm A})$ and the intrinsic orbital period decay $\dot{P}_{\rm b}^{\rm intr}(m_{\rm A}, m_{\rm B}, I_{\rm A})$. Since both now $\dot{\omega}^{\rm intr}$ and $\dot{P}_{\rm b}^{\rm intr}$ depend on the MOI, we cannot directly use $\dot{P}_{\rm b}^{\rm intr}$ and s to determine the masses and hence measure $I_{\rm A}$ from $\dot{\omega}^{\rm intr}$ as in Kehl et al. (2017). Instead, a self-consistent method is employed to solve for the masses $(m_{\rm A}, m_{\rm B})$ and $I_{\rm A}$ jointly from $\dot{P}_{\rm b}^{\rm intr}(m_{\rm A}, m_{\rm B}, I_{\rm A})$, $s\,(m_{\rm A}, m_{\rm B})$ and $\dot{\omega}^{\rm intr}\,(m_{\rm A}, m_{\rm B}, I_{\rm A})$. To estimate the probability distribution function

[7] http://tempo.sourceforge.net/

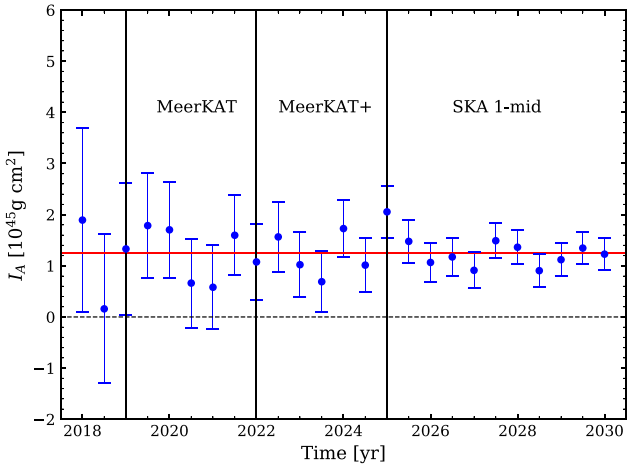

Figure 4. Simulated measurements of the MOI of PSR J0737−3039A with time, where two full orbits observation per month are assumed. The red line indicates the theoretical value of the MOI for the chosen EOS AP4 (I_A^{AP4}).

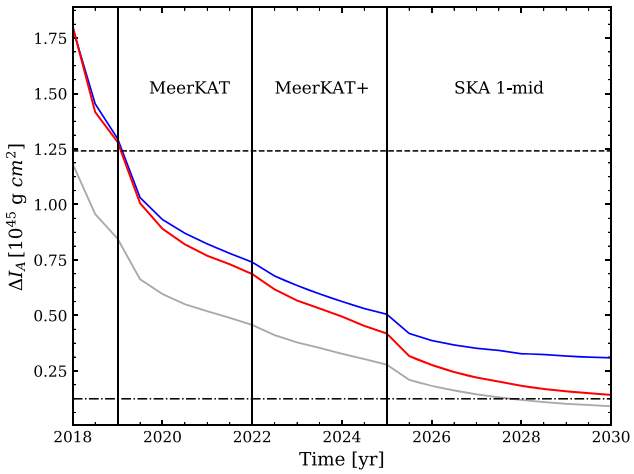

Figure 5. Predicted uncertainty of I_A as a function of time. The blue line adopts the Galactic measurements (R_0, Θ_0) by Gravity Collaboration (2019) and slope measurement by Reid et al. (2014), whereas the red line assumes no errors in the Galactic model. The grey line is same as the red line but ignores the influence of mass-loss to the orbital period change. The theoretical value I_A^{AP4} is indicated by the dashed black line, whereas the dash-dotted line is 10 per cent of the theoretical value.

for I_A, we perform a Monte Carlo simulation to randomize the observed parameters according to their uncertainties. This process is repeated for the measurements from 2018 to 2030.

Fig. 4 shows the predicted measurements of I_A with time, where the new telescopes clearly help to narrow down the uncertainty of I_A. Here we adopt the Galactic measurements (R_0, Θ_0) by Gravity Collaboration (2019) and the slope measurement by Reid et al. (2014). The predicted uncertainty of I_A with time is also illustrated as the blue line in Fig. 5. In this case, we expect to achieve an MOI measurement with 25 per cent precision at 68 per cent C.L. by the year 2030. Our simulation shows that, although the uncertainty of $\dot{P}_b^{obs}$ is initially higher than the Galactic acceleration, it decreases with additional years of precise timing observations (see Fig. 2), and by 2030, the error in the Galactic acceleration is three times higher than the error in $\dot{P}_b^{obs}$, which becomes the limiting factor for measuring the MOI.

However, the measurements of the Galactic potential is expected to improve through various observational methods, such as *Gaia* mission (Gaia Collaboration 2016) and ongoing observations of Galactic masers (Reid et al. 2014). A recent study by Eilers et al. (2019) provides a precise measurement of the circular velocity curve of the Milky Way from 5 to 25 kpc. With the distance from the Sun to the Galactic centre $R_0 = 8.122 \pm 0.031$ kpc (Gravity Collaboration 2018), they determine the rotation speed of the local standard of rest $\Theta_0 = 229.0 \pm 0.2\,\mathrm{km\,s^{-1}}$, with a slope of $-1.7 \pm 0.1\,\mathrm{km\,s^{-1}\,kpc^{-1}}$ (statistical errors), corresponding to $b_0 = 0.0603 \pm 0.0035$. The total uncertainties (including systematic errors) given by Eilers et al. (2019) are similar to the measurements used in the previous case (blue line), but here we assume the systematic errors can be well understood in the near future, and only consider the statistical errors. With this assumption, we expect to measure the MOI with 11 per cent precision at 68 per cent C.L. in 2030. This is nearly the same as using an error-free Galactic model, which is indicated by the red line in Fig. 5. Therefore, with future measurements of the Galactic potential and a better understanding of the systematic errors, an MOI measurement with 11 per cent precision from the Double Pulsar seems realistic.

One important factor for the result is the influence of the mass-loss in pulsar A, which was neglected in the previous study by Kehl et al. (2017). Without considering this contribution, the uncertainty of I_A significantly reduces and reaches 7 per cent by 2030 (see the grey line in Fig. 5), in contrast to the red line. In addition, we find that increasing the observing cadence does not significantly improve the precision of MOI measurements.

As mentioned in Section 4.2, different approaches provide very different measurement of the distance of the Double Pulsar, and a compromise distance of 0.8 kpc is thereby employed in our study. To investigate how distance influences the MOI measurement, we consider two extreme cases, $d = 0.4$ kpc and $d = 1.6$ kpc, with the same setups as in the $d = 0.8$ kpc simulations. Using the current Galactic measurements, we find that the uncertainty of the MOI measurement reaches 17 per cent by 2030 when $d = 0.4$ kpc, and has a much higher uncertainty (43 per cent) when $d = 1.6$ kpc. However, with negligible error in the Galactic potential, both predict ∼11 per cent measurements by 2030, same as for the case of $d = 0.8$ kpc. Since an improved Galactic model is expected in the near future, the value we employ for the distance should not have a significant impact on the prediction of the MOI uncertainty.

An 11 per cent precision measurement of the MOI would further improve the constraints of the EOS of NSs (Lattimer & Schutz 2005; Greif et al. 2020). Fig. 6 shows the MOIs of a number of EOSs, which are scaled by a factor of $M^{3/2}$ in order to reduce the range of the ordinate (cf. Lattimer & Schutz 2005). The 11 per cent measurement predicted from our simulation is illustrated by the red bar centred at the assumed EOS AP4, and located at the precisely measured mass of pulsar A. To compare with the constraints from other methods, we mark the curves in different styles. The observations of the binary NS merger event GW170817 by LIGO/Virgo (Abbott et al. 2018) placed a constraint for the radii of both NSs, 11.9 ± 1.4 km (90 per cent C.L.), which excludes the EOSs in grey dashed curves. Recently, a more stringent constraint combining GW170817 with nuclear theory was obtained by Capano et al. (2020), where they found the radius for a $1.4M_\odot$ NS is $11.0^{+0.9}_{-0.6}$ km (90 per cent C.L.). This further excludes the EOSs in blue dashed curves. The remaining promising EOSs from this constraint are marked in blue solid curves, which is already very close to our 11 per cent prediction from the MOI measurement in 2030. With more and more binary NS mergers expected to be detected in the coming years, tighter constraints

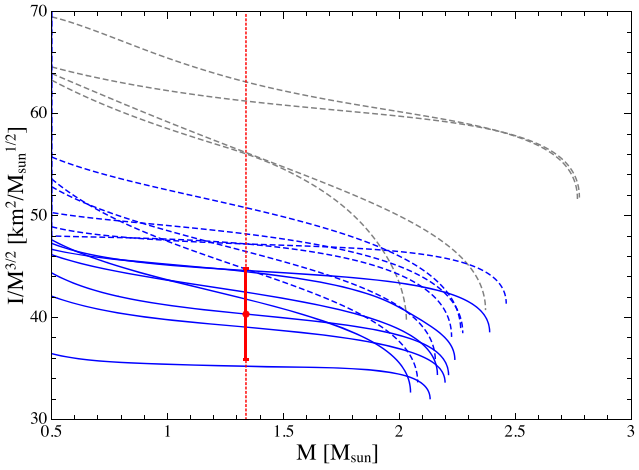

Figure 6. Constraints of EOSs from an 11 per cent measurement of the MOI of PSR J0737−3039A (red). EOS AP4 was assumed in the simulation (curve through red dot). The grey dashed curves indicate EOSs that are disfavoured by the LIGO/Virgo observations of the GW170817 binary neutron-star merger (Abbott et al. 2018). The blue dashed curves are additionally excluded by the refined (combined with nuclear theory) GW170817 analysis by Capano et al. (2020). The following EOSs have been plotted (ascending in their intersection with the left border): WFF1, WFF2, AP4, BSk20, AP3, SLy4, BSk25, MPA1, BSk21, SLy9, BL, BSk22, H4, PAL1, MS2, MS0 (https://compose.obspm.fr). All these EOSs are able to support a NS of 1.98 $M_\odot$, the current lower limit for the maximum mass (see Section 1 for details).

on the EOS are likely to be achieved. Meanwhile, recent NICER observation delivered a joint mass–radius measurement for PSR J0030+0451 from two independent analyses. Riley et al. (2019) found an inferred mass and equatorial radius of $1.34^{+0.15}_{-0.16} M_\odot$ and $12.71^{+1.14}_{-1.19}$ km (68 per cent C.L.), while Miller et al. (2019) found $1.44^{+0.15}_{-0.14} M_\odot$ and $13.02^{+1.24}_{-1.06}$ km. This is a weak constraint on the EOS, but is expected to improve with more observations in the near future. The upcoming X-ray missions, such as eXTP (Zhang et al. 2016) and ATHENA (Barret et al. 2013), are also promising to improve our understanding of the mass–radius relation for NSs.

Therefore, it is fair to assume that the GWs and X-ray observations will place a more stringent constraint on the EOS within the next 10 yr, and if the EOS can be known with sufficient precision, we can in turn use this information as an input to our analysis, test the LT precession, and constrain theories of gravity with the Double Pulsar. We will discuss this scenario in detail in the next section.

7 TESTING LENSE–THIRRING PRECESSION

As discussed in the previous section, the MOI measurement of PSR J0737−3039A is expected to reach 11 per cent accuracy by 2030, whereas GWs and X-ray observations are likely to give a better constraint on the EOS. In this section, we discuss the prospects of testing LT precession and constraining theories of gravity using the Double Pulsar, if the EOS is known.

We again adopt EOS AP4 and this time assume that a precision of 5 per cent could be achieved when calculating the MOI of pulsar A, based on a (hypothesized) future improvement in our understanding of super-dense matter. Given I_A as an input to our simulations, only the masses are unknown for the intrinsic orbital period decay $\dot{P}_b^{\rm intr}$ and the Shapiro shape parameter s. With the masses measured from ($\dot{P}_b^{\rm intr}$, s) and the given I_A, we can directly test the LT contribution to the periastron advance $\dot{\omega}^{\rm LT,A}$. To discuss the physical meaning of such a test, we use the generic framework for relativistic gravity theories introduced by Damour & Taylor (1992), which is fully conservative and based on a Lagrangian that includes a generic term $L_{\rm SO}$ for spin-orbit interaction. As in Damour & Taylor (1992), we will make no assumption about the (strong-field) coupling function Γ_A^B, which enters $L_{\rm SO}$. Since the spin axis of pulsar A has been found to be practically parallel to the orbital angular momentum, the general form of the LT contribution to the periastron advance can be written as

$$\dot{\omega}^{\rm LT,A} = -\frac{2n_b^2 I_A \Omega_A}{\left(1-e_T^2\right)^{3/2} M} \frac{\sigma_A}{\mathcal{G}}, \tag{21}$$

where σ_A is a generic strong-field spin-orbit coupling constant, defined by

$$\sigma_A = \frac{1}{c^2}\left[\Gamma_A^B + \left(\Gamma_A^B - \frac{1}{2}\mathcal{G}\right)\frac{m_B}{m_A}\right]. \tag{22}$$

In GR, the generalized gravitational constant $\mathcal{G}$ equals G, and the coupling function Γ_A^B equals $2G$ (Damour & Taylor 1992), so that

$$\sigma_A^{\rm GR} = \frac{G}{c^2}\left(2 + \frac{3}{2}\frac{m_B}{m_A}\right). \tag{23}$$

But in other theories, Γ_A^B is expected to deviate from $2G$, including modifications by self-gravity contributions from the strongly self-gravitating masses in the system.

We define a parameter $\delta_{\rm LT}$ to measure the relative deviation of the theory-independent parameter $\sigma_A/\mathcal{G}$ from its GR prediction,

$$\delta_{\rm LT} = \left(\frac{\sigma_A}{\mathcal{G}}\right)\left(\frac{\sigma_A^{\rm GR}}{G}\right)^{-1} - 1. \tag{24}$$

By inserting equation (22) into the above definition, one obtains for the spin-orbit coupling function

$$\frac{\Gamma_A^B}{2\mathcal{G}} - 1 = \left(\frac{3+x_A}{4}\right)\delta_{\rm LT}. \tag{25}$$

To assess potential constraints on a non-GR spin-orbit coupling, we multiply the expression of $\dot{\omega}^{\rm LT,A}$ in GR (last term in equation 2) by $(1+\delta_{\rm LT})$, and solve for the parameter $\delta_{\rm LT}$ using the three PK parameters $\dot{P}_b^{\rm intr}(m_A, m_B)$, s (m_A, m_B), and $\dot{\omega}^{\rm intr}(m_A, m_B, \delta_{\rm LT})$. One has to keep in mind that, for simplicity, we make here the assumption that the non-spin related parts of the orbital dynamics and signal propagation are (to sufficient approximation) given by their GR expressions. It goes without saying, that in practice one has to conduct a fully self-consistent analysis within a given class of alternative gravity theories. For a discussion that purely focuses on the measurability of a potential deviation in the LT contribution, our approach is sufficient.

Fig. 7 shows the expected decrease in the uncertainty of $\delta_{\rm LT}$ with future observations. With R_0 and Θ_0 measurements from Gravity Collaboration (2019) and the slope measurement from Reid et al. (2014), we expect to measure $\delta_{\rm LT}$ with 18 per cent precision at 68 per cent C.L. by 2030, which is indicated by the blue line. The red line adopts the Galactic measurements from Eilers et al. (2019), where we expect to achieve a 9 per cent precision by 2030. In the ideal case, we assume that the Galactic potential, the distance to the Double Pulsar, and the MOI can be precisely measured in the future, so that we could leave out the errors. In this scenario, we expect to measure $\delta_{\rm LT}$ with 7 per cent precision by 2030 (green line). We have seen in Section 6 that change from the Galactic measurements by Eilers et al. (2019) to an error-free Galactic model has little enhancement on the measurements of the MOI, and the uncertainty of the timing parallax is relatively small, therefore, the improvement

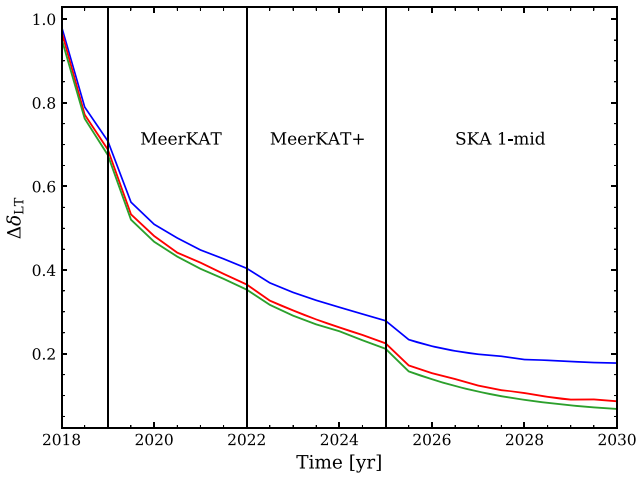

Figure 7. Predicted uncertainty of δ_{LT} as a function of time. The blue line adopts Galactic measurements (R_0, Θ_0) by Gravity Collaboration (2019) and slope measurement by Reid et al. (2014), the red line adopts Galactic and slope measurements by Eilers et al. (2019), and the green line assumes no errors in the Galactic model, the distance and the MOI.

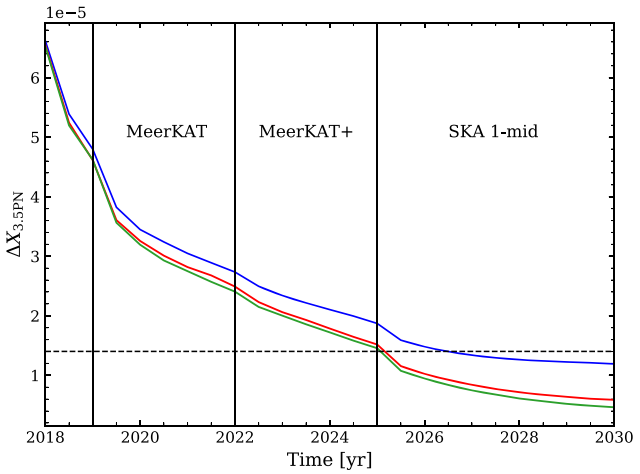

Figure 8. Same as Fig. 7 but for the uncertainty of the 3.5PN order GW correction $X_{3.5PN}$. The dashed line denotes the theoretical value of $X_{3.5PN}$.

from 9 per cent (red line) to 7 per cent (green line) is to a fair fraction (nearly half) related to the uncertainty of the MOI.

Breton et al. (2008) have conducted a different experiment for spin-orbit coupling in the Double Pulsar system. Studying the geodetic precession of pulsar B, they were able to show that $\sigma_B/\mathcal{G}$ is in agreement with GR, with a precision of about 13 per cent. Analogously to equation (22), σ_B is related to Γ_B^A. A priori there is no reason to assume that Γ_B^A and Γ_A^B are equal (see discussion in Damour & Taylor 1992). Consequently, a LT test with pulsar A would nicely complement the geodetic precession test of Breton et al. (2008), when investigating the relativistic interaction between the proper rotation of the two NSs and their orbital motion.

Finally, short range modifications of gravity, related to the strong gravitational field of a NS, could significantly change the structure of the star and therefore its MOI, without any 'direct' impact on the orbital dynamics or the signal propagation in a binary pulsar system. Examples of such theories are scalar-tensor theories with a massive scalar field having a sufficiently short Compton wavelength (see e.g. Ramazanoğlu & Pretorius 2016; Yazadjiev, Doneva & Popchev 2016). While in such a scenario, PK parameters related to time dilation, GW damping, and Shapiro delay remain (practically) unaffected (see e.g. Alsing et al. 2012), one could still expect a deviation in the precession of periastron of the Double Pulsar. The reason is that due to the modification of the MOI the spin of pulsar A and therefore the spin-orbit coupling is modified. Testing the LT precession in the Double Pulsar can therefore be used to constrain such deviations from GR. It is important to note, that $\dot{P}_b^{\rm int}$ would also be modified accordingly, and therefore has to be accounted for. Hence, limits on δ_{LT} would consequently be somewhat weaker than given above (cf. Section 6). In such a scenario it could generally be difficult to disentangle uncertainties in the EOS and deviations from GR by astronomical observations. For this, a combination of various experiments, like GWs from binary NS mergers, X-ray observations, and radio pulsar timing might turn out to be necessary. Nonetheless, the future measurement of the LT precession in the Double Pulsar is expected to provide important contributions when constraining such deviations from GR.

8 NEXT-TO-LEADING ORDER GRAVITATIONAL WAVE DAMPING

In GR, the loss of energy of a material system due to GWs is to leading order sourced by a time-dependent mass quadrupole (Einstein 1918; Eddington 1922). This also holds for binary systems where a change in the mass quadrupole is driven by gravity itself. It enters the two-body equations of motion at the 2.5PN order (see e.g. Damour 1987). When computing the next-to-leading order contribution to GW damping, one also has to account for the mass-octupole and the current quadrupole moments (Thorne 1980). Next-to-leading order contributions enter the equations of motion at 3.5PN ($\mathcal{O}(c^{-7})$), and therefore correspond to the 1PN corrections in the radiation reaction force (Iyer & Will 1995; Pati & Will 2002; Königsdörffer, Faye & Schäfer 2003; Nissanke & Blanchet 2005). The corresponding change in the orbital period of a binary system has been determined out by Blanchet & Schäfer (1989) and is given by equation (12). In this section we will investigate if next-to-leading order corrections to the GW damping are expected to become important in the near future for the timing observation of the Double Pulsar.

Again we assume EOS AP4 and a 5 per cent error in the knowledge of the MOI I_A. We implement the 3.5PN contribution into our model by using equation (12), and adjust the TOAs accordingly. After running simulations as described in Section 5, we obtain the measured PK parameters. We use equation (13) to solve for the relative correction of the 3.5PN order $X_{3.5PN}$ using the three PK parameters $\dot{P}_b^{\rm intr}(m_A, m_B, X_{3.5PN})$, $s\,(m_A, m_B)$, and $\dot{\omega}^{\rm intr}(m_A, m_B)$.

Fig. 8 illustrates the predicted uncertainty of $X_{3.5PN}$ with observing phase, which will fall below its theoretical value $X_{3.5PN}^{\rm theo}$ in the SKA1-mid era. The colours of the lines represent the same conditions as in Fig. 7. The blue line shows the improvements in $\Delta X_{3.5PN}$ with Galactic parameters from Gravity Collaboration (2019) and the slope measurement by Reid et al. (2014), which will reach a precision of 85 per cent at 68 per cent C.L. by 2030. Adopting the Galactic measurements (statistical errors) by Eilers et al. (2019), the red line shows that $X_{3.5PN}$ can be constrained with a precision of 42 per cent by 2030. By contrast, in the ideal case where there are no errors in the Galactic model, the distance and the MOI, $X_{3.5PN}$ can be constrained with a precision of 33 per cent by 2030, where nearly half of the improvement is contributed from the MOI.

9 POTENTIAL NEW DISCOVERIES

Large pulsar surveys with MeerKAT, FAST, and the forthcoming SKA, such as TRAPUM (Stappers & Kramer 2016) and CRAFTS (Li et al. 2018), can potentially discover more relativistic double neutron star (DNS) systems, preferably with a more compact orbit than PSR J0737−3039. An example of such a system, PSR J1946+2052, with a more relativistic orbit than the Double Pulsar ($P_b \simeq 1.88$ h) and larger periastron advance ($\dot{\omega} \approx 26\,\mathrm{deg\,yr^{-1}}$) and LT precession ($\dot{\omega}_{\rm LT} \approx 0.001\,\mathrm{deg\,yr^{-1}}$), was recently discovered in the PALFA survey (Stovall et al. 2018). In its orbital parameters, the PSR J1946+2052 system resembles a system similar to the Double Pulsar, but that has evolved further due to GW damping, by about 40 Myr. While it is still unclear, if for PSR J1946+2052 the necessary precision in the mass determination can be reached to rival the Double Pulsar in the tests proposed here,[8] it certainly adds confidence to the hope of finding more relativistic 'cousins' of the Double Pulsar in the coming years. Such binary pulsars would quite likely enable MOI measurements with superior precision within a comparably short period of time, and improve the constraints of the EOS.

Here we consider two scenarios, one with an orbital period of 100 min and one with 50 min, which are within the expected acceleration searches by MeerKAT. Assuming such systems can be found in 2020 and we start timing them regularly from 2021, with two orbits per month, we run our simulation again to predict the measurements of the MOI. To simplify the simulation, we assume these systems satisfy the conditions of the Double Pulsar (inclination i close to 90 degrees, similar distance and brightness, etc.) but with modified orbital parameters, assuming that these systems had an orbit like the Double Pulsar some time in the past, and then evolved by GW damping to an orbital period of 100 or 50 min. In reality, these systems are likely to be further away. Nonetheless, it is also possible that such systems are bright and nearby, but were missed in the past surveys due to their high acceleration (see Johnston & Kulkarni 1991; Ransom 2001; Jouteux et al. 2002; Ng et al. 2014; Cameron et al. 2018).

We calculate the evolved semimajor axis using Kepler's third law and the evolved eccentricity using the $a - e$ relation in Peters (1964), for the orbital period of 100 and 50 min, respectively. Then we calculate the PK parameters and run simulations as described in Sections 5 and 6. Assuming the same distance as the Double Pulsar, we convert the uncertainty of timing parallax into an uncertainty for the distance. The Galactic measurement by Eilers et al. (2019) is adopted in the simulation and, as before, we assume the systematic uncertainties can be well understood in the future.

Our results show that, for the DNS system with an orbital period of 100 min, we could measure the MOI with 12 per cent precision by 2030 and with 4.5 per cent by 2035 at 68 per cent C.L. As for an orbital period of 50 min, we expect an MOI measurement with 1.5 per cent precision by 2030 and with 0.5 per cent by 2035 at 68 per cent C.L. Such measurements would probably be comparable to the by then available constraints from other methods (GWs and X-ray observations, nuclear physics, etc.) and help for determining the EOS of NSs.

Furthermore, LISA has the potential to discover ultra relativistic DNS systems with a characteristic orbital frequency of 0.8 mHz (Lau et al. 2020). Thrane, Osłowski & Lasky (2020) suggested that following up such systems with SKA for 10 yr could potentially measure the mass–radius relation with a precision <1 per cent. To this end, we perform a simulation for a DNS system with 20 min orbital period, and find an MOI precision of ∼0.2 per cent (68 per cent C.L.) may be possible with 10 yr of timing with SKA 1-mid.

However, there is a low chance that the new discovered DNS systems will be edge-on to our line of sight, as is the case for PSR J0737−3039, hence a precise measurement of s might not be possible. Instead, we may need to use γ to constrain the masses and MOI, whose fractional error is usually a few orders of magnitude larger than s (see Fig. 2). This is indeed the case for PSR J1946+2052, despite its relativistic nature, determining the masses with sufficient precision will be challenging.

Moreover, not all DNS systems are ideal to test the Lense–Thirring precession in terms of periastron advance $\dot{\omega}^{\rm LT}$. Systems like the aforementioned PSR J1757−1854 have a large eccentricity most likely caused by a large kick (Tauris et al. 2017) causing a significant misalignment between the spin of pulsar and the orbital angular momentum, and hence $\dot{\omega}^{\rm LT}$ cannot be determined as straightforwardly as in the Double Pulsar. However, as pointed out in Section 2.2, this allows an alternate test using the contribution of LT precession to the rate of change of the projected semimajor axis $\dot{x}^{\rm LT}$ (Cameron et al. 2018) if profile changes due to geodetic precession can be accounted for in the timing process and the spin orientation can be determined with sufficient precision.

10 CONCLUSION

In this paper, we have developed a consistent method to measure the MOI of radio pulsars, which has been applied to mock data for the Double Pulsar. We simulated TOAs of PSR J0737−3039A assuming future observations with MeerKAT, MeerKAT+, and SKA 1-mid which cover two orbits per month. We found a MOI measurement with 11 per cent accuracy (68 per cent C.L.) could be achievable by the end of this decade, if we have sufficient knowledge of the Galactic gravitational potential (e.g. from *Gaia* mission; Gaia Collaboration 2016). We also found that the mass-loss of pulsar A has a considerable impact on the measurement of the MOI. Neglecting this contribution to the orbital period change leads to an overoptimistic prediction. This is the main reason why, even with the better timing precision used in this paper as compared to Kramer & Wex (2009), by ∼2030 we would still only reach the same accuracy level as predicted by Kramer & Wex (2009). Additionally, the assumptions made in this paper are more realistic compared to Kehl et al. (2017), with timing precision from MeerKAT observation, as well as updated timeline and size of upcoming telescopes.

In the second part of the paper, Sections 7 and 8, we have assumed that a better constraint on the EOS might be achieved with GWs and X-ray observations in the future, so as to investigate the capability of testing LT precession and 3.5PN order contributions to the GW damping. This assumption coincides with Landry, Essick & Chatziioannou (2020) where they found that constraints from GWs and X-ray observations are likely to have larger contributions in constraining the EOS than the MOI measurement of J0737−3039A. Assuming a 5 per cent error in the determination of the MOI, we simulated measurements of the relative deviation of the theory-independent spin-orbit coupling parameter $\sigma_A/\mathcal{G}$ from GR's prediction. We found a 9 per cent precision measurement is possible by 2030 with an improved Galactic model, whereas a 7 per cent precision measurement in the ideal case – no errors in the Galactic model, the distance, and the MOI. This test is a complement to Breton et al. (2008), where they found a 13 per cent constraint on $\sigma_B/\mathcal{G}$. This measurement would enable a constraint for the coupling function Γ_A^B

[8]Since PSR J1946+2052 is less luminous compared to the Double Pulsar, and s is not measurable due to its orientation.

that enters the spin-orbit Lagrangian of the two-body interaction for strongly self-gravitating masses. Such a measurement could be sensitive to short range deviations from GR, which otherwise would not show up in the orbital dynamics of such systems.

We have also studied the measurability of GR's next-to-leading (3.5PN) order GW-damping contribution. We predicted that the uncertainty of the 3.5PN order correction $X_{3.5\mathrm{PN}}$ will fall below its theoretical value at the beginning of SKA 1-mid (∼2026) and a measurement of $X_{3.5\mathrm{PN}}$ with 3σ-significance is possible in ∼10 yr, if by then we have sufficient knowledge of the Galactic gravitational potential, pulsar distance, and the EOS. This means that from the SKA 1-mid era, we will have to include the 3.5PN term in our analysis in order to avoid any bias. Binary mergers detected by LIGO/Virgo do provide constraints on post-Newtonian (PN) terms (Abbott et al. 2016). Their way of counting the PN contributions is relative to the Einstein quadrupole formula, i.e. the order they enter the radiation reaction force (Blanchet 2014). Their 1PN term therefore contains 3.5PN contributions from the equations of motion. As a comparison to our 3.5PN 3-σ result, (Abbott et al. 2019) provide a ∼10 per cent measurement (90 per cent C.L.) of the (radiative) 1PN coefficient with GW170817. Future merger events will most likely lead to even more precise measurements of this term. While at the 2.5PN (0PN radiative) level, the Double Pulsar is still many orders of magnitude more precise than LIGO/Virgo mergers (Kramer 2016, Kramer et al., in preparation). When it comes to higher order PN contributions, we conclude that binary pulsars are not expected to be competitive, simply because of the much smaller orbital velocity.

Finally, we discussed potential new discoveries of DNS systems with radio telescopes like MeerKAT, FAST, and SKA, as well as the space-based future GW observatory LISA. We demonstrated that for a DNS system which mimics the evolved PSR J0737−3039 with an orbital period of 50 min, the MOI measurement is expected to reach 1.5 per cent precision (68 per cent C.L.) after 10 yr observation with MeerKAT, MeerKAT+, and SKA 1-mid, and 0.5 per cent precision after 15 yr. Moreover, LISA is expected to find DNS systems with a characteristic orbital period of 20 min in the near future (Lau et al. 2020). Such discoveries can significantly tighten the constraints for the EOS.

To conclude, although the EOS constraints resulting from a future MOI measurement with the Double Pulsar are not likely to exceed those with LIGO/Virgo mergers and X-ray observations in the coming years, we are still anticipating other aspects of science coming from this unique gravity laboratory in future studies based on an improved understanding of the NS EOS as an input. Furthermore, the discovery of more relativistic binary pulsars, possible with the unprecedented surveying capabilities of new and upcoming radio telescopes and advances in data analysis (e.g. Lentati et al. 2018), could ultimately lead to EOS constraints quite competitive with other methods.

ACKNOWLEDGEMENTS

We are grateful to Vivek Venkatraman Krishnan and Aditya Parthasarathy for helpful discussions, and Paulo Freire for carefully reading the manuscript. We would also like to thank our reviewer, Gerhard Schäfer, for his helpful comments. HH is a member of the International Max Planck Research School for Astronomy and Astrophysics at the Universities of Bonn and Cologne. NW and MK gratefully acknowledge support from ERC Synergy Grant 'BlackHoleCam' Grant Agreement Number 610058. This work has been supported by the Chinese Academy of Sciences (CAS) and the Max-Planck Society (MPG) in the framework of LEGACY cooperation on low-frequency gravitational wave astronomy.

DATA AVAILABILITY

The data underlying this article will be shared on reasonable request to the corresponding author.

REFERENCES

Abbott B. P. et al., 2016, Phys. Rev. Lett., 116, 221101
Abbott B. P. et al., 2017, Phys. Rev. Lett., 119, 161101
Abbott B. P. et al., 2018, Phys. Rev. Lett., 121, 161101
Abbott B. P. et al., 2019, Phys. Rev. Lett., 123, 011102
Alsing J., Berti E., Will C. M., Zaglauer H., 2012, Phys. Rev. D, 85, 064041
Antoniadis J. et al., 2013, Science, 340, 448
Arzoumanian Z. et al., 2018, ApJS, 235, 37
Bailes M. et al., 2018, Proceedings of Science, 277, 011
Bailes M. et al., 2020, Publ. Astron. Soc. Austr., 37, e028
Barker B. M., O'Connell R. F., 1975, Phys. Rev. D, 12, 329
Barret D. et al., 2013, in Cambresy L., Martins F., Nuss E., Palacios A., eds, SF2A-2013: Proceedings of the Annual meeting of the French Society of Astronomy and Astrophysics, Société Francaise d'Astronomie et d'Astrophysique, Montpellier, p. 447
Bauböck M., Berti E., Psaltis D., Özel F., 2013, ApJ, 777, 68
Berti E., White F., Maniopoulou A., Bruni M., 2005, MNRAS, 358, 923
Bhat N. D. R., Bailes M., Verbiest J. P. W., 2008, Phys. Rev. D, 77, 124017
Blanchet L., 2014, Liv. Rev. Relat., 17, 2
Blanchet L., Schäfer G., 1989, MNRAS, 239, 845
Breton R. P. et al., 2008, Science, 321, 104
Burgay M. et al., 2003, Nature, 426, 531
Cameron A. D. et al., 2018, MNRAS, 475, L57
Camilo F., 2018, Nat. Astron., 2, 594
Capano C. D. et al., 2020, Nat. Astron., 4, 625
Ciufolini I., Pavlis E. C., 2004, Nature, 431, 958
Ciufolini I. et al., 2019, Eur. Phys. J. C, 79, 872
Cordes J. M., Lazio T. J. W., 2002, preprint (astro–ph/0207156)
Cromartie H. T. et al., 2019, Nat. Astron., 4, 72
Damour T., 1987, in Hawking S. W., Israel W., eds, Three Hundred Years of Gravitation, Cambridge Univ. Press, Cambridge, p. 128
Damour T., Deruelle N., 1985, Ann. Inst. Henri Poincaré Phys. Théor, 43, 107
Damour T., Deruelle N., 1986, Ann. l'inst. Henri Poincaré (A) Phys. théor., 44, 263
Damour T., Schäfer G., 1988, Nuovo Cimento B Serie, 101B, 127
Damour T., Taylor J. H., 1991, ApJ, 366, 501
Damour T., Taylor J. H., 1992, Phys. Rev. D, 45, 1840
Deller A. T., Bailes M., Tingay S. J., 2009, Science, 323, 1327
Demorest P. B., Pennucci T., Ransom S. M., Roberts M. S. E., Hessels J. W. T., 2010, Nature, 467, 1081
Desvignes G. et al., 2019, Science, 365, 1013
Eddington A. S., 1922, Proc. Roy. Soc. Lond. A, A102, 268
Eilers A.-C., Hogg D. W., Rix H.-W., Ness M. K., 2019, ApJ, 871, 120
Einstein A., 1918, Sitzungsber. Preuss. Akad. Wiss. Berlin (Math. Phys.), 1918, 154
Esposito L. W., Harrison E. R., 1975, ApJ, 196, L1
Ferdman R. D. et al., 2008, in Bassa C., Wang Z., Cumming A., Kaspi V. M., eds, AIP Conf. Proc. Vol. 983, 40 Years of Pulsars: Millisecond Pulsars, Magnetars and More. Am. Inst. Phys., New York, p. 474
Ferdman R. D. et al., 2013, ApJ, 767, 85
Gaia Collaboration, 2016, A&A, 595, A1
Glover S. C. O., Mac Low M. M., 2011, MNRAS, 412, 337
Gorda T., 2016, ApJ, 832, 28
Gravity Collaboration et al., 2018, A&A, 615, L15
Gravity Collaboration, 2019, A&A, 625, L10

Gravity Collaboration et al., 2020, A&A, 636, L5
Greif S. K., Hebeler K., Lattimer J. M., Pethick C. J., Schwenk A., 2020, preprint (arXiv:2005.14164)
Holmberg J., Flynn C., 2004, MNRAS, 352, 440
Imgrund M., Champion D. J., Kramer M., Lesch H., 2015, MNRAS, 449, 4162
Iyer B. R., Will C. M., 1995, Phys. Rev. D, 52, 6882
Jeans J. H., 1924, MNRAS, 85, 2
Jeans J. H., 1925, MNRAS, 85, 912
Johnston H. M., Kulkarni S. R., 1991, ApJ, 368, 504
Jouteux S., Ramachandran R., Stappers B. W., Jonker P. G., van der Klis M., 2002, A&A, 384, 532
Junker W., Schäfer G., 1992, MNRAS, 254, 146
Kehl M. S., 2015, Master's thesis. University of Bonn, Germany
Kehl M. S., Wex N., Kramer M., Liu K., 2017, in Bianchi M., Jantzen R. T., Ruffini R., eds, in 14th Marcel Grossmann Meeting on Recent Developments in Theoretical and Experimental General Relativity, Astrophysics, and Relativistic Field Theories, World Scientific Publishing Co. Pte. Ltd., Singapore, p. 1860
Kopeikin S. M., 1996, ApJ, 467, L93
Kramer M., 1998, ApJ, 509, 856
Kramer M., 2016, Int. J. Mod. Physics D, 25, 1630029
Kramer M., Stappers B., 2015, Proceedings of Science, 215, 36
Kramer M., Wex N., 2009, Class. Quantum Gravity, 26, 073001
Kramer M. et al., 2006, Science, 314, 97
Königsdörffer C., Faye G., Schäfer G., 2003, Phys. Rev. D, 68, 044004
Landry P., Essick R., Chatziioannou K., 2020, Phys. Rev. D, 101, 123007
Lattimer J. M., Prakash M., 2001, ApJ, 550, 426
Lattimer J. M., Prakash M., 2016, Phys. Rep., 621, 127
Lattimer J. M., Schutz B. F., 2005, ApJ, 629, 979
Lau M. Y. M., Mandel I., Vigna-Gómez A., Neijssel C. J., Stevenson S., Sesana A., 2020, MNRAS, 492, 3061
Lazaridis K. et al., 2009, MNRAS, 400, 805
Lense J., Thirring H., 1918, Phys. Zeitschr., 19, 156
Lentati L., Champion D. J., Kramer M., Barr E., Torne P., 2018, MNRAS, 473, 5026
Li D. et al., 2018, IEEE Microwave Mag., 19, 112
Lim Y., Holt J. W., Stahulak R. J., 2019, Phys. Rev. C, 100, 035802
Lyne A. G. et al., 2004, Science, 303, 1153
Manchester R. et al., 2015, Tempo: Pulsar timing data analysis, record ascl:1509.002
Miller M. C. et al., 2019, ApJ, 887, L24
Morrison I. A., Baumgarte T. W., Shapiro S. L., Pand haripande V. R., 2004, ApJ, 617, L135
Nan R. et al., 2011, Int. J. Mod. Phys. D, 20, 989
Neininger N., Guélin M., Ungerechts H., Lucas R., Wielebinski R., 1998, Nature, 395, 871
Ng C. et al., 2014, MNRAS, 439, 1865
Nice D. J., Taylor J. H., 1995, ApJ, 441, 429
Nissanke S., Blanchet L., 2005, Class. Quantum Gravity, 22, 1007
Özel F., Freire P., 2016, ARA&A, 54, 401
Pati M. E., Will C. M., 2002, Phys. Rev. D, 65, 104008
Peters P. C., 1964, Phys. Rev., 136, 1224
Peters P. C., Mathews J., 1963, Phys. Rev., 131, 435
Pfister H., 2007, Gen. Relativ. Gravit., 39, 1735
Pol N., McLaughlin M., Kramer M., Stairs I., Perera B. B. P., Possenti A., 2018, ApJ, 853, 73
Ramazanoğlu F. M., Pretorius F., 2016, Phys. Rev. D, 93, 064005
Ransom S. M., 2001, PhD thesis. Harvard University
Reid M. J., McClintock J. E., Steiner J. F., Steeghs D., Remillard R. A., Dhawan V., Narayan R., 2014, ApJ, 796, 2
Rezzolla L., Most E. R., Weih L. R., 2018, ApJ, 852, L25
Rickett B. J. et al., 2014, ApJ, 787, 161
Riley T. E. et al., 2019, ApJ, 887, L21
Schäfer G., Wex N., 1993, Phys. Lett. A, 174, 196
Shibata M., Zhou E., Kiuchi K., Fujibayashi S., 2019, Phys. Rev. D, 100, 023015
Shklovskii I. S., 1970, Sov. Astron., 13, 562
Smarr L. L., Blandford R., 1976, ApJ, 207, 574
Smits R., Tingay S. J., Wex N., Kramer M., Stappers B., 2011, A&A, 528, A108
Stairs I. H., Thorsett S. E., Arzoumanian Z., 2004, Phys. Rev. Lett., 93, 141101
Stairs I. H., Thorsett S. E., Dewey R. J., Kramer M., McPhee C. A., 2006, MNRAS, 373, L50
Stairs I. H., Thorsett S. E., Taylor J. H., Wolszczan A., 2002, ApJ, 581, 501
Stappers B., Kramer M., 2016, Proceedings of Science, 277, 9
Stovall K. et al., 2018, ApJ, 854, L22
Tauris T. M. et al., 2017, ApJ, 846, 170
Thorne K., 1980, Rev. Mod. Phys., 52, 299
Thrane E., Osłowski S., Lasky P. D., 2020, MNRAS, 493, 5408
van Leeuwen J. et al., 2015, ApJ, 798, 118
Venkatraman Krishnan V., Bailes M., van Straten W., Keane E. F., Kramer M., Bhat N. D. R., Flynn C., Osłowski S., 2019, APJL, 873, L15
Venkatraman Krishnan V. et al., 2020, Science, 367, 577
Wagoner R. V., 1975, ApJ, 196, L63
Watts A. L. et al., 2016, Rev. Mod. Phys., 88, 021001
Wex N., 1995, Class. Quantum Gravity, 12, 983
Wex N., 1998, MNRAS, 298, 67
Will C. M., 2018, Theory and Experiment in Gravitational Physics, Second Edition. Cambridge Univ. Press, Cambridge, England
Yazadjiev S. S., Doneva D. D., Popchev D., 2016, Phys. Rev. D, 93, 084038
Zhang L., Rix H.-W., van de Ven G., Bovy J., Liu C., Zhao G., 2013, ApJ, 772, 108
Zhang S. N. et al., 2016, in den Herder J.-W. A., Takahashi T., Bautz M., eds, Proc. SPIE Conf. Ser. Vol. 9905, Space Telescopes and Instrumentation 2016: Ultraviolet to Gamma Ray. SPIE, Bellingham, p. 99051Q

This paper has been typeset from a TEX/LATEX file prepared by the author.

Paper II: Gravitational signal propagation in the double pulsar studied with the MeerKAT telescope

---

A&A 667, A149 (2022)
https://doi.org/10.1051/0004-6361/202244825

Astronomy & Astrophysics

Gravitational signal propagation in the double pulsar studied with the MeerKAT telescope

H. Hu (胡奂晨)[1], M. Kramer[1,2], D. J. Champion[1], N. Wex[1], A. Parthasarathy[1], T. T. Pennucci[3], N. K. Porayko[1], W. van Straten[4], V. Venkatraman Krishnan[1], M. Burgay[5], P. C. C. Freire[1], R. N. Manchester[6], A. Possenti[5], I. H. Stairs[7], M. Bailes[8,9], S. Buchner[10], A. D. Cameron[8,9], F. Camilo[10], and M. Serylak[11,12]

[1] Max-Planck-Institut für Radioastronomie, Auf dem Hügel 69, 53121 Bonn, Germany
e-mail: huhu@mpifr-bonn.mpg.de
[2] Jodrell Bank Centre for Astrophysics, The University of Manchester, Oxford Road, Manchester M13 9PL, UK
[3] Institute of Physics, Eötvös Loránd University, Pázmány P.s. 1/A, 1117 Budapest, Hungary
[4] Institute for Radio Astronomy & Space Research, Auckland University of Technology, Private Bag 92006, Auckland 1142, New Zealand
[5] INAF-Osservatorio Astronomico di Cagliari, Via della Scienza 5, 09047 Selargius, Italy
[6] Australia Telescope National Facility, CSIRO Space and Astronomy, PO Box 76, Epping, NSW 1710, Australia
[7] Dept. of Physics and Astronomy, University of British Columbia, 6224 Agricultural Road, Vancouver, BC V6T 1Z1, Canada
[8] Centre for Astrophysics and Supercomputing, Swinburne University of Technology, PO Box 218, Hawthorn, VIC 3122, Australia
[9] ARC Centre of Excellence for Gravitational Wave Discovery (OzGrav), Mail H29, Swinburne University of Technology, PO Box 218, Hawthorn, VIC 3122, Australia
[10] South African Radio Astronomy Observatory, Cape Town 7925, South Africa
[11] SKA Observatory, Jodrell Bank, Lower Withington, Macclesfield SK11 9FT, UK
[12] Department of Physics and Astronomy, University of the Western Cape, Bellville, Cape Town 7535, South Africa

Received 29 August 2022 / Accepted 22 September 2022

ABSTRACT

The double pulsar PSR J0737−3039A/B has offered a wealth of gravitational experiments in the strong-field regime, all of which general relativity has passed with flying colours. In particular, among current gravity experiments that test photon propagation, the double pulsar probes the strongest spacetime curvature. Observations with MeerKAT and, in the future, the Square Kilometre Array (SKA) can greatly improve the accuracy of current tests and facilitate tests of next-to-leading-order (NLO) contributions in both orbital motion and signal propagation. We present our timing analysis of new observations of PSR J0737−3039A, made using the MeerKAT telescope over the last three years. The increased timing precision offered by MeerKAT yields a measurement of Shapiro delay parameter s that it twice as good, and an improved mass measurements compared to previous studies. In addition, our results provide an independent confirmation of the NLO signal propagation effects and already surpass the previous measurement from 16 yr data by a factor of 1.65. These effects include the retardation effect due to the movement of the companion and the deflection of the signal by the gravitational field of the companion. We also investigate the novel effects that have been expected. For instance, we search for potential profile variations near superior conjunctions caused by shifts of the line of sight due to latitudinal signal deflection, and we find insignificant evidence with our current data. With simulations, we find that the latitudinal deflection delay is unlikely to be measured with timing because of its correlation with Shapiro delay. Furthermore, although it is currently not possible to detect the expected lensing correction to the Shapiro delay, our simulations suggest that this effect may be measured with the full SKA. Finally, we provide an improved analytical description for the signal propagation in the double pulsar system that meets the timing precision expected from future instruments such as the full SKA.

Key words. stars: neutron – pulsars: individual: J0737–3039A – gravitation – binaries: eclipsing

1. Introduction

The double pulsar PSR J0737−3039A/B is a rich laboratory for strong-field gravity experiments. The system consists of a 23-ms recycled pulsar ('A') and a 2.8-s 'normal' pulsar ('B') in a nearly edge-on and slightly eccentric 2.45-h orbit (Burgay et al. 2003; Lyne et al. 2004). Various relativistic effects have been precisely measured in previous works (Kramer et al. 2006a, 2021a), including periastron precession, time dilation (gravitational redshift and second-order Doppler effect), Shapiro delay due to light propagation in the curved spacetime of the companion, and the orbital period decay, which currently provides the most precise test of quadrupolar gravitational waves predicted by general relativity (GR). In addition, the relativistic spin precession of B was measured by Breton et al. (2008) and the relativistic deformation of the orbit was newly detected in this system (Kramer et al. 2021a). All these make it a still unique system for gravity experiments.

Comparing with other gravity experiments, the Shapiro delay measured in the double pulsar probes the strongest spacetime curvature ($\sim 10^{-21}$ cm^{-2}) in a precision experiment with photons, that is, the interaction between gravitational and electromagnetic fields (Wex & Kramer 2020). In addition, with 16 yr of data, Kramer et al. (2021a) were able, for the first time, to measure higher-order effects of signal propagation in the strong gravitational field of a neutron star, which are currently not accessible

via any other method. These include the retardation effect due to the movement of the companion (B) and aberrational light deflection by the gravitation of the companion. The latter confirms the prograde rotation of A, which is consistent with the results measured by Pol et al. (2018) using the emission properties of B and is in line with the expectations from binary evolution models.

In this work, we present observations of PSR J0737−3039A with the MeerKAT telescope, a precursor for the Square Kilometre Array (SKA) at mid-frequency range. Thanks to its location in the Southern Hemisphere, it permits a timing precision more than two times better than that of the Green Bank Telescope for this pulsar (Bailes et al. 2020; Kramer et al. 2021b). This superior precision enables an independent and improved measurement of signal propagation effects within a very short time span. We also investigate effects that have been expected but not been studied in detail before. These include potential profile variations due to latitudinal deflection, the detectability of latitudinal deflection delay, and the prospects of measuring the effect of lensing on the propagation time separately.

This paper is organised as follows. Section 2 describes the MeerKAT observations on the double pulsar and data processing. In Sect. 3, we introduce the concepts of gravitational signal propagation effects, including higher-order contributions to the Shapiro and aberration delay. The timing results and mass measurements are presented in Sect. 4. We then provide an in-depth study on the higher-order signal propagation effects in Sect. 5, with a focus on latitudinal deflection and lensing. In addition, we provide an improved analytical description for the signal propagation in the double pulsar. Finally, we discuss the results and future prospects in Sect. 6.

2. Observations and data processing

2.1. MeerKAT observations

The observations presented in this paper come from the MeerKAT telescope as part of the MeerTIME project (Bailes et al. 2020), which performs timing of known pulsars with various scientific themes. Observations on PSR J0737−3039A are conducted under the Relativistic Binary theme (RelBin, Kramer et al. 2021b), which focuses on testing the relativistic effects in binary pulsars to achieve measurements of neutron star masses and tests of theories of gravity. MeerTime observations are generally recorded using the Pulsar Timing User Supplied Equipment (PTUSE) signal processor. This processor receives channelised tied-array beamformed voltages from the correlator-beamformer engine of the MeerKAT observing system and is capable of producing coherently de-dispersed full-Stokes data in both the filterbank (search) mode and the fold (timing) mode, where the data are folded at the topocentric period of the pulsar. Details on the pulsar observing setup with MeerTime are explained by Bailes et al. (2020).

PSR J0737−3039A is regularly observed with a typical cadence of one month and duration of 3 h. As the orbital period of this pulsar is ∼2.45 h, the observations are scheduled to start shortly before an eclipse and finish after the second eclipse, in order to observe the eclipses twice in one observing session. The session is typically composed of a 30 min observation with the fold mode and search mode in parallel, followed by a 2 h fold-mode observation and another 30 min fold-search dual-mode observation. This specific arrangement is designed to maximise our sensitivity in detecting signal propagation effects, as well as in studying the magnetosphere of pulsar B (Lower et al., in prep.). Observations are performed with two receivers: the *L*-band receiver that covers the frequency range 856–1712 MHz, and the UHF receiver that covers the frequency range 544–1088 MHz, both with 1024 channels. The data presented here started in March 2019 and ran until May 2022. For the analysis in this paper, we use 29 full-orbit timing observations and 62 search-mode eclipse data sets, which amounts to a total of ∼87 h.

2.2. Timing data reduction

The raw timing data from the PTUSE machines are folded every eight seconds, which are then processed with the MEERPIPE data reduction pipeline. MEERPIPE carries out radio frequency interference (RFI) removal using a modified COASTGUARD algorithm (Lazarus et al. 2016), followed by flux and polarisation calibration. Details on polarisation and flux calibration are described in Serylak et al. (2021) and Spiewak et al. (2022), respectively.

After processing with MEERPIPE, the calibrated data products are reduced using the pulsar software package PSRCHIVE[1] (Hotan et al. 2004). We first correct for the rotation measure (RM) with the value measured in Kramer et al. (2021b), that is, RM = 120.84 rad m^{-2}. As the *L*-band observations between March 2019 and February 2020 were restricted to 928 frequency channels (dropping 48 channels each from the top and bottom bands), to maintain consistency throughout the analysis, we reduce the later *L*-band data to the same frequency channels. We treat the UHF-band data in the same way, as the roll-off adversely affects sensitivity of the top and bottom bands.

For this system, a complete timing model is only available in the pulsar timing software TEMPO[2] (Nice et al. 2015, more details are given in Sect. 4). Therefore, to fold the data more accurately, all data are supplied with a `polyco`-format ephemeris with the values measured in Kramer et al. (2021a). Since the double pulsar rapidly changes its orbital phase, the time span (TSPAN) of a predicted pulse phase solution has to be as small as possible to retain good precision[3]. With the PSRCHIVE version 2022-01-14, we set TSPAN to the minimum possible value, which is 3 min.

There is a known data processing issue with this pulsar, which is that the pulsar moves rapidly to a different orbital phase during the dispersion delay time. Thus, the pulses received at the same time at different frequencies correspond to different orbital phases and cannot be folded with the same phase prediction. If not properly accounted for, this folding issue will cause frequency-dependent orbital smearing. Standard pulsar software such as PSRCHIVE do not take this effect fully into consideration, even with the frequency-resolved TEMPO2 predictor[4]. To avoid this issue, we first de-disperse the total intensity data so that all frequencies correspond to the same orbital phase, then average the data, first in frequency and then in time[5]. Because of the profile frequency evolution and scintillation effects, data are sub-banded in frequency, with 32 sub-bands for the UHF-band and 16 sub-bands for the *L*-band.

[1] http://psrchive.sourceforge.net/
[2] http://tempo.sourceforge.net/
[3] Our analysis suggests that the choice of TSPAN has a significant impact on the Shapiro parameters: a larger TSPAN leads to a large deviation from the expected values.
[4] This issue is going to be addressed in PSRCHIVE 2.0, which is under development.
[5] The order of processing matters. If reversed, the pulse phase appears to be different and phase offsets may be introduced.

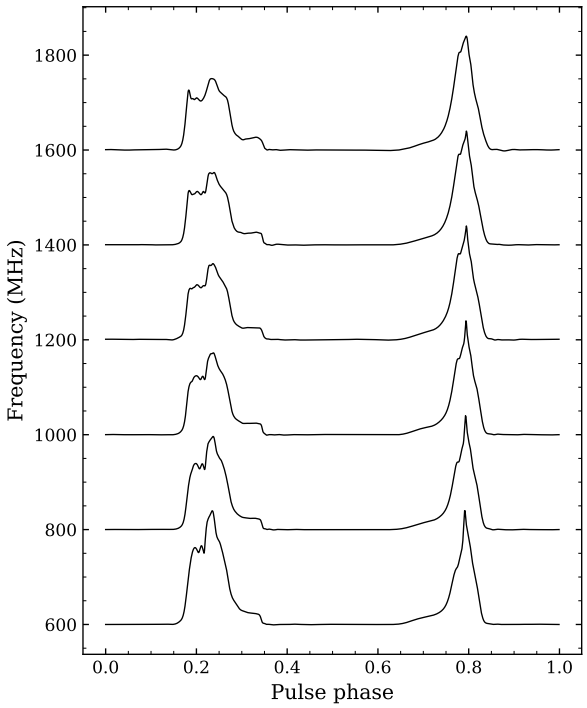

Fig. 1. Pulse profile of PSR J0737−3039A observed at multiple frequencies with the MeerKAT UHF- and *L*-band receivers.

As for the time-averaging, the integration time needs to be short enough in order to properly resolve the Shapiro delay and the next-to-leading-order (NLO) signal propagation contributions ($q_{\rm NLO}$, see Sect. 3), which are largest at superior conjunction. We perform a simulation to test the measurability of these NLO contributions with different integration times. The results show that a good measurement of Shapiro delay and $q_{\rm NLO}$ can be achieved if the integration time is $\lessapprox$32 s, but it becomes significantly worse if the integration time is longer than 1 min for $q_{\rm NLO}$ and 2 min for Shapiro delay. Therefore, we average all data with a 32-s integration time, consistent with the analysis by Kramer et al. (2021a). After frequency and time averaging, data are re-dispersed to allow measurements of dispersion measure (DM) in the timing analysis.

2.3. Wide-band templates and TOA extraction

Wide-band observations such as MeerTIME can suffer significant profile evolution in frequency, and thus the traditional 1D template is not favoured. To best determine the pulse time of arrivals (TOAs) at multiple frequencies, we employ frequency-dependent 2D templates. With this technique, DM measurements are dependent on the DM value used to align (de-disperse) the 2D template. Due to the correlation between the DM and profile evolution, DM measurements are to some extent frequency dependent, which can lead to a DM offset between *L*-band and UHF-band data. This could potentially be solved with a simultaneous observation with *L*-band and UHF-band receivers, which is missing in our case. Therefore, to avoid this problem, we choose a bright observation from each band for making 2D templates, and measure DM using data from their overlapping frequencies. Then, we use these DM values to de-disperse the corresponding full-bandwidth data. This minimises the DM offset between *L*-band and UHF-band data, which can be seen in Fig. 2. These data are then sub-banded and averaged in time. Finally, by smoothing the profiles with `psrsmooth`/PSRCHIVE, we obtain 2D templates, with 16 sub-bands at *L*-band and 32 sub-bands at UHF-band. These templates are then used to measure frequency-resolved TOAs by cross-correlating with the reduced data using `pat`/PSRCHIVE. The pulse profile of PSR J0737−3039A at multiple frequencies is shown in Fig. 1. More information on the observing systems and data sets is given in Table 1.

2.4. DM variation

The wide-band observation and high precision of MeerKAT telescope make it possible to obtain an accurate DM measurement on a per-epoch basis so as to minimise the influence of DM noise in the data. To do so, we fit for only DM and spin frequency ν for each observing epoch using 4-min TOAs, and keep the other parameters fixed. The DM measurements are shown in Fig. 2. Following Kramer et al. (2021a), we use a modified version of TEMPO for our timing analysis, which corrects dispersive delays for each TOA based on the exact DM measurement of that epoch.

One should note that our data set does not show the apparent DM variation as a function of orbital phase, as was seen in Ransom et al. (2004). It had been demonstrated that this effect occurs due to an unaccounted Doppler shift of the observational frequency as the pulsar moves in a binary system[6], and this will be revisited by Hu, Porayko et al. (in prep.). A more thorough investigation of this effect, as well as the frequency-dependent orbital smearing (see Sect. 2.2), is ongoing and will be presented in detail in the future publication.

3. Signal propagation effects at superior conjunction

In this section, we recapitulate the necessary concepts of signal propagation effects in the double pulsar, including the NLO contributions in the Shapiro delay and aberration delay. These concepts were described in greater detail in Kramer et al. (2021a).

Being a nearly edge-on binary system (i.e. $i \sim 90°$), the curved spacetime of the companion star (pulsar B) has a significant effect on the propagation of the pulsar's signal. To leading-order this is the well-known Shapiro delay (Shapiro 1964), which is expressed in the following form for binary pulsars (Blandford & Teukolsky 1976; Damour & Deruelle 1986):

$$\Delta_{\rm S}^{\rm (LO)} = -2r \ln \Lambda_u, \tag{1}$$

$$\Lambda_u = 1 - e_{\rm T} \cos u - s \Big[\sin\omega (\cos u - e_{\rm T}) + (1 - e_{\rm T}^2)^{1/2} \cos\omega \sin u \Big]. \tag{2}$$

Here, u denotes the eccentric anomaly (from Kepler's equation with eccentricity $e_{\rm T}$), and ω denotes the longitude of periastron measured from the ascending node. The time eccentricity $e_{\rm T}$ corresponds to the eccentricity parameter in the Damour-Deruelle (DD) timing model (Damour & Deruelle 1986) that can be fitted in the pulsar timing software TEMPO or TEMPO2 (Hobbs et al. 2006). The two post-Keplerian (PK) parameters r and s represent the 'range' and 'shape' of Shapiro delay, respectively. The shape parameter is generally identified with the sine of the orbital inclination i as $s \equiv \sin i$, whereas the range parameter is linked to the mass of the companion $m_{\rm B}$, which in GR follows $r = T_\odot m_{\rm B}$. The constant $T_\odot \equiv (\mathcal{GM})^{\rm N}_\odot / c^3$, where c is the speed of light in vacuum and $(\mathcal{GM})^{\rm N}_\odot \equiv 1.327\,124\,4 \times 10^{26}$ cm^3 s^{-2} is the nominal

[6] https://arxiv.org/e-print/astro-ph/0406321v2

Table 1. Information on the MeerKAT observations and data set for PSR J0737−3039A.

Receiver	Centre frequency (MHz)	Bandwidth (MHz)	Number of channels [(a)]	Number of sub-bands	Time span (MJD)	Number of TOAs
L-band	1283.582	775.75	928	16	58568–59721	83 930
UHF-band	815.734	493	928	32	58936–59663	137 451

Notes. Information presented here is for the trimmed data set, see Sect. 4.1. [(a)]Effective usable channels.

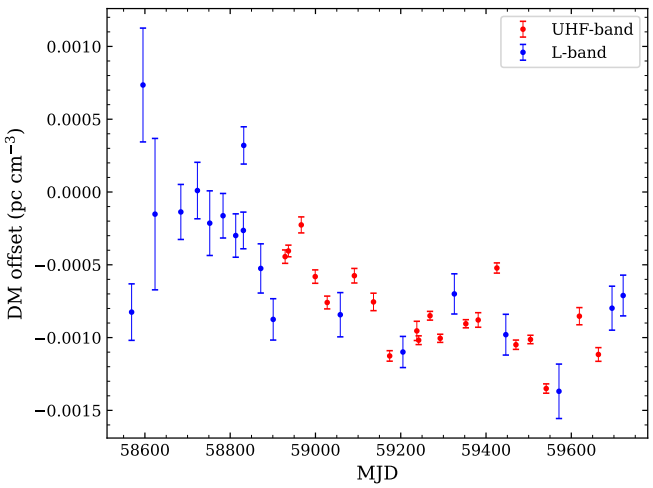

Fig. 2. DM measurement per observing epoch relative to the reference value 48.913 pc cm^{-3} (see Sect. 2.4).

solar mass parameter defined by the IAU 2015 Resolution B3 (Prša et al. 2016). Throughout the paper, all masses expressed in solar mass $M_\odot$ are referred to the nominal solar mass by taking the ratio $Gm_i/(\mathcal{G}\mathcal{M})^{\rm N}_\odot$ $(i = A, B)$, where G is the gravitational constant.

The leading-order expression Eqs. (1) and (2) were obtained by integrating along a straight line (in harmonic coordinates) and assuming a static mass distribution when the pulsar's signal propagates through the system (Blandford & Teukolsky 1976). In reality, the pulsar's signal propagates along a curved path due to the deflection in the gravitational field of the companion and leads to a 'lensing correction' to the Shapiro delay. This actually results in a reduced propagation time as a consequence of Fermat's principle (Perlick 2004). The effect of lensing is not yet observable in any pulsar systems, but for completeness, one can extend Eq. (2) by an adapted version of the approximation in Klioner & Zschocke (2010, Eq. (73)): $\Lambda_u \to \Lambda_u + \delta\Lambda_u^{\rm len}$ with

$$\delta\Lambda_u^{\rm len} = 2rc/a_{\rm R}, \tag{3}$$

where the semi-major axis of the relative orbit $a_{\rm R} = (x + x_{\rm B})/s$, with x and $x_{\rm B}$[7] being the projected semi-major axes of pulsar A and pulsar B, respectively. For the double pulsar, one needs to account for the fact that the companion star moves while the pulsar's signal propagates across the system. This effect is known as the 'retardation effect' or 1.5PN correction to the Shapiro delay (Kopeikin & Schäfer 1999; Rafikov & Lai 2006a). To sufficient approximation, the signal propagation delay can be extended to

$$\Delta_{\rm S} = -2r \ln\left(\Lambda_u + \delta\Lambda_u^{\rm len} + \delta\Lambda_u^{\rm ret}\right), \tag{4}$$

[7] $x_{\rm B}$ had been observed in Kramer et al. (2006a).

where the retardation correction $\delta\Lambda_u^{\rm ret}$ can be taken directly from Kopeikin & Schäfer (1999, Eq. (130)) as

$$\begin{aligned}\delta\Lambda_u^{\rm ret} = {} & \frac{2\pi}{s}\frac{x}{P_{\rm b}}\frac{m_{\rm A}}{m_{\rm B}} e_{\rm T}\sin u - \frac{2\pi s}{(1-e_{\rm T}^2)^{1/2}}\frac{x}{P_{\rm b}}\frac{m_{\rm A}}{m_{\rm B}} \\ & \times\left[\sin\omega\,(\cos u - e_{\rm T}) + (1-e_{\rm T}^2)^{1/2}\cos\omega\sin u\right] \\ & \times\left[e_{\rm T}\cos\omega + \frac{(\cos u - e_{\rm T})\cos\omega - (1-e_{\rm T}^2)^{1/2}\sin\omega\sin u}{1 - e_{\rm T}\cos u}\right].\end{aligned} \tag{5}$$

The quantity $P_{\rm b}$ denotes the orbital period and $m_{\rm A}$ denotes the mass of pulsar A. It should be noted that in the double pulsar, the mass ratio $m_{\rm A}/m_{\rm B}$ can be obtained in a theory-independent way (Kramer et al. 2006a; Damour 2007). Hence, apart from the Shapiro shape parameter s, Eq. (5) contains only Keplerian parameters.

Moreover, the classical aberration expression (Smarr & Blandford 1976) assumes a flat spacetime for the propagation of the pulsar signals, which is no longer sufficient for describing the observations of the double pulsar, particularly near the superior conjunction of pulsar A. One needs to account for the gravitational deflection of the pulsar's signal caused by its companion (Doroshenko & Kopeikin 1995; Rafikov & Lai 2006b), which adds a lensing correction to the classical aberration. For pulsar A the misalignment angle between its spin vector and the orbital angular momentum is very small (<3.2°, Ferdman et al. 2008, 2013), which is in line with a low-kick birth event (cf. Piran & Shaviv 2004; Willems & Kalogera 2004; Willems et al. 2006; Stairs et al. 2006; Tauris et al. 2017). Since the spin of A is practically parallel to the orbital angular momentum, the aberration delay can be simplified as

$$\Delta_{\rm A} = \mathcal{A}\,(\sin\psi + e_{\rm T}\sin\omega) + \delta_{\rm A}^{\rm londef}. \tag{6}$$

The first term on the right-hand side of Eq. (6) is the classical aberration delay, where $\psi = \omega + \theta$ is the longitude of the pulsar with respect to the ascending node (θ is the true anomaly, which defines the angle between the direction of the pulsar and the periastron), and the aberration coefficient

$$\mathcal{A} = \frac{x}{\nu P_{\rm b}(1-e_{\rm T}^2)^{1/2}\sin^2 i} \simeq 3.65\,\mu{\rm s}. \tag{7}$$

As $\mathcal{A}$ is practically not observable and can be absorbed by a shift in various timing parameters (see discussions in Damour & Deruelle 1986; Damour & Taylor 1992), we a priori add the aberration coefficient $\mathcal{A}$ as a fixed parameter in our timing model with the value given in Eq. (7).

The second term $\delta_{\rm A}^{\rm londef}$ in Eq. (6) is the higher-order correction originating from the 'longitudinal deflection delay', and can be written as (Doroshenko & Kopeikin 1995)

$$\delta_{\rm A}^{\rm londef} = \mathcal{D}\,\frac{\cos\left(\psi + \delta\psi^{\rm ret}\right)}{\Lambda_u + \delta\Lambda_u^{\rm ret}}, \text{ with } \mathcal{D} = \frac{1}{\pi\nu}\frac{r}{x + x_{\rm B}}. \tag{8}$$

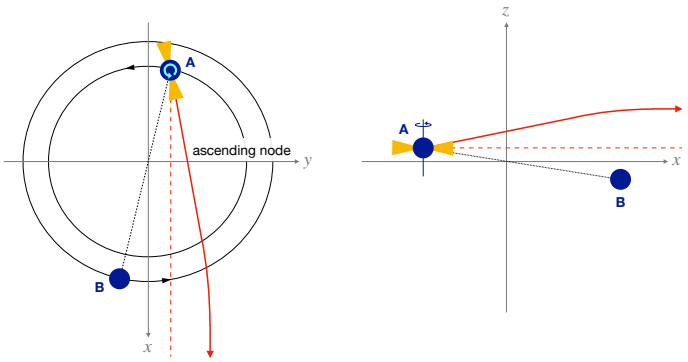

Fig. 3. Simplified illustration of effects related to the deflection of A's radio signals (solid red) in the gravitational field of B (top down and side perspective). The observer is located at a large distance along the x-axis. Apart from modifications in the propagation time due to a curved path in the gravitational field of B (lensing), one has a longitudinal deflection delay ($\delta_{\rm A}^{\rm londef}$) due to the fact that the pulsar has to rotate by more than 360° between two pulses while approaching the conjunction. After conjunction, it is less than 360°, which makes pulsar signals arrive earlier at the observer. In addition, there is a latitudinal effect, due to a latitudinal shift in the emission direction towards the observer. This can lead to changes in the pulse profile since the line of sight cuts a different part of the emission region, which can also be accompanied by changes in the pulse arrival times (more details in Sects. 5.1 and 5.2).

Just as in the Shapiro delay, retardation correction is also accounted for here. As a sufficiently good approximation, the position of B when the signal reaches its minimum distance from B can be used (retardation corrected position; cf. Kopeikin & Schäfer 1999; Rafikov & Lai 2006a). The angle $\delta\psi^{\rm ret}$ denotes the retardation related correction for the angle between the (coordinate) vector from B to A and the ascending node.

As already discussed in Kramer et al. (2021a), the NLO contributions in the Shapiro and aberration delays cannot be tested separately in the double pulsar due to the similarity of their effects on signal propagation. In addition, the lensing correction to the propagation delay (Eq. (3)) is challenging to measure as it can be absorbed in the fit of Shapiro shape s (see Sect. 5.3 and discussions in Kramer et al. 2021a). Therefore, to test the significance of the NLO contributions and to obtain an unbiased timing result, a common factor $q_{\rm NLO}$ is multiplied by these contributions and can be fitted for in our timing model:

$$\Lambda_u^{\rm ret} = \Lambda_u^{\rm ret} \times q_{\rm NLO}, \tag{9}$$

$$\Lambda_u^{\rm len} = \Lambda_u^{\rm len} \times q_{\rm NLO}, \tag{10}$$

$$\delta_{\rm A}^{\rm londef} = \delta_{\rm A}^{\rm londef} \times q_{\rm NLO}. \tag{11}$$

In GR, the scaling factor $q_{\rm NLO} = 1$. Figure 3 illustrates the different effects related to signal deflection in the double pulsar system.

4. Timing results

For the timing analysis, we use the timing model in TEMPO known as DDS, which is a modification of the DD model (Damour & Deruelle 1986) that uses a different parameterisation of the Shapiro delay. In DDS, the Shapiro shape parameter s is replaced by the logarithmic Shapiro shape parameter $z_{\rm s}$ via

$$z_{\rm s} \equiv -\ln(1-s), \tag{12}$$

which is more suitable when s is very close to one (see Kramer et al. 2006b, 2021a). The NLO contributions in the Shapiro and aberration delays are also implemented in the latest DDS model, which can be measured through a common factor $q_{\rm NLO}$. Because the analytic inversion of the timing model developed in Damour & Deruelle (1986) is no longer sufficient for the double pulsar, primarily due to the NLO contributions, a numerical inversion of the timing model was also implemented in the latest DDS model in TEMPO (see Kramer et al. 2021a).

4.1. Timing parameters

In our analysis, the full MeerKAT data set shows a large deviation in the Shapiro range parameter r compared to the 16 yr result (Kramer et al. 2021a). We perform a drop-out analysis by removing each observing epoch and fitting the parameters. We find that r is dependent on specific observing epochs, where six epochs affect r by a significant amount while the rest of the epochs do not. These six epochs are marked as black crosses in Fig. 4. After excluding all these six epochs, r is consistent with the 16-yr result and the mass measurement in GR (Kramer et al. 2021a). Even though a number of tests and simulations have been made, we are still unclear about the cause of this problem. Possible reasons could be systematic errors in the observations or folding techniques. It should be noted that all data were folded with the TEMPO2 phase predictor during observations, which has shown outliers in this pulsar and has been doubly confirmed by our simulations. These outliers disappear after reinstalling a TEMPO `polyco` ephemeris in data processing (see Sect. 2.2), but we cannot rule out underlying problems due to the folding technique. The results shown here are based on data processed with the `polyco` scheme[8]. In any case, this issue should not affect the measurement of NLO signal propagation effects, which is the main focus of this paper. Therefore, we leave this question to future studies. In the following analysis, we use a trimmed data set that excludes these six epochs.

Table 2 and Fig. 4 present the results obtained from fitting the TEMPO DDS model to the trimmed MeerKAT data set. We fix the proper motion (μ_α, μ_δ) and parallax $\pi_{\rm x}$ to the more precise values determined from the 16 yr timing and the very long baseline interferometry measurements (see Kramer et al. 2021a). As the time span of our data is not sufficient to obtain a reliable measurement of the orbital period derivative $\dot{P}_{\rm b}$ and the orientation of the orbit ($\omega_0 \approx 0°$) is not at a favourable position for a precise measurement of the Einstein delay amplitude $\gamma_{\rm E}$, we choose to fix these parameters to the more precise measurements from 16 yr data (Kramer et al. 2021a). Fixing the above parameters has no impact on the measurements of signal propagation effects and masses. The two PK parameters that describe the relativistic deformation of the orbit, $\delta_{\rm r}$ and δ_θ (Damour & Deruelle 1986), are also held fixed at the GR value in our analysis, as $\delta_{\rm r}$ cannot be measured (see Kramer et al. 2021a) and δ_θ is not yet measurable with the current MeerKAT data.

The values shown in Table 2 are the result of 1000 Monte Carlo (MC) runs, where in each run, a random realisation of proper motion, parallax, DM, $\gamma_{\rm E}$, and $\dot{P}_{\rm b}$ is selected. The DM value is selected according to the DM measurements and uncertainties shown in Fig. 2. We use the aforementioned modified version of TEMPO to correct the DM for each TOA and fit for

[8] With the same set of observations, data processed with TEMPO `polyco` and TEMPO2 `predictor` show a noticeable difference (~3σ) in the Shapiro parameters, where the result with `polyco` is closer to the 16 yr results and shows a smaller χ^2.

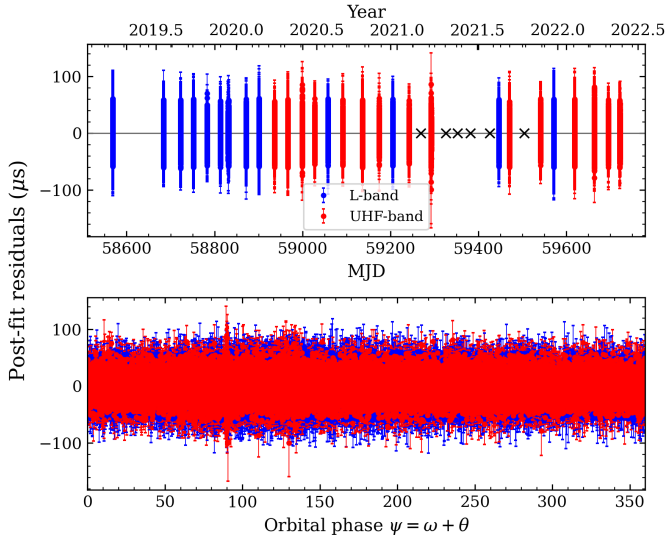

Fig. 4. Post-fit residuals of PSR J0737−3039A using the DDS binary model as a function of time (*top panel*) and the orbital phase of pulsar A with respect to the ascending node ψ (*bottom panel*). The MeerKAT *L*-band data are plotted in blue, whereas the UHF-band data are in red. The epochs of the excluded six observations are marked as black crosses.

all other timing parameters in each run. The numbers shown in Table 2 are the mean values of the distribution of each parameter after 1000 MC runs, whereas the uncertainties are taken from the larger one among the standard deviation of the distributions and the maximum error from TEMPO in all MC runs.

In order to allow direct comparisons with previous publications, parameters shown in Table 2 are measured with respect to the same epochs and the same terrestrial time standard UTC (NIST)[9] within the 'Barycentric Dynamical Time' (TDB) timescale as implemented in TEMPO. Even though TDB runs at a slower rate than 'Barycentric Coordinate Time (TCB)', which was recommended by IAU 2006 Recolution B3[10] (see also Soffel et al. 2003), this choice does not have any impact on the results presented in this paper (see discussions in Kramer et al. 2021a). To transfer the topocentric TOAs to the Solar System Barycentre (SSB), the DE436 Solar System ephemeris published by the Jet Propulsion Laboratory[11] is used.

All binary parameters in Table 2 are consistent with the 16-yr data, except for x being different by $\sim 3\sigma$. This is because x is highly correlated with γ_E, which is kept fixed in our fit. This should be improved in the future, once we have enough MeerKAT data to fit for x and γ_E simultaneously. In our fit, the root mean square (rms) is very close to the mean TOA uncertainty, and the reduced χ^2 of the individual observation is close to one, suggesting that our result is not affected by jitter noise. We also perform simulations and single-pulse analysis following the methods in Parthasarathy et al. (2021) and find little evidence of jitter noise.

The rms of the MeerKAT data shown in Table 4 is more than two times better than that of the Green Bank Telescope (see Kramer et al. 2021b). Thanks to this much improved precision, the measurements of the Shapiro parameters improve quickly. Compared to Kramer et al. (2021a), the shape parameter s improves by a factor of two and the range parameter r improves by a factor of 1.3 (see Table 2).

[9] https://www.nist.gov/pml/time-and-frequency-division/time-realization/utcnist-time-scale-0

[10] https://www.iau.org/static/resolutions/IAU2006_Resol3.pdf

[11] https://ssd.jpl.nasa.gov/planets/eph_export.html

Table 2. Timing parameters for PSR J0737−3039A using the TEMPO DDS binary model.

Parameter	Value
Solar system ephemeris	DE436
Terrestrial time standard	UTC(NIST)
Timescale	TDB
Position epoch (MJD)	55045.0
Timing epoch, t_0	55700.0
Astrometric parameters	
Right ascension (RA), α (J2000)	07:37:51.248 121(26)
Declination (Dec), δ (J2000)	−30:39:40.705 36(42)
Proper motion RA, μ_α (mas yr^{-1})	−2.567(30) (*)
Proper motion Dec, μ_δ (mas yr^{-1})	2.082(38) (*)
Parallax, π_x (mas)	1.36(+0.12, −0.10) (*)
Spin parameters	
Rotational frequency (freq.), ν (Hz)	44.054 068 642 001(56)
First freq. derivative, $\dot{\nu}$ (Hz s^{-1})	$-3.415\,92(37) \times 10^{-15}$
Second freq. derivative, $\ddot{\nu}$ (Hz s^{-2})	$-9.5(12) \times 10^{-27}$
Binary parameters	
Orbital period, P_b (days)	0.102 251 559 297 2(29)
Projected semi-major axis, x (s)	1.415 028 299(88)
Eccentricity, e_T	0.087 777 036(48)
Epoch of periastron, T_0 (MJD)	55700.233 017 54(10)
Longitude of periastron, ω (deg)	204.753 72(36)
Periastron advance, $\dot{\omega}$ (deg yr^{-1})	16.899 321(37)
Orbital period derivative (10^{-12}), $\dot{P}_b$	−1.247 920(78) (*)
Einstein delay amplitude, γ_E (ms)	0.384 045(94) (*)
Logarithmic Shapiro shape, z_s	9.669(77)
Range of Shapiro delay, r (μs)	6.163(16)
NLO factor for signal prop., q_{NLO}	0.999(79)
Derived parameters	
$s \equiv \sin i = 1 - e^{-z_s}$	0.999 936 9(+46/−51)
Orbital inclination, i (deg)	89.36(3) or 90.64(3)
Mass of pulsar A, m_A ($M_\odot$)	1.338 186(10)
Mass of pulsar B, m_B ($M_\odot$)	1.248 866(7)
Total mass, M ($M_\odot$)	2.587 052(11)

Notes. Numbers in parentheses are 1σ uncertainties applicable to the last digits, obtained from the standard deviation of 1000 MC runs or maximum error from TEMPO, whichever is larger. The overall reduced χ^2 is 0.99. (*)Values adopted from Kramer et al. (2021a).

4.2. Mass measurements

The standard approach for measuring the masses of a binary pulsar system is using two PK parameters. Assuming GR, one can calculate the two a priori unknown masses based on the measurements of Keplerian parameters. For the double pulsar, the two most precisely measured PK parameters are periastron advance $\dot{\omega}$ and the Shapiro shape parameter s.

For the advance of periastron, in addition to the 1PN contribution, we also need to account for higher-order corrections due to 2PN effects and Lense-Thirring (LT) precession caused by spin-orbit coupling of pulsar A, as they are much larger than the measurement error of $\dot{\omega}$ (see Hu et al. 2020; Kramer et al. 2021a). For the analysis of this paper, the total

intrinsic contribution to the periastron advance can be expressed, with sufficient precision, as (Damour & Schäfer 1988)

$$\dot{\omega} = \dot{\omega}^{\rm 1PN} + \dot{\omega}^{\rm 2PN} + \dot{\omega}^{\rm LT,A}. \tag{13}$$

The first and second post-Newtonian (PN) terms $\dot{\omega}^{\rm 1PN}$ and $\dot{\omega}^{\rm 2PN}$ are functions of masses and observed Keplerian parameters. The situation is more complicated for the LT contribution $\dot{\omega}^{\rm LT,A}$, as it requires the knowledge of the moment of inertia (MOI) of pulsar A, which is still not very constrained because of our limited knowledge of the equation of state (EOS) of neutron stars. As discussed in detail in Hu et al. (2020), one could measure the masses and the MOI simultaneously by introducing a third PK parameter $\dot{P}_{\rm b}$ into the $\dot{\omega} - s$ test. Such a test has already been carried out by Kramer et al. (2021a) using the 16 yr data with an upper limit obtained: $I_{\rm A} < 3.0 \times 10^{45}\,{\rm g\,cm^2}$ with 90% confidence. This measurement is expected to improve with the combination of the 16 yr data with MeerKAT data in a forthcoming paper, and should improve considerably in the coming years as more data becomes available. This promises an important complementary constraint on the EOS (Hu et al. 2020). For the calculations here, we take the value of $\dot{\omega}^{\rm LT,A}$ from Eq. (35) in Kramer et al. (2021a), which uses the constraints on the EOS from Dietrich et al. (2020):

$$\dot{\omega}^{\rm LT,A} = -4.83\,(+29, -35) \times 10^{-4}\,{\rm deg\,yr^{-1}}. \tag{14}$$

The Shapiro shape parameter s is the sine of the orbital inclination i. In Newtonian gravity, the orbital inclination is linked to the projected semi-major axis x via the binary mass function (e.g. Lorimer & Kramer 2004):

$$\sin i = \frac{(n_{\rm b} M)^{2/3} x}{T_\odot^{1/3} m_{\rm B}}, \tag{15}$$

where x and the orbital frequency $n_{\rm b} \equiv 2\pi/P_{\rm b}$ are both measured Keplerian parameters. Equation (15) gets modified by a 1PN term in the 1PN approximation for Kepler's third law (see Eq. (3.7) in Damour & Deruelle 1985 and Eq. (3.9) in Damour & Taylor 1992):

$$\sin i = \frac{(n_{\rm b} M)^{2/3} x}{T_\odot^{1/3} m_{\rm B}} \left[1 + \left(3 - \frac{m_{\rm A} m_{\rm B}}{3M^2}\right)(T_\odot M n_{\rm b})^{2/3}\right]. \tag{16}$$

Taking the measurements of $P_{\rm b}$, x, and masses from Table 2, one can calculate that the 1PN correction is approximately 1.27×10^{-5}. This correction was considered for the first time in pulsar analysis by Kramer et al. (2021a), where the significance was about 1.3σ. Now with MeerKAT data, this 1PN correction is 2.5σ significant and cannot be ignored in the analysis. We hereby use the full 1PN mass function Eq. (16) to measure the masses.

Combining the PK parameters $\dot{\omega}$ and s, one obtains the (Doppler-shifted) masses, which are listed in Table 2. These measurements are fully consistent with those obtained with 16 yr data (Kramer et al. 2021a), and the precision of $m_{\rm A}$ and $m_{\rm B}$ are also better.

Alternatively, one can fit for masses using the timing model known as DDGR (Taylor & Weisberg 1989), which is based on the DD model where the PK parameters are explicitly calculated from the masses and the Keplerian parameters, assuming GR. Beside the Keplerian parameters, it fits explicitly for the total mass M and the companion mass $m_{\rm B}$. To make the measurements, we modify the DDGR model so that it incorporates all NLO contributions that need to be accounted for in this system, including NLO signal propagation effects, LT contribution $\dot{\omega}^{\rm LT,A}$, NLO gravitational wave damping and mass-loss contribution to $\dot{P}_{\rm b}$ (see Hu et al. 2020; Kramer et al. 2021a). An MOI needs to be provided to the model for the calculation of $\dot{\omega}^{\rm LT,A}$ and the mass loss contribution to $\dot{P}_{\rm b}$. For periastron advance $\dot{\omega}$, the uncertainty from the MOI is still smaller than that from MeerKAT observations (see Eq. (14) and Table 2). Therefore, based on the EOS constraint from Dietrich et al. (2020), we fix the MOI to $I_{\rm A} = 1.28 \times 10^{45}\,{\rm g\,cm^2}$ in our fit. Table 3 shows the mass measurements obtained using the DDGR model. The results are fully consistent with the measurements derived from the DDS model, with smaller uncertainties in $m_{\rm B}$ and M.

Table 3. Mass measurements with a new modified DDGR model that accounts for NLO contributions in the orbital motion and signal propagation in this system.

Parameter	Value
Mass of pulsar A, $m_{\rm A}$ ($M_\odot$)	1.338 186(10)
Mass of pulsar B, $m_{\rm B}$ ($M_\odot$)	1.248 886(5)
Total mass, M ($M_\odot$)	2.587 050(8)

Notes. The MOI has been chosen to be $I_{\rm A} = 1.28 \times 10^{45}\,{\rm g\,cm^2}$ in the fit.

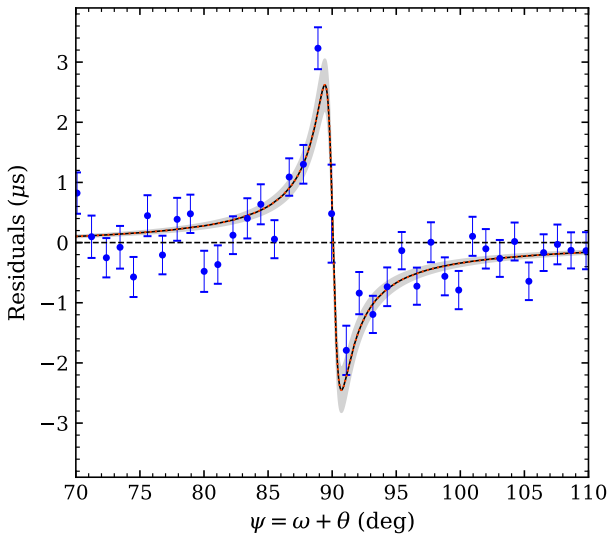

Fig. 5. Aggregated residuals (blue) due to NLO contributions in Shapiro and aberration delay, shown in the orbital phase ψ. Residuals are rescaled by $(1 + e_{\rm T}\cos\theta)^{-1}$ to account for secular variations in amplitude due to the precession of periastron. The black curve indicates the fitted $q_{\rm NLO}$ (see Table 2) with the 2σ range shown by the grey shaded areas, which agrees very well with the theoretical prediction indicated by the red dotted line.

Following Kramer et al. (2021a), one could test the agreement of r in GR by comparing $m_{\rm B}^{(r)} = r/T_\odot = 1.2512\,(33)\,M_\odot$ (cf. Table 2) with the companion mass determined here, which gives

$$r^{\rm obs}/r^{\rm GR} = 1.0019\,(26). \tag{17}$$

This leads to a 5.3×10^{-3} (95% confidence) test of GR.

5. Studying NLO signal propagation effects

Because the double pulsar system is nearly edge-on to our line of sight (LOS, see i in Table 2), it is ideal for measuring signal propagation effects caused by the gravitational field of the companion

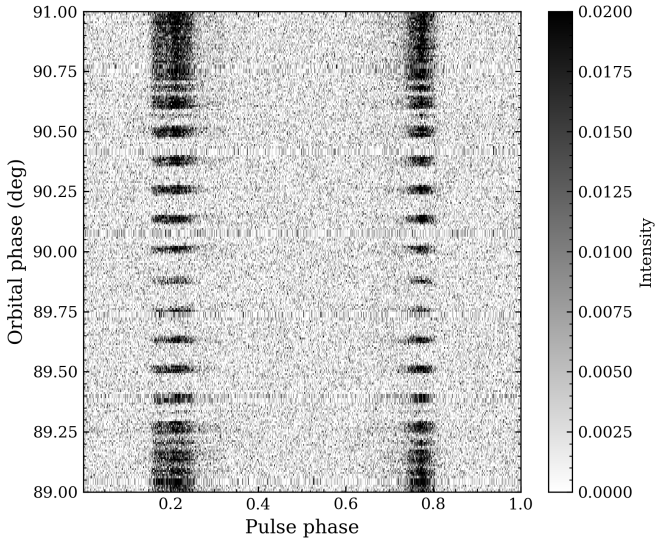

Fig. 6. Example of one eclipse observation at UHF band, plotted in intensity against orbital phase ψ and pulse phase. The intensity modulation occurs when pulsar A is eclipsed by the magnetosphere of pulsar B. Each integration is a sum of eight pulses. When plotting, the discontinuities between recordings are patched with the previous sub-integration.

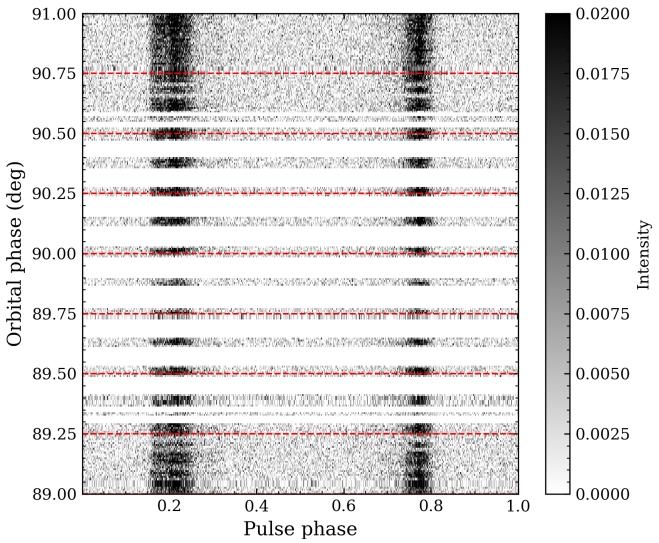

Fig. 7. Same as for Fig. 6, but masking out the regions without pulses (blocked by the magnetosphere of pulse B). The dashed red lines indicate the orbital phase bins used in Figs. 8 and 9.

near superior conjunction. The leading-order expression Eq. (1) is no longer sufficient for describing the signal propagation in the double pulsar. Such a model would result in significant residuals near superior conjunction when aggregating residuals in the orbital phase, as shown in Fig. 5. These residuals agree very well with the expected NLO contributions discussed in Sect. 3, which are shown by the red curve. The significance of the NLO corrections can be tested by scaling these corrections collectively by a common factor $q_{\rm NLO}$ (cf. Eqs. (9)–(11); $q_{\rm NLO} = 1$ in GR) and fitting for it. We find, with the trimmed data set,

$$q_{\rm NLO} = 0.999\,(79), \tag{18}$$

which has surpassed the 16 yr result by 1.65 times with only ~3 yr of data, thanks to the much improved precision offered by MeerKAT.

Following the definition of $q_{\rm NLO}$ in Sect. 3, a fit for this parameter involves two aspects of gravity: a 1.5PN correction of the Shapiro delay due to the movement of the companion $\delta\Lambda_u^{\rm ret}$, and corrections related to the signal deflection in the gravitational field of the companion $\delta\Lambda_u^{\rm len}$ and $\delta_{\rm A}^{\rm londef}$. Even though these contributions cannot be tested individually in a simultaneous fit because of their similarity, one can still test one at a time while keeping the other one fixed (cf. Kramer et al. 2021a). We find

$$q_{\rm NLO}[\text{deflection}] = 1.00\,(15), \tag{19}$$

$$q_{\rm NLO}[\text{retardation}] = 1.00\,(17). \tag{20}$$

5.1. Searching for profile variation at eclipse

The lensing correction to the aberration delay may not only lead to a shift in time in the longitudinal aspect but can also result in a change of the co-latitude of the emission direction towards Earth, namely the 'latitudinal deflection delay'. This would cause profile variations as the LOS cuts a different region of the pulsar beam (Rafikov & Lai 2006a,b). An illustration of the latitudinal deflection effect is shown in the right panel of Fig. 3. Various analyses have confirmed that pulsar A is an orthogonal rotator (Guillemot et al. 2013; Ferdman et al. 2013; Kramer et al. 2021b), meaning that the main pulse and the interpulse come from opposite magnetic poles. Therefore, we do not expect shifts of pulse components in phase, as discussed in Rafikov & Lai (2006b), based on the (incorrect) assumption of an aligned rotator suggested by Demorest et al. (2004).

The profile variation is expected to be maximum at the superior conjunction and symmetric around $\psi = 90°$ (retardation corrected). This study requires high time resolution, for which we use the search mode data. We select the data that are near the eclipses and fold them into single pulses using TEMPO `polyco` (with TSPAN = 1 min). Data are then combined, cleaned, and polarisation calibrated before integrated into total intensity and averaged in frequency. As the single pulses are still very weak, we average over every eight pulses to increase the signal-to-noise ratio (S/N). An example of eclipse data is shown in Fig. 6.

In order to get a high S/N profile, we first mask the regions where pulsar A's emission is blocked by pulsar B (see Fig. 7) and split the data into orbital phases with a step of $\Delta\psi = 0.25°$ for $89° < \psi < 91°$. Then for each phase interval, we integrate pulses from all observations of a given band (L or UHF) together to increase the S/N. The resulting profiles are shown in Fig. 8 for the L-band data and in Fig. 9 for the UHF-band data, which are summed from 25 and 37 eclipses respectively. The difference between the added profiles at the eclipse and a 2 h integrated profile at the non-eclipse part of the orbit is insignificant. The subtle residual structures in these figures can result from interstellar medium effects (DM variation and scintillation) based on our simulations. Therefore, we conclude that the current data are not (yet) sensitive to profile variations caused by the latitudinal aberration delay, or are not significant in the region that is seen by our LOS. These profiles will be used in a subsequent study on the geometry of the system.

5.2. Simulation for latitudinal deflection delay

To investigate whether the deflection delay caused by latitudinal deflection is measurable from pulsar timing, we perform a simulation based on a simple emission model, which consists of a set of circular cones. Following Doroshenko & Kopeikin (1995) and Rafikov & Lai (2006b), the latitudinal deflection delay for

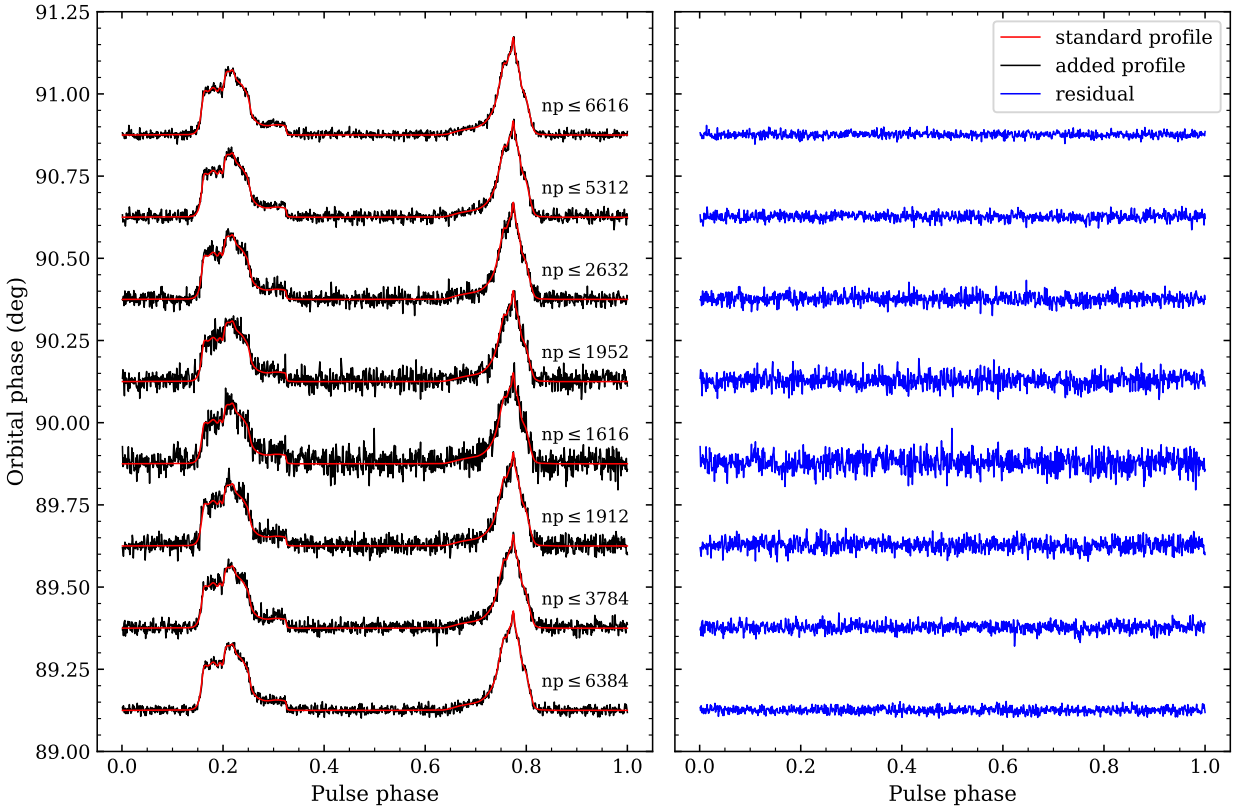

Fig. 8. Profile variation with respect to orbital phase. *Left*: black lines indicate the integrated profile of *L*-band data summed from 25 eclipses for orbital phases $89° < \psi < 91°$ with an interval of $\Delta\psi = 0.25°$. The baseline of the profile is placed at the centre of each interval, and the numbers on the right side of the profiles (np) indicate the estimated upper limit for the number of pulses in that interval. The red curves indicate the reference (standard) profile integrated over a 2 h observation excluding the eclipse part. *Right*: residuals of the added profile with respect to the reference profile.

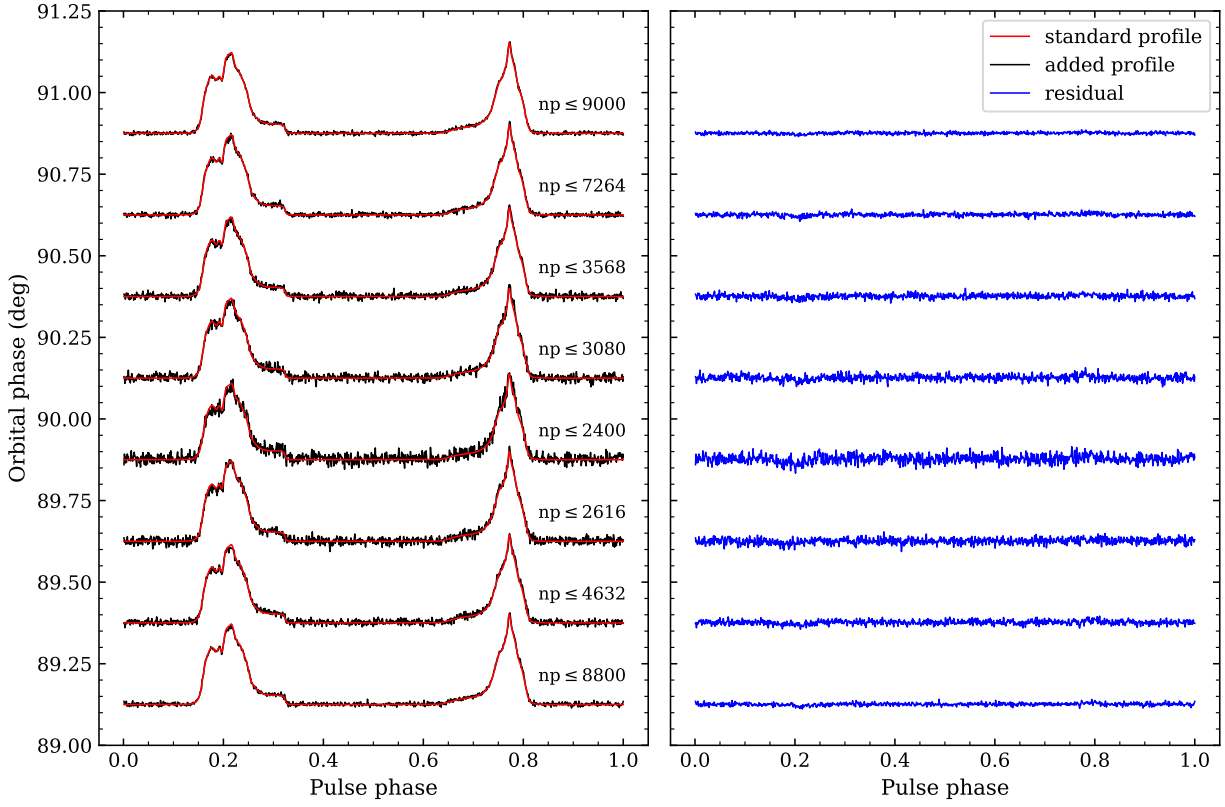

Fig. 9. Same as for Fig. 8, but for the UHF-band data summed from 37 eclipses.

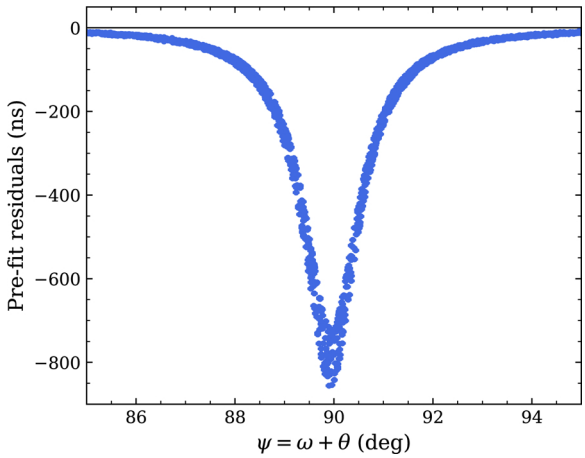

Fig. 10. Lensing simulation: pre-fit residual plotted against orbital phase ψ. Data displayed here are centred on $\omega = 180°$ and span a decade. The scattering at the lower end of the curve is due to the precession of periastron.

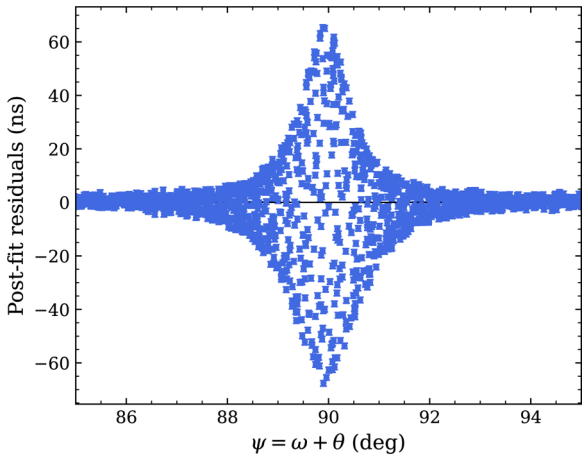

Fig. 11. Lensing simulation: post-fit residual plotted against orbital phase ψ.

pulsar A can be written as

$$\delta_{\rm A}^{\rm latdef} = -\mathcal{D}\,\frac{\cos i \sin(\psi + \delta\psi^{\rm ret})}{(\Lambda_u + \delta\Lambda_u^{\rm ret})\tan\chi_0}, \tag{21}$$

where χ_0 is the angle between the arc connecting the LOS and spin axis and the arc connecting LOS and magnetic axis. It should be noted that Eq. (21) is based on the approximation of Doroshenko & Kopeikin (1995) for the deflection angle, and therefore assumes that the impact parameter is (sufficiently) large compared to the Einstein radius. While this is sufficient, at least until full SKA becomes operational, we present an improved description further below in Sect. 5.4.

We include this deflection time delay in our test model assuming $\chi_0 = 45°$ [12] (i.e. a relatively large latitudinal deflection delay) and scale it with a factor $q^{\rm latdef}$. We simulate high-precision TOAs using this test model and fit for the scaling factor. The pre-fit residuals show an advance signature with an amplitude of $-2.8\,\mu$s and symmetric to $\psi = 90°$, which is in a similar shape to Shapiro delay but with the opposite sign and a smaller amplitude. However, after fitting for Shapiro parameters, the signature gets mostly absorbed and leaves residuals below 42 ns at superior conjunction.

5.3. Prospects of lensing measurement

Even though the retardation and deflection effects can be tested separately while keeping the other one fixed, as shown in Eqs. (19) and (20), measuring the lensing correction to Shapiro delay $\delta\Lambda_u^{\rm len}$ independently is challenging. As already pointed out by Kramer et al. (2021a), this effect is difficult to observe because of its strong covariance with s, or equivalently $z_{\rm s}$. Our simulation also confirms that the lensing signature can be mostly absorbed by $z_{\rm s}$ in timing due to its symmetry with respect to conjunction. For demonstration purposes, we simulate 1-ns TOAs, which model all NLO signal propagation contributions, then keep the retardation and deflection delay fixed in the model and fit for the scaling factor attached to the lensing correction, $q^{\rm len}$ (corresponding to $q_{\rm NLO}$ in Eq. (10)). Figure 10 shows the residuals when lensing correction is not taken into account, leading to a reduced propagation time of about 850 ns as a result of Fermat's principle. However, after fitting for $z_{\rm s}$, the lensing signature gets absorbed and leaves the residuals to be below 70 ns (Fig. 11), making a detection with the current timing precision certainly impossible.

To investigate whether lensing can be measured separately in the near future, we simulate TOAs for MeerKAT, MeerKAT extension, and the first phase of the SKA (SKA 1) until 2030 based on similar assumptions made in Hu et al. (2020). In addition, as the TOA precision reduces significantly due to the intermittent signals during the eclipse (see Fig. 6), we account for this in our simulations by increasing the uncertainty of these TOAs based on MeerKAT observations. As a simple estimate, we assume GR and perform the simulation using the modified DDGR model with a grid fit to $q^{\rm len}$. If lensing is measurable, the value of $q^{\rm len}$ should be close to one. However, it turns out that with the observed and simulated data from 2019 to 2030, the uncertainty of $q^{\rm len}$ is still larger than one.

To further push the precision, we assume that an instrument will be available in the future that is capable of providing a timing accuracy one order of magnitude better than that of the SKA 1 (i.e. 100 ns for an integration time of 30 s), for example, a future full SKA. As a rough estimate, here we only consider radiometer noise and ignore any other noise sources, such as jitter noise or scintillation noise. The uncertainty of $q^{\rm len}$ against the time span of the simulated data is shown in Fig. 12. With such precision, one would expect to get a 5-σ test of lensing with ∼4 yr of data.

From the simulation, we also obtain an estimated uncertainty for the common factor of NLO contributions $q_{\rm NLO}$ in the near future. Assuming no jitter noise, with MeerKAT and the SKA 1, we can expect a 50-σ detection by 2030.

5.4. Improvements in the timing model for ≲50 ns precision

Equations (8) and (21) are based on the approximation for the signal deflection used by Doroshenko & Kopeikin (1995). As discussed in detail in Kramer et al. (2021a), this is still sufficient for the analysis of current timing data. For that reason, the analysis in this paper is still based on Doroshenko & Kopeikin (1995), which (including corrections for retardation) is already part of

[12] It should be noted that χ_0 is not a constant, but our purpose here is to get a feeling for the measurability of the effect in timing rather than a proper account of the effect, which requires knowledge of the latitudinal variation in the emission pattern of the pulsar. Furthermore, as discussed at the beginning of Sect. 5.1, the beam geometry adopted by Rafikov & Lai (2006b) is not the correct one anyway.

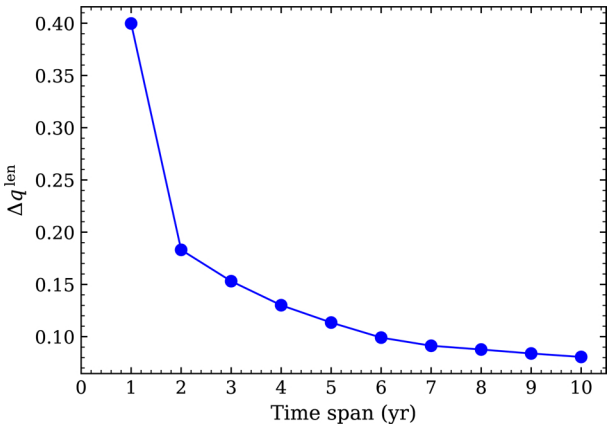

Fig. 12. Uncertainty of factor $q^{\rm len}$ as a function of time span for the simulated data assumed to be ten times better than the SKA 1.

the TEMPO distribution. However, in the future we can expect to obtain a timing precision of better than ∼50 ns near conjunction (±1°), so that an improved treatment of the deflection is required. In a series of papers, Rafikov and Lai used the standard lensing equation to treat the signal propagation in the double pulsar near conjunction (Lai & Rafikov 2005; Rafikov & Lai 2006a,b). This allowed them to drop the assumption that the impact parameter is much larger than the Einstein radius. The standard lensing equation, however, is based on the assumption of small angles (see e.g. Schneider et al. 1992). Therefore, strictly speaking, Lai and Rafikov's calculations are only valid near conjunction. Similar to the calculations of Shapiro (1967) and Ward (1970), Wucknitz (2008) studied the deflection of photons in the gravitational field of a 'point mass' for general lensing scenarios not limited to regions close to the optical axis. Based on these results, we give an analytic expression for the signal deflection that is valid for the whole orbit, and recovers the calculations by Lai and Rafikov near conjunction, and those of Doroshenko & Kopeikin (1995) if the impact parameter is large compared to the Einstein radius.

In the following paragraphs, Θ is the angle between $\boldsymbol{r}_{\rm AB'}$ and the direction towards the observer, where $\boldsymbol{r}_{\rm AB'}$ denotes the vector from the position of pulsar A at emission to the (retardation corrected) position of pulsar B (the underlying geometry for our calculations is illustrated in Fig. 13). The deflection ΔΘ of A's radio signal by pulsar B can be obtained from Eq. (24) in Wucknitz (2008), with the replacements $\alpha \to \Delta\Theta$, $\theta \to \Theta + \Delta\Theta$, and $m \to \alpha_{\rm E}^2$, where the quantity $\alpha_{\rm E}$ is the angle corresponding to the Einstein radius, and is given by

$$\alpha_{\rm E} = \frac{2}{c}\sqrt{\frac{G m_{\rm B}}{|\boldsymbol{r}_{\rm AB'}|}} \ll 1. \tag{22}$$

This is the maximum value ΔΘ can assume. The distance $D_{\rm d}$ in Wucknitz (2008) corresponds to $|\boldsymbol{r}_{\rm AB'}|$[13]. Consequently, one obtains

$$\Delta\Theta \sin(\Theta + \Delta\Theta) - \frac{\alpha_{\rm E}^2}{2}\left[1 + \cos(\Theta + \Delta\Theta)\right] = 0. \tag{23}$$

Since $\Delta\Theta \le \alpha_{\rm E} \ll 1$ for all angles of Θ, we can expand the equation above in ΔΘ while keeping terms only up to order $\alpha_{\rm E}^2$.

[13] We note that the $D_{\rm d}$ in Eq. (24) of Wucknitz (2008) is a typo and should not be there since it is already part of the definition of m.

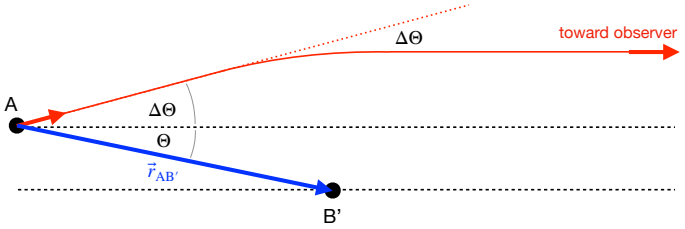

Fig. 13. Schematic picture of the lensing geometry as used in Sect. 5.4. B′ denotes the retardation corrected position of B (cf. Klioner & Kopeikin 1992; Kopeikin & Schäfer 1999). In principle there is a second photon path towards the observer (below B′). However, for the double pulsar, this signal is not only significantly weaker, but the path also comes so close to pulsar B that the photons are absorbed by the plasma-filled magnetosphere of B (cf. Lai & Rafikov 2005; Rafikov & Lai 2006b).

This leads to a quadratic equation:

$$\Delta\Theta^2 + \Delta\Theta \sin\Theta - \frac{\alpha_{\rm E}^2}{2}(1 + \cos\Theta) \simeq 0, \tag{24}$$

which has, under the assumptions made, one solution:

$$\Delta\Theta \simeq \frac{1}{2}\left(\sqrt{\sin^2\Theta + 2\alpha_{\rm E}^2(1 + \cos\Theta)} - \sin\Theta\right). \tag{25}$$

For $\Theta \ll 1$ this agrees with the standard lensing equation (see e.g. Schneider et al. 1992).

The angle $\Theta \in [0, \pi]$ needs to be computed from the retardation-corrected orbital phase via $\cos\Theta = \sin i \sin(\psi + \delta\psi^{\rm ret})$. The longitudinal and latitudinal deflection delay are given by

$$\delta_{\rm A}^{\rm londef} = \frac{\Delta\Theta}{2\pi\nu}\frac{\cos(\psi + \delta\psi^{\rm ret})}{\sin\Theta \sin i}, \tag{26}$$

$$\delta_{\rm A}^{\rm latdef} = -\frac{\Delta\Theta}{2\pi\nu}\frac{\sin(\psi + \delta\psi^{\rm ret})}{\sin\Theta \tan i \tan\chi_0}, \tag{27}$$

respectively (cf. Eqs. (10) and (24) in Rafikov & Lai 2006b), with $\zeta = \pi - i$ and $\eta = -\pi/2$ spin of A aligned with orbital angular momentum). If Θ is much larger than $\alpha_{\rm E}$, one has $\Delta\Theta \simeq \alpha_{\rm E}^2(1 + \cos\Theta)/(2\sin\Theta)$. This corresponds to the approximation of Doroshenko & Kopeikin (1995) for the deflection angle, and one recovers Eqs. (8) and (21).

6. Discussion

In this paper, we have presented results from 3-yr timing observations of the double pulsar using the MeerKAT telescope, with a specific focus on studying higher-order signal propagation effects in the gravitational field of the companion. In order to minimise the effects from profile evolution and DM variation, we used frequency-dependent 2D templates to generate TOAs and a DM model to correct dispersive delay in TOAs.

Thanks to its high inclination and orbital compactness, the double pulsar is a unique pulsar system for testing NLO signal propagation effects in strong fields. The significantly increased precision offered by MeerKAT permits an independent verification of NLO signal propagation effects and has already surpassed the 16 yr result with only ∼3 yr of data. In our analysis, the Shapiro shape parameter s has been improved by a factor of two compared to the previous result (Kramer et al. 2021a), which also leads to a better mass measurement. The Shapiro

range parameter r agrees with GR at 5.3×10^{-3} (95% confidence). The precision of the measurement of NLO signal propagation effects $q_{\rm NLO}$ has been improved by a factor of 1.65. In this work, we investigated the potential profile variation due to latitudinal deflection delay and the possibility of measuring lensing correction to the Shapiro delay, which has never been studied in detail before in pulsar analysis. With the current MeerKAT data, we found little evidence of profile variation at superior conjunction. It could be that the profile variation is not significant at the region we are looking at, or our current data are not sensitive enough to identify it. We also performed simulations on latitudinal deflection delay based on a simple emission model and found it unlikely to be detected because of its correlation with Shapiro delay. As for the lensing correction $\delta\Lambda_u^{\rm len}$, we found it can be mostly absorbed by the Shapiro shape parameter. Our simulation showed that lensing is unlikely to be measured separately from timing before the full SKA or similarly powerful instruments, and may then be measurable with a few years of timing observations if noises such as phase jitter and scintillation do not limit our precision.

However, our analysis also showed that adding certain epochs has a significant impact on the measured Shapiro parameters, but not on $q_{\rm NLO}$. This could be due to the fact that the phase predicted using the `polyco` scheme is particularly worse at the superior conjunction, which caused the discrepancies in the Shapiro parameters. Comparison of `polyco` with different TSPAN values showed residuals oscillating near the superior conjunction, and we may already be limited by the precision of `polyco` scheme. Of course, there may exist other unknown systematic errors in the data.

To support our timing analysis and study of profile variations at eclipse due to latitudinal deflection, we also checked profiles from all observations. We found variations in the total profile from epoch to epoch. The differences in the profiles are more prominent at lower frequencies and broadband. Our simulation suggested that these profile variations are likely to be associated with DM variation and scintillation. Even though we have subbanded data into 16/32 frequency bands and used 2D templates, profile variations may still have an impact on timing. The study of profile variations will be continued in a subsequent work to improve the constraint on the geometry of the system.

Moreover, although not discussed in this paper, we found evidence of red noise in the spectrum of timing residuals with an amplitude two orders of magnitude larger than for typical millisecond pulsars. If not taken into account, it may strongly affect astrometric parameters, as well as influence binary parameters, according to our simulations. This makes it more difficult to combine the 3 yr MeerKAT data set and the 16 yr data set. Given that the timing precision of the former significantly outperforms the latter, the weighting of MeerKAT data already exceeds the 16 yr data and can dominate noise modelling. For the purpose of this paper, we did not include 16 yr data because of their minor contribution to the $q_{\rm NLO}$ measurement (~10% improvement). However, for studying secular relativistic effects, an appropriate noise modelling may be required to combine these data. We will investigate this in further ongoing studies.

In the future, continuing observations with MeerKAT and the SKA will further improve the precision of tests on signal propagation effects, and a 50-σ detection of $q_{\rm NLO}$ can be expected by 2030. For that, we have also provided an improved analytical description of the signal propagation in the double pulsar. Furthermore, as demonstrated by Hu et al. (2020), the precision of secular relativistic effects will also be greatly improved and will eventually enable the measurement of the MOI of pulsar A and the NLO gravitational wave damping in the near future. The timing precision of the MeerKAT data used in this work is even better than that assumed in Hu et al. (2020), which is based on early L-band data from MeerKAT (see Table 4). This makes their predictions conservative and we are likely to achieve even better measurements with future observations.

Table 4. Comparison of the MeerKAT timing precision $\sigma_{\rm rms}$ assumed in Hu et al. (2020) and from real observations with L-band and UHF-band receivers, scaled to a 5 min integration time over the full bandwidth.

Telescope/receiver	Reference	$\sigma_{\rm rms}$ (μs)
MeerKAT L band	Hu et al. (2020)	1.06
MeerKAT L band	This work	0.90
MeerKAT UHF band	This work	0.55

Acknowledgements. We acknowledge Kuo Liu for helpful discussions on data processing and analysis, and Olaf Wucknitz for carefully reading the manuscript and discussions on gravitational lensing which were particularly helpful in Sect. 5.4. The MeerKAT telescope is operated by the South African Radio Astronomy Observatory, which is a facility of the National Research Foundation, an agency of the Department of Science and Innovation. MeerTime data is housed on the OzSTAR supercomputer at Swinburne University of Technology. H.H. is a member of the International Max Planck Research School for Astronomy and Astrophysics at the Universities of Bonn and Cologne. This work is supported by the Max-Planck Society as part of the 'LEGACY' collaboration with the Chinese Academy of Sciences on low-frequency gravitational wave astronomy. Pulsar research at UBC is supported by an NSERC Discovery Grant and by the Canadian Institute for Advanced Research. Part of this work has been funded using resources from the research grant 'iPeska' (P.I. Andrea Possenti) funded under the INAF national call Prin-SKA/CTA approved with the Presidential Decree 70/2016.

References

Bailes, M., Jameson, A., Abbate, F., et al. 2020, PASA, 37, e028
Blandford, R., & Teukolsky, S. A. 1976, ApJ, 205, 580
Breton, R. P., Kaspi, V. M., Kramer, M., et al. 2008, Science, 321, 104
Burgay, M., D'Amico, N., Possenti, A., et al. 2003, Nature, 426, 531
Damour, T. 2007, arXiv e-prints [arXiv:0704.0749]
Damour, T., & Deruelle, N. 1985, Ann. Inst. Henri Poincaré Phys. Théor., 43, 107
Damour, T., & Deruelle, N. 1986, Ann. Inst. Henri Poincaré Phys. Théor., 44, 263
Damour, T., & Schäfer, G. 1988, Nuovo Cimento B Serie, 101B, 127
Damour, T., & Taylor, J. H. 1992, Phys. Rev. D, 45, 1840
Demorest, P., Ramachandran, R., Backer, D. C., et al. 2004, ApJ, 615, L137
Dietrich, T., Coughlin, M. W., Pang, P. T. H., et al. 2020, Science, 370, 1450
Doroshenko, O. V., & Kopeikin, S. M. 1995, MNRAS, 274, 1029
Ferdman, R. D., Stairs, I. H., Kramer, M., et al. 2008, AIP Conf. Ser., 983, 474
Ferdman, R. D., Stairs, I. H., Kramer, M., et al. 2013, ApJ, 767, 85
Guillemot, L., Kramer, M., Johnson, T. J., et al. 2013, ApJ, 768, 169
Hobbs, G. B., Edwards, R. T., & Manchester, R. N. 2006, MNRAS, 369, 655
Hotan, A. W., van Straten, W., & Manchester, R. N. 2004, PASA, 21, 302
Hu, H., Kramer, M., Wex, N., Champion, D. J., & Kehl, M. S. 2020, MNRAS, 497, 3118
Klioner, S. A., & Kopeikin, S. M. 1992, AJ, 104, 897
Klioner, S. A., & Zschocke, S. 2010, Class. Quant. Grav., 27, 075015
Kopeikin, S. M., & Schäfer, G. 1999, Phys. Rev. D, 60, 124002
Kramer, M., Stairs, I. H., Manchester, R. N., et al. 2006a, Science, 314, 97
Kramer, M., Stairs, I. H., Manchester, R. N., et al. 2006b, Ann. Phys., 15, 34
Kramer, M., Stairs, I. H., Manchester, R. N., et al. 2021a, Phys. Rev. X, 11, 041050
Kramer, M., Stairs, I. H., Venkatraman Krishnan, V., et al. 2021b, MNRAS, 504, 2094
Lai, D., & Rafikov, R. R. 2005, ApJ, 621, L41
Lazarus, P., Karuppusamy, R., Graikou, E., et al. 2016, MNRAS, 458, 868
Lorimer, D. R., & Kramer, M. 2004, Handbook of Pulsar Astronomy (Cambridge: Cambridge University Press), 4

Lyne, A. G., Burgay, M., Kramer, M., et al. 2004, Science, 303, 1153
Nice, D., Demorest, P., Stairs, I., et al. 2015, Astrophysics Source Code Library [record ascl:1509.002]
Parthasarathy, A., Bailes, M., Shannon, R. M., et al. 2021, MNRAS, 502, 407
Perlick, V. 2004, Liv. Rev. Relativ., 7, 9
Piran, T., & Shaviv, N. J. 2004, arXiv e-prints [arXiv:astro-ph/0401553]
Pol, N., McLaughlin, M., Kramer, M., et al. 2018, AJ, 853, 73
Prša, A., Harmanec, P., Torres, G., et al. 2016, AJ, 152, 41
Rafikov, R. R., & Lai, D. 2006a, Phys. Rev. D, 73, 063003
Rafikov, R. R., & Lai, D. 2006b, ApJ, 641, 438
Ransom, S. M., Backer, D. C., Demorest, P., et al. 2004, arXiv e-prints [arXiv:astro-ph/0406321]
Schneider, P., Ehlers, J., & Falco, E. E. 1992, Gravitational Lenses (New York: Springer-Verlag)
Serylak, M., Johnston, S., Kramer, M., et al. 2021, MNRAS, 505, 4483
Shapiro, I. I. 1964, Phys. Rev. Lett., 13, 789
Shapiro, I. I. 1967, Science, 157, 806
Smarr, L. L., & Blandford, R. 1976, ApJ, 207, 574
Soffel, M., Klioner, S. A., Petit, G., et al. 2003, AJ, 126, 2687
Spiewak, R., Bailes, M., Miles, M. T., et al. 2022, PASA, 39, e027
Stairs, I. H., Thorsett, S. E., Dewey, R. J., Kramer, M., & McPhee, C. A. 2006, MNRAS, 373, L50
Tauris, T. M., Kramer, M., Freire, P. C. C., et al. 2017, ApJ, 846, 170
Taylor, J. H., & Weisberg, J. M. 1989, ApJ, 345, 434
Ward, W. R. 1970, ApJ, 162, 345
Wex, N., & Kramer, M. 2020, Universe, 6, 156
Willems, B., & Kalogera, V. 2004, ApJ, 603, L101
Willems, B., Kaplan, J., Fragos, T., Kalogera, V., & Belczynski, K. 2006, Phys. Rev. D, 74, 043003
Wucknitz, O. 2008, MNRAS, 386, 230

Paper III: A new pulsar timing model for scalar-tensor gravity: with applications to PSR J2222−0137 and pulsar-black hole binaries

---

The paper **Batrakov, Hu et al. (2023), A&A, DOI: 10.1051/0004-6361/202245246** is attached below.

Astronomy & Astrophysics manuscript no. output
April 25, 2023

A new pulsar timing model for scalar-tensor gravity

with applications to PSR J2222−0137 and pulsar-black hole binaries

A. Batrakov[1], H. Hu[1], N. Wex[1], P. C. C. Freire[1], V. Venkatraman Krishnan[1], M. Kramer[1,2], Y. J. Guo[1], L. Guillemot[3,4], J. W. McKee[5,6,7], I. Cognard[3,4], and G. Theureau[3,4]

[1] Max-Planck-Institut für Radioastronomie, Auf dem Hügel 69, 53121 Bonn, Germany
e-mail: abatrakov@mpifr-bonn.mpg.de
[2] Jodrell Bank Centre for Astrophysics, The University of Manchester, M13 9PL, United Kingdom
[3] Observatoire Radioastronomique de Nançay, Observatoire de Paris, Université PSL, Université d'Orléans, CNRS, 18330 Nançay, France
[4] Laboratoire de Physique et Chimie de l'Environnement et de l'Espace, Université d'Orléans/CNRS, 45071 Orléans Cedex 02, France
[5] Canadian Institute for Theoretical Astrophysics, University of Toronto, 60 St. George Street, Toronto, ON M5S 3H8, Canada
[6] E.A. Milne Centre for Astrophysics, University of Hull, Cottingham Road, Kingston-upon-Hull, HU6 7RX, UK
[7] Centre of Excellence for Data Science, Artificial Intelligence and Modelling (DAIM), University of Hull, Cottingham Road, Kingston-upon-Hull, HU6 7RX, UK

Received MM DD, YYYY; accepted MM DD, YYYY

ABSTRACT

Context. Scalar-tensor gravity (STG) theories are well-motivated alternatives to general relativity (GR). One class of STG theories, the Damour-Esposito-Farèse (DEF) gravity, has a massless scalar field with two arbitrary coupling parameters. We are interested in this theory because, despite its simplicity, it predicts a wealth of different phenomena, such as dipolar gravitational wave emission and spontaneous scalarisation of neutron stars (NSs). These phenomena of DEF gravity can be tested by timing binary radio pulsars. In methods used so far, intermediate phenomenological post-Keplerian (PK) parameters are measured by fitting the corresponding timing model to the timing data whose values are then compared to the predictions from the alternative theory under test. However, this approach loses information between intermediate steps and does not account for possible correlations between PK parameters.
Aims. We aim to develop a new binary pulsar timing model DDSTG to enable more precise tests of STG theories based on a minimal set of binary parameters. The expressions for PK parameters in DEF gravity are self-consistently incorporated into the model. PK parameters depend on two masses which are now directly fitted to the data without intermediate steps. The new technique takes into account all possible correlations between PK parameters naturally.
Methods. Grids of physical parameters of NSs are calculated in the framework of DEF gravity for a set of 11 equations of state. The automatic Differentiation (AutoDiff) technique is employed, which aids in the calculation of gravitational form factors of NSs with higher precision than in previous works. The pulsar timing program TEMPO is selected as a framework for the realisation of the DDSTG model. The implemented model is applicable to any type of pulsar companions. We also simulate realistic future radio-timing data-sets for a number of large radio observatories for the binary pulsar PSR J2222−0137 and three generic pulsar-black hole (PSR-BH) systems.
Results. We apply the DDSTG model to the most recently published observational data for PSR J2222−0137. The obtained limits on DEF gravity parameters for this system confirm and improve previous results. New limits are also the most reliable because DEF gravity is directly fitted to the data. We argue that future observations of PSR J2222−0137 can significantly improve the limits and that PSR-BH systems have the potential to place the tightest limits in certain areas of the DEF gravity parameter space.

Key words. gravitation – binaries : close – gravitational waves – pulsars : pulsars – general : individual (J2222−0137)

1. Introduction

General Relativity (GR) proved to be the most successful theory of gravity for more than a century. Up to now, it has passed all experimental tests with flying colours. The weak field regime is verified by the Solar System experiments (Will 2014), whereas strong field effects are especially well tested by the timing of binary pulsars (Wex & Kramer 2020). Among other things, pulsar tests enable precise tests of the radiative properties of gravity and the strong equivalence principle (SEP). Furthermore, the large-scale behaviour of gravity (low spacetime curvature and temporal variation) is tested in cosmological observations (Clifton et al. 2012a). Finally, in the last few years, ground-based gravitational wave (GW) detectors observed GWs from coalescing binary black holes (Abbott et al. 2016, 2017c, 2019a, 2021b), binary neutron stars (Abbott et al. 2017a,b, 2019b) and also black hole-neutron star binaries (Abbott et al. 2021a); probing the hitherto unexplored highly dynamic, strong-field regime of gravity. Thus far, GR can account for all observed effects both in weak and strong gravitational fields, in the quasi-static and the highly dynamical regime, and on small as well as on large scales.[1]

Despite such successes, there are still convincing reasons to investigate modified theories of gravity (Berti et al. 2015). GR

[1] Within GR, the large scale requires the introduction of dark matter and dark energy (latter in form of the cosmological constant Λ).

describes gravitational interaction by a single massless, spin-2 tensor field $g_{\mu\nu}$, known as the metric of spacetime. Some of the best motivated alternative gravity theories, the scalar-tensor gravity (STG) theories, incorporate additional scalar degrees of freedom to mediate gravity. Such scalar fields arise naturally in higher dimensional theories in their low energy limits, e.g., the old Kaluza-Klein theory (Kaluza 1921; Klein 1926) and string theories (Fujii & Maeda 2007). Scalar-tensor gravity theories are also motivated by cosmological questions of inflation, dark energy and even the thus far undiscovered quantum gravity (Clifton et al. 2012b).

The STG theory that for many years was considered as the only natural competitor of GR is known as Jordan-Fierz-Brans-Dicke (JFBD) gravity (Jordan 1955, 1959; Fierz 1956; Brans & Dicke 1961).[2] JFBD gravity is a metric theory (matter and non-gravitational fields couple only to one specific spacetime metric) and therefore fulfils the Einstein equivalence principle by design (Will 1993; Damour 2012). However, an additional scalar field is nonminimally coupled to matter via the choice of a special conformal coupling function; thus, the strong equivalence principle (SEP) is violated (Will 2014). This coupling function depends on a single parameter $\omega_{\rm BD}$, which by now is tightly constrained, in particular with the pulsar in the stellar triple system (Voisin et al. 2020). Bergmann (1968) and Wagoner (1970) presented the most general STG with one scalar field which is in its action at most quadratic in the derivatives of the fields. The most general mono-scalar–tensor theory with second-order field equations is Horndeski gravity (Horndeski 1974). In 1992, Damour & Esposito-Farèse (1992b) presented a generic class of STG theories with an arbitrary number of scalar fields. In the scope of this paper, we mainly focus on *DEF gravity* (Damour & Esposito-Farèse 1993). DEF gravity is a Bergman-Wagoner theory which has a massless scalar field and a quadratic coupling function with two arbitrary parameters.

Apart from being well-motivated, DEF gravity predicts interesting effects which are not present in weak fields of the Solar System but could be tested by employing pulsar astronomy. Neutron stars (NSs) have strong gravitational fields and large gravitational binding energies due to their high compactness. Because of this, in STG theories they can have large gravitational form-factors (also known as scalar charges), unlike weakly self-gravitating objects like normal stars and white dwarfs (WDs). Consequently, while STG theories generally predict the emission of dipolar and monopolar GWs, which increase the rate of orbital period decay relative to the GR expectation; this is expected to be especially strong in asymmetric binary systems containing a NS and a WD, due to the significant differences in their compactness and scalar charges.

Furthermore, Damour & Esposito-Farèse (1993, 1996) found a specific phenomenon in NSs called "spontaneous scalarisation". This fully non-perturbative effect excites the scalar field above the cosmological background value in NSs, allowing scalar charges of order unity, even if there is no deviation from GR in the weak-field regime. This could produce, for binary systems containing NSs with specific masses, a highly enhanced rate of dipolar GW emission.

Some of the tightest tests of gravity with strongly self-gravitating objects are provided by the high precision timing of binary pulsars (Stairs 2003; Wex 2014; Shao & Wex 2016; Wex & Kramer 2020; Kramer et al. 2021). These tests are performed in a quasi-stationary strong-field gravity regime, where the gravitational field is strong near and inside NSs and produces high curvature, whereas the velocities are small compared to the speed of light $v/c \sim 10^{-3}$. The first timing model (BT) was introduced by Blandford & Teukolsky (1976) and allowed to extract information from the timing of binary pulsars. An extended model covering all relativistic effects in the dynamics of a binary system up to the first post-Newtonian level was proposed later by Damour & Deruelle (1985, 1986) (DD).

The DD model gave an opportunity to perform self-consistent tests of gravity by means of the parametrised post-Keplerian (PPK) formalism (see, for instance, applications by Taylor & Weisberg 1989). In this generic framework, theory-independent Keplerian and post-Keplerian (PK) timing parameters, which quantify the relativistic motion of the pulsar and the propagation of its radio signals, are fitted to the observational timing data. Apart from the well measured Keplerian parameters of the orbit, each PK parameter depends only on the masses of the pulsar and its companion. As soon as the expressions for the PK parameters in a particular gravity theory are known, these two masses can be derived from the PK parameters once at least two of them are known. If more than two PK parameters become available, then a test of the consistency of that gravity theory can be made. Later, Damour & Taylor (1992) expanded the DD model and introduced pulse structure parameters. They also showed that the DD model can be applied to a large set of fully-conservative theories of gravity and presented phenomenological PK expressions in a framework of generic boost-invariant theories (the modified Einstein-Infeld-Hoffmann formalism).

However, such an independent measurement of PK parameters means that any correlations between them inadvertently reduce the sensitivity of their measurements. Taylor & Weisberg (1989) solved this problem for GR with the introduction of the DDGR model, where the GR expressions for PK parameters are incorporated in the model, and two masses are directly fitted to the observational timing data. This mitigates or breaks any correlations between the PK parameters.

In this work we present a new pulsar timing model, the "DDSTG" model. The idea is very similar to that of the DDGR model: fitting directly for the masses of the components from pulsar timing data, but instead of GR using a particular member of the two-parametric DEF gravity. Apart from the theoretical predictions for all PK parameters within that theory, the model uses pre-calculated grids of physical parameters (gravitational form-factors) of NSs in that particular gravity theory. The direct fit of two masses of the companions reduces the model to a minimal set of parameters and naturally solves all the issues of possible correlations between the observed parameters. This feature, achieved by the construction, makes the DDSTG model superior to the traditional methods, e.g. the "PK method" based on the measurement of PK parameters.

As an application of the new timing model DDSTG, we use the most recently published timing data for PSR J2222−0137 from Cognard et al. (2017) and Guo et al. (2021b). This pulsar is interesting for several reasons: It is one of the closest pulsars known and has a good timing precision. A precise measurement of the variation of the orbital period ($\dot{P}_{\rm b}$) and the high asymmetry in compactness between the pulsar and its companion allows tight constraints on the emission of dipolar GWs. Moreover, the pulsar's mass $m_{\rm p} = 1.831(10) M_\odot$ (Guo et al. 2021b) lies in the range ($m_{\rm p} \gtrsim 1.5 M_\odot$) subject to the spontaneous scalarisation effect; the non-detection of dipolar GW emission in this system has introduced strong constraints on the existence of that phenomenon, at least within the DEF framework (Zhao et al. 2022).

[2] The first to formulate JFBD gravity was actually Willy Scherrer in the early 1940s (see Goenner (2012) for a historical review on the genesis of STG).

We organise the paper as follows: in Section 2, we introduce the basics of the Damour-Esposito-Farèse (DEF) gravity and present our machinery preparations necessary for the implementation of the new model. In Section 3, we discuss so far used standard timing models and introduce our new model DDSTG for testing STG theories. The next sections are devoted to the applications of our new timing model. In Section 4, we provide a brief description of the Guo et al. (2021b) data-set on PSR J2222−0137 and apply the DDSTG model to it, discuss the limits on DEF gravity and demonstrate that our new method provides indeed tighter and more reliable constraints than previous methods. In Section 5, based on simulated data-sets for the largest radio observatories, we discuss what limits on these theories might be achieved in the near future with continued timing of PSR J2222−0137 . In Section 6, we show possible future constraints from reasonable pulsar-black hole (PSR-BH) binary systems. We also briefly discuss the possible origin of PSR-BH systems and how it affects the test if such a system is located in a globular cluster (GC). Section 7 is devoted to a discussion of other alternative gravity theories and possibilities of DDSTG extensions beyond DEF gravity. In Section 8 we discuss the effect of the time-varying gravitational constant as a perspective future extension of the DDSTG model. In Section 9 we summarise our results.

2. Damour-Esposito-Farèse gravity

This paper investigates STG theories, natural alternatives to GR. Specifically, we mainly focus on DEF gravity. In the following we summarise aspects of that class of gravity theories that are relevant for this paper.

2.1. Theoretical aspects

DEF gravity is a STG theory with one long range, massless scalar field φ non-minimally coupled to the curvature scalar. The theory is fully described by the action, which is most simply presented in the *Einstein frame* (Damour & Esposito-Farèse 1993, 1996)

$$S = \frac{c^4}{16\pi G_*}\int \frac{d^4x}{c} g_*^{1/2}(R_* - 2g_*^{\mu\nu}\partial_\mu\varphi\partial_\nu\varphi) + S_m\left[\psi_m; A^2(\varphi)g^*_{\mu\nu}\right], \tag{1}$$

where G_* is the bare gravitational coupling constant, g_* and R_* are the determinant and the Ricci scalar associated with the Einstein metric ($g^*_{\mu\nu}$). The last term in Eq. (1) describes an action associated with any matter fields (ψ_m). $A(\varphi)$ is the coupling function and takes a specific exponential form in DEF gravity: $A(\varphi) = \exp[\alpha_0(\varphi-\varphi_0) + \frac{1}{2}\beta_0(\varphi-\varphi_0)^2]$. Introduced quantities $\{\alpha_0, \beta_0\}$ are two arbitrary parameters of the theory and φ_0 is the scalar field at spatial infinity. The coupling function $A(\varphi)$ plays the role of a conformal factor connecting the "physical metric" $\tilde{g}_{\mu\nu} = A^2(\varphi)g^*_{\mu\nu}$ with the Einstein metric. The metric $\tilde{g}_{\mu\nu}$ is the one measured by laboratory clocks and rods due to the universal coupling of matter to this metric. The bare gravitational constant is simply related to the one measured in a Cavendish experiment by $G_{\rm Cav} = G_*(1+\alpha_0^2)$. GR corresponds to vanishing coupling parameters, i.e. $\alpha_0 = \beta_0 = 0$, and JFBD gravity is recovered by setting $\beta_0 = 0$ while keeping $\alpha_0 \neq 0$.

The field equations are derived by variation of the action in Eq. (1) and are most simply formulated in terms of the pure-spin field variables $(g^*_{\mu\nu}, \varphi)$ in the Einstein frame:

$$R^*_{\mu\nu} = 2\partial_\mu\varphi\partial_\nu\varphi + \frac{8\pi G_*}{c^4}\left(T^*_{\mu\nu} - \frac{1}{2}T^* g^*_{\mu\nu}\right), \tag{2}$$

$$\Box_{g^*}\varphi = -\frac{8\pi G_*}{c^4}\alpha(\varphi)T_*, \tag{3}$$

with a material stress-energy tensor $T^{\mu\nu}_* = 2cg_*^{-1/2}\delta S_m/\delta g^*_{\mu\nu}$ and $\alpha(\varphi) = \partial \ln A(\varphi)/\partial\varphi$, which measures the coupling strength between the scalar field and matter.

All weak-field deviations from GR may be described in terms of the asymptotic behaviour of $\alpha(\varphi)$ at spatial infinity. The theory parameters $\alpha_0 = \alpha(\varphi_0)$, $\beta_0 = \beta(\varphi_0)$ can be interpreted as asymptotic values of the function $\alpha(\varphi)$ and its derivative $\beta(\varphi) = \partial\alpha(\varphi)/\partial\varphi$.

In this work, without loss of generality, we use the formulation of DEF gravity with $\varphi_0 \equiv 0$, two parameters $\{\alpha_0, \beta_0\}$ appearing in the form of $A(\varphi)$ and $A(\varphi_0) = 1$. There is an equivalent formulation in terms of parameters $\{\beta_0, \varphi_0\}$, where $A(\varphi) = \exp(\beta_0\varphi^2/2)$ and $\varphi_0 = \alpha_0/\beta_0$. But the latter formulation is not well determined for the JFBD limit $\beta_0 = 0$ (Damour 2007).

The parameterised post-Newtonian (PPN) framework allows describing a wide range of metric theories of gravity in their weak field approximation by ten independent PPN parameters. DEF gravity is a fully conservative theory and has only two PPN parameters that deviate from their GR values, which are also called Eddington parameters (Will 1993):

$$\gamma_{\rm Edd} = 1 - \frac{2\alpha_0^2}{1+\alpha_0^2}, \tag{4}$$

$$\beta_{\rm Edd} = 1 + \frac{\beta_0\alpha_0^2}{2(1+\alpha_0^2)^2}. \tag{5}$$

The PPN parameter $\gamma_{\rm Edd}$ measures the spatial curvature induced by unit rest mass and $\beta_{\rm Edd}$ is a measure of the amount of nonlinearity in the superposition law of gravity. Solar System experiments put limits on these parameters. The $|\gamma_{\rm Edd} - 1| \lesssim 2.3\times10^{-5}$ limit comes from the Shapiro time delay observed by the Cassini spacecraft (Bertotti et al. 2003; Will 2014). The $|\beta_{\rm Edd} - 1| \lesssim 8\times10^{-5}$ limit comes from observations of the perihelion shift of Mercury (Will 2014). The Cassini experiment yields a direct limit on $\alpha_0^2 \lesssim 1.15\times10^{-5}$, whereas β_0 remains unconstrained from weak-field Solar System experiments, since α_0 can be arbitrarily small.

2.2. Scalarisation of neutron stars in DEF gravity

To place firm limits on β_0 parameter, we need to explore the strong-field effects of DEF gravity. One can expect deviations from GR in the presence of highly compact massive objects, in particular for NSs, due to the scalar field sourced by the strong internal gravitational field of the star. When placing limits on β_0 it is important that for certain areas in the DEF gravity parameter space one has a significant growth of the scalar field in the NS interior, even if the deviations for weakly self-gravitating bodies are very small, or even zero (Damour & Esposito-Farèse 1992a; Damour & Esposito-Farèse 1993, 1996). The origin of this spontaneous scalarisation lies in the tachyonic instability of the field equations happening when a NS reaches a sufficiently high compactness. The mechanism of this instability is similar to what happens in ferromagnets during spontaneous magnetisation (Damour & Esposito-Farèse 1996). It is a fully nonlinear

non-perturbative effect, thus it requires accurate techniques to be properly analysed.

For testing DEF gravity, it is crucial to introduce three gravitational form-factors appearing in the expressions for PK parameters

$$\alpha_A = \frac{\partial \ln m_A}{\partial \varphi_0}\Big|_{\bar{m}_A}, \quad \beta_A = \frac{\partial \alpha_A}{\partial \varphi_0}\Big|_{\bar{m}_A}, \quad k_A = -\frac{\partial \ln I_A}{\partial \varphi_0}\Big|_{\bar{m}_A}, \tag{6}$$

where all the derivatives are taken for a fixed baryonic mass ($\bar{m}_A$). The important quantity α_A counts the effective couple strength between the ambient scalar field and a NS. The subscript A refers to the star A. α_A is a strong-field counterpart to the parameter α_0, which is its weak field approximation. If a NS mass exceeds the critical mass of $m_{\rm crit}$ then $\alpha_{\rm NS}$ can become suddenly of order of unity $\alpha_{\rm NS} \sim O(1)$ due to the scalarisation effect, while its weak field counterpart stays close to zero $\alpha_0 \sim 0$. The value of the critical mass depends on β_0 and the chosen equation of state (EOS). The second parameter β_A reflects a change of the scalar charge when the asymptotic scalar field changes. The derivative β_A can also obtain very large values in the transition scalarisation region, where α_A changes fast with the change of a mass. The last quantity k_A describes the field dependence of the moment of inertia I_A and can become important in the eccentric systems.

2.3. Calculating grids of NSs

To test DEF gravity in precision timing experiments of binary pulsars, one must know the exact properties of NSs in that specific class of alternative gravity. In our work, we follow the procedure described in Damour & Esposito-Farèse (1996) for calculating NSs in DEF gravity. We assume the slowly rotating NS approximation with a stationary axisymmetric metric. Assuming this axial symmetry and neglecting terms of rotational velocity squared (or higher), the Einstein equations can be written as a system of 8 first-order ordinary differential equations (ODEs) for a set of radial functions (see the representation by Damour & Esposito-Farèse (1996)). The equations are complemented by appropriate boundary conditions placed at spatial infinity and the NS centre. Boundary conditions at spatial infinity and thus properties of NSs depend on the values of the theory parameters $\{\alpha_0, \beta_0\}$.

For solving NS structures, we developed a modular program in the Julia language (Bezanson et al. 2017). The program enables us to calculate both single NSs for selected parameters and grids of NSs for many desired parameters. The calculations are performed accurately and efficiently using the methods of parallel programming. Currently, DEF gravity is implemented as the chosen theory of gravity, but our program allows to use any coupling function $A(\varphi)$ to extend our tests beyond DEF gravity parametrisation.

The internal structure and NSs parameters significantly depend on EOS. The strong dependence of the scalarisation phenomenon on the choice of EOS was extensively analysed by Shao et al. (2017) and Zhao et al. (2022) in order to put constraints on this non-linear phenomenon from radio pulsars. In our work, we use a piece-wise polytropic approximation for the EOSs following the procedure in Read et al. (2009). We select 11 EOSs that allow us to cover a range from soft to stiff while still being in agreement with the maximum mass observed for a NS (for more information about selected EOS we refer to Appendix A.2). For tests in the present paper, we select MPA1 high-density EOS (Müther et al. 1987) in its piece-wise polytropic form (Read et al. 2009) with three polytropic pieces. MPA1 is a stiff EOS with a maximum mass of a NS equal to $2.46\,M_\odot$. For low densities, we use an analytic form of the SLy EOS proposed by Douchin & Haensel (2001) and approximated by four polytropic pieces (Read et al. 2009). In general stiff EOSs (e.g. MPA1) produce more conservative limits in most parts of DEF gravity parameter space.

In our program, we utilise the Automatic Differentiation (AutoDiff) technique (see e.g. Margossian (2018)) for calculating derivatives of NSs quantities. AutoDiff is a powerful alternative to numerical differentiation deprived of numerical errors (for detailed explanation see Appendix A.1). AutoDiff algorithm utilises exact expressions of derivatives for elementary functions and a chain rule to calculate complex derivatives with the working machine-precision. Thus our program with applied AutoDiff technique calculates gravitational form-factors $\{\alpha_A, \beta_A, k_A\}$, presented as derivatives in Eq. (6), with very high numerical precision.

Using the developed program, we calculate gravitational form-factors and masses for an extensive grid of DEF parameters and central pressures $\{\alpha_0, \beta_0, p_c\}$ assuming a specific EOS. Our grids cover ranges of $\alpha_0 \in [-10^{-1}, -10^{-5}]$, $\beta_0 \in [-6, +10]$, $p_c \in [10^{34}, 10^{36}]$ dyn/cm^2 and are sampled linearly for $\log \alpha_0, \log p_c$ and β_0. The size of each grid is $\{101, 351, 121\}$ points respectively. More technical details about the procedure of calculating NS properties, the AutoDiff technique, and the structure of pre-calculated grids can be found in Appendix A. We stick to pre-calculating grids because it is numerically costly to calculate NS structures for a particular mass on the fly. Further one can perform interpolation over these pre-calculated grids or methods beyond interpolation, e.g reduced-order models in Guo et al. (2021a). The achieved accuracy of grid values and further interpolation over the grid is sufficient for our purposes.

The accuracy of the calculations can be checked by comparison of the scalar charge (α_A) calculated as the derivative from Eq. (6) $\alpha_{A,\,\rm deriv}$ and its direct value from the asymptotic behaviour of the external scalar field obtained after integration $\alpha_{A,\,\rm asympt}$ (Damour & Esposito-Farèse 1993). The relative accuracy expressed by $\delta_{\rm rel} = |1 - \alpha_{A,\,\rm deriv}/\alpha_{A,\,\rm asympt}|$ lies in the range $\delta_{\rm rel} \sim 10^{-7} - 10^{-13}$ for our calculations. The calculated scalar charges are significantly more accurate compared to previous works, e.g., Anderson & Yunes (2019) with typical accuracy of $\delta_{\rm rel} \sim 10^{-1} - 10^{-5}$. However, it is essential to mention that the accuracy of several percent is already sufficient for testing DEF gravity with binary pulsar timing.

Besides, we also find that the NS structure appears to be very sensitive to internal thermodynamic consistency. The piece-wise polytropic EOSs fulfil the thermodynamic consistency by their definition. However, often one uses tabulated EOSs instead, which must be interpolated. Unfortunately, a commonly used log-log interpolation of tabulated EOSs can lead to significant numerical errors in the scalar derivatives of Eq. (6) because of its thermodynamic inconsistency.[3] For this reason, we use piece-wise polytropic approximations instead of tabulated

[3] Doing an interpolation of a tabulated EOS in a way that correctly accounts for the first law of thermodynamics is not a trivial problem and requires a formulation in terms of Helmholtz free energy (Swesty 1996). If one uses a simple linear interpolation in $\{\log n, \log p\}$ and $\{\log n, \log \varepsilon\}$ planes for a tabulated EOS (n is the baryon number density and ε is the energy density), the accuracy check can fail by the amount of $\delta_{\rm rel} \sim O(1) - O(0.1)$ in the region of strong scalarisation. The reason is that such interpolations do not obey the first law of thermodynamics $\frac{dn}{d\epsilon} = \frac{n}{\epsilon + p}$ which is assumed for structure equations and defines the baryonic mass $\bar{m}_A$ (Hartle 1967; Damour & Esposito-Farèse 1996). As a consequence, this not only affects NS masses but even more so the

EOSs, which is absolutely sufficient for conducting our tests and for exploring the EOS dependence of pulsar constraints on DEF gravity.

3. A new timing model for scalar-tensor gravity

To place constraints on a gravity theory from the observations of a binary pulsar, one must know its predictions for the binary system's motion and the propagation of the electromagnetic signal in the curved spacetime of the binary system. The timing formula is the tool to capture the relativistic effects predicted by the theory from a sequence of pulse arrival times on Earth. The timing formula relates the observed (topocentric) time of arrival (TOA) of the pulse and its time of emission.

3.1. Binary pulsar timing models

The first timing model (BT) was introduced by Blandford & Teukolsky (1976) in order to describe the timing of the first binary pulsar, PSR B1913+16, which had been discovered earlier by Hulse & Taylor (1975). The BT model assumes that the pulsar and its companion follow a Keplerian motion with additional secular changes in the Keplerian parameters of the orbit. utilised Keplerian parameters are the orbital period (P_b), the epoch of periastron passage (T_0), the orbital eccentricity (e), the longitude of periastron (ω), and the projected semi-major axis of the pulsar's orbit (x). The model accounts for a combination of a special-relativistic time dilation and a gravitational redshift; this periodic effect is described by an extra parameter called the Einstein delay (γ). The BT model accounts for (linear-in-time) secular changes in P_b, e, ω and x, introducing PK parameters: rates of change of the orbital period ($\dot{P}_\mathrm{b}$), eccentricity ($\dot{e}$), longitude of periastron ($\dot{\omega}$) and projected semi-major axis ($\dot{x}$). These secular changes can be caused by both relativistic and astrometric effects (Damour & Taylor 1992; Lorimer & Kramer 2004).

Later, Damour & Deruelle (1986) proved that all of the independent $O(v^2/c^2)$ timing effects could be described in a simple mathematical way for a wide range of alternative gravity theories. They developed a phenomenological (i.e. theory independent) timing model based on the full first post-Newtonian description of the two-body problem, which we will refer to as the "DD" model that uses a quasi-Keplerian solution to the equations of motion of a 2-body problem. This model allows working within a parametrised post-Keplerian approach (PPK). Damour & Taylor (1992) then showed that the DD model could be used to constrain a wide range of conservative theories of gravity obeying the modified Einstein-Infeld-Hoffmann (mEIH) framework (see also Will 1993).

For the binary system part, the timing formula of the DD model reads as:

$$t_\mathrm{b} - t_0 = D^{-1}\left[T + \Delta_R(T) + \Delta_E(T) + \Delta_S(T) + \Delta_A(T)\right], \tag{7}$$

where t_b is the Solar System barycentric (infinite-frequency) arrival time, t_0 is a chosen reference epoch, T is the pulsar's proper time, and D is a Doppler factor accounting for the relative radial motion of the centre of mass of the binary system and the Solar System barycentre. The quantities Δ_i in Eq. (7) are different time delays introducing corrections due to internal binary effects.

Splitting the timing formula into a set of different contributions is to some extent a coordinate-dependent concept, however, within the approximations used it is convenient to work with these individual expressions for timing delays. The term $\Delta_R(T)$ is called "Roemer delay" and counts for the classical light travel time through the binary. $\Delta_E(T)$ is the "Einstein delay" and relates the proper emission time to the coordinate time of emission. $\Delta_S(T)$ is the "Shapiro delay" arising from the effect of the gravitational potential of the companion on the propagation of the pulsar signals. The "aberration delay" $\Delta_A(T)$ places corrections due to the periodic changes in the direction of pulse emission (as seen in the frame of the rotating pulsar) while the pulsar follows its binary motion.

All the expressions depend on three sets of parameters. Keplerian parameters are

$$\{p^\mathrm{K}\} = \{P_\mathrm{b}, T_0, e_0, \omega_0, x_0\} \tag{8}$$

and remain the same as for the BT model (the subscript 0 means a value at a given epoch). Separately measurable PK parameters are

$$\{p^\mathrm{PK}\} = \{k, \gamma, \dot{P}_\mathrm{b}, r, s, \delta_\theta, \dot{e}, \dot{x}\}\,. \tag{9}$$

The DD model introduces a periastron-shift parameter $k = \dot{\omega}P_\mathrm{b}/(2\pi)$, Shapiro "shape" ($s = \sin i$, where i is the inclination angle) and Shapiro "range" (r) parameter for the signal propagation, and a relativistic deformation of the orbit (δ_θ). Not separately measurable PK parameters are

$$\{q^\mathrm{PK}\} = \{\delta_r, A, B, D\}\,, \tag{10}$$

including a second parameter for the relativistic deformation (δ_r), two aberration parameters (A and B) and a Doppler factor (D).

The mentioned delays in the framework of the DD model are presented by expressions

$$\Delta_R(T) = x\sin\omega\left[\cos u - e(1+\delta_r)\right] + x\left[1 - e^2(1+\delta_\theta)^2\right]^{1/2}\cos\omega\sin u\,, \tag{11}$$

$$\Delta_E(T) = \gamma\sin u\,, \tag{12}$$

$$\Delta_S(T) = -2r\ln\Big\{1 - e\cos u - s\big[\sin\omega(\cos u - e) + (1-e^2)^{1/2}\cos\omega\sin u\big]\Big\}\,, \tag{13}$$

$$\Delta_A(T) = A\left\{\sin\left[\omega + A_e(u)\right] + e\sin\omega\right\} + B\left\{\cos\left[\omega + A_e(u)\right] + e\cos\omega\right\}\,, \tag{14}$$

where the secular changes incorporated in the projected semi-major axis x and eccentricity e are given by

$$x = x_0 + \dot{x}(T - T_0)\,, \tag{15}$$

$$e = e_0 + \dot{e}(T - T_0)\,. \tag{16}$$

The true anomaly (A_e) and ω depend on the eccentric anomaly (u) via following the relations

$$A_e(u) = 2\arctan\left[\left(\frac{1+e}{1-e}\right)^{1/2}\tan\frac{u}{2}\right], \tag{17}$$

$$\omega = \omega_0 + kA_e(u)\,, \tag{18}$$

where u is itself a function of T and defined by solving Kepler's equation

$$u - e\sin u = 2\pi\left[\left(\frac{T-T_0}{P_\mathrm{b}}\right) - \frac{1}{2}\dot{P}_\mathrm{b}\left(\frac{T-T_0}{P_\mathrm{b}}\right)^2\right]. \tag{19}$$

derivatives in Eq. (6), including the expression of α_A from Eq. (6) as the derivative of the mass which enters the accuracy check.

The parameters in Eq. (10) cannot be measured separately from the parameters in Eqs. (9) and (8) as shown by Damour & Deruelle (1986). It means that all not separately measurable parameters can be fully absorbed into the change of other parameters. More details about measurable parameters and the connection between observed parameters and the intrinsic parameters can be found in Damour & Taylor (1992). The redefinition of orbital parameters can absorb the Doppler factor (D). Such a redefinition does not affect the tests because it is only a rescaling of physical units, thus D is set to 1.[4] The aberration parameters A and B can be absorbed as well by redefinition of T_0, x, e, δ_r and δ_θ.

3.2. A timing model in DEF gravity

The DD model can be applied to a wide range of fully-conservative theories of gravity. DEF gravity is a fully-conservative theory (Will 1993), thus we can investigate it in the framework of the DD model.

In different theories of gravity, the functional dependence of the PK parameters, i.e.

$$p_i^{\rm PK} = f_i^{\rm theory}(m_{\rm p}, m_{\rm c}; P_{\rm b}, e_0, x_0; {\rm EOS})\,, \tag{20}$$

can differ substantially because of strong-field effects involving a highly compact NS and its companion. The PK parameters are functions of two masses, thus one can perform gravity tests if at least 3 PK parameters are measurable. In general, if there are n measured PK parameters, one can do $n-2$ independent tests for a given gravity theory. A common procedure of making tests using expressions for PK parameters is discussed in detail in Section 4, devoted to applications of a new model and comparison between different techniques.

The core part of the new timing model is the predictions for PK parameters (20) in DEF gravity. We use expressions for PK parameters in DEF gravity provided in the literature (Damour & Esposito-Farèse 1992b; Damour & Esposito-Farèse 1993, 1996). However, for parameters δ_θ, δ_r, A and B there are only more general expressions. A phenomenological theory-independent description of PK parameters from which we derive their expressions in DEF gravity is presented in Damour & Taylor (1992). The expressions of PK parameters and details are given in Appendix B.

The aberration parameters A and B can also be calculated in DEF gravity, provided we know the system's geometry. The applications we use in the paper assume a special situation when the pulsar's spin axis is aligned to the orbital angular momentum of the system. The alignment is a reasonable assumption for a recycled pulsar with a WD companion due to the preceding accretion process during the system's evolution. In this special case, A is calculated according to Eq. (B.7) assuming angles $\eta = -\pi/2$ and $\lambda = i$ (Damour & Taylor 1992). The second aberration parameter $B = 0$ in this special situation. In general, an alignment may not be the case for a particular binary pulsar (e.g. double neutron star systems), but the new model can also handle this misalignment. Once the system's geometry is assumed, real A and B values can be calculated for a given epoch without the necessity to redefine other parameters.[5]

[4] Note, however, that a temporal change of D is of relevance for pulsar timing experiments, as we will discuss later.

[5] If the spin of the pulsar is misaligned, this can lead to a further complication of the analysis. In such a case geodetic precession leads to apparent changes in the binary parameters (Damour & Taylor 1992; Lorimer & Kramer 2004).

The PK parameters from Eq. (20) depend on the orbital parameters of the system and the physical properties of the pulsar. However, we also have to know properties of the companion. The PK expressions (B.1 - B.13) depend on gravitational form-factors of the companion $\{\alpha_{\rm c}, \beta_{\rm c}\}$. The quantity $k_{\rm c}$ does not appear in the expressions because they take into account only leading order terms, and is therefore of no interest. These quantities, in turn, depend on the type of companion. If the companion is a NS, they are calculated in the same way as for the primary pulsar using Eq. (6). If the companion is a black hole (BH), then the gravitational form-factors all vanish:

$$\alpha_{\rm BH} = 0, \quad \beta_{\rm BH} = 0, \quad k_{\rm BH} = 0\,. \tag{21}$$

This is a consequence of the "no-hair" theorem; the BH is not scalarised in DEF gravity (Hawking 1972; Damour & Esposito-Farèse 1992a). Section 6 is dedicated to a more thorough discussion on binary pulsar systems with a BH and the results which we can obtain from timing of a pulsar in a relativistic orbit with a BH. For a WD companion, the gravitational form-factors are approximated by their weak field expressions

$$\alpha_{\rm WD} \simeq \alpha_0, \quad \beta_{\rm WD} \simeq \beta_0, \quad k_{\rm WD} \simeq 0\,. \tag{22}$$

Such an approximation is sufficient for our purposes because WDs are not compact enough to show the strong field effects present in NSs and BHs. The next order approximation for weakly self-gravitating objects is $\alpha_A \simeq \alpha_0(1 - 2s_A)$, where $s_A \simeq G_* m_A/(Rc^2)$ is the sensitivity (R is the object's radius) and has a typical value of $s_{\rm WD} \sim 10^{-5} - 10^{-3}$ for a WD (Damour & Esposito-Farèse 1992a; Damour & Esposito-Farèse 1993; Will 2018b). Thus the usage of weak field counterparts $\{\alpha_0, \beta_0\}$ for a WD companion instead of precisely calculated values is justified.

To summarise, the timing model in DEF gravity is defined by two theory parameters $\{\alpha_0, \beta_0\}$, the chosen EOS for a NS, and the type of the companion among {WD, NS, BH}. We name the new model DDSTG arises as direct extension of the DD model for STG theories.

3.3. DDSTG implementation into TEMPO

Once we obtain the theoretical part of the new DDSTG timing model, we need to apply it to the timing data. We implemented the DDSTG model into one of the commonly used pulsar timing software – the TEMPO[6] program (Nice et al. 2015). The local implementation of DDSTG model in TEMPO and precalculated grids of masses and gravitational form-factors are supplied with the paper[7]. The authors intend to make DDSTG a part of the official TEMPO distribution to ensure forward compatibility.

There is a standard procedure of analysing radio pulsar timing data. The preprocessed TOAs are obtained after radio observations of the desired pulsar system. During the procedure, TEMPO reads TOAs, parameters of the binary model, and some coded instructions from supplied files. Then TEMPO fits the selected timing model accounting for the transformation to the Solar System barycentre, pulsar rotation, and its spin down for a chosen binary model.

Specifically for DDSTG, a user selects theory parameters $\{\alpha_0, \beta_0\}$, EOS, and the type of a companion. During the initialisation TEMPO reads pre-calculated 3D grids of gravitational form-factors and NS masses $\{\alpha_A, \beta_A, k_A, m_A\}$ (see Section 2.3)

[6] http://tempo.sourceforge.net

[7] https://github.com/AlexBatrakov/tempo-13.103_ddstg

for the chosen EOS. Each 3D grid depends on $\{\alpha_0, \beta_0, p_c\}$ parameters, where p_c is the central pressure. Then gravitational form-factors and masses are interpolated for the selected $\{\alpha_0, \beta_0\}$ values and saved into a smaller 1D grids (depending only on p_c) in the program memory. The final 1D grids remain unchanged and are used to interpolate gravitational form-factors for a particular theory in the mass range during the fitting procedure of TEMPO.

TEMPO with the selected DDSTG model fits two masses: the total mass ($m_{\rm tot}$) of the system and the companion's mass ($m_{\rm c}$). Every time when these masses change, the model recalculates the gravitational form-factors for the pulsar and the companion. Once the gravitational form-factors (Eq. (6)) are known, the model calculates all PK parameters (Eqs. (9) and (10)) using equations given in Appendix B. These calculated PK parameters are used afterwards in the timing formula (7). The details about the DDSTG implementation and the description of model parameters can be found in Appendix C.

In the timing formula (7), the Solar System barycentric arrival time ($t_{\rm b}$) is known. However, to obtain the proper pulsar time (T), one has to perform the inversion of the timing formula, i.e. get T as a function of $t_{\rm b}$: $T = t_{\rm b} - \bar{\Delta}(t_{\rm b})$. The original DD model utilises an approximate analytic inversion, which sometimes is not accurate enough, for example, for the Double Pulsar (Kramer et al. 2021). In contrast, our DDSTG model performs accurate numerical inversion. Eq. (7) is solved iteratively for T for each TOA. The discrepancy due to an inaccurate inversion may influence the test for precise timing in the future or PSR-BH systems discussed further below. Nowadays, numerical inversion is considered a new standard and implemented in the DDS model of TEMPO (Kramer et al. 2021) and generally used in PINT (Luo et al. 2021).

The DDSTG model produces the best fit to the data for DEF gravity with a selected set of parameters and a given EOS. The output of TEMPO stays the same as for other binary models, e.g. the calculated χ^2 value and root mean square error of fit. The χ^2 statistics may be applied for further tests to compare the results for different theory parameters.

3.4. Advantages of DDSTG

The tests with pulsar data allow placing constraints on the gravity theory parameters. The most simple and common way to achieve this is to compare the measured PK parameters with the theoretical predictions from the theory. PK parameters are obtained by fitting a phenomenological model to the observational data, e.g., DD model. A phenomenological model estimates PK parameters and their uncertainties.

Within a particular gravity theory, each PK parameter depends on the masses of the pulsar and the companion and thus corresponds to a curve in a mass-mass space. Together with the measurement error, each PK parameter produces a strip in the $\{m_{\rm p}, m_{\rm c}\}$ space. If there are two measured parameters, one may find the intersection area and obtain the estimated mass values. If the number of measured parameters is more than two, one can perform a test of that particular gravity theory. The test is passed if all three curves intersect in the range of errors at one point. Generally, n measured PK parameters result in $n - 2$ independent tests.

If a gravity theory has arbitrary parameters, tests can be done for any fixed values of theory parameters. For DEF gravity, this procedure results in an "allowed" area in $\{\alpha_0, \beta_0\}$ space that pass gravity tests within the measurement uncertainties. This area is bounded within the selected confidence limit by a curve, which is usually plotted. To date, the regions allowed by different tests have always included GR.

If the companion is optically bright, one can get information about the system from optical observations. For example, for a binary pulsar system with a bright WD it is possible to obtain the mass ratio and the companion mass using high-resolution optical spectroscopy of the companion (e.g., Antoniadis et al. 2012, 2013). In such cases, we do not have to measure three independent PK parameters based on the radio data, but we can combine several multi-wavelength constraints.

Another issue are possible correlations between PK and other parameters. Observed correlations can come from the theoretical correlation of parameters within the binary model (e.g. $T_0 \leftrightarrow \omega$ and $P_{\rm b} \leftrightarrow \dot{\omega}$ in a low eccentric case) and from a nonuniform data sampling (e.g. a nonlinear correlation in a parametrisation of Shapiro delay $r \leftrightarrow s$). Often in the past, measured PK parameters were published without any information about observed correlations. This additional information from the timing data is lost in such cases. These days it became a common practice to publish observed correlations and even provide them explicitly. Anderson & Yunes (2019) and Anderson et al. (2019) accounted for possible observed and theoretical correlations between PK parameters within DEF and MO gravity via computationally highly demanding Markov chain Monte Carlo (MCMC) simulations utilising the correlation matrix from the TEMPO output. However, this elaborate approach would not work if the relativistic effect is not well measured or the dependence between the parameters is highly nonlinear. If the relation is nonlinear, the correlation matrix gives information only about the linear contribution. To fully account for a nonlinear relation one has to obtain a full probability density function in the parameter space.

Contrary to the PK method, the DDSTG model accounts for all even nonlinear correlations naturally and breaks them by a direct fit of the masses. This was already one of the main advantages of the DDGR model; and is one of the reasons why the DDSTG uses the same superior approach while extending it to STG theories. The model accounts for all effects internally and extracts all the information from the timing data. The information is not lost even if the correlating parameter cannot be measured but influences other parameters. Such possible correlations are relevant for PSR J1141−6545 (Venkatraman Krishnan 2019; Venkatraman Krishnan et al. 2020), where there is a correlation between the time dilation parameter (γ) of the Einstein delay and the rate of change of the projected semi-major axis due to the spin-orbit coupling caused by the fast rotating WD companion ($\dot{x}^{\rm SO}$). Furthermore, the Shapiro delay cannot be measured independently but is still essential (see e.g. Bhat et al. 2008). We expect the DDSTG model to be of particular advantage for PSR J1141−6545 and there will be a dedicated paper (Venkatraman Krishnan et al. in prep.) about applying the new model to this system.

Compared to conventional methods, the constraints obtained by DDSTG may, in general, become either tighter or weaker depending on the particular case. However, the resulting restrictions are more reliable by the construction. This weakening of the limits can happen because of unaccounted correlations.

4. Application to PSR J2222−0137

As a demonstration of the DDSTG model, we now apply it to published timing data of a binary pulsar. We select PSR J2222−0137 because of its unusual characteristics, which we now list in detail.

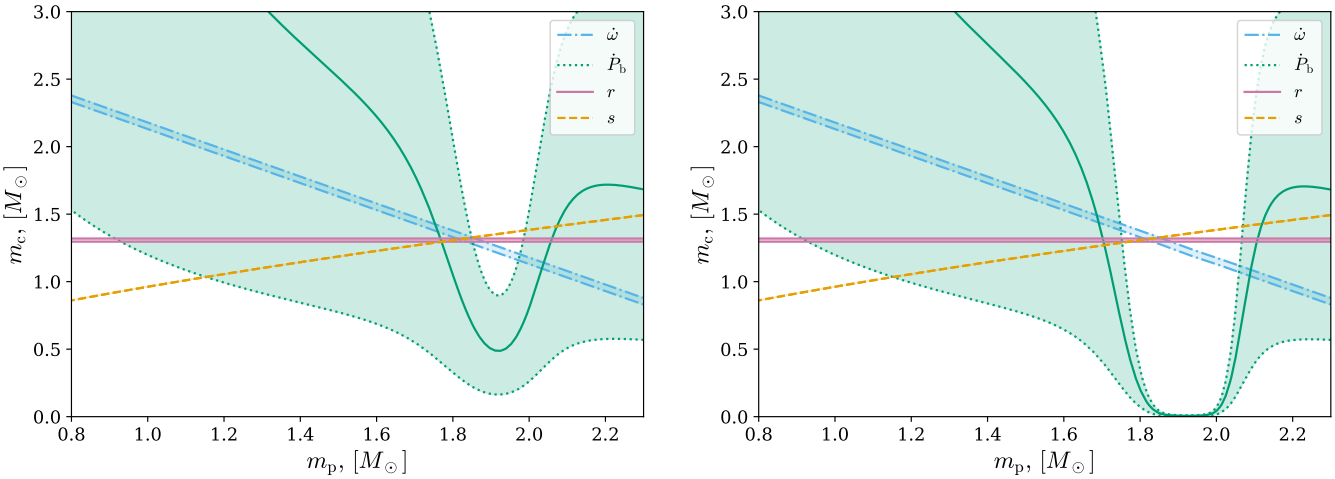

Fig. 1. Mass-mass diagrams for the PSR J2222−0137 system at the zone of high nonlinearity where a fast transition to a strongly scalarised pulsar happens. PK parameters are obtained by fitting the DD model to the timing data from Guo et al. (2021b). Calculations are preformed within DEF gravity for the MPA1 EOS allowing NSs with maximum mass in GR of $M_{\rm GR} \simeq 2.46 M_\odot$. Left panel corresponds to the point in the DEF parameter space with $\alpha_0 = -10^{-4}, \beta_0 = -4.3$, which is not excluded by the test. Right panel shows the same test but for $\alpha_0 = -10^{-4}, \beta_0 = -4.35$. The prediction of a strong dipolar contribution $\dot{P}_{\rm b}^D$ fails the test for the more negative $\beta_0 = -4.35$. The axes correspond to the masses of the pulsar $m_{\rm p}$ and the companion c. The shadowed area is the allowed region at 68% CL limit for a corresponding PK parameter. The solid green line corresponds to the observed value of $\dot{P}_{\rm b}^{GW}$ due to the GW emission.

4.1. About the system

We are particularly interested in recycled pulsars because of their, in general, better timing precision essential for precise gravity tests. The radio pulsar PSR J2222−0137 was discovered in the Green Bank Telescope (GBT) 350 MHz drift scan pulsar survey (Boyles et al. 2013). It is a mildly recycled pulsar which has a spin period (P) of 32.8 ms. The pulsar is in a binary system with $P_{\rm b}$ of 2.44576 days and x of 10.848 light-seconds. We also expect the pulsar's spin axis to be aligned to the orbital angular momentum of the system. The alignment happens as a consequence of the pulsar recycling process, when the pulsar accretes matter from the companion.

PSR J2222−0137 is already known as a unique laboratory for testing gravity theories because of its special characteristics; for more detailed information, we refer the reader to Cognard et al. (2017) and Guo et al. (2021b). It is one of the closest pulsars known, with the most precise distance measured with Very Large Baseline Interferometry (VLBI, see Deller et al. 2013) and excellent timing precision. The system has a highly significant detection of the Shapiro delay as well as the measured rate of advance of periastron ($\dot{\omega}$), which yield precise mass measurements and $\sim 1\%$ test of the GR predictions for the Shapiro delay (Guo et al. 2021b).

The most important characteristic in the scope of this paper is the precise measurement of $\dot{P}_{\rm b}$. Given the precise masses, this can be compared with a precise prediction for the orbital decay due to GW damping, furthermore the kinematic contributions to $\dot{P}_{\rm b}$ (see Section 4.4) can be estimated precisely because of the good distance measurement. The $\dot{P}_{\rm b}$ measurement constrains dipolar GW emission in this system, which would arise in DEF gravity (Damour & Esposito-Farèse 1992a) because of the large difference in the compactness of the components (NS and WD). Finally, the mass of the pulsar ($m_{\rm p} = 1.831(10) M_\odot$) (Guo et al. 2021b) lies in the range where spontaneous scalarisation happens, yielding strong limits on this highly non-linear phenomenon (Shao et al. 2017; Zhao et al. 2022).

4.2. Observational data

The PSR J2222−0137 timing data used in this work are the same as used by Guo et al. (2021b). This includes observations of this pulsar going back to its original follow-up, which started on 2009 June 23 using the Green Bank Telescope (GBT); however these ended on 2011 December 26. Regular observations with the three largest European radio telescopes (3ERT) started the following years: the Nançay Radio Telescope on 2012 October 4, The Lovell Telescope at Jodrell Bank on 2012 November 20 and the dense orbital campaigns with the Effelsberg 100-m radio telescope on 2015 October 26. These observations continue to the present day; however Guo et al. (2021b) only analysed the data obtained until 2021 May 2; their processing and how the resulting ToAs were analysed is described in detail by Cognard et al. (2017) and Guo et al. (2021b).

Observations with the MeerKAT radio telescope array and the Five hundred meter Aperture Spherical Telescope (FAST) started in 2019 September 24 and 2020 October 5, but these timing data were not used by Guo et al. (2021b). However, the latter authors did use FAST data for a detailed study of the emission properties of PSR J2222−0137. In this work, we also extend the existing data by simulated data assuming the same timing properties of all of these telescopes to simulate how the timing parameters for this system will improve in the near future (see Section 5).

4.3. Mass-mass diagrams in DEF gravity

The illustrative and straightforward way to explore if a given gravity theory agrees with binary pulsar observational data is to calculate mass-mass diagrams. As mentioned in Section 3.4, firstly, one measures values of PK parameters with their uncertainties by fitting the phenomenological binary model DD to binary pulsar data. Then the observed PK values can be compared with their theoretical predictions of a specific gravity theory. The PK parameters from Eq. (20) depend on the mass of the pulsar ($m_{\rm p}$) and the mass of the companion ($m_{\rm c}$) (see Appendix B). For

PSR J2222−0137 we use the measured PK parameters from Guo et al. (2021b).

To illustrate how the tests are performed, we select two points in DEF gravity parameter space near the scalarisation region with large negative β_0 and calculate mass-mass diagrams for them. The test is sensitive to the predicted dipolar contribution to $\dot{P}_\mathrm{b}$, which rises dramatically in the region of spontaneous scalarisation. The first point with $\alpha_0 = -10^{-4}, \beta_0 = -4.3$ does not predict a strong enough dipolar contribution and passes the test within a 1σ limit. The corresponding mass-mass diagram is presented in the left panel of Figure 1. In contrast, the second point with $\alpha_0 = -10^{-4}$ and a bit smaller $\beta_0 = -4.35$ is already excluded because of a rather strong scalarisation of the pulsar leading to significant dipolar GW damping (see the right panel of Figure 1). The $\dot{P}_\mathrm{b}$ curve nicely shows that a significant enhancement in the scalarisation happens for a particular interval in the mass range defined by the EOS.

4.4. Various contributions to $\dot{P}_\mathrm{b}$

At this point we need to discuss the different contributions to the observed $\dot{P}_\mathrm{b}^\mathrm{obs}$ and their influence on our results. The observed orbital decay of the system consists of many terms

$$\dot{P}_\mathrm{b}^\mathrm{obs} = \dot{P}_\mathrm{b}^\mathrm{GW} + \dot{P}_\mathrm{b}^\mathrm{Gal} + \dot{P}_\mathrm{b}^\mathrm{Shk} + \dot{P}_\mathrm{b}^\mathrm{Tid} + \dot{P}_\mathrm{b}^{\dot{M}} + \dot{P}_\mathrm{b}^{\dot{G}}\,, \tag{23}$$

where the first term $\dot{P}_\mathrm{b}^\mathrm{GW}$ is due to GW damping and can include dipolar and monopolar terms in DEF gravity, besides the general quadrupolar prediction of GR. The full expressions of different GW contributions are presented in Appendix (B.9). The next two terms are of kinematic origin: the Shklovskii effect ($\dot{P}_\mathrm{b}^\mathrm{Shk}$) and the Galactic contribution ($\dot{P}_\mathrm{b}^\mathrm{Gal}$). They are the result of a time-varying Doppler factor D due to an (apparent) radial acceleration between the pulsar binary and the Solar System (Damour & Taylor 1991). The last three terms come from tidal effects, mass loss in the system, and a possible temporal variation of the gravitational constant G.

We are mainly interested in measuring the GW emission term ($\dot{P}_\mathrm{b}^\mathrm{GW}$) and comparing it with the prediction of DEF gravity. The most significant additional effects in PSR J2222−0137 come from kinematic contributions $\dot{P}_\mathrm{b}^\mathrm{Gal}$ and $\dot{P}_\mathrm{b}^\mathrm{Shk}$. These two effects arise beyond the binary system and can be combined in the overall external contribution

$$\dot{P}_\mathrm{b}^\mathrm{ext} = \dot{P}_\mathrm{b}^\mathrm{Gal} + \dot{P}_\mathrm{b}^\mathrm{Shk}\,. \tag{24}$$

The last three terms in Eq. (23) are parts of the internal contribution

$$\dot{P}_\mathrm{b}^\mathrm{int} = \dot{P}_\mathrm{b}^\mathrm{GW} + \dot{P}_\mathrm{b}^\mathrm{Tid} + \dot{P}_\mathrm{b}^{\dot{M}} + \dot{P}_\mathrm{b}^{\dot{G}}\,, \tag{25}$$

and can be neglected for PSR J2222−0137. Thus the internal contribution has only one significant term left, the GW term. For the discussion about possible account of $\dot{P}_\mathrm{b}^{\dot{G}}$ we refer the reader to Section 8. Within the DDSTG model, the parameter XPBDOT in TEMPO is used for treating both external and internal effects $\dot{P}_\mathrm{b}^\mathrm{ext} + \dot{P}_\mathrm{b}^\mathrm{int} - \dot{P}_\mathrm{b}^\mathrm{GW}$ simultaneously subtracting the GW term. In our case XPBDOT accounts for only external Shklovskii and Galactic effects.

There is an extensive analysis of the external terms for PSR J2222−0137 by Guo et al. (2021b) and their determined values are: $\dot{P}_\mathrm{b}^\mathrm{Gal} = -0.0142(13) \times 10^{-12}$ s s^{-1} and $\dot{P}_\mathrm{b}^\mathrm{Shk} = 0.2794(12) \times 10^{-12}$ s s^{-1}. These values correspond to the external variation of the observed orbital period of

$$\dot{P}_\mathrm{b}^\mathrm{ext} = 0.2652(18) \times 10^{-12}\ \mathrm{s\,s^{-1}}\,, \tag{26}$$

which is consistent within 2σ with the total observed value

$$\dot{P}_\mathrm{b}^\mathrm{obs} = 0.2509(76) \times 10^{-12}\ \mathrm{s\,s^{-1}}\,, \tag{27}$$

leaving the internal contribution $\dot{P}_\mathrm{b}^\mathrm{int} = \dot{P}_\mathrm{b}^\mathrm{obs} - \dot{P}_\mathrm{b}^\mathrm{ext} = -0.0143(78) \times 10^{-12}$ s s^{-1} consistent with the GR prediction for quadrupolar GW emission $\dot{P}_\mathrm{b}^\mathrm{GR} = -0.00809(5) \times 10^{-12}$ s s^{-1} (Guo et al. 2021b).

According to Damour & Taylor (1991), Nice & Taylor (1995), and Lazaridis et al. (2009), the Galactic differential acceleration may be analytically approximated with the expression

$$\frac{\dot{P}_\mathrm{b}^\mathrm{Gal}}{P_\mathrm{b}} = -\frac{K_z |\sin b|}{c} - \frac{\Theta_0^2}{cR_0}\left(\cos l + \frac{\beta}{\beta^2 + \sin^2 l}\right)\cos b\,, \tag{28}$$

where l is Galactic longitude, b the Galactic latitude and $\beta = (d/R_0)\cos b - \cos l$. The quantity K_z is the vertical component of the Galactic acceleration, which for Galactic heights $z \equiv |d \sin b| \leq 1.5$ kpc can be approximated with sufficient accuracy by

$$K_z(10^{-9}\ \mathrm{cm\,s^{-2}}) \simeq 2.27 z_\mathrm{kpc} + 3.68(1 - e^{-4.31 z_\mathrm{kpc}})\,, \tag{29}$$

where $z_\mathrm{kpc} \equiv z(\mathrm{kpc})$ (Holmberg & Flynn 2004; Lazaridis et al. 2009). From Gravity Collaboration et al. (2021) we can take a value for the Sun's Galactocentric distance $R_0 = 8275 \pm 9 \pm 33$ pc. The Galactic circular velocity at the location of the Sun (Θ_0) is taken to be 240.5(41) km/s (see Guo et al. 2021b, and references therein).

The Shklovskii contribution (Shklovskii 1970) can be calculated using

$$\dot{P}_\mathrm{b}^\mathrm{Shk} = \frac{(\mu_\alpha^2 + \mu_\delta^2)\, d}{c} P_\mathrm{b}\,, \tag{30}$$

where μ_α and μ_δ are the proper motion in Right Ascension (RA) and Declination, respectively, and d is the distance to the pulsar. The astrometric values and uncertainties for PSR J2222−0137 are taken from Guo et al. (2021b). For PSR J2222−0137, the uncertainty in $\dot{P}_\mathrm{b}^\mathrm{ext}$ is small compared to the precision of the $\dot{P}_\mathrm{b}$ measurement. The uncertainty of $\dot{P}_\mathrm{b}^\mathrm{ext}$ in our case can be neglected and therefore we can provide the fixed XPBDOT parameter in TEMPO.

4.5. Results of applying DDSTG

Our main goal is to obtain limits on DEF gravity parameters $\{\alpha_0, \beta_0\}$ by applying the DDSTG model. TEMPO allows to calculate a χ^2 value for every particularly selected pair of values (α_0, β_0). Therefore we obtain χ^2 values for a grid of parameters and compare them to each other. For straightforward comparison we subtract the minimum χ^2_min over the $\{\alpha_0, \beta_0\}$ grid from calculated χ^2. The location of the minimum χ^2_min is statistically in agreement with GR ($\alpha_0 = 0, \beta_0 = 0$). The shifted quantity $\Delta\chi^2 = \chi^2 - \chi^2_\mathrm{min}$ has a $\chi^2(\mathrm{d.o.f.} = 2)$ distribution with 2 degrees of freedom. Finally we construct contours of a fixed $\Delta\chi^2$ value corresponding to desired confidence levels. In this paper we adhere to 90% confidence level limits with $\Delta\chi^2 \simeq 4.6$.

During each run, TEMPO fits spin parameters, astrometric parameters, Keplerian parameters, two masses, and other parameters of interest, e.g. $\dot{x}$. A value of the external contribution to the rate of the orbital period change ($\dot{P}_\mathrm{b}^\mathrm{ext}$) is fixed and selected, so that it fully accounts for Shklovskii effect and the Galactic $\dot{P}_\mathrm{b}$ contributions (Shklovskii 1970; Brumberg et al. 1975; Damour

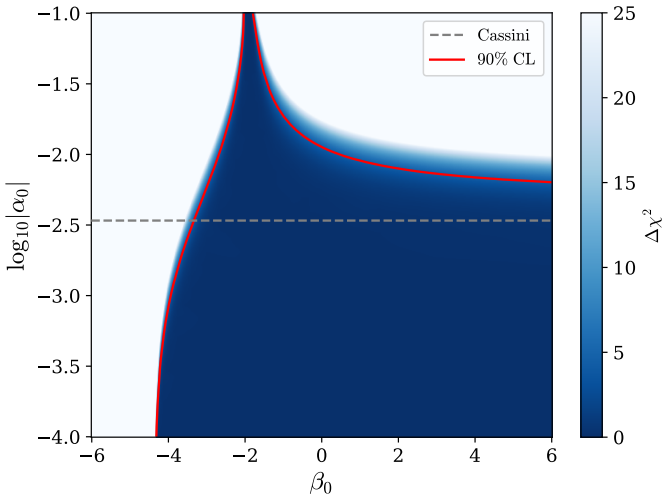

Fig. 2. $\Delta\chi^2$ map in DEF gravity parameter space for PSR J2222−0137. The test is performed by applying the DDSTG model to the timing data of Guo et al. (2021b) and the assuming rather stiff MPA1 EOS. The red line corresponds to 90% CL limit ($\Delta\chi^2 \simeq 4.6$), the area above the grey line is restricted by Cassini mission. GR with $\alpha_0 = 0, \beta_0 = 0$ lies beyond the plotted domain in the blue region at the bottom at the infinity.

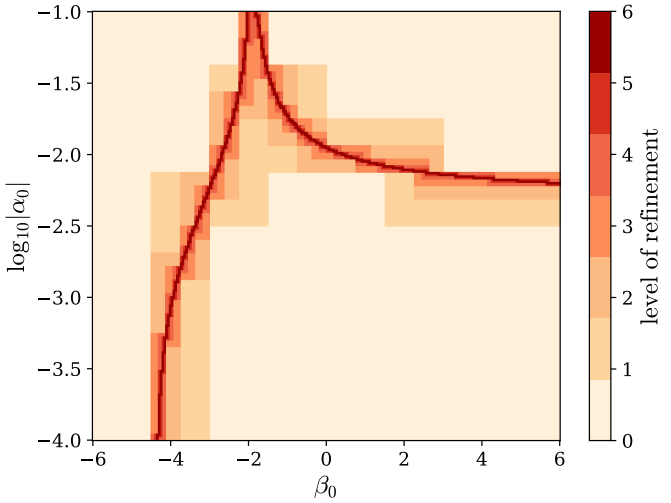

Fig. 3. Map of the refinement level in DEF parameter space. The test is the same as in Figure 2. Areas in the parameter space with a higher refinement level have an exponentially growing resolution. The adaptive refinement procedure resolves the contour of 90% CL limit and saves computational time dramatically.

& Taylor 1992). The resulting $\Delta\chi^2$ map in $\{\alpha_0, \beta_0\}$ space for PSR J2222−0137 is presented in Figure 2. The limit on DEF parameters is placed by a contour of 90% confidence level limit of χ^2(d.o.f. = 2) statistics.

Generally, the uncertainty of $\dot{P}_{\rm b}^{\rm ext}$ can be important for other systems where it is not well constrained. In this case, the DDSTG model allows a complete description with account for all the uncertainty due to external effects $\dot{P}_{\rm b}^{\rm ext}$. First we have to assume a prior distribution for the $\dot{P}_{\rm b}^{\rm ext}$ value. Then we have to calculate the χ^2 value for a 3-dimensional map with $\{\alpha_0, \beta_0, \dot{P}_{\rm b}^{\rm ext}\}$ as parameters of the three axes. Finally, we marginalise the probability density for the $\dot{P}_{\rm b}^{\rm ext}$ axis using Bayes' theorem and obtain the corrected 2-dimensional map of $\chi^2_{\rm corr}$. The details of the procedure are presented in Appendix E.

Calculating an extensive grid in a 2-dimensional parameter space with a lot of points (e.g. ∼ 500) for each axis to obtain a finely resolved contour of the desired $\Delta\chi^2$ value is too computationally demanding. In this work, we use an adaptive mesh refinement technique to trace the location of the desired contour. We start from the sparse grid with 9×9 points in the $\{\alpha_0, \beta_0\}$ space. Then, the algorithm resolves all the cells that can have the contour line inside them. The algorithm repeats the refinement of important cells until we obtain the desired curve fineness.

For a $N \times N$ grid, the naive approach utilises $O(N^2)$ iterations, whereas adaptive mesh refinement has only $O(N \log_2 N)$ complexity. For the present work we use the refinement level of 6, resulting in the final grid with 513×513 points. We need such a large resolution in the parameter space because of the "horn" feature at large α_0 values near $\beta_0 \simeq -2$. A simple analysis shows that adaptive refinement requires to calculate 56 times fewer points to resolve a single contour for a grid with 513×513 points. In Figure 3 we present an adaptive refinement map corresponding to the search of a contour from Figure 2. A high level of refinement is performed only along the contour of 90% CL limit. In Appendix D one can also find the mass-mass diagram showing what happens in the region of the "horn" in terms of PK parameters.

4.6. Comparison with the PK method

In this section we compare the constraining power of the newly developed approach of this paper with that of existing procedures. For this reason we perform the test with the traditional "PK method" based on the PK parameters from the timing data. The corresponding PK parameters are measured by means of fitting the DD model (Damour & Deruelle 1986) to the same timing data. Then for each specific choice of the theory parameters $\{\alpha_0, \beta_0\}$ we fit two masses $m_{\rm p}$ and $m_{\rm c}$ to minimise the χ^2 value. The χ^2 is calculated by comparison of the observed PK parameters $p_i^{\rm obs}$ and predicted values $p_i^{\rm theory}$ from the theory

$$\chi^2(p_i^{\rm obs}; m_{\rm p}, m_{\rm c}) = \sum_i \left(\sigma_{p_i}^{\rm obs}\right)^{-2} \left(p_i^{\rm theory}(m_{\rm p}, m_{\rm c}) - p_i^{\rm obs}\right)^2 , \qquad (31)$$

where $\sigma_{p_i}^{\rm obs}$ is the standard deviation of the i-th measured PK parameter. Finally, we calculate the grid of χ^2 values over the desired $\{\alpha_0, \beta_0\}$ space with the same settings as for the DDSTG approach and shift χ^2 values by its minimum $\chi^2_{\rm min}$. The detailed explanation of this common "PK method" can be found in Damour & Esposito-Farèse (1998). For both methods the minimum $\chi^2_{\rm min}$ is in statistical agreement with the GR value $\chi^2_{\rm GR}$.

Figure 4 shows the comparison between the two methods. Each point on the plot presents a particular pair of $\{\alpha_0, \beta_0\}$ parameters. The analysis shows that, for PSR J2222−0137, the DDSTG model produces higher or equal values of $\Delta\chi^2$ compared to the traditional "PK method". Despite the absence of any strong correlations between the PK parameters in PSR J2222−0137, the new approach produces slightly more restrictive results for the area with negative β_0. For certain areas in $\{\alpha_0, \beta_0\}$ space the difference in the shifted $\Delta\chi^2 = \chi^2 - \chi^2_{\rm min}$ values becomes statistically significant when we calculate contours of 90% confidence level limit ($\Delta\chi^2 \simeq 4.6$).

5. Predictions for PSR J2222−0137

Our next step is to estimate what enhancement in limits we can expect with future observations of PSR J2222−0137. For this

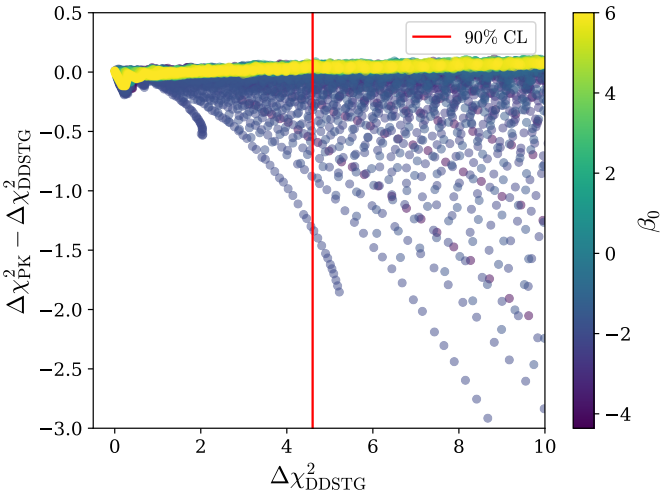

Fig. 4. Comparison in the constraining power between the DDSTG model and the method based on measured PK parameters with the DD model. Both methods calculate χ^2 values for a grid in $\{\alpha_0, \beta_0\}$ space, each point corresponds to a unique theory. β_0 values are presented by the colour, while α_0 values cover the $[-10^{-1}, -10^{-4}]$ range. Red vertical line corresponds to the 90% CL limit, all points to the left are allowed by the test.

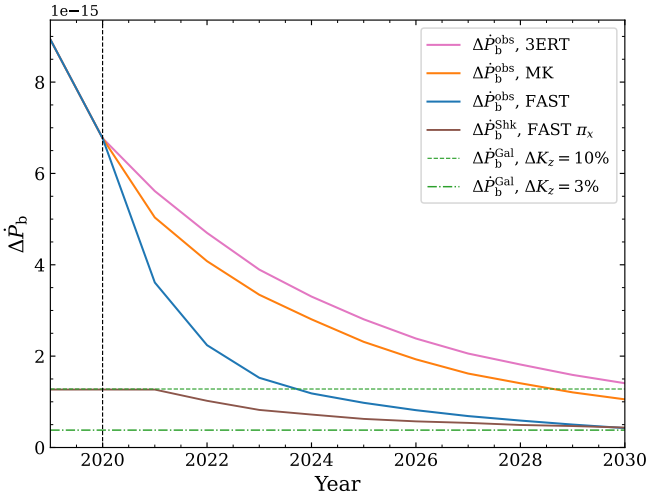

Fig. 5. Comparison of different contributions in the uncertainty of $\dot{P}_{\rm b}$ for simulated data from 2021 to 2030. The pink, orange and blue lines show the uncertainty of $\dot{P}_{\rm b}$ using the simulated data from 3ERT (EFF, NC, LT), MeerKAT and FAST, respectively. The brown line indicates the uncertainty of $\dot{P}_{\rm b}^{\rm Shk}$ when using the timing parallax (π_x) measured from simulated FAST data. The green lines indicate the uncertainties of $\dot{P}_{\rm b}^{\rm Gal}$ when assuming 10% (dashed) and 3% (dash-dotted) uncertainties in the vertical component of Galactic acceleration K_z.

Table 1. Parameters of telescopes used in simulations.

Telescope	$\oslash_{\rm eff}$ (m)	Bandwidth (MHz)	$\sigma_{\rm TOA}$ (μs)
Effelsberg	100	200/400	2.67
Nançay	94	512	2.02
Lovell	76	400	3.66
MeerKAT	108	856	0.84
FAST	300	500	0.12

Notes. Effective diameter of telescopes, observing bandwidth, and TOA uncertainties of PSR J2222−0137 used in the simulations. All information is based on the L-band data from real observations, and is scaled to 15-min integration over the full bandwidth.

purpose we simulate fake TOAs for a set of radio observatories, assuming realistic timing precision estimated from real timing data.

5.1. Simulated data-sets for FAST, MeerKAT and 3ERT

The PSR J2222−0137 timing data used up to this point are described in Section 4.2. We will now describe our simulations, which show what we might be able to achieve in the near and foreseeable future with timing from this system.

We simulate TOAs spanning 10 years from 2021 to 2030 based on the current precision of the TOAs obtained with the 3ERT telescopes, as well as the TOA precisions from ongoing observations from MeerKAT and FAST. These simulations are conservative since they assume that there will be no improvement in the existing capabilities at these telescopes.

For TOAs from FAST, the radiometer noise reduces significantly thanks to its large collecting area, while the jitter noise becomes the primary limitation of timing precision. We find, however, that increasing the integration time to 15 min can largely reduce the jitter noise and eliminate its contribution to the timing precision (as it scales with the number of averaged pulses (N_p) as $\sigma_{\rm J} \propto 1/\sqrt{N_p}$ (Lorimer & Kramer 2004). Therefore, the median TOA uncertainty from 15-min TOAs are adopted in the simulation.

Table 1 lists the telescopes assumed in our simulation, with the information on their effective diameter ($\oslash_{\rm eff}$), observing bandwidth, and TOA uncertainties at L-band. All TOA uncertainties are scaled to an integration time of 15 min over the full bandwidth. For each telescope, we assume one full orbit observation (~60 hours) per year, and split the observations into a monthly cadence, i.e. 5 hours per month[8], to allow a good estimation of timing parallax (which requires a good coverage of Earth's orbit). This is important for the estimation of uncertainties in the external $\dot{P}_{\rm b}$ contributions shown in the next section.

The simulations are performed using the program developed in Hu et al. (2020). First, we simulate TOAs based on the above assumptions, and add the TOAs from Effelsberg, Nançay, and Lovell telescopes together to be compared with MeerKAT and FAST. For 3ERT, the simulated TOAs are combined with the existing TOAs in Guo et al. (2021b). We then adjust the TOAs to perfectly match the timing parameters measured in Guo et al. (2021b), and add a Gaussian white noise to each TOA based on its $\sigma_{\rm TOA}$. Finally, we fit for timing parameters and obtain their uncertainties, among which $\dot{P}_{\rm b}$ and timing parallax are of most important here. The whole process is done with the TEMPO DDSTG model.

5.2. Contributions to the uncertainty of $\dot{P}_{\rm b}$

The predicted uncertainties of $\dot{P}_{\rm b}$ are shown in Figure 5, where the pink, orange, and blue lines show the improvement in time

[8] This may be unrealistic as telescopes may be oversubscribed. However, we found, e.g. for FAST, that with a more realistic assumption of 30 minutes per month, the uncertainty in the observed $\dot{P}_{\rm b}$ is only 5% worse than observing 5 hours per month after 10-yr timing.

with the simulated data from 3ERT, MeerKAT, and FAST, respectively. As discussed in Section 4.4, we also need to account for uncertainties from external effects, $\dot{P}_{\rm b}^{\rm ext}$. They are also expected to become more precise in the future because of anticipated improvements in the model for the Galactic gravitational potential, distance, and proper motion from future observations. Correspondingly improved values for $\dot{P}_{\rm b}^{\rm Gal}$ and $\dot{P}_{\rm b}^{\rm Shk}$ may then be estimated using Eqs. (28) and (30). For the Shklovskii effect, we find that it is mostly limited by the uncertainty in the distance, which comes from VLBI parallax or timing parallax measurement, whichever is better. With the simulated FAST data, the measurements of timing parallax and proper motion improve quickly with time. In particular, the uncertainty of timing parallax will soon surpass the VLBI parallax and hence improve the distance measurement. The corresponding uncertainty in $\dot{P}_{\rm b}^{\rm Shk}$ will decrease with time as shown by the brown line in Figure 5. This line is below the predicted uncertainties from observed $\dot{P}_{\rm b}$ most of the time, except at the very end of the simulation when compared to $\Delta\dot{P}_{\rm b}^{\rm obs}$ with FAST (blue line). In addition, future VLBI parallax measurements will likely be improved so that Shklovskii effect will not be a limiting factor for $\dot{P}_{\rm b}$.

As for the contribution from the Galactic acceleration, a typical uncertainty in its vertical component (ΔK_z) is about 10%, which contributes the most in $\Delta\dot{P}_{\rm b}^{\rm Gal}$, shown as the green dashed line in Figure 5. With FAST, $\dot{P}_{\rm b}$ will then be limited by ΔK_z from 2024 onwards, if there is no improvement for this quantity. In fact, we find that ΔK_z needs to be improved to $\lesssim 3\%$ (see the green dash-dotted line) to not limit the precision of $\dot{P}_{\rm b}$ before 2030. The uncertainties in the Galactic potential do not limit the precision in this case. For the scope of further analysis, we assume that with future observations on pulsar timing, VLBI parallax, and Galactic acceleration, the precision of $\dot{P}_{\rm b}$ will not be limited by Shklovskii and Galactic effects. For Shklovskii contribution it is a reasonable assumption at least up to 2030. We also expect our knowledge about the Galactic potential to improve in the future especially in the proximity of the Solar System, thus we assume the improvement of ΔK_z for the selected very close pulsar to be 3%.

5.3. Potential future constraints on DEF gravity from PSR J2222–0137

We apply the same techniques as described in Section 4 including the adaptive mesh refinement for contours. The map of $\Delta\chi^2$ for a combined simulated data is presented in Figure 6. By 2030, we can expect a significant improvement in the limits for large positive β_0. This region is susceptible to dipolar gravitational emission. The significant improvement in $\dot{P}_{\rm b}$ measurement pushes the limit below the Cassini limit.

In Figure 6 we also present the comparison of constraining power for different observatories. The tightest constraints may be obtained for the combination of all three observatories. However, the precision of FAST is high enough to be significantly constraining on its own.

6. Simulations for PSR-BH systems

As a further application of the new timing model, we investigate what limits on DEF gravity we can obtain from a pulsar-black hole (PSR-BH) system. As mentioned above, our DDSTG implementation already allows to specify a BH as a companion, even though such a system has so far not been found. We apply

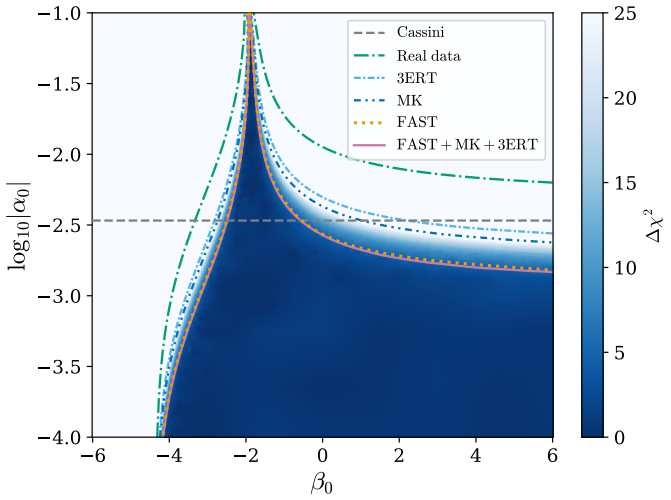

Fig. 6. $\Delta\chi^2$ map for PSR J2222−0137 from simulated data (2021–2030) combining different observatories and using MPA1 EOS. Assumed 1 orbit per year for FAST, MeerKAT, and 3ERT (EFF, NC, LT) based on their observation precision, appending to the existing data-set (Guo et al. 2021b). Each contour corresponds to 90% CL limits on DEF gravity parameters from different data-sets, grey line depicts the limit from the Cassini mission.

Table 2. Properties of pulsar-black hole systems taken for investigation.

Parameters	Values
RA (α, J2000)	21:20:01.2
DEC (δ, J2000)	12:10:38.2
DM (pc cm^{-3})	67.1
Pulsar mass ($m_{\rm p}$, $M_\odot$)	1.4
BH mass ($m_{\rm BH}$, $M_\odot$)	10.0
Eccentricity (e)	0.6
Orbital period ($P_{\rm b}$, d)	{1/3, 1, 3}
TOA uncertainty (μs)	{1, 10}
Number of TOAs	3144

the same technique used in Sections 4 and 5 to synthetic TOAs for three different hypothetical PSR-BH systems.

6.1. Simulated FAST data-sets

To investigate possible limits on DEF gravity from PSR-BH systems, we select presumed realistic parameters for simulating fake TOAs. These systems are assumed to comprise a 1.4 $M_\odot$ pulsar and a 10.0 $M_\odot$ BH in a highly eccentric orbit ($e = 0.6$). As PSR-BH systems are more likely to reside in GCs (see the discussion in Section 6.4 and references therein), we assume that our hypothetical systems are located in the GC M15 and take the position (right ascension "RA" and declination "DEC") and dispersion measure (DM) of PSR B2127+11C (M15C) for our simulations. To investigate how the limits on DEF gravity depend on the orbital period, we consider three cases with orbital periods of 3 d, 1 d, and 8 h, respectively. The selected parameters for PSR-BH systems are presented in Table 2.

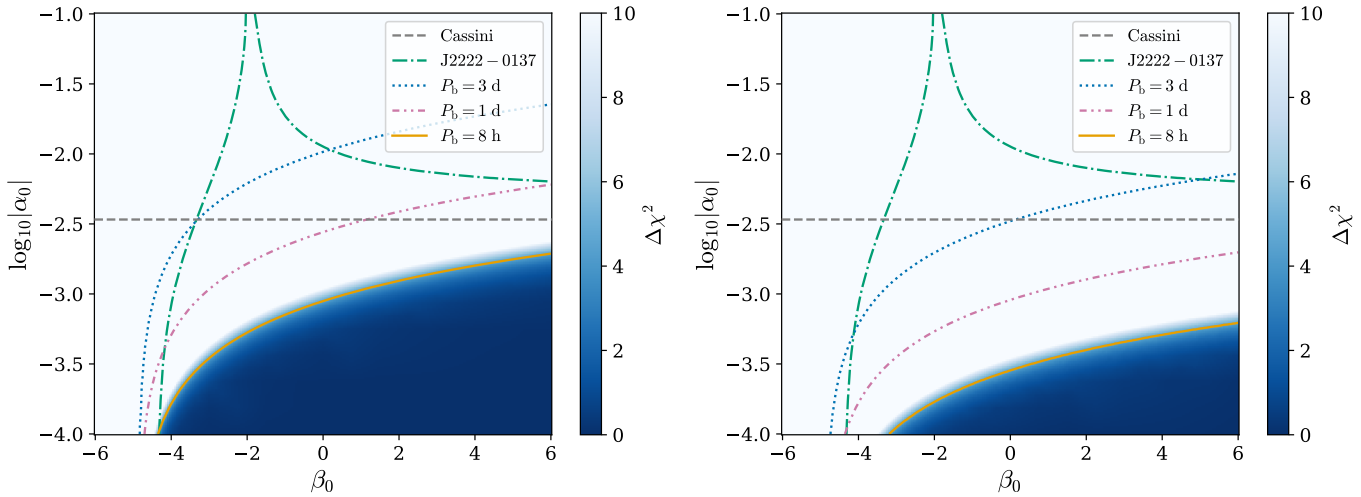

Fig. 7. $\Delta\chi^2$ map in the DEF gravity parameter space from the simulated 5-yr timing data for three different PSR-BH systems. The left panel corresponds to 10 μs TOA uncertainty, the right panel to 1 μs. Solid lines show the 90% CL limits for PSR-BH systems with different orbital periods: 3 d, 1 d and 8 h. The grey dashed line depicts the limit from the Cassini mission and green dash-dotted line is the current limit from PSR J2222−0137 discussed in Sec. 4 (see Fig. 2).

We simulate data-sets with two different TOA uncertainties (for 15-min integration time): moderate 10 μs (which is typical for pulsars in GCs), and precise 1 μs. Taking these two, by an order of magnitude different TOA uncertainties helps to explore the dependence of the DEF gravity test on the TOA precision. We effectively assume a recycled millisecond pulsar, because they in general produce a better timing precision. We assume 6 hours of timing observation on these systems every two weeks, each session starts at a random orbital phase. All simulations cover a time span of 5 years and have the same number of TOAs ($n_{\rm TOA} = 3144$).

6.2. How does a BH companion change the test of DEF gravity?

Binary systems consisting of a pulsar and a white dwarf (PSR-WD) are particularly interesting for constraining STG theories due to their high asymmetry in compactness ($\alpha_{\rm WD} \simeq \alpha_0$). The theory predicts a higher rate of orbital energy loss due to dipolar radiation from such asymmetric systems (Will 1993; Damour & Esposito-Farèse 1996). However, generally, PSR-BH systems are expected to be even more asymmetric up to a certain positive β_0, as was pointed out by Damour & Esposito-Farèse (1998). As a result of the no-scalar-hair theorem to BHs in STG one has (Hawking 1972; Damour & Esposito-Farèse 1992a)

$$\alpha_{\rm BH} = 0, \quad \beta_{\rm BH} = 0\,. \tag{32}$$

This approximation is only valid for stationary BHs with an asymptotically flat spacetime and an asymptotically constant scalar field (Berti et al. 2013), which is not true anymore in the presence of a compact scalarised companion. However, a justification that it is still an excellent approximation can be found in Liu et al. (2014). The pulsar orbiting in an eccentric orbit will eventually induce a time-dependent scalar field at the location of the BH. This scalar field results in an induced effective scalar charge ($\alpha_{\rm BH}^{\rm induced}$) which, however, is totally negligible ($\lesssim 8 \times 10^{-14}\,\alpha_{\rm p}$; cf. Eq. (50) in Liu et al. 2014).

The absence of scalar charges for the BH results in simplified relations of the PK parameters. The main consequence of a BH presence is that all PK parameters except $\dot{P}_{\rm b}$ are identical to their GR expressions with an appropriate rescaling of the masses. In the GW damping sector, all the multipoles, e.g., monopolar, dipolar and quadrupolar modes, are still present. Thus PSR-BH systems are susceptible but only to the test of GW damping via $\dot{P}_{\rm b}$ (Damour & Esposito-Farèse 1992a; Mirshekari & Will 2013; Liu et al. 2014).

Table 3. Orbital period properties of simulated PSR-BH systems.

$P_{\rm b}$ (d)	$\dot{P}_{\rm b}^{\rm GR}$ (10^{-12} s s^{-1})	$\Delta\dot{P}_{\rm b}$, 10 μs	$\Delta\dot{P}_{\rm b}$, 1 μs
3	−0.22220	0.08031	0.00827
1	−1.38661	0.01723	0.00185
1/3	−8.65279	0.00532	0.00055

Notes. The rate of the orbital period change in GR ($\dot{P}_{\rm b}^{\rm GR}$) for selected PSR-BH systems and corresponding uncertainty in $\dot{P}_{\rm b}$ measurement for three different orbital periods and two TOA uncertainties. The values of $\dot{P}_{\rm b,GR}$ and $\Delta\dot{P}_{\rm b}$ are given in 10^{-12} s s^{-1}.

6.3. Results

The limits obtained from the DDSTG model for the simulated PSR-BH systems are shown in Figure 7. For the tests presented here we do not include any potential uncertainty in the observed $\dot{P}_{\rm b}^{\rm obs}$ value due to the external effects. The restrictive power of the test increases for more relativistic systems with shorter orbital periods. To place new limits on DEF gravity with a moderate TOA precision of 10 μs the orbital period should be a fraction of a day.

Another way to improve the restrictive power is to increase the precision of the TOAs (compare left and right panels of Figure 7). The obtained limits strongly depend on the accuracy of $\dot{P}_{\rm b}$ measurement as most of the deviations from GR come from the predicted dipolar GW emission. Table 3 shows the predicted GR values of $\dot{P}_{\rm b}$ and compares them to the corresponding $\Delta\dot{P}_{\rm b}$ uncertainties. The lower uncertainty and the higher the predicted value the better the test.

We expect a dramatic improvement of limits on DEF gravity from relativistic PSR-BH system. Due to higher asymmetry, the test is extremely sensitive to the precision of $\dot{P}_{\rm b}$ measurement. To answer the possibility of obtaining accurate enough TOAs, we have to argue where we can find such a system.

6.4. Pulsar-black hole systems origin

A binary pulsar system with a stellar-mass BH may originate from several different evolutionary scenarios. The first way is a standard evolution of a massive binary system (Voss & Tauris 2003). It results in a PSR-BH system with a young slow spin-period ($\sim 0.1-1$ s) pulsar and a wide, eccentric orbit. The second path is a reversal mechanism (Sipior et al. 2004) taking place under a specific set of circumstances. The pulsar is formed first and later spun-up by accretion during the red-giant phase of the companion (Pfahl et al. 2005), later becomes a BH. This is similar to the origin of PSR J1141−6545, a system where a massive WD star formed before a more massive NS (Tauris & Sennels 2000). The reversal mechanism may give a more desirable result of a recycled pulsar in a system with a BH, because recycled pulsars have generally more precise timing and a more stable rotation than the slow "normal" pulsars (Verbiest et al. 2009).

Moreover, the third possible way to form a PSR-BH system is a multiple body encounter, happening in regions of high stellar density, e.g., GCs and the Galactic Centre region (Verbiest et al. 2009; Clausen et al. 2014). Such encounters are the reason why there are $\sim 10^3$ times more low-mass X-ray binaries (LMXBs) per unit stellar mass in GCs than in the Galactic disk (Clark 1975), which results in a similarly enhanced proportion of millisecond pulsars (MSPs). In these encounters, an old, inactive NS approaches a main sequence (MS) binary so closely that a chaotic interaction ensues. The most likely result of such an interaction is that the two most massive objects (in this case the old, recycled NS and the more massive MS star) will form a more compact binary system, with the lighter MS star component being ejected at high velocity (see review by Phinney 1992). That MS will evolve, fill its Roche lobe, and start transferring matter onto the NS, which is spun up in the process, this is the aforementioned LMXB stage.

If left undisturbed, many of these then evolve into binary MSP systems. A consequence of this is that GCs not only have many MSPs, but that the number of MSPs in each cluster appears to be roughly proportional to its rate of stellar encounters (Γ) (Verbunt & Hut 1987).

However, in some GCs - especially those with collapsed cores - stellar densities are so high that only few binaries evolve without being disturbed; these GCs have a large interaction rate *per binary* ($\gamma_{\rm GC}$) (Verbunt & Freire 2014). This means that, even after being recycled, an MSP has a high probability of undergoing further ("secondary") exchanges.

In such exchanges, an incoming massive star interacts chaotically with the components of either a LMXB or a MSP binary. Again, the least massive object is the most likely to be ejected, in this case that will be the low-mass star that recycled (or was still recycling) the NS. A new binary will form, consisting of the NS and the intruding massive star. If the latter is degenerate, then the system will not undergo accretion and the orbital circularisation that comes with it, but will keep the orbital eccentricity it acquired after formation.

Several such obvious products of secondary exchange encounters have been found in GCs, invariably with a large $\gamma_{\rm GC}$: PSR B2127+11C, in the core-collapsed M15 GC (Prince et al. 1991; Jacoby et al. 2006), PSR J0514−4002A, in NGC 1851 (Freire et al. 2004; Ridolfi et al. 2019) (recently two additional such systems, D and E, were found in the same GC, see Ridolfi et al. 2022), PSR J1807−2500B, in the core-collapsed NGC 6544 (Lynch et al. 2012), PSR J835−3259A, in the core-collapsed NGC 6652 (DeCesar et al. 2015) and PSR J1823−3021G, in the core-collapsed NGC 6624 (Ridolfi et al. 2021). These discoveries suggest (but by no means assure us) of the possibility that similar secondary exchange encounters might produce MSP binaries with even more massive companions, such as BHs. As for the massive MSP binaries above, such MSP-BH systems would be preferentially produced in the GCs with large $\gamma_{\rm GC}$; this is one of the reasons why they are targeted by the MeerKAT TRAPUM survey (Ridolfi et al. 2021).

These secondary exchange products are that their orbital periods vary between 8 h in the case of B2127+11C and 18.8 d in the case of PSR J0514−4002A, their orbital eccentricities are between 0.38 and 0.90. Thus the simulated PSR-PH systems listed in Table 2 have realistic orbital periods and eccentricities.

6.5. Influence of a globular cluster origin

For the pulsars observed in GCs, the derivatives of the spin period, P, and in the case of binary pulsars, the derivative of the orbital period, $\dot{P}_{\rm b}$ are contaminated (and in most cases dominated) by the line-of-sight component of the acceleration of the pulsar (or binary) in the gravitational potential of the GC ($a_{\rm GC}$); this enters Eq. (23) as an additional term that is similar to $\dot{P}_{\rm b}^{\rm Gal}$:

$$\dot{P}_{\rm b}^{\rm GC} = \frac{a_{\rm GC}}{c} P_{\rm b} \,. \tag{33}$$

For pulsars in GCs, the only radiative test done to date was with PSR B2127+11C (Jacoby et al. 2006). The orbital decay observed in this system is $-3.95 \pm 0.13 \times 10^{-12}\,{\rm s\,s^{-1}}$, which is within $\sim 3\%$ of the predicted value. That test, however, is limited by the fact that the maximum value for $|a_{\rm GC}/c| \sim 6 \times 10^{-18}\,{\rm s^{-1}}$ (Phinney 1993), i.e., in this case the maximum value for $|\dot{P}_{\rm b}^{\rm GC}| \sim 0.17 \times 10^{-12}\,{\rm s\,s^{-1}}$. This is of the same order as their measurement precision, which means that this radiative test cannot be improved, unless one could measure the acceleration of the pulsar independently. The situation would be much worse if PSR B2127+11C were closer to the cluster centre, where accelerations are much larger. For instance, PSR B2127+11A, a couple of arcseconds from the centre, has $P = 0.1106$ s and $\dot{P} = -2.107 \times 10^{-17}$; this implies that $|a_{\rm GC}/c| > 1.9 \times 10^{-16}\,{\rm s^{-1}}$ and thus $|\dot{P}_{\rm b}^{\rm GC}| > 5.5 \times 10^{-12}\,{\rm s\,s^{-1}}$, a value larger than the orbital decay predicted by GR.

For the three PSR-BH systems in Table 3, the situation would be similar. If they were at the locations of PSR B2127+11C, their values of $P_{\rm b}$ would imply that the maximum values for $\dot{P}_{\rm b}^{\rm GC}$ would be 9, 3 and 1 times larger respectively, i.e., 1.53, 0.51 and $0.17 \times 10^{-12}\,{\rm s\,s^{-1}}$. This corresponds to, respectively, ~ 6.9, ~ 0.37 and 0.02 times the values of $\dot{P}_{\rm b}^{\rm GR}$ in Table 3. That means that, for the latter system, a $\sim$ 50-σ test of the radiative properties of a PSR-BH system would be possible. These numbers illustrate the immense advantage of an increasingly shorter $P_{\rm b}$, either for GW tests in GCs or in the Galaxy: on one hand, the $\dot{P}_{\rm b}^{\rm GR}$ increases with $P_{\rm b}^{-5/3}$, the "polluting" part $\dot{P}_{\rm b}^{\rm GC}$ decreases as $P_{\rm b}$. Thus, the significance of a particular GW test grows, everything else being identical, with $P_{\rm b}^{-8/3}$.

However, if the 8-h PSR-BH system is placed at the location of PSR B2127+11A, the test would lose its significance almost entirely. Fortunately, even in this case, we can get a firm upper limit for $|\dot{P}_{\rm b}^{\rm GR}|$; the reason is that we also measure the spin period

derivative. That is also affected by the acceleration in the cluster and by other terms, such as the Shklovskii effect. Adding the equations for $\dot{P}$ and $\dot{P}_\mathrm{b}$, we obtain:

$$\dot{P}_\mathrm{b}^\mathrm{GR} = \dot{P}_\mathrm{b}^\mathrm{obs} - P_\mathrm{b}\left(\frac{\dot{P}}{P}\right)^\mathrm{obs} + \frac{1}{2\tau_c}P_\mathrm{b}\,. \tag{34}$$

Note that all the terms on the right can be measured precisely, except for the characteristic age of the pulsar, τ_c, which cannot be measured independently. Therefore, the last term then quantifies the uncertainty of the test, which is, again, proportional to P_b, which implies that the significance of the test is again proportional to $P_\mathrm{b}^{-8/3}$.

However, that last term is necessarily positive. If we assume the pulsar is extremely old, then this term will be very small and we obtain, from the other two terms, a hard lower limit for $\dot{P}_\mathrm{b}^\mathrm{GR}$. Since the latter is negative, this represents a hard upper limit of its magnitude. This means that such a test could still, in principle, falsify GR. An upper limit on the last term can be obtained from the lowest likely value for τ_c; for most MSPs $\tau_c < 1\,\mathrm{Gyr}$. This means that, for the 8-h PSR-BH system, this unknown term would be at most $0.46 \times 10^{-12}\,\mathrm{s\,s^{-1}}$, implying a $\sim$ 20-σ test of GR. Thus, this test will be the more significant the larger τ_c is compared to the orbital decay timescale for the binary.

Despite such possible mitigation, it is clear that the location in a GC always degrades the quality of radiative tests. For the 8-h PSR-BH system discussed above, significances of 50 and 20 σ in the measurement of $\dot{P}_\mathrm{b}$ represent a significant degradation relative to the tests listed in Table 3, where for a 8-h PSR-BH system timed with 10μs the significance of the $\dot{P}_\mathrm{b}$ measurement is larger than 1600.

7. DDSTG and other gravity theories

The approach developed in this work is not restricted to DEF gravity. It can straightforwardly be extended to investigate a larger set of alternative gravity theories. Broadly speaking, every theory that maps to the DD phenomenological model (Damour & Deruelle 1986; Damour & Taylor 1992) can be put into the DDSTG framework with a new implementation of appropriate PK formulae. The DD model is a quasi-Keplerian solution in the first post-Newtonian approximation to the dynamics of a 2-body system within the modified Einstein-Infeld-Hoffmann (mEIH) framework (Damour & Taylor 1992; Will 1993, 2018b). The mEIH formalism covers a large set of fully-conservative gravity theories without the "Whitehead term" in the post-Newtonian limit. Later it was extended by Will (2018a) from fully conservative to semi-conservative theories of gravity. However, this extension requires additional terms in mEIH Lagrangian, which are not accounted for in the DD model.

The DDSTG model can be directly applied to a certain class of gravity theories without a modification of the PK parameter equations. For example, DEF gravity is a specific case of a massless mono-scalar tensor gravity theory with a particular expression of the conformal coupling $A(\varphi)$. DDSTG covers STG theories with any conformal coupling function depending on two arbitrary parameters $\{\alpha_0, \beta_0\}$ and a single massless scalar field. To work, the model only requires pre-calculated gravitational form-factors for the new coupling function. In case of a more complex coupling function depending on a higher number of parameters the TEMPO code needs to be adapted.

Recently, Mendes and Ortiz (MO, Mendes & Ortiz 2016) introduced an extension of DEF gravity. MO gravity is an example of a theory that can be easily incorporated into the DDSTG model. Its difference from DEF gravity is in the form of the conformal coupling

$$A(\varphi) = \left[\cosh\left(\sqrt{3}\beta_0\varphi\right)\right]^{1/(3\beta_0)}\,, \tag{35}$$

where β_0 is a free parameter. The second parameter α_0 is hidden in MO gravity to the scalar field at infinity. MO theory received attention in recent years and was originally introduced as an analytical approximation to a more fundamental theory, where the action includes quadratic terms of the scalar field coupled to curvature. The developed framework can therefore be straightforwardly extended to MO gravity without the change of the TEMPO implementation.

8. DDSTG and a time-varying gravitational constant

Another interesting extension of the DDSTG model—planned for a future release—is the inclusion of the effects of a temporal variation of the gravitational constant (G). A time-evolving asymptotic scalar field (φ_0) of a gravitating system, generally, leads to a temporal variation of the local gravitational constant. In DEF gravity, such a change of the Newtonian gravitational constant as measured in the Solar System reads

$$\frac{\dot{G}_\mathrm{Cav}}{G_\mathrm{Cav}} = 2\left(1 + \frac{\beta_0}{1+\alpha_0^2}\right)\alpha_0\dot{\varphi}_0 \tag{36}$$

(see e.g. Uzan 2011). Generally, one expects a temporal change in φ_0 to arise from the expansion of the universe and $\dot{\varphi}_0$ to result from a cosmological model based on DEF gravity (see e.g. Damour & Nordtvedt 1993). However, as part of a more agnostic approach, $\dot{\varphi}_0$ can be treated as an additional, independent timing parameter.

The main impact on the orbital motion of a binary system that arises from a time-varying gravitational constant is a secular change in the orbital period (Damour et al. 1988). For two weakly self-gravitating masses, one simply has $\dot{P}_\mathrm{b}^{\dot{G}}/P_\mathrm{b} = -2\dot{G}/G$. However, for binary pulsar systems, this simple expression needs to be extended by body-dependent contributions (Nordtvedt 1990, 1993). One then has

$$\frac{\dot{P}_\mathrm{b}^{\dot{G}}}{P_\mathrm{b}} = -2\left(\frac{\dot{G}_\mathrm{Cav}}{G_\mathrm{Cav}}\right)\mathcal{F}_{AB}\,, \tag{37}$$

where the factor $\mathcal{F}_{AB}$ accounts for all the corrections related to the strong gravitational fields of the pulsar and its companion, if the latter is also a NS. More specifically, following Nordtvedt (1993), $\mathcal{F}_{AB}$ accounts for a change in the body-dependent part in the effective gravitational constant G_{AB} as well as a change in the masses resulting directly from $\dot{\varphi}_0$.[9]

It has been demonstrated by Wex (2014) that, depending on the parameter space, pulsar mass and EOS, strong-field effects can considerably enhance the effect of a time-varying gravitational constant, i.e. $\mathcal{F}_{AB} \gg 1$. Consequently, accounting for $\dot{P}_\mathrm{b}^{\dot{G}}$ in binary pulsar tests not only provides an independent test for a varying gravitational constant but also probes strong-field aspects related to a time-varying gravitational constant.

[9] Detailed expressions for $\mathcal{F}_{AB}$ will be given in a future publication. See also Wex (2014).

9. Discussion and conclusions

In this work, we developed a new, improved approach for testing STG. We examined a specific class of STG theories known as "DEF gravity". This approach is based on a new timing model, called the DDSTG model, which is an extension of the DD model to work within DEF gravity. Analysis of pulsar timing data with this model overcomes some of the problems of conventional methods, which we have discussed in detail. The DDSTG timing model uses theoretical predictions for PK parameters in DEF gravity and therefore uses a minimal set of binary parameters. For that reason, it accounts for all the possible correlations between these parameters. All the information from the observational data is used to provide the most reliable tests of an alternative theory, directly without intermediate steps with phenomenological parameters of the DD model.

As a demonstration of the DDSTG model, we applied it to the most recently published timing data of the binary pulsar PSR J2222−0137 described and used by Guo et al. (2021b). This system is of great importance for testing alternative gravity theories because it is very close to us (resulting in the most precise VLBI distance for any pulsar), has precise timing and shows a set of well measured relativistic effects. The system has a high asymmetry in the compactness between the components: it comprises a massive NS ($m_{\rm NS} \sim 1.82 M_\odot$) and a massive WD ($m_{\rm WD} \sim 1.31 M_\odot$). This high asymmetry results, for some areas in the DEF gravity parameter space, in the prediction of a very strong dipolar GW contribution to the rate of orbital decay ($\dot{P}_{\rm b}^{D}$). The non-detection of dipolar GWs in this system is used to constrain the DEF gravity parameter space. Moreover the mass of the pulsar lies in the "scalarisation gap" ($m_{\rm NS} \gtrsim 1.5 M_\odot$); this means that strict limits on the occurrence of spontaneous scalarisation, a highly non-linear phenomenon, can be placed (Zhao et al. 2022).

The results from the new method confirmed and improved the existing limits on DEF gravity parameters from this system. The DDSTG model appeared to be more constraining in the area near spontaneous scalarisation ($\beta_0 \lesssim -4.0$) when compared to the commonly used PK method. It suggests that the combination of the DDSTG model with an EOS agnostic approach can improve limits placed on the spontaneous scalarisation.

Moreover, we applied the DDSTG timing model to the simulated TOA for PSR J2222−0137 covering the period of 2021–2030 to see what improvement we can expect from that system in the future. The mock timing data-sets were simulated for several large observatories FAST, 3ERT (EFF+NC+LT), MeerKAT with TOAs uncertainties based on the real timing data. We discussed the future importance of kinematic contributions (Shklovskii and Galactic) to $\dot{P}_{\rm b}$, and consequently to the precision of these tests. The main limiting factor to $\dot{P}_{\rm b}$ comes from the uncertainty in the Galactic contribution ($\dot{P}_{\rm b}^{\rm Gal}$). In particular, the limit comes from the current uncertainty in the vertical component of the Galactic acceleration (ΔK_z). Our analysis predicts that this limitation will disappear if the current uncertainty of $\Delta K_z \sim 10\%$ can be improved to $\Delta K_z \lesssim 3\%$, which is likely to be the case in the future with improvement of models for the gravitational potential of our Galaxy. Future observations are expected to significantly improve the limits on DEF gravity, especially with the use of FAST data.

One of the most promising systems for testing gravity, which we hope to have in the near future, are binary pulsar-black hole systems (PSR-BH). We simulated artificial timing data-sets for three eccentric PSR-BH systems with reasonable orbital parameters for three different orbital periods. The results of applying the DDSTG model to the simulated PSR-BH data strongly depended on the precision of the $\dot{P}_{\rm b}$ measurement. We briefly discussed possible evolution scenarios leading to the formation of the PSR-BH system, such as GC origin and reversal mechanism. Depending on the place of origin, there might be issues in obtaining a precise intrinsic $\dot{P}_{\rm b}$, i.e. accounting for the contamination of $\dot{P}_{\rm b}$ from a kinematic contribution due to the acceleration of the system in the gravitational field of the GC. Depending on the timing precision and orbital properties, PSR-BH can place stringent limits on DEF gravity.

In the future, the DDSTG model can be applied to a range of different binary pulsar systems to improve the limits on DEF gravity. We expect especially interesting results from PSR J1141−6545 where DDSTG is expected to be superior to standard approaches (Venkatraman Krishnan 2019). PSR J1141−6545 is an asymmetric PSR-WD system in 4.7 hours orbit with significant spin-orbit coupling due to the fast rotating WD. Due to the spin-orbit coupling the system shows a change of the projected semi-major axis $\dot{x}^{\rm SO}$ which has a strong correlation with the time dilation parameter γ. The latter parameter is caused by the precession which cannot be calculated, because we do not know the exact spin properties of the WD. Moreover, PSR J1141−6545 shows a weak Shapiro delay in the timing data which the DDSTG model can fully exploit resulting in a significant improvement of the test. The high asymmetry in the compactness between the components ($m_{\rm p} \sim 1.26 M_\odot$ NS and $m_{\rm c} \sim 1.02 M_\odot$ WD) makes this system a perfect tool for radiative tests of gravity. We expect the DDSTG model to be of particular advantage because it accounts for both possible correlations and weak relativistic effects (Venkatraman Krishnan et al., in prep.).

Another perspective system to perform DEF gravity tests with the DDSTG model is the Double Pulsar PSR 0737−3039A which shows the largest number of PK parameters in the timing data (Kramer et al. 2021). The system consists of two radio pulsars with masses of $m_{\rm p} \simeq 1.34\ M_\odot$ and $m_{\rm c} \simeq 1.25\ M_\odot$. Properties of NSs in DEF gravity (gravitational form-factors) strongly depend on the choice of the EOS, which in turn affects the test. Thus to put reliable limits on DEF gravity from PSR 0737−3039A independent of a choice of EOS, one must perform an EOS-agnostic analysis. EOS-agnostic test means that it is performed with a set of EOSs which are diverse in their properties (see Voisin et al. 2020, who used such an EOS-agnostic approach to constrain DEF gravity with a pulsar in a stellar triple system). With this paper we included a set of 11 EOSs varying from soft to stiff (see Appendix A.2) which can be used for such agnostic tests in the future.

Acknowledgements. We thank Lijing Shao for carefully reading the manuscript and giving important comments. We further thank Thomas Tauris and Selma de Mink for useful discussions and suggestions. AB and HH are members of the International Max Planck Research School for Astronomy and Astrophysics at the Universities of Bonn and Cologne. HH acknowledges the support by the Max-Planck Society as part of the "LEGACY" collaboration with the Chinese Academy of Sciences on low-frequency gravitational wave astronomy. This study is partly based on observations with the 100-m telescope of the MPIfR (Max-Planck-Institut für Radioastronomie) at Effelsberg. The Nançay Radio Observatory is operated by the Paris Observatory, associated with the French Centre National de la Recherche Scientifique (CNRS). LG, IC, and GT acknowledge financial support from the "Programme National Gravitation, Références, Astronomie, Métrologie (PNGRAM)" of CNRS/INSU, France. J. W. McKee gratefully acknowledges support by the Natural Sciences and Engineering Research Council of Canada (NSERC), [funding reference #CITA 490888-16]. This publication made use of open source libraries including DifferentialEquations.jl[10] (Rackauckas & Nie 2017), Optim.jl (Mogensen & Riseth 2018), ForwardDiff.jl (Revels et al. 2016), Matplotlib (Hunter 2007), along with a pulsar analysis package TEMPO[6] (Nice et al. 2015).

References

Abbott, B. P., Abbott, R., Abbott, T. D., et al. 2016, Phys. Rev. Lett., 116, 221101
Abbott, B. P., Abbott, R., Abbott, T. D., et al. 2019a, Phys. Rev. D, 100, 104036
Abbott, B. P., Abbott, R., Abbott, T. D., et al. 2017a, Phys. Rev. Lett., 119, 161101
Abbott, B. P., Abbott, R., Abbott, T. D., et al. 2017b, ApJ, 848, L12
Abbott, B. P., Abbott, R., Abbott, T. D., et al. 2017c, Phys. Rev. Lett., 118, 221101
Abbott, B. P., Abbott, R., Abbott, T. D., et al. 2019b, Phys. Rev. Lett., 123, 011102
Abbott, R., Abbott, T. D., Abraham, S., et al. 2021a, ApJ, 915, L5
Abbott, R., Abbott, T. D., Abraham, S., et al. 2021b, Phys. Rev. D, 103, 122002
Anderson, D., Freire, P., & Yunes, N. 2019, Classical and Quantum Gravity, 36, 225009
Anderson, D. & Yunes, N. 2019, Classical and Quantum Gravity, 36, 165003
Antoniadis, J., Freire, P. C. C., Wex, N., et al. 2013, Science, 340, 448
Antoniadis, J., van Kerkwijk, M. H., Koester, D., et al. 2012, MNRAS, 423, 3316
Bergmann, P. G. 1968, International Journal of Theoretical Physics, 1, 25
Berti, E., Barausse, E., Cardoso, V., et al. 2015, ArXiv:1501.07274 [arXiv:1501.07274]
Berti, E., Cardoso, V., Gualtieri, L., Horbatsch, M., & Sperhake, U. 2013, Phys. Rev. D, 87, 124020
Bertotti, B., Iess, L., & Tortora, P. 2003, Nature, 425, 374
Bezanson, J., Edelman, A., Karpinski, S., & Shah, V. B. 2017, SIAM Review, 59, 65
Bhat, N. D. R., Bailes, M., & Verbiest, J. P. W. 2008, Phys. Rev. D, 77, 124017
Blandford, R. & Teukolsky, S. A. 1976, ApJ, 205, 580
Boyles, J., Lynch, R. S., Ransom, S. M., et al. 2013, ApJ, 763, 80
Brans, C. & Dicke, R. H. 1961, Phys. Rev., 124, 925
Brumberg, V. A., Zeldovich, I. B., Novikov, I. D., & Shakura, N. I. 1975, Soviet Astronomy Letters, 1, 2
Clark, G. W. 1975, ApJ, 199, L143
Clausen, D., Sigurdsson, S., & Chernoff, D. F. 2014, MNRAS, 442, 207
Clifton, T., Ferreira, P. G., Padilla, A., & Skordis, C. 2012a, Phys. Rep., 513, 1
Clifton, T., Ferreira, P. G., Padilla, A., & Skordis, C. 2012b, Phys. Rep., 513, 1
Cognard, I., Freire, P. C. C., Guillemot, L., et al. 2017, ApJ, 844, 128
Damour, T. 2007, arXiv e-prints, arXiv:0704.0749
Damour, T. 2012, Classical and Quantum Gravity, 29, 184001
Damour, T. & Deruelle, N. 1985, Ann. Inst. H. Poincaré (Physique Théorique), 43, 107
Damour, T. & Deruelle, N. 1986, Ann. Inst. H. Poincaré (Physique Théorique), 44, 263
Damour, T. & Esposito-Farèse, G. 1998, Phys. Rev. D, 58, 1
Damour, T. & Esposito-Farèse, G. 1992a, Class. Quant Grav., 9, 2093
Damour, T. & Esposito-Farèse, G. 1992b, Phys. Rev. D, 46, 4128
Damour, T. & Esposito-Farèse, G. 1993, Phys. Rev. Lett., 70, 2220
Damour, T. & Esposito-Farèse, G. 1996, Phys. Rev. D, 54, 1474
Damour, T., Gibbons, G. W., & Taylor, J. H. 1988, Phys. Rev. Lett., 61, 1151
Damour, T. & Nordtvedt, K. 1993, Phys. Rev. D, 48, 3436
Damour, T. & Taylor, J. H. 1991, ApJ, 366, 501
Damour, T. & Taylor, J. H. 1992, Phys. Rev. D, 45, 1840
DeCesar, M. E., Ransom, S. M., Kaplan, D. L., Ray, P. S., & Geller, A. M. 2015, ApJ, 807, L23
Deller, A. T., Boyles, J., Lorimer, D. R., et al. 2013, ApJ, 770, 145
Douchin, F. & Haensel, P. 2001, A&A, 380, 151
Fierz, M. 1956, Helv. Phys. Acta, 29, 128
Fonseca, E., Cromartie, H. T., Pennucci, T. T., et al. 2021, ApJ, 915, L12
Freire, P. C., Gupta, Y., Ransom, S. M., & Ishwara-Chandra, C. H. 2004, ApJ, 606, L53
Fujii, Y. & Maeda, K.-i. 2007, The Scalar-Tensor Theory of Gravitation (Cambridge University Press)
Goenner, H. 2012, General Relativity and Gravitation, 44, 2077
Gravity Collaboration, Abuter, R., Amorim, A., et al. 2021, A&A, 647, A59
Guo, M., Zhao, J., & Shao, L. 2021a, Phys. Rev. D, 104, 104065
Guo, Y. J., Freire, P. C. C., Guillemot, L., et al. 2021b, A&A, 654, A16
Hartle, J. 1967, ApJ, 150, 1005
Hawking, S. W. 1972, Communications in Mathematical Physics, 25, 167
Holmberg, J. & Flynn, C. 2004, MNRAS, 352, 440
Horndeski, G. W. 1974, International Journal of Theoretical Physics, 10, 363
Hu, H., Kramer, M., Wex, N., Champion, D. J., & Kehl, M. S. 2020, MNRAS, 497, 3118
Hulse, R. A. & Taylor, J. H. 1975, ApJ, 195, L51
Hunter, J. D. 2007, Computing in Science and Engineering, 9, 90
Jacoby, B. A., Cameron, P. B., Jenet, F. A., et al. 2006, ApJ, 644, L113
Jordan, P. 1955, Schwerkraft und Weltall, Die Wissenschaft (Vieweg)
Jordan, P. 1959, Z. Phys., 157, 112
Kaluza, T. 1921, Sitzungsberichte der Königlich Preußischen Akademie der Wissenschaften (Berlin, 966
Klein, O. 1926, Zeitschrift fur Physik, 37, 895
Kramer, M., Stairs, I. H., Manchester, R. N., et al. 2021, Physical Review X, 11, 041050
Lazaridis, K., Wex, N., Jessner, A., et al. 2009, MNRAS, in press, arXiv:0908.0285
Liu, K., Eatough, R. P., Wex, N., & Kramer, M. 2014, MNRAS, 445, 3115
Lorimer, D. R. & Kramer, M. 2004, Handbook of Pulsar Astronomy, Vol. 4 (Cambridge University Press)
Luo, J., Ransom, S., Demorest, P., et al. 2021, ApJ, 911, 45
Lynch, R. S., Freire, P. C. C., Ransom, S. M., & Jacoby, B. A. 2012, ApJ, 745, 109
Margossian, C. C. 2018, arXiv e-prints, arXiv:1811.05031
Mendes, R. F. P. & Ortiz, N. 2016, Phys. Rev. D, 93, 124035
Mirshekari, S. & Will, C. M. 2013, Phys. Rev. D, 87, 084070
Mogensen, P. K. & Riseth, A. N. 2018, Journal of Open Source Software, 3, 615
Müther, H., Prakash, M., & Ainsworth, T. L. 1987, Physics Letters B, 199, 469
Nice, D., Demorest, P., Stairs, I., et al. 2015, Tempo: Pulsar timing data analysis
Nice, D. J. & Taylor, J. H. 1995, ApJ, 441, 429
Nordtvedt, K. 1990, Phys. Rev. Lett., 65, 953
Nordtvedt, K. 1993, ApJ, 407, 5
Pfahl, E., Podsiadlowski, P., & Rappaport, S. 2005, ApJ, 628, 343
Phinney, E. S. 1992, Philos. Trans. Roy. Soc. London A, 341, 39
Phinney, E. S. 1993, in Structure and Dynamics of Globular Clusters, ed. S. G. Djorgovski & G. Meylan (Astronomical Society of the Pacific Conference Series), 141–169
Prince, T. A., Anderson, S. B., Kulkarni, S. R., & Wolszczan, W. 1991, ApJ, 374, L41
Rackauckas, C. & Nie, Q. 2017, The Journal of Open Research Software, 5, exported from https://app.dimensions.ai on 2019/05/05
Read, J. S., Lackey, B. D., Owen, B. J., & Friedman, J. L. 2009, Phys. Rev. D, 79, 124032
Revels, J., Lubin, M., & Papamarkou, T. 2016, arXiv:1607.07892 [cs.MS]
Ridolfi, A., Freire, P. C. C., Gautam, T., et al. 2022, A&A, 664, A27
Ridolfi, A., Freire, P. C. C., Gupta, Y., & Ransom, S. M. 2019, MNRAS, 490, 3860
Ridolfi, A., Gautam, T., Freire, P. C. C., et al. 2021, MNRAS, 504, 1407
Shao, L., Sennett, N., Buonanno, A., Kramer, M., & Wex, N. 2017, Physical Review X, 7, 041025
Shao, L. & Wex, N. 2016, Science China Physics, Mechanics, and Astronomy, 59, 699501
Shklovskii, I. S. 1970, Sov. Astron., 13, 562
Sipior, M. S., Portegies Zwart, S., & Nelemans, G. 2004, MNRAS, 354, L49
Splaver, E. M., Nice, D. J., Arzoumanian, Z., et al. 2002, ApJ, 581, 509
Stairs, I. H. 2003, Living Reviews in Relativity, 6, 5
Swesty, F. D. 1996, Journal of Computational Physics, 127, 118
Tauris, T. M. & Sennels, T. 2000, A&A, 355, 236
Taylor, J. H. & Weisberg, J. M. 1989, ApJ, 345, 434
Uzan, J.-P. 2011, Living Reviews in Relativity, 14, 2
Venkatraman Krishnan, V. 2019, PhD thesis, Swinburne University of Technology, Australia
Venkatraman Krishnan, V., Bailes, M., van Straten, W., et al. 2020, Science, 367, 577
Verbiest, J. P. W., Bailes, M., Coles, W. A., et al. 2009, MNRAS, 400, 951
Verbunt, F. & Freire, P. C. C. 2014, A&A, 561, A11
Verbunt, F. & Hut, P. 1987, in The Origin and Evolution of Neutron Stars, IAU Symposium No. 125, ed. D. J. Helfand & J. Huang (Dordrecht: Reidel), 187–197
Voisin, G., Cognard, I., Freire, P. C. C., et al. 2020, A&A, 638, A24
Voss, R. & Tauris, T. M. 2003, MNRAS, 342, 1169
Wagoner, R. V. 1970, Phys. Rev. D, 1, 3209
Wex, N. 2014, ArXiv e-prints [arXiv:1402.5594], to appear in the Brumberg Festschrift (ed. S. M. Kopeikein), de Gruyter, Berlin.
Wex, N. & Kramer, M. 2020, Universe, 6, 156
Will, C. M. 1993, Theory and Experiment in Gravitational Physics (Cambridge: Cambridge University Press)
Will, C. M. 2014, Living Rev. Relativity, 17, 4
Will, C. M. 2018a, Classical and Quantum Gravity, 35, 085001
Will, C. M. 2018b, Theory and Experiment in Gravitational Physics, 2nd edn. (Cambridge University Press)
Zhao, J., Freire, P. C. C., Kramer, M., Shao, L., & Wex, N. 2022, Classical and Quantum Gravity, 39, 11LT01

Appendix A: Details on calculating grids of NSs

We select slowly rotating axisymmetric approximation of NSs following Damour & Esposito-Farèse (1996). The internal structure of such a NS in DEF gravity is described by a set of 8 ordinary differential equations depending on the radial variable (r). To calculate a single NS the program solves the system of ODEs by applying appropriate boundary conditions at the centre of a NS and spatial infinity. We use a shooting technique to match initial internal parameters with the external structure of the space-time. The differential equations are solved by means of the Julia library DifferentialEquations.jl[10] (Rackauckas & Nie 2017).

A particular solution is determined by the choice of two theory parameters $\{\alpha_0, \beta_0\}$, the EOS and the central pressure p_c. The central value of the scalar field φ_c is determined by the shooting procedure to correspond to the scalar field value at spatial infinity $\varphi_0 = \varphi(r = \infty)$, which in our case is, without loss of generality, set to zero. Thus φ_c is not an arbitrary parameter. The central density (p_c) uniquely corresponds to the gravitational mass m_A for most masses of interest and fixed theory parameters $\{\alpha_0, \beta_0\}$. In general, this is not the case — there may be several stable solutions for a fixed mass in the area of strong scalarisation. However, multiple solutions happen for large NS masses and very negative $\beta_0 < -4.5$ which is already ruled out and thus of no interest.

In the recent papers devoted to the calculation of NSs in scalar-tensor gravity (Anderson & Yunes 2019), the gravitational form-factors from Eq. (6) (they are also often called "scalar charges") are calculated using numerical differentiation. Numerical differentiation is performed on a grid of dependent variables. The precision of this approach is determined by two factors: a) the error in the calculation of the desired quantity and b) the error due to the numerical differentiation formula. The first error depends on the precision of the numerical integration of the structure equations. The second error strongly depends on the fineness of the grid on which the derivatives are calculated. If the grid is too sparse the formula such as the central difference formula $f'(x) \simeq [f(x+\delta x) - f(x-\delta x)] / [2\delta x]$ is not accurate enough. On the other hand, if the grid is too fine, the error arises because of the subtraction of two close numbers in the computer memory. The total relative errors for calculating gravitational form-factors usually lie in the range of $\delta_{\rm rel} \sim 10^0 - 10^{-5}$. In our work, we propose a more precise way to calculate all the quantities.

Appendix A.1: Automatic Differentiation

In our program, we utilise the Automatic Differentiation (AutoDiff) technique. It is a special technique to calculate derivatives, when the algorithm knows the exact expressions for derivatives of all elementary functions and uses the chain rule to unfold complex derivatives. A review on the AutoDiff can be found, for instance, in Margossian (2018). We use an implementation of the AutoDiff technique in Julia from ForwardDiff.jl library, which is a part of a broad JuliaDiff framework (Revels et al. 2016). AutoDiff allows calculating complex derivatives of quantities with respect to their arguments with the machine-precision (for Double Float numbers the corresponding precision is $\delta \sim 2{\times}10^{-16}$ on 64-bit systems). It is done by internal implementation of sophisticated arithmetic on a special type of numbers (dual numbers) in the programming language. A derivative is calculated exactly in the desired point and does not require points in the vicinity. The precision of the method is constant and thus does not depend anymore on the fineness of the grid.

Automatic differentiation enables us to simultaneously calculate both the function $F = F(x, y)$ and its derivatives with respect to arguments $\frac{\partial F}{\partial x}, \frac{\partial F}{\partial y}$. It takes twice as long as calculating a mere function itself and both are done with the machine-precision . To calculate a complex derivative, then the arguments are also functions $B = B(x, y)$, $C = C(x, y)$ we apply the chain rule:

$$\frac{\partial A(B,C)}{\partial B}\Big|_C = \left(\frac{\partial A}{\partial x}\frac{\partial C}{\partial y} - \frac{\partial A}{\partial y}\frac{\partial C}{\partial x}\right) \Big/ \left(\frac{\partial B}{\partial x}\frac{\partial C}{\partial y} - \frac{\partial B}{\partial y}\frac{\partial C}{\partial x}\right). \quad \text{(A.1)}$$

In our program, we calculate the gravitational form-factors from Eq. (6), which are complex derivatives of quantities (e.g. a mass (m_A) and moment of inertia (I_A) of a NS) taken with respect to external parameters (the value of the scalar field at spatial infinity (φ_0). The properties of NSs are obtained through numerical integration of the structure equations and depend on the central scalar field (φ_c) and central pressure (p_c). For example for α_A using Eq. (A.1) we simply obtain:

$$\alpha_A = \frac{\partial \ln m_A}{\partial \varphi_0}\Big|_{\bar{m}_A} = \left(\frac{\partial \ln m_A}{\partial \varphi_c}\frac{\partial \bar{m}_A}{\partial p_c} - \frac{\partial \ln m_A}{\partial p_c}\frac{\partial \bar{m}_A}{\partial \varphi_c}\right) \Big/ \left(\frac{\partial \varphi_0}{\partial \varphi_c}\frac{\partial \bar{m}_A}{\partial p_c} - \frac{\partial \varphi_0}{\partial p_c}\frac{\partial \bar{m}_A}{\partial \varphi_c}\right), \quad \text{(A.2)}$$

where every simple derivative is calculated with the machine-precision due to the AutoDiff.

As a result, the total precision of calculated gravitational form-factors is determined only by the accuracy of the differential equation solver and may be easily enhanced. We use the Julia library DifferentialEquations.jl which allows using AutoDiff on the results of the numerical integration. The numerical integration can take advantage of the AutoDiff itself because the Jacobian of the system can be calculated more accurately and used to integrate the ODE system. We obtain a higher precision if we select a finer adaptive step in the radial variable r. For our grids we set the integrator to the relative error of $\delta_{\rm Int,rel} \sim 10^{-11}$. The obtained relative precision for gravitational form-factors typically lies in $\delta_{\rm rel} \sim 10^{-7} - 10^{-13}$ range, which is more precise than previous calculations.

Appendix A.2: pre-calculated grids of neutron stars

To place limits on the DEF gravity parameters $\{\alpha_0, \beta_0\}$ we need to know the gravitational form factors $\{\alpha_A, \beta_A, k_A\}$ in Eq. (6) as functions of the mass m_A. To approximate these relations we have to calculate grids of NSs. We calculate grids for several EOSs, including MPA1 used in this paper. Each grid contains 4 calculated values: masses m_A and gravitational form factors $\{\alpha_A, \beta_A, k_A\}$ for a range of values of $\{\alpha_0, \beta_0, p_c\}$ with number of points in each axis respectively $\{101, 351, 121\}$. The grid properties are shown in the Table A.1. α_0 and p_c are selected to be logarithmically distributed. Whereas, the parameter β_0 is piece-wise linearly distributed. The grid for p_c is more dense near the common masses of NSs $1.4 - 2.0 M_\odot$. We also include more points in the region of spontaneous scalarisation with $\beta_0 \in [-5.0, -4.0]$. The resulting calculated gravitational form-factors are saved in files which then can be used in DEF gravity tests, the DDSTG model in particular.

With the developed DDSTG model we supply grids for 11 different EOSs ranging from soft to stiff. Each EOS satisfies the

[10] https://diffeq.sciml.ai

Table A.1. Properties of the pre-calculated grids of NSs.

Axis	Type	# of points	Range
α_0	Log	101	$[-10^{-1}, -10^{-5}]$
β_0	Lin	21	$[-6.0, -5.0]$
		51	$[-5.0, -4.0]$
		281	$[-4.0, +10.0]$
p_c (dyn/cm^2)	Log	21	$[10^{34}, 5\times10^{34}]$
		81	$[5\times10^{34}, 5\times10^{35}]$
		21	$[5\times10^{35}, 10^{36}]$

Notes. The grids are 3-dimensional and depend on $\{\alpha_0, \beta_0, p_c\}$. Each axis of a grid can be divided into several intervals and be either linearly or logarithmically separated.

requirement on a maximal mass in GR: $M^{\rm GR}_{\rm NS,max} > 2M_\odot$ (Antoniadis et al. 2013; Fonseca et al. 2021). Table B.1 presents the selected EOSs with their maximum masses in GR. In our work we use the piece-wise polytropic approximation described in Read et al. (2009).

Appendix B: PK parameters in DEF gravity

In this Appendix we present the expressions for the PK parameters in DEF gravity as functions of the masses of pulsar ($m_{\rm p}$) and companion ($m_{\rm c}$), and the three Keplerian timing parameters $P_{\rm b}$, e, and x. The formulae for the PK parameters $\{\gamma, k, r, s\}$ can be found in Damour & Esposito-Farèse (1992a) and Damour & Esposito-Farèse (1996). For the PK parameters $\{\delta_r, \delta_\theta, A, B\}$ there are only more general theory-independent presentations in Damour & Taylor (1992), from which the expressions in DEF gravity, however, can be straightforwardly derived. The total set of PK parameters in DEF gravity reads:

$$\gamma = \frac{e}{n}\frac{X_{\rm c}\beta_O^2}{1+\alpha_{\rm p}\alpha_{\rm c}}\left[X_{\rm c}(1+\alpha_{\rm p}\alpha_{\rm c}) + 1 + k_{\rm p}\alpha_{\rm c}\right], \tag{B.1}$$

$$k = \frac{3\beta_O^2}{1-e^2}\left[\frac{1-\frac{1}{3}\alpha_{\rm p}\alpha_{\rm c}}{1+\alpha_{\rm p}\alpha_{\rm c}} - \frac{X_{\rm p}\beta_{\rm c}\alpha_{\rm p}^2 + X_{\rm c}\beta_{\rm p}\alpha_{\rm c}^2}{6(1+\alpha_{\rm p}\alpha_{\rm c})^2}\right], \tag{B.2}$$

$$r = \frac{G_* m_{\rm c}}{c^3}, \tag{B.3}$$

$$s = \frac{nx}{X_{\rm c}\beta_O}\left[1 + \frac{1}{3}\left(\frac{9-\alpha_{\rm p}\alpha_{\rm c}}{1+\alpha_{\rm p}\alpha_{\rm c}} - X_{\rm p}X_{\rm c}\right)\beta_O^2\right], \tag{B.4}$$

$$\delta_r = \frac{\beta_O^2}{m_{\rm tot}^2(1+\alpha_{\rm p}\alpha_{\rm c})}\left[(3-\alpha_{\rm p}\alpha_{\rm c})m_{\rm p}^2 + (6-\alpha_{\rm p}\alpha_{\rm c}-k_{\rm p}\alpha_{\rm c})m_{\rm p}m_{\rm c} + (2-\alpha_{\rm p}\alpha_{\rm c}-k_{\rm p}\alpha_{\rm c})m_{\rm c}^2\right], \tag{B.5}$$

$$\delta_\theta = \frac{\beta_O^2}{m_{\rm tot}^2(1+\alpha_{\rm p}\alpha_{\rm c})}\left[\left(\frac{7}{2} - \frac{1}{2}\alpha_{\rm p}\alpha_{\rm c}\right)m_{\rm p}^2 + (6-\alpha_{\rm p}\alpha_{\rm c}-k_{\rm p}\alpha_{\rm c})m_{\rm p}m_{\rm c} + (2-\alpha_{\rm p}\alpha_{\rm c}-k_{\rm p}\alpha_{\rm c})m_{\rm c}^2\right], \tag{B.6}$$

$$A = -\frac{\beta_O X_{\rm c}}{2\pi\nu_{\rm p}(1-e^2)^{1/2}}\frac{\sin\eta}{\sin\lambda}, \tag{B.7}$$

$$B = -\frac{\beta_O X_{\rm c}}{2\pi\nu_{\rm p}(1-e^2)^{1/2}}\frac{\cos i\cos\eta}{\sin\lambda}, \tag{B.8}$$

$$\dot{P}_{\rm b} = \dot{P}_{\rm b}^{\varphi,\rm mon} + \dot{P}_{\rm b}^{\varphi,\rm dip} + \dot{P}_{\rm b}^{\varphi,\rm quad} + \dot{P}_{\rm b}^{g,\rm quad}, \tag{B.9}$$

Table B.1. EOSs selected for the calculation of grids of NSs.

Name	$M_{\rm max}$ ($M_\odot$)	$R_{1.4}$ (km)	Name	$M_{\rm max}$ ($M_\odot$)	$R_{1.4}$ (km)
SLy	2.049	11.736	APR3	2.390	12.094
APR4	2.213	11.428	WFF1	2.133	10.414
WFF2	2.198	11.159	ENG	2.240	12.059
MPA1	2.461	12.473	MS1	2.767	14.918
MS1b	2.776	14.583	H4	2.032	13.759
ALF2	2.086	13.188			

Notes. All EOSs have the maximum mass of a NS in GR $M^{\rm GR}_{\rm NS,max} > 2M_\odot$ and taken in piece-wise polytropic approximation from Read et al. (2009). $R_{1.4}$ is the radius of a $1.4M_\odot$ NS.

where we used variables $\beta_O = \left(G_{\rm pc}Mn/c^3\right)^{1/3}$, $G_{\rm pc} = G_*(1+\alpha_{\rm p}\alpha_{\rm c})$, $m_{\rm tot} = m_{\rm p} + m_{\rm c}$, $X_{\rm p} = m_{\rm p}/m_{\rm tot}$, and $X_{\rm c} = m_{\rm c}/m_{\rm tot} = 1 - X_{\rm p}$. Moreover, $n = 2\pi/P_{\rm b}$ is the orbital circular frequency and $\nu_{\rm p} = 1/P$ is the pulsar's rotational frequency. The angle i is the inclination of the orbital plane with respect to the plane of sky, while angles λ and η are the polar angles of the spin axis. In the special case of alignment between the orbital and spin axes $\lambda = i$ and $\eta = -\pi/2$ forcing $B = 0$.

The expression for $\dot{P}_{\rm b}$ is composed from 4 different contributions (Damour & Esposito-Farèse 1992a)

$$\dot{P}_{\rm b}^{\varphi,\rm mon} = -\frac{3\pi X_{\rm p}X_{\rm c}}{1+\alpha_{\rm p}\alpha_{\rm c}}\beta_O^5\frac{e^2(1+e^2/4)}{(1-e^2)^{7/2}} \times\left[\alpha_{\rm p}+\alpha_{\rm c}+\frac{2}{3}(\alpha_{\rm p}X_{\rm c}+\alpha_{\rm c}X_{\rm p}) + \frac{\beta_{\rm p}\alpha_{\rm c}+\beta_{\rm c}\alpha_{\rm p}}{1+\alpha_{\rm p}\alpha_{\rm c}}\right]^2, \tag{B.10}$$

$$\dot{P}_{\rm b}^{\varphi,\rm dip} = -\frac{2\pi X_{\rm p}X_{\rm c}}{1+\alpha_{\rm p}\alpha_{\rm c}}\beta_O^3\frac{1+e^2/2}{(1-e^2)^{5/2}}(\alpha_{\rm p}-\alpha_{\rm c})^2 - \frac{4\pi X_{\rm p}X_{\rm c}}{1+\alpha_{\rm p}\alpha_{\rm c}}\beta_O^5\frac{1}{(1-e^2)^{7/2}}\left[\frac{8}{5}\left(1+\frac{31e^2}{8}+\frac{19e^4}{32}\right)(\alpha_{\rm p}-\alpha_{\rm c}) \times(\alpha_{\rm p}X_{\rm p}+\alpha_{\rm c}X_{\rm c})(X_{\rm p}-X_{\rm c}) + \left(1+3e^2+\frac{3e^4}{8}\right) \times\frac{(\alpha_{\rm p}-\alpha_{\rm c})(\beta_{\rm c}\alpha_{\rm p}X_{\rm p}-\beta_{\rm p}\alpha_{\rm c}X_{\rm c})}{1+\alpha_{\rm p}\alpha_{\rm c}}\right], \tag{B.11}$$

$$\dot{P}_{\rm b}^{\varphi,\rm quad} = -\frac{32\pi X_{\rm p}X_{\rm c}}{5(1+\alpha_{\rm p}\alpha_{\rm c})}\beta_O^5\frac{1+73e^2/24+37e^4/96}{(1-e^2)^{7/2}} \times(\alpha_{\rm p}X_{\rm c}+\alpha_{\rm c}X_{\rm p})^2, \tag{B.12}$$

$$\dot{P}_{\rm b}^{g,\rm quad} = -\frac{192\pi X_{\rm p}X_{\rm c}}{5(1+\alpha_{\rm p}\alpha_{\rm c})}\beta_O^5\frac{1+73e^2/24+37e^4/96}{(1-e^2)^{7/2}}, \tag{B.13}$$

where scalar field φ gives rise to a monopolar $\dot{P}_{\rm b}^{\varphi,\rm mon}$, a dipolar $\dot{P}_{\rm b}^{\varphi,\rm dip}$ and a quadrupolar $\dot{P}_{\rm b}^{\varphi,\rm quad}$ contribution. Another quadrupolar term $\dot{P}_{\rm b}^{g,\rm quad}$ is associated with metric $g^*_{\mu\nu}$. Following Damour & Esposito-Farèse (1992a), we have ignored a term of order $(\alpha_{\rm p}-\alpha_{\rm c})^2\beta_O^5$ in Eq. (B.11).

Appendix C: DDSTG implementation into TEMPO

As part of this work, we implement a new timing model DDSTG into an independent version of the standard timing software TEMPO[7]. The new model is based on the DD (Damour & Deruelle 1986) and DDGR (Taylor & Weisberg 1989) models but

Table C.1. Parameters used in DDSTG timing model in TEMPO.

Name	Description
ALPHA0	α_0 value $\in [-10^{-1}, -10^{-5}] \cup \{0\}$
BETA0	β_0 value $\in [-6, +10]$
EOS	EOS ID, e.g. MPA1
COMP_TYPE	selected from {WD, NS, BH}

modified to work within STG theories. In addition to the parameters present in the DDGR model, the DDSTG model utilises four additional parameters, added to the corresponding parameter input file. New parameters and their possible values are presented in Table C.1.

The first two parameters "ALPHA0" and "BETA0" correspond to the values of two arbitrary DEF gravity parameters $\{\alpha_0, \beta_0\}$. They can be selected to be zero to recover GR. Otherwise, the applicable range of values is determined by the range of the supplementary data files, containing grids of the calculated gravitational form-factors and masses. The grids are calculated as part of this work and supplied with the model. The supplied grids cover $\alpha_0 \in [-10^{-1}, -10^{-5}]$ and $\beta_0 \in [-6, +10]$ in the DEF gravity parameter space.

The third parameter "EOS" selects the equation of state to be used to perform the test. In the present work, we generally select the rather stiff EOS MPA1. TEMPO reads the supplied pre-calculated grids of the gravitational form factors and masses corresponding to the selected EOS (see also Table B.1).

The last parameter "COMP_TYPE" is used to select the type of the companion to the pulsar, among a white dwarf ("WD"), a neutron star ("NS") and a black hole ("BH"). These three compact objects have different properties in terms of gravitational form factors. NSs in DEF gravity can be moderately $|\alpha_{\rm NS}| \lesssim |\alpha_0|$ or strongly $|\alpha_{\rm NS}| \sim O(1)$ scalarised depending on the mass m_A and the chosen DEF parameters. WDs are not enough compact to significantly deviate from the weak-field approximation $|\alpha_{\rm WD}| \lesssim |\alpha_0|$. Thus for WDs we apply $\alpha_{\rm WD} = \alpha_0, \beta_{\rm WD} = \beta_0$.[11] In contrast, BHs in DEF gravity fulfil a no-hair theorem and they are completely descalarised $\alpha_{\rm BH} = 0$ and $\beta_{\rm BH} = 0$. The choice of the companion type plays a significant role for the calculated values of PK parameters.

During initialisation, TEMPO reads the parameter file and the file with the TOAs. When the $\{\alpha_0, \beta_0\}$ values and the EOS are provided, it reads the supplementary grids for the selected EOS. The supplied grids are three-dimensional and consist of the masses of NSs m_A and their gravitational form factors $\{\alpha_A, \beta_A, k_A\}$. Two axes are $\{\alpha_0, \beta_0\}$ and the third axis is a fixed range of central pressure (p_c) of a NS.

Bilinear interpolation is performed in the $\{\alpha_0, \beta_0\}$ parameter space for the selected parameters. The result of the interpolation are four single-dimensional arrays for masses and gravitational form factors depending on a range of central pressures. Interpolated one-dimensional arrays are saved in the computer memory and used further without being changed. From this point gravitational form factors are ready to be interpolated in the mass range during the fitting procedure.

TEMPO with selected DDSTG model fits two masses in addition to spin, astrometric and Keplerian parameters. The masses are iteratively changed during the fitting procedure. Only when the masses change TEMPO interpolates the gravitational form factors from the pre-calculated one-dimensional grids. Gravitational form factors are calculated for both the pulsar and the companion and are kept constant for all TOAs within a single iteration.

TEMPO tries to find the companion mass ($m_{\rm c}$) and the total mass ($m_{\rm tot} = m_{\rm p} + m_{\rm c}$) corresponding to the best fit. During the fitting, it utilises the derivatives of the timing formula (7) with respect to these two masses. We calculate derivatives separately for each delay in Equations (11 – 14). We used the approximated expressions for the derivatives of the delays with respect to PK parameters provided by Damour & Deruelle (1986). After applying the chain rule for our derivatives we come to expressions depending on the derivatives of PK parameters with respect to the two masses. The model calculates the derivatives of the the PK parameters of DEF gravity (Eqs. B.1 – B.9) with respect to the two masses of the timing model,

$$\left(\frac{\partial p_i^{\rm PK}(m_{\rm c}, m_{\rm tot})}{\partial m_{\rm c}}\right)\Bigg|_{m_{\rm tot}}, \quad \left(\frac{\partial p_i^{\rm PK}(m_{\rm c}, m_{\rm tot})}{\partial m_{\rm tot}}\right)\Bigg|_{m_{\rm c}}, \tag{C.1}$$

which are certainly different to those in GR. Moreover, for proper convergence of the model in highly nonlinear areas the additional corrections to the derivatives related to variation of gravitational form-factors with respect to masses (i.e. $\partial\alpha_A/\partial m_A, \partial\beta_A/\partial m_A$) are required.

The formulae in Eq. (C.1) are large but can be obtained by straightforward differentiation of the PK formulae in Appendix B. The expressions are incorporated in the model and depend on gravitational form factors, masses and Keplerian parameters which are known on each iteration. Once the derivatives of PK parameters are calculated, the model calculates the derivatives of the timing delays with respect to the two masses and proceeds the iteration. The outcome of the DDSTG model in TEMPO is the same as for the DDGR model. The most important result is the χ^2 value, which is used further to perform tests of gravity.

The DDSTG timing model converges well if the eccentricity of the orbit is not too small and TEMPO is supplied with a reasonable initial guess of the orbital parameters. The model can run into difficulties in the convergence for solutions if those parameters are far away from GR or if the orbit is almost circular. The problem can happen if TEMPO changes masses significantly during the iteration and reaches a point where the Shapiro shape parameter calculated with new masses using Eq. (B.4) becomes greater than one, i.e. $s > 1$. In this case the expression of the Shapiro delay from Eq. (13) does not have a physical meaning and TEMPO breaks with an error for TOAs near conjunction, as the argument of the logarithm becomes negative. The convergence can be enforced by applying the special parameter GAIN, which however comes at the cost of increased computational time. A GAIN parameter of less than one forces TEMPO to use smaller steps while iterating. Another way which ensures the convergence is to supply TEMPO with a good initial guess for the masses in DEF gravity. The rough estimate of the masses in DEF gravity can be obtained from the traditional PK method. The combination of these two methods help to converge systems with small eccentricity and Shapiro shape parameter near one ($s \simeq 1$) even in the strongly nonlinear part of the $\{\alpha_0, \beta_0\}$ plane.

Appendix D: Mass-mass diagram near the horn

Many binary pulsar tests are not sensitive at high $|\alpha_0|$ values and $\beta_0 \sim -2$. In this region near the "horn", $\alpha_{\rm NS} \approx \alpha_0$ and the

[11] Since this is the case for any weakly self-gravitating body, the setting "WD" can also be selected for any non-degenerate companion such as a main-sequence star.

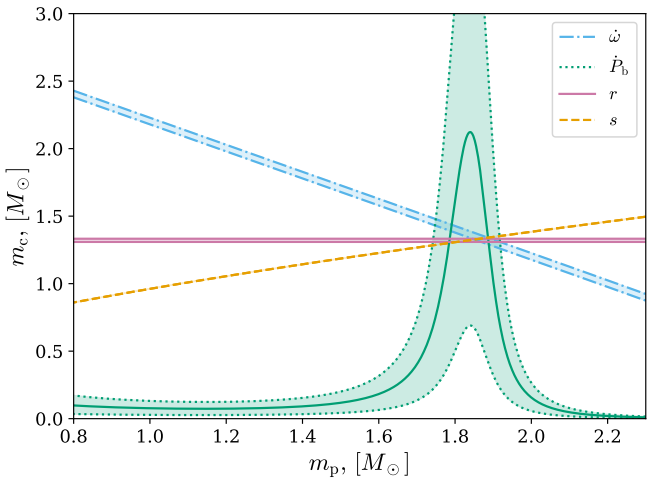

Fig. D.1. Mass-mass diagram in DEF gravity corresponding to a point near the "horn" with $\alpha_0 = -10^{-1}$, $\beta_0 = -1.9$. The performed test is the same as for Figure 1. The shadowed area is the allowed region at 68 % CL limit for a corresponding PK parameter. The solid green line corresponds to the observed value of $\dot{P}_b^{\rm int}$.

overall $\dot{P}_b$ is close to the GR value, as the dipolar contribution is greatly suppressed. As a consequence, the test is passed. In Figure D.1 we show a mass-mass diagram in DEF gravity with $\alpha_0 = -0.1, \beta_0 = -1.9$. This point in the DEF gravity parameter space passes the test with timing data but is excluded by Cassini experiment ($|\alpha_0| \lesssim 3.4 \times 10^{-3}$). The picture is dramatically different from what we see in the zone of scalarisation in Figure 1.

Appendix E: Proper account of $\dot{P}_b^{\rm ext}$ uncertainty

If the observed $\dot{P}_b$ is measured more precisely than the external contribution $\dot{P}_b^{\rm ext}$ we have to take the uncertainty of the external contribution into account. In most situations $\dot{P}_b^{\rm ext}$ consists of the Shklovskii and the Galactic contribution. The calculation of the Shklovskii contribution is limited by the uncertainty in the distance and the one in the proper motion. The uncertainty in the estimation of the Galactic contribution is determined by the uncertainty in the distance and our imperfect knowledge of the Galactic gravitational potential. The latter is partly systematic in nature and therefore somewhat more difficult to quantify. If the uncertainty $\Delta\dot{P}_b^{\rm ext}$ is the limiting factor we no longer can have $\dot{P}_b^{\rm ext}$ fixed on one value for the whole experiment (i.e. provide a fixed value for parameter XPBDOT in TEMPO) because its uncertainty can affect the derived limits.

To properly account for the uncertainty in $\dot{P}_b^{\rm ext}$ we follow the method described in Splaver et al. (2002) based on Bayes inference. On the first stage TEMPO calculates χ^2 grid for three independent parameters $\{\alpha_0, \beta_0, \dot{P}_b^{\rm ext}\}$. Then the shifted value $\Delta\chi^2 = \chi^2 - \chi^2_{\rm min}$ is described by χ^2 distribution with 3 degrees of freedom. The number of degrees of freedom is important when we calculate confidence level limits. The $\Delta\chi^2$ maps as usual to a Bayesian likelihood function,

$$p(\{t_j\} \,|\, \alpha_0, \beta_0, \dot{P}_b^{\rm ext}) = \frac{1}{2} e^{-\Delta\chi^2/2}, \tag{E.1}$$

where $\{t_j\}$ refers to the used timing data. We treat the obtained probability density $p(\{t_j\} \,|\, \alpha_0, \beta_0, \dot{P}_b^{\rm ext})$ as the likelihood for Bayes' theorem

$$p(\alpha_0, \beta_0, \dot{P}_b^{\rm ext} \,|\, \{t_j\}) = \frac{p(\{t_j\} \,|\, \alpha_0, \beta_0, \dot{P}_b^{\rm ext})}{p(\{t_j\})} p(\alpha_0, \beta_0, \dot{P}_b^{\rm ext}), \tag{E.2}$$

where $p(\alpha_0, \beta_0, \dot{P}_b^{\rm ext} \,|\, \{t_j\})$ is the desired joint posterior probability function and $p(\alpha_0, \beta_0, \dot{P}_b^{\rm ext})$ is the prior. The Bayesian evidence $p(\{t_j\})$ is obtained from normalisation of posterior probability over the whole grid $\{\alpha_0, \beta_0\}$.

In the next stage we select the prior $p(\alpha_0, \beta_0, \dot{P}_b^{\rm ext})$. We assume no prior information about α_0 and β_0, so their distributions are taken uniformly for $\beta_0 \in (-\infty, +\infty)$ and $\alpha_0 \in (-\infty, 0]$. At this step, we utilise the information about the uncertainties in $\dot{P}_b^{\rm ext}$. For example, we can select the prior $p(\dot{P}_b^{\rm ext})$ to be normally distributed with the mean measured value $\dot{P}_b^{\rm ext}$ and its standard deviation $\Delta\dot{P}_b^{\rm ext}$. Or we can use more elaborate probability distribution accounting for our uncertainty in the measurements of distance, proper motion, and Galactic gravitational potential,

$$p(\alpha_0, \beta_0, \dot{P}_b^{\rm ext}) = p(\alpha_0) \times p(\beta_0) \times p(\dot{P}_b^{\rm ext}). \tag{E.3}$$

The last step is to marginalise over the $\dot{P}_b^{\rm ext}$ variable using the correct joint posterior probability with desired priors

$$p(\alpha_0, \beta_0 \,|\, \{t_j\}) = \int d\dot{P}_b^{\rm ext}\, p(\alpha_0, \beta_0, \dot{P}_b^{\rm ext} \,|\, \{t_j\}), \tag{E.4}$$

where the integral is calculated on the grid of $\dot{P}_b^{\rm ext}$ parameter. The marginalised probability than can be used to derive limits, for instance going back to χ^2 representation with 2 degrees of freedom.